Magnetic Resonance Studies of

Transport and Reaction in Vortical Flow

by

Antoine Vallatos

A thesis submitted to
The University of Birmingham
For the degree of
DOCTOR OF PHILOSOPHY

School of Chemistry
College of Engineering and Physical Sciences
The University of Birmingham
October 2013

UNIVERSITY OF BIRMINGHAM

University of Birmingham Research Archive

e-theses repository

Abstract

This thesis explores the coupling of autocatalytic reactions, such as the oscillating Belousov-Zhabotinsky reaction, with vortical flows produced in a Couette cell. Similarly to many Reaction-Diffusion-Advection (RDA) systems found in nature, the resulting systems are characterised by chemical cycles maintained out of equilibrium by transport processes involving complex flow properties, such as periodicity and vorticity. In this project, an integrated approach was developed, combining optical and magnetic resonance techniques with modelling, to study transport and reaction in vortical flows.

Flow structure and molecular displacements within stationary and translating vortices were investigated using a combination of magnetic resonance (MR) velocity and diffusion mapping with MR propagator experiments. A model based on MR experimental data was developed to simulate molecular displacements and provide quantitative information on micro-mixing and long time-scale axial dispersion. Simulations of molecular displacements allow linkage of molecular transport with the propagation of chemical waves travelling through vortical flows. The macroscopic patterns arising from these RDA systems, in combination with modelling results, allowed understanding coupling mechanisms between flow and chemistry and characterising inter- and intra- vortex mixing. Finally, MR imaging of chemical waves was shown to compare well with molecular displacement simulations, providing with a means for characterising the interplay of flow and chemistry in reactive flow systems.

With love to my three beautiful families

Acknowledgments

Time and space appeared as the unbreakable constraints to the holistic acknowledgment approach I would have liked: pages and pages acknowledging every single human interaction that through these years helped me make small steps in the little odyssey that ended with the book you hold in your hands. Inevitably, before focusing on the beautiful people that had major contributions to this work, I owe some sincere excuses to those that will not see their name in the following pages. From the bottom of my heart and soul, I would like to thank:

- My supervisor and research companion over these years, the explosive Dr. Melanie M. Britton, for accepting me in her group, for teaching me, for believing in me and for challenging me enough to make me feel that I deserve to be called a doctor.

- My research group, past and present: Dr. Jan Novak, for setting the grounds of my research and transmitting me his precious knowledge (including slang). Rhys Evans for tolerating my obsessive supervision and producing some wonderful pattern formation data. Dr. Heather Rose, for taking care of me when I joined the team and making sure that I do not kill myself in the lab. Sue Law for following her dreams: love, passion, pain, science and rock'n'roll. Amanda Mills, for helping me understand all these little magnetic things. Matt Berwick, for his funky T-shirts and swirly peptides. Ismailla Abdullahi, for keeping the smile alive. Catherine Smith, for rocking the bars of Cambridge with me.

- My collaborators: Dr. Annette F. Taylor and Dr. Mark C.T. Wilson, for our intense and productive meetings that lead to the publications that arouse from this work.

- My examiners: Dr. Andy Sederman and Prof. David Parker, for reading this text, providing me with a challenging but extremely instructing viva and with corrections that raised the level of this work. Dr. Josephine Bunch and Prof. Roy L. Johnston for reading my first year report.

Contents

1 Introduction

1.1 Prologue

Understanding the coupling between chemical reactions and transport processes is crucial in a wide variety of disciplines as biology, chemical engineering and atmospheric science. This coupling is ubiquitous in nature and can give rise to pattern formations both at the microscopic and macroscopic length scales, generating phenomena as diverse as the movement of cellular contents[1] (streaming) or the growth of plankton colonies[2] (blooming) in oceanic currents. Many of these systems are characterised by the presence of non-linear autocatalytic chemical cycles, maintained out of equilibrium by the supply of new reactants. The transport processes that are mobilised to ensure this supply of matter, often involve the flow properties of three-dimensionality, periodicity, vorticity and anisotropic diffusion. The complexity of the resulting systems tends to restrict their analysis to specific field approaches (e.g. fluid mechanics, physical chemistry), and the multitude of influencing parameters introduces difficulties in bringing together experimental and theoretical results.

This thesis has taken an integrated approach, combining optical and magnetic resonance (MR) techniques with modelling, to study the coupling between transport and reaction in vortical flows. Particular attention is given to pattern formation arising from the combination of the oscillating Belousov-Zhabotinsky (BZ) reaction with translating vortical flow in a Couette cell. As for the biological processes mentioned earlier, maintaining the system far from equilibrium is achieved by sustaining a flux of matter and energy. Molecular processes taking place in such systems can lead to macroscopic patterns many orders of magnitude

greater than the molecular scale.

The BZ reaction is the most famous example of an autocatalytic reaction exhibiting temporal oscillations[3–5]. Since its discovery, several studies have been conducted to understand its ability to self-organise. Because of its oscillatory behaviour, the BZ reaction is known to produce travelling chemical waves that are spatially distributed through transport processes as diffusion and advection. The resulting reaction-diffusion (RD) or reaction-diffusion-advection (RDA) systems have been very studied because, under certain conditions, they give rise to very particular pattern formation phenomena, as stationary chemical waves.

Taylor vortices are produced in the annulus between a rotating inner cylinder and a fixed outer cylinder of a Couette cell. Above a critical rotation rate of the inner cylinder, the flow reorganises in a series of counter rotating vortices stacked along the length of the cell[6]. Taylor Vortex Flow (TVF) has been the object of numerous publications[7]. The addition of axial pipe flow to TVF was shown to cause a translation of the vortices, producing a vortex flow reactor (VFR). At certain regimes, flow in a VFR exhibits plug-like properties that are of particular interest to several applications in various fields such as chemical engineering[8] or biochemistry[9].

Most of experimental pattern formation studies using the BZ reaction and involving flow have been done in two-dimensions using optical imaging techniques[10]. Similarly most of the existing studies on the flow properties within a Couette cell have used optical techniques like Particule Imaging Velocimetry (PIV)[11] or dye visualisation[12]. Optical techniques present limitations in addressing microscopic properties as they necessitate the introduction of tracers

that can perturb the system. The ability of MR techniques to probe, non-invasively, both chemical patterns and flow properties[13] makes them ideally suited for studying the interplay of chemistry and flow within these fragile systems. This project has focussed on developing both the techniques and the methodology that enable the systematic study of the coupling between chemistry and flow using magnetic resonance.

The combination of flow and chemistry can lead to complex behaviour of the system, producing data that are not easy to analyse. To deal with this, an analytic approach was used to produce models that reduce the amount of data to handle, in order to obtain accessible qualitative and quantitative information. This approach has necessitated the definition of the appropriate levels of description[4,14] that allow identifying correlations between various parameters:

- A **molecular level** where individual molecules and collisions are considered. Depending on Arrhenius parameters, a percentage of these collisions lead to reactions. At this level, temperature and diffusion set a common ground between chemistry and molecular transport possesses.

- A **microscopic level** that deals with volume elements that are big enough to define densities of molecules at different phases (chemical concentrations) and average velocity or diffusion/dispersion (flow properties). At any given time, and for each volume element, inlets and outlets can be defined by flow properties and chemical state can be defined by concentration of different species.

- A **macroscopic level**, where vortices can be presented as elementary units of vortical flow systems and pattern-forming systems can be studied as entities that arise through the inseparable coupling between flow and chemistry.

Throughout this project, one or more of these levels of description have been employed. It should be stressed that, for a same system, the information provided at each description level is not equivalent. One can notice that the macroscopic pattern formation arising from the combination of flow and chemistry provides with properties that are not existent at the molecular level.

1.2 Thesis outline

This study draws upon previous research conducted across a diverse range of scientific disciplines: non-linear chemistry, fluid mechanics, fluid/chemistry coupling and NMR/MRI techniques. The first part of this presentation (Chapter 1) will set the background for the flow and chemistry coupling studies that will follow, while trying to make the necessary links with the field of magnetic resonance (MR). This background review will introduce both autocatalytic oscillating reactions and flow properties in chemical reactors, before presenting the flow distributed chemical structures that arise from the combination of flow and chemistry. Chapter 2 introduces the MR techniques that are encountered in this thesis. The first experimental chapter (Chapter 3) presents MR studies, combining velocity and dispersion mapping with measurements of molecular displacements, for the characterisation of stationary vortex flow. The next chapter (Chapter 4) expands these studies to translating vortex flow. In chapter 5, simulations of molecular displacements using MR experimental results are performed in order to allow the prediction of axial dispersion and molecular paths in stationary and travelling vortex flows. Results presented in chapters 3 to 5 have been published in Europhysics letters[15] (Appendix C). Chapter 6 introduces oscillating chemical reactions and examines the macroscopic patterns formed by the combination of chemistry and

travelling vortices (Flow Distributed Oscillations). Results presented in this chapter have been published in Chaos[16] (Appendix D). The last part of this thesis focuses on MR studies of the coupling between oscillating autocatalytic chemistry and vortical flow (Chapter 7). This presentation ends with an overview of the results and questions that arose throughout this project and a discussion on future research possibilities (Chapter 8).

1.3 Autocatalysis and oscillating chemistry

1.3.1 From autocatalysis and feedback to clocks and fronts

A chemical reaction is said to be autocatalytic, if the reaction product is also a catalyst for the reaction[17]. An example of this is a reaction where $A + B \rightarrow 2B$, with B being the autocatalytic species. In this model scheme, the rate r of the reaction is of the form $r = k[A][B]$, showing that an increase in [B] produces a rate increase.

Typically, such model schemes are composed of several elementary steps, and feedback arises when the products of the later steps influence the rate of some of the earlier steps, and, hence, the rate of their own production. This may take the form of either positive feedback (self-acceleration) or negative feedback (self-inhibition), and result in rapid changes in the concentration of intermediate species. If the colour of these species is visible and the reactants well stirred, this acceleration can lead to a sharp colour change of the entire solution. Where only a single positive feedback process is present, the result is a clock reaction characterised by an induction time before the observation of the rapid concentration change. This is due to the fact that the autocatalytic species needs to attain a sufficient concentration for the

autocatalytic step to be initiated. Other elementary steps often compete for the autocatalytic species, delaying the onset of the autocatalytic step. Species involved in such steps are called inhibitors. In an unstirred vessel, if the reaction is initiated in a localised region, there will be a rapid increase in the concentration of the autocatalyst, which will then propagate into neighbouring space through diffusion producing an autocatalytic front. In an isotropic aqueous-phase mixture, an autocatalytic front propagates with a constant waveform and at a constant velocity[18]. This velocity will mainly depend on the diffusion coefficient of the autocatalytic species and the rate constant of the reaction.

Clock reactions and single travelling fronts typically arise through a single autocatalytic process taking the initial reactants through to the final product. For multiple waves, such as that found in an oscillatory reaction, there must be some way of 'resetting the clock'.

1.3.2 The BZ oscillating reaction

1.3.2.1 The BZ reaction mechanism

In an oscillatory reaction, the positive feedback step is coupled with a negative feedback process. This enables the system to cycle between positive and negative feedback steps. In the case of the BZ reaction[19], malonic acid is oxidised by an acidified bromate solution in the presence of a metal ion catalyst. The most commonly used catalyst couple is $[Fe(II)(phen)]^{2+}/[Fe(III)(phen)]^{3+}$ (ferroin/ferriin). In a well-stirred closed system, the reaction starts oscillating, typically following a short induction period, depending on the catalyst used. In the case of the ferroin-catalysed BZ reaction, there is a colour change which alternates between red (ferroin) and blue (ferriin), with periods varying from of a few seconds to several

minutes[17]. At every cycle, a proportion of the main reactants (bromate and malonic acid) is consumed. That causes the oscillations to occur for a finite period, as the system moves towards chemical equilibrium.

More than 80 elementary steps have been identified in the BZ reaction. A simplification of the involved mechanisms was necessary for the understanding of the chemical oscillation behaviour. The most used scheme describing the BZ reaction is the Field-Körös-Noyes (FKN) mechanism[20,21], which identifies 3 main processes (induction - A, positive feedback - B and negative feedback - C).

Process A: Removal of the inhibitor

$$BrO_3^- + 2Br^- + 3H^+ \rightarrow 3HOBr \qquad\qquad\qquad\qquad (\textit{1.1})$$

For the autocatalytic process to be initiated, bromide ion concentration must be sufficiently low. This is due to the fact that bromide ions are competing for the autocatalytic species, playing the role of an inhibitor. The process for the removal of the inhibitor is shown in reaction 1.1.

Process B: Autocatalysis

$$BrO_3^- + HBrO_2 + 2M_{red} + 3H^+ \rightarrow 2HBrO_2 + 2M_{ox} + H_2O \qquad\qquad (\textit{1.2})$$

$HBrO_2$ is the autocatalytic species involved in the BZ reaction. The autocatalytic process is given in reaction 1.2. During this process one molecule of $HBrO_2$ is giving two molecules of $HBrO_2$ (autocatalysis) and the metal catalyst (M) is oxidised. If the oxidised and reduced

forms of the catalyst produce different colours, then a sharp colour change will characterise the autocatalytic step.

Put Together, processes A and B constitute a typical clock reaction. To obtain an oscillation a third process is needed in order to 'reset the clock'.

Process C: Resetting the clock

$$2M_{ox} + MA + BrMA \rightarrow fBr^- + 2M_{red} + \text{other products} \qquad (\,1.3\,)$$

By providing bromide ions (inhibitor) and reducing the catalyst back to its lower oxidation state process C brings the reaction back to process A. During this process, both malonic acid (MA) and bromomalonic acid (BrMA) react with M_{ox} to give the reduced form of the catalyst and, in the case of BrMA, to produce bromide ions. The stochiometric factor f represents the bromide ions produced when two M_{ox} ions are reduced.

The introduction of the simplified FKN mechanism allowed the development of systems of kinetic equations characterising the BZ system, such as the Oregonator[21] and Brusselator[22] models. The Oregonator model retains the dominant reactions of the FKN reaction mechanism and their rate constants k_n. The model reactions can be expressed by a set of differential equations describing the kinetic behaviour of the main reactants. Under certain conditions this model can be reduced to a two-variable one, which allows using the analytical theorems for two-variable systems. Also, by combining the model with diffusion or flow equations, one obtains reaction-diffusion (RD) or reaction-diffusion-advection (RDA) equations[23] that allow analysing the spatial behaviour of the chemical systems. The use of such models allows prediction of complex behaviour when the BZ reaction is coupled with flow.

8

1.3.2.2 BZ reaction variants

There is a rich literature on variations of the BZ reaction[24], with many possible reductants and the bromate oxidant as the only constant reagent. For the catalyst, several ions have been successfully used as Ce, Mn, Fe and Ru. For the cerium- and manganese-catalysed BZ reactions, a critical concentration of bromomalonic acid needs to be reached before the onset of the oscillations, resulting in an induction period[25]. This is not observed in the ferroin- or ruthenium-catalysed reactions[26].

1.3.2.3 Studying the oscillatory behaviour

Zhabotinsky *et al.*[27] related the BZ oscillations with the initial reagent concentrations using parameter space plots. Various waveforms were found in the oscillatory regions (ranging from sinusoidal to relaxation) and multipeak oscillations were identified near the limits. In parallel to the study of the chemical oscillations, several techniques for their measurement emerged.

Optical measurements in well-stirred vessels were mainly performed on the ferroin-catalysed BZ reaction, offering the best colour contrast between the oxidised and reduced phases (red/blue). For manganese- or cerium-catalysed BZ reactions, where the colour change is less distinct, oscillations can be better observed using a UV-visible spectrophotometer[28].

A more accurate way to visualise the temporal oscillations of the system is potentiometry (Figure 1.1). What is usually measured is the concentration of bromide ions (bromide ion sensitive electrode) or the oxidation state of the metal-ion catalyst (platinum electrode).
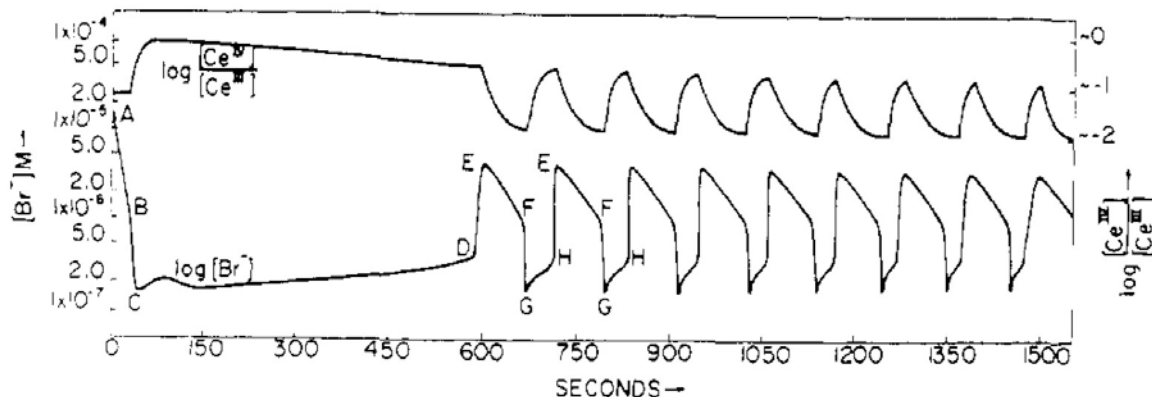
Figure 1.1. Oscillations in the cerium-catalysed BZ reaction measured using potentiometric methods: The lower trace shows oscillations in bromide concentration, and the upper trace shows oscillations in the oxidation state of the cerium catalyst[21]. Reprinted from ref.21, Copyright 1972 American Chemical Society.

Nuclear magnetic resonance (NMR) has been also used to probe the BZ reaction oscillations. Adding paramagnetic species has a strong effect on the MR relaxation rates of water protons measured by ^{1}H NMR. This makes NMR able to probe redox reactions and kinetics involving paramagnetic ions. The first ^{1}H NMR study of the BZ reaction was reported by Schluter and Weiss in 1981[29]. To probe temporal oscillations of the MR relaxation rate, they used the Mn^{2+} / Mn^{3+} catalyst. The interaction between Ce^{3+} and the water protons was shown to be too weak to be probed and the ferromagnetic ferroin/ferriin couple is not adapted to NMR measurements[28]. Hansen *et al.*[30] also showed that the transverse MR relaxation time of water protons is more strongly affected by Mn^{2+} than by Mn^{3+}. The induction and oscillation periods they measured were found to be in qualitative agreement with electrode measurements, revealing the ability of NMR to perform in situ monitoring of organic species

variations during the oscillations. Other techniques used for measuring BZ oscillations are calorimetric measurements[31] and CO_2 release measurements[32].

1.3.2.4 Main parameters influencing the BZ reaction behaviour

The BZ reaction is very sensitive to external perturbations. For temperatures below 35 °C and for different stirring rates, increase in temperature has been shown to increase the BZ reaction rates, therefore decreasing the oscillation and induction period[33,34]. Above 15°C, a stirring rate increase is followed by an increase in oscillation period in closed systems[33] and a decrease in oscillation period in open systems[34]. Oxygen has also been shown to have important influence on the BZ reaction[35], with an increase in oxygen causing an increase in induction period and decrease in oscillation period. Finally, gravity[36] can also affect the BZ behaviour but becomes significant in very specific systems.

1.3.3 Oscillatory system studies

In reaction-diffusion (RD) systems, the BZ reactants are distributed in space by the interplay of diffusion with local chemical reactions converting substances into each other. When the BZ reaction occurs in a homogeneous medium, sustained oscillations in the chemical concentrations appear for certain ranges of initial composition of the mixture. In an unstirred shallow layer (e.g. in a Petri dish), the reaction produces various forms of wave-like patterns[37], the most common being concentric circles (Figure 1.2) or rotating spirals (Figure 1.3). Typically, an area exceeding the critical reactant concentration acts as an excitation site from where the waves are initiated.
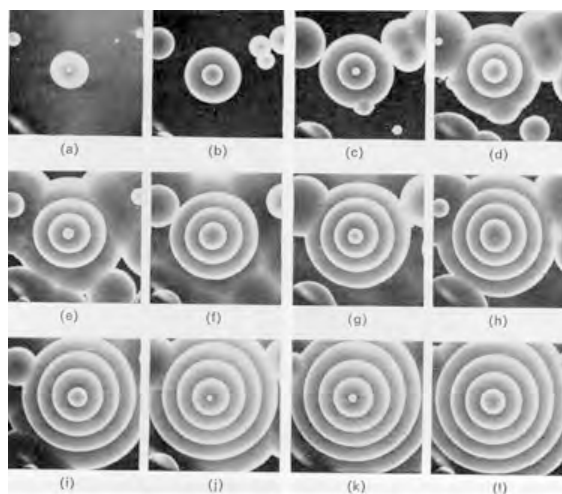
Figure 1.2. Propagation of 2D concentric waves of the BZ reaction. From the left to the right, time is increasing of 1 minute between each image[37]. Reprinted from ref.37, Copyright 1970 Macmillan Publishers Ltd.

The patterns created by the BZ reaction in a Petri dish can present several similarities with biological systems, as slime mold expansion[38] (Figure 1.3). However, unlike cases such as this starving slime mold example, most biological systems are open systems, where matter and energy exchange continuously with their environment. In 1987, Noszticzius *et al.*[39] coupled the BZ reaction with an open flow gel reactor and observed sustained travelling waves for a wide range of parameters. This work opened the way for the studies of spatiotemporal patterns in open systems.
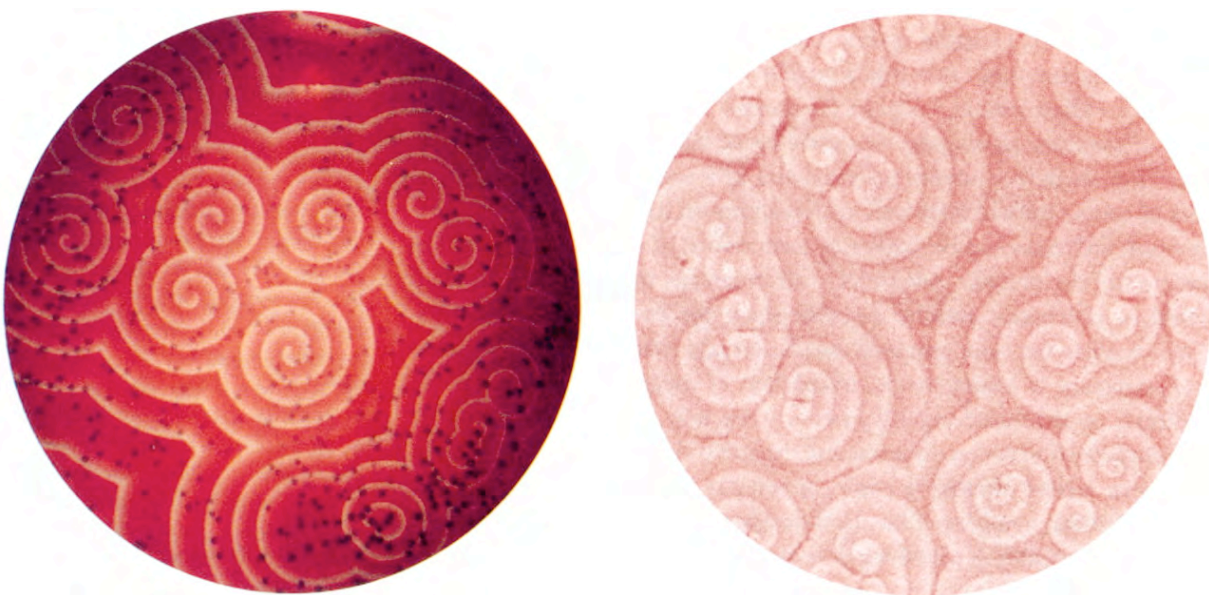
Figure 1.3. Similarities between the BZ reaction rotating spiral waves (left hand) and a starving Dictyostelium discoideum slime mold aggregation picture (right hand)[38]. Reprinted from ref.38, Copyright 2006 National Academy of Sciences, USA.

In open systems, the distribution of molecules is produced both by diffusion and mass transport (convection). The distinction between these two must be very carefully considered, as interaction between convection and diffusion is encountered in all mixing phenomena. When chemical reactions couple with flow, reaction-diffusion-advection (RDA) systems are produced. In the case of continuous flow, the molecules spend only a finite time into the reactor, and if this time is short enough, the reaction is not able to approach the chemical equilibrium state: the system is maintained 'far from equilibrium'. Such systems, initially considered inappropriate for studying pattern production in chemistry, progressively became very important. One reason was the discovery that oscillating reactions can create stationary patterns when flowing through open reactors. But the main reason comes from their resemblances with various biological ecological systems and phenomena going from cell

morphogenesis[40] to plankton blooming[41] in the ocean. In fact, most living organisms are open flow and 'far from equilibrium' systems.

Before addressing these pattern forming RDA systems, it is important to have a closer view on some of the transport properties of chemical reactors.

1.4 Flow properties of chemical reactors

Since all of the liquids studied in this thesis are low concentration aqueous solutions at laminar flow regimes, an overview of transport processes in laminar flow will be given prior to the presentation of the reactor properties.

1.4.1 Introduction to Newtonian laminar flow properties

1.4.1.1 Temperature and diffusion

Fick's laws describe the diffusion of solute molecules from higher to lower concentrations in order to equalise concentration gradients in a system. For a local concentration gradient of particles $\boldsymbol{n}(\boldsymbol{r},t)$, thefirst Fick's law is given by:

$$J = -D\nabla\boldsymbol{n}(r,t) \qquad\qquad (\ 1.4\ )$$

Where J is the diffusion flux caused by the concentration gradient $\nabla\boldsymbol{n}$. The time rate of change of $\boldsymbol{n}(r,t)$ is related to the local flux divergence, $\nabla \cdot J = D\nabla^2\boldsymbol{n}$, which is leading to the diffusion equation, the second Fick law:

$$\frac{\partial \boldsymbol{n}}{\partial t} = D\nabla^2\boldsymbol{n} \qquad\qquad (\ 1.5\ )$$

This behaviour of solute molecules is often termed mutual diffusion, as opposed to self-diffusion, which is applied in the case of liquids comprising a single molecular component. In the latter case, no concentration gradient exists and the random motion of molecules, also called Brownian motion, is driven by thermal energy. The Stokes-Einstein equation, describes a relationship between temperature, diffusion and viscosity:

$$D = \frac{k_B T}{6\pi\mu R} \qquad\qquad (\ 1.6\ )$$

where D is the self-diffusion coefficient, k_B is Boltzman's constant, T is the temperature, μ is the dynamic viscosity and R is the radius of a sphere containing each molecule.

To see how the self-diffusion coefficient can give information on molecular motion, one needs to consider an ensemble of molecules sufficiently large and the probabilistic distribution of three dimensional molecular coordinates $r(t)$. $p(r,t)dr$ is the probability that $r(t)$ is found between r and $r + dr$. Since there is a random motion of molecules, $p(r,t)$ obeys Fick's laws and so does the conditional probability density $P(r|r',t)$ where r are the initial coordinates and r' the final coordinates. One can then write:

$$p(r',t) = \int p(r,0)P(r|r',t)dr \qquad\qquad (\ 1.7\ )$$

and since $p(r',t)$ obeys Fick's diffusion law for arbitrary initial conditions $p(r,0)$, then the conditional probability also obeys the following partial differential equation:

$$\frac{\partial P(r|r',t)}{\partial t} = D\nabla_{r'}^2 P(r|r',t) \qquad\qquad (\ 1.8\ )$$

For an infinite extent fluid and taking $P(r|r',0) = \delta(r'-r)$ as the initial condition, the solution to the equation is:

$$P(r|r',t) = (4\pi Dt)^{-3/2} \exp(-\frac{(r'-r)^2}{4Dt}) \qquad (1.9)$$

This equation, only valid for an isotropic medium where $P(r|r',t)$ is Gaussian in nature, leads to a relationship between the average displacement and the diffusion coefficient:

$$\langle (r'-r)^2 \rangle = 6Dt \qquad (1.10)$$

In one dimension (*z*), this relationship becomes $\langle (Z'-Z)^2 \rangle = 2Dt$ and the dependence of $P(Z|Z',t)$ on time can be seen on Figure 1.4. The normal distribution broadening at the average height is equal to $\sqrt{2Dt}$.
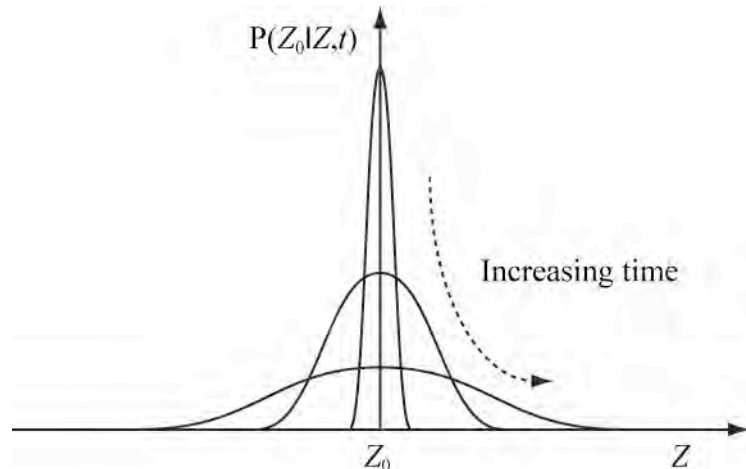
Figure 1.4. Plot of the conditional probability of displacement along Z for an ensemble of particles diffusing. Each curve corresponds to a different diffusion time.

But for most of the systems presented in this work the effects of velocity and dispersion have dominant roles making the motion of particles strongly anisotropic.

1.4.1.2 Velocity and dispersion

In the case of a liquid of constant dynamic viscosity μ, the application of Newton's second law leads to Navier-Stokes (NS) equation, which relates the molecular acceleration to the forces applied on the system (pressure gradients, body forces, gravitational forces):

$$-\nabla p + \mu \nabla^2 U + f = \rho \frac{DU}{Dt} \qquad (1.11)$$

where p is the pressure, ρ is the density, U the velocity and f the body force acting on the fluid. If this liquid is incompressible we also have the additional equation $\nabla \cdot U = 0$. Solving this equation allows to obtain $U(r,t)$. The non-dimensional form of the NS equation provides with the dimensionless Reynolds number, giving the relative size of convective to viscous effects:

$$Re = \frac{\rho U^2 / L}{\mu U / L^2} = \frac{UL}{\nu} \qquad (1.12)$$

where μ is the dynamic viscosity, ν is the kinematic viscosity, U a characteristic velocity and L a characteristic length of the system. For low Re it is possible to calculate exact solutions of the NS equation. For higher Re, convective effects become dominant, inducing turbulent solutions. This work will focus on low Re, laminar flows. A steady-state laminar flow is a flow in which local velocities do not change over time. Steady-state can be found even in complex flows. In the case of steady vortical flow for example, characterised by the spinning motion of a fluid near some point there are velocity gradients in space but not in time. Those gradients generate molecular movements that diffusion alone cannot characterise. The phenomenon in which initially adjacent molecules tend to become separate during flow is referred as dispersion. Dispersion is generated by the interplay between diffusion, velocity

gradients and boundary layer effects. Where dispersion is present, molecular transport can lose its linear dependence on time and equation 1.10 has to be rewritten as:

$$\left\langle (\boldsymbol{r}' - \boldsymbol{r})^2 \right\rangle \sim t^{\gamma} \qquad\qquad (\textit{ 1.13 })$$

When γ is different than 1, molecular displacements follow anomalous transport processes[42]. Sub-diffusion occurs for $\gamma < 1$, and the flows are characterised by the presence of "sticking regions", where molecular displacements can be smaller that self-diffusion. Sticking regions have been identified in both vortical[43] and time-dependant[44] flows. When $\gamma > 1$, molecular displacements are characterised by the presence of long distance displacements. Such displacements, termed Lévy flights[45], have also been observed in 2D vortical flow[46].

Solomon *et al.*[47] studied the mixing of a fluorescent uranine dye into a 2D chain of counter-rotating vortices. The flow was produced using a magnetohydrodynamic technique to periodically force the fluid (Figure 1.5).
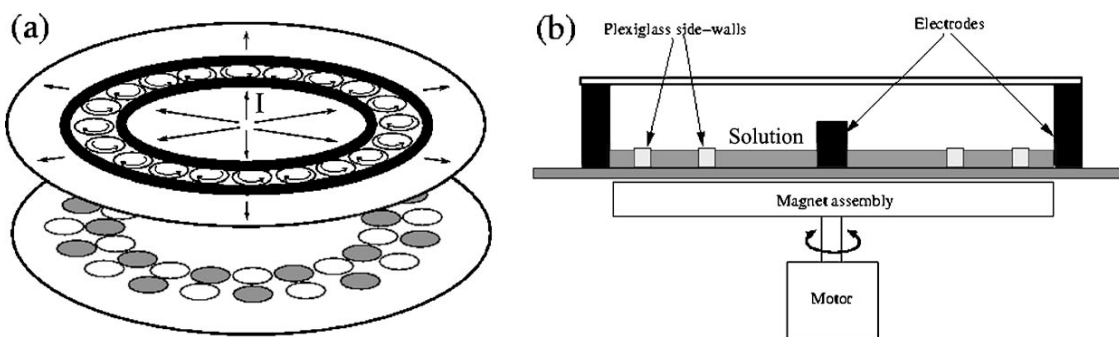
Figure 1.5. (a) Exploded view of the magnetohydrodynamic forcing technique[48] used to obtain an annular vortex chain bounded by two plexiglass rings (shown in black) and (b) side view of the apparatus, showing the motor activated magnet assembly used to force the flow. Reprinted from ref.48, Copyright 2006 American Physical Society.

Fluorescent black light lamps were used to illuminate the fluid and the system was imaged from above using a camera. Figure 1.6 shows a series of decurled images obtained from this system. These images reveal complex mixing behaviours that can be observed in vortical flow, as the presence of lobes in the dye propagation. Three of these lobes can be seen on the top image, with two carrying dye to neighbouring vortices and one carrying clear solution into the dye region. In the successive images, these lobes are stretched by the flow and folded back several times before the dye mixed with the core region. The phenomenon of unmixed vortex cores was attributed to the presence of barriers to fluid mixing. Mixing in the vortex core is obtained only through diffusion/dispersion and a weak secondary flow that brings molecules from below the vortex surface to the vortex core. This effect can be seen on the last image of these series, where the vortex core starts becoming clear, suggesting that clear fluid is circulated through the centre.
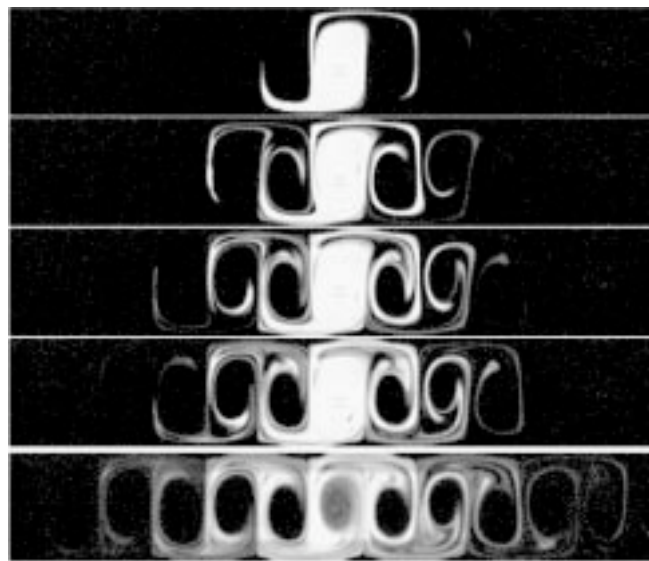
Figure 1.6. A series of decurled images images showing the mixing of uranine dye in the chain of vortices[47]. Images (from the top) were taken at intervals corresponding to 1, 2, 3, 4, and 10 oscillation periods of the flow. Reprinted from ref.47, Copyright 2006 American Physical Society.

In the case of time-dependant 3D vortical flow, Solomon *et al.*[49] showed that uniform mixing could also occur via a resonant mixing mechanism. Resonance phenomena seem to occur when the system is forced at a period that is resonant with the circulation times. Due to the complexity of molecular displacements, a probabilistic approach is usually used for the analysis of such systems.

1.4.1.3 Propagator analysis

In order to present the features of the probability distribution of molecular displacements in the presence of flow and dispersion, it is better to consider the simple case of a steady-state laminar flow where all molecules move at constant velocity $U = U_c$. In this system, the conditional probability of displacement, P, is independent of the starting position and depends only on the displacement $\boldsymbol{R} = \boldsymbol{r}' - \boldsymbol{r}$.

$$P(\boldsymbol{r}|\boldsymbol{r}',t) = \delta(\boldsymbol{r}' - (\boldsymbol{r} + U_c t)) \tag{ 1.14 }$$

Where both flow and diffusion are present it is possible to convolve flow and diffusion conditional probabilities. The final conditional probability, also known as the average propagator, is obtained after averaging over all starting positions is therefore very similar to the diffusion one:

$$\bar{P}(\boldsymbol{R},t) = (4\pi Dt)^{-3/2} \exp(-\frac{(\boldsymbol{R} - U_c t)^2}{4Dt}) \tag{ 1.15 }$$

The relative contribution of diffusion and flow involved in this convolution are shown in Figure 1.7, for one dimension (z).
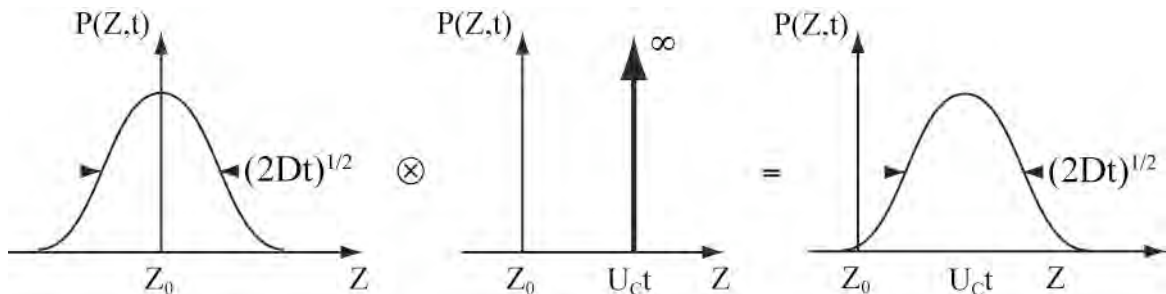
Figure 1.7. Convolution of the conditional probability of uniform diffusion and conditional probability for uniform velocity profile flow gives the average propagator for a flow combining both features.

Unfortunately, in reality, the presence of velocity gradients causing dispersion or anomalous diffusion is very common, so the conditional probability of molecular displacements looses the Gaussian shape that characterises simple diffusion processes. The average propagator will take more complex forms since small changes in position transverse to the flow due to diffusion might induce big changes in the longitudinal position due to big changes in velocity. This interplay between diffusion and flow heterogeneity, known as Taylor dispersion[50], can become dominant for complex flows such as those found in chemical reactors.

1.4.2 Packed-Bed Reactors (PBRs)

Packed-bed reactors are typically tubular reactors filled with either inert or catalytic solid particles[51,52]. The feed is connected to one end and the product leaves from the other end. As a consequence, the properties of such reactors will vary from one point to another, both in the

radial and axial directions. Under certain conditions, the PBR can be considered as a plug–flow reactor made of translating, well-stirred batch reactors (Figure 1.8). These conditions involve negligible mixing in the direction of the flow, complete radial mixing and a constant velocity in the radial direction. The validity of the plug-flow approximation of a PBR depends both on the geometry of the reactor and the imposed flow properties. Deviations are always present but their importance will depend on the chemical system that is flowing through the reactor. Generally, the plug-flow assumptions tend to hold at high Reynolds numbers (good radial mixing) and / or high L/R ratios (axial mixing is neglected).
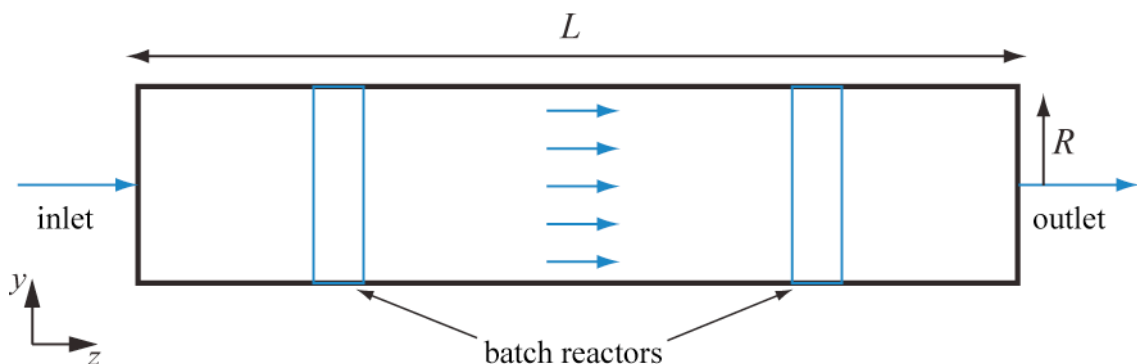
Figure 1.8. Schematic diagram of a plug-flow reactor.

Considering the plug-flow approximation, a PBR can be modelled as a series of batch reactors. Uniform mixing in each batch reactor of volume dV composing the PBR allows to perform material balance: accumulation = input – output – loss through reaction.

By substituting mathematical expressions to the given terms it is possible to calculate the design equation of this reactor as:

$$r_A = \frac{dn_A}{dV}$$

(1.16)

where r_A is the reaction rate of a given component A, and dn_A is the molar flow rate of a volume element dV. The system can be characterised by the mean residence time, defined by the volumetric flow rate of the reactor. Reactors are also characterised by the relationship between r_A and the conversion rate of a reactant A, $x_A = \frac{n_{A0} - n_A}{n_{A0}}$. For example, Figure 1.9 gives the inverse reaction rate versus conversion for a given positive order reaction. The area under the curve is proportional to the volume passing through the reactor.
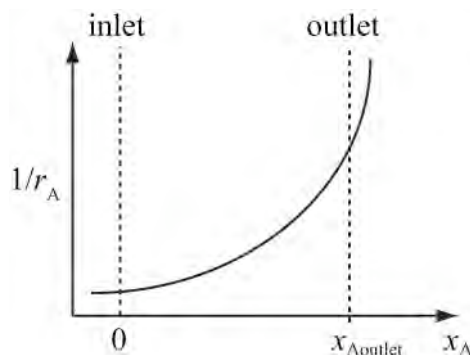
Figure 1.9. Inverse of the reaction rate against conversion for a positive order reaction in a plug-flow reactor.

1.4.3 Continuous Stirred Tank Reactors (CSTRs)

Continuous Stirred Tank Reactors (Figure 1.10) are simple open batch reactors commonly used in chemical engineering processes[51,52].
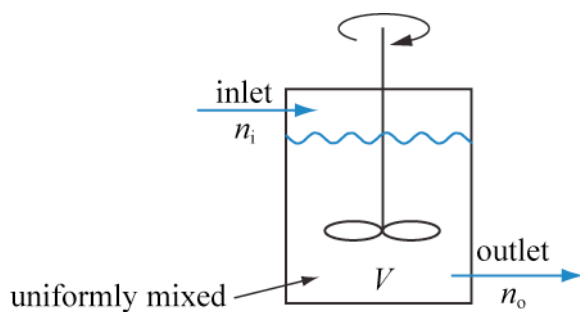
Figure 1.10. Schematic diagram of a CSTR of volume V. The stirring bar ensures uniform mixing in the reactor.

Mixing in a CSTR is assumed to be high enough so as to consider temperature and composition of the reaction mixture as uniform throughout the reactor. The CSTR operation is often modelled in three stages (beginning to overflow, overflow to steady state, steady state). In this work we will consider only mass transfer in CSTRs where steady state has been reached, but the initial unsteady states might help us interpret some of the observed results. Material balance for the entire volume of the system is given by: accumulation = input – output – loss through reaction. Where there is no accumulation, the input and output are molar flows (n_i and n_o respectively) to and from the reactor and the reaction loss will be the product of the reaction rate (r) and the volume of the reactor. Material balance within the CSTR resumes to $n_i - n_o - rV = 0$ and the design equation is given by:

$$r = \frac{(n_i - n_o)}{V} \qquad (1.17)$$

As with the PBR, a CSTR can be characterised by the relationship between r_A and the conversion rate of the reactant A. Figure 1.11a shows the inverse reaction rate versus conversion for the same positive order reaction used for the PBR with plug-flow properties. The grey area is proportional to the volume passing through the CSTR. The volume necessary

to obtain the same conversion will always be bigger for a CSTR than a PBR in a positive order reaction.

When using CSTRs in series, the reaction is the same at the inlet of a CSTR and the outlet of the previous one. Figure 1.11b shows how this can allow for simulating a plug-flow behaviour with CSTRs. If the number of CSTRs in series tends to infinity, the volume that has to pass through the CSTR chain to attain a certain rate of conversion tends to the plug-flow reactor one.
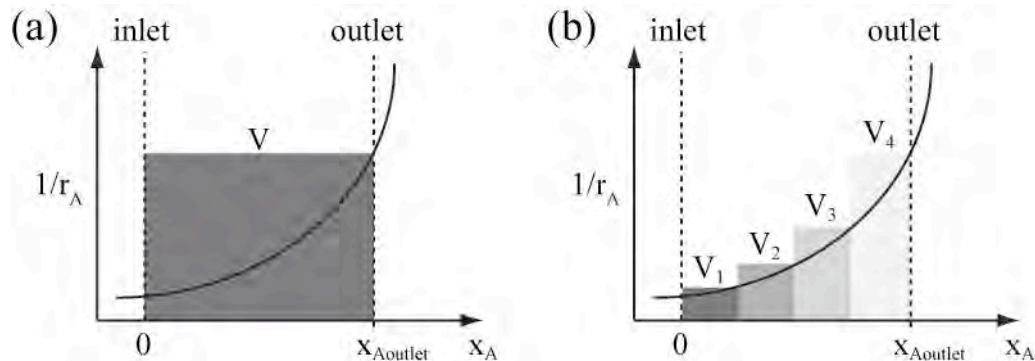
Figure 1.11. Inverse of reaction rate against conversion for a positive order reaction: (a) in a single CSTR of volume V and (b) in a chain of four CSTRs of volumes V_1, V_2, V_3 and V_4. The shaded areas are proportional to the volume of the corresponding CSTRs. The black line indicates the curve obtained for a plug-flow reactor.

1.4.4 Stationary vortices in a Couette cell

The Taylor-Couette flow[53,54] refers to an instability formed in the annulus between a rotating inner cylinder and a resting outer cylinder. Above a critical rotation speed, ω, centrifugal forces overcome viscous ones inside the fluid and Taylor vortices form. The patterns, caused

by the addition of strong secondary flows, initially have shapes of torroidal counter-rotating vortex pairs of wavelength λ stacked along the length of the Couette cell (Figure 1.12).
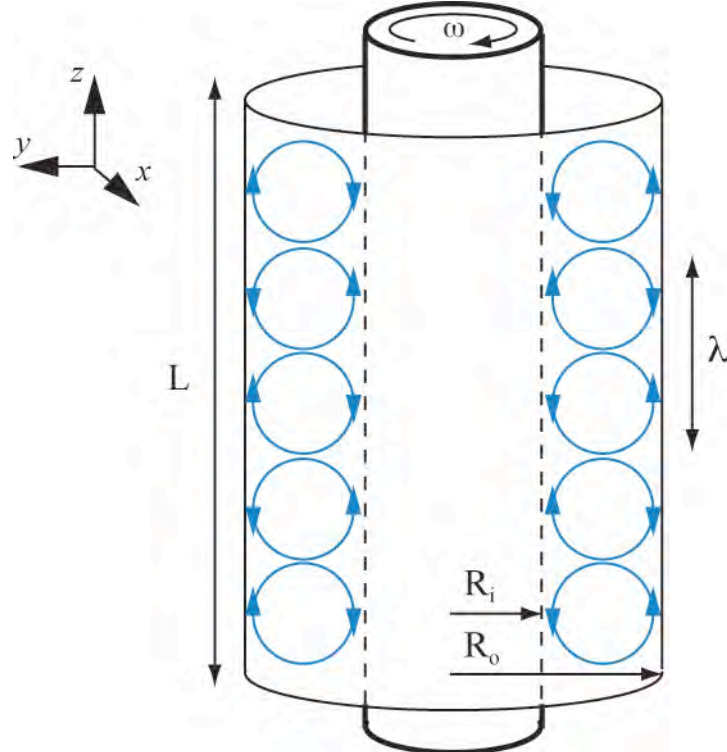
Figure 1.12. Schematic diagram of the Taylor-Couette cell mechanism and of counter-rotating axisymmetric vortices.

In most of the existing literature this flow, referred as Taylor Vortex Flow (TVF), is characterised by a series of dimensionless numbers.

Γ is the length to gap ratio, given by the ratio of the annulus gap length, L, to the annulus gap, d.

$$\Gamma = \frac{L}{d} \qquad (1.18)$$

η is the radius ratio, given by the ratio of the inner cylinder radius, R_i, to the outer cylinder

inner radius, R_o.

$$\eta = \frac{R_i}{R_o} \qquad (1.19)$$

TVF is also characterised by the Taylor number, *Ta*, that gives the importance of centrifugal

forces, due to rotation of fluid about the inner cylinder, relative to viscous forces. *Ta* comes

from the dimensionless form of the NS equation. Many expressions of the *Ta* number can be

found in the literature. In this thesis, an expression that has the same structure as the

Reynolds number will be used, as it has been shown to replace more complicated forms of *Ta*

without significant information loss[55]:

$$Ta = \frac{\omega R_i d}{\nu} \qquad (1.20)$$

Above a critical *Ta* value, which is dependant on each system, Taylor vortices will appear. By

raising the inner rotation rate (and hence *Ta*), TVF progressively transforms in different

recognisable stages. In his review, Koschmieder[53] identifies four main segments: linear or

non-linear axisymmetric TVF, non-linear wavy TVF, irregular or chaotic TVF and turbulent

TVF. This thesis will focus on the laminar and steady axisymmetric TVF regime.

Initial works on the mixing properties of the linear TVF suggested that the system was

characterised by poor inter-vortex mixing, behaving like a chain of CSTRs connected by

dispersion and diffusion. In 1996, Desmet[56] challenged the concept of non-intermixing vortex

units by demonstrating the existence of a strong inter-vortex exchanges in TVF. Later,

Dusting[12] provided additional evidences of inter-vortex mixing, especially near the inner

cylinder, proving that Taylor vortex flow cannot be simply assumed as a series of well-mixed

tanks. However, it has been shown[57] that mixing intensity can be enhanced with a smaller increase in axial dispersion than for more conventional flow types. The problem of unsteady axial mixing between the vortices remains important for the study of the coupling between chemistry and flow in such systems, and chemistry is often used to analyse mixing properties of TVF[58,59].

In 1994, Kose[60] used a fast MR imaging sequence to obtain cross sectional radial velocity maps of the wavy TVF. Hopkins *et al.*[61] showed that it is also possible to analyse the TVF velocity field using NMR stroboscopic techniques. Seymour *et al.*[62] were the first to produce MR velocity maps of laminar TVF in all directions (Figure 1.13).
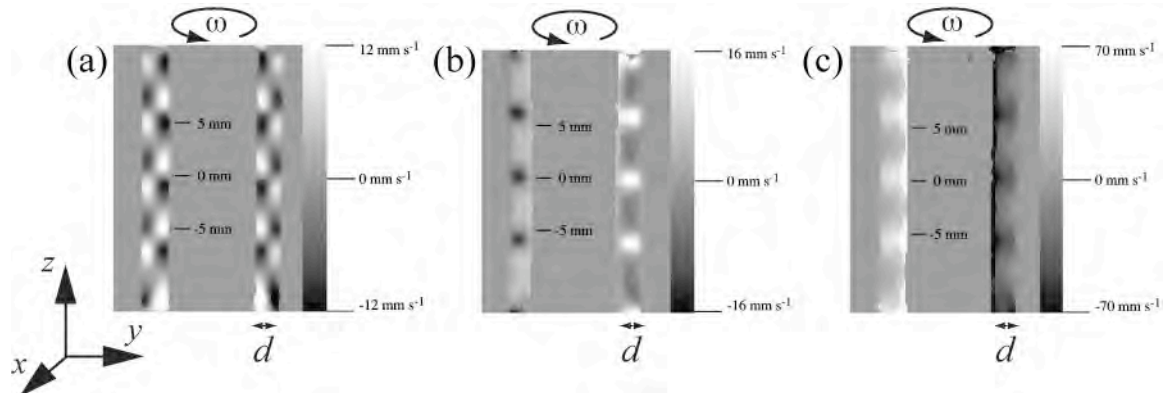
Figure 1.13.Velocity maps of water TVF flow at Ta=246 obtained through the centre of the Couette cell[62]. Velocity magnitude is given by the image intensity, the scale of which is represented on the colour bars on the right of each image. Positive velocities (white) indicate flow in the direction of the axis; negative velocities (black) indicate flow in the opposite direction. Images show velocities in the z direction (a), in the y direction (b) and in the x direction (c). Reprinted from ref.62, Copyright 1999 American Institute of Physics.

1.4.5 Travelling vortices in a Couette cell

A Vortex flow reactor (VFR) is obtained by superimposing steady pipe flow, of average velocity U_{ax}, onto the Taylor vortex flow formed in a Couette cell. The resulting flow produces vortices travelling at velocity U_{TV} along the cell. Figure 1.14a shows a schematic diagram of the VFR. These reactors are widely used because under certain conditions the addition of TVF seems to transform the parabolic velocity profile of the pipe flow (Figure 1.14b) into a plug like-flow made of vortices travelling at constant superficial speed U_{TV} (Figure 1.14c).
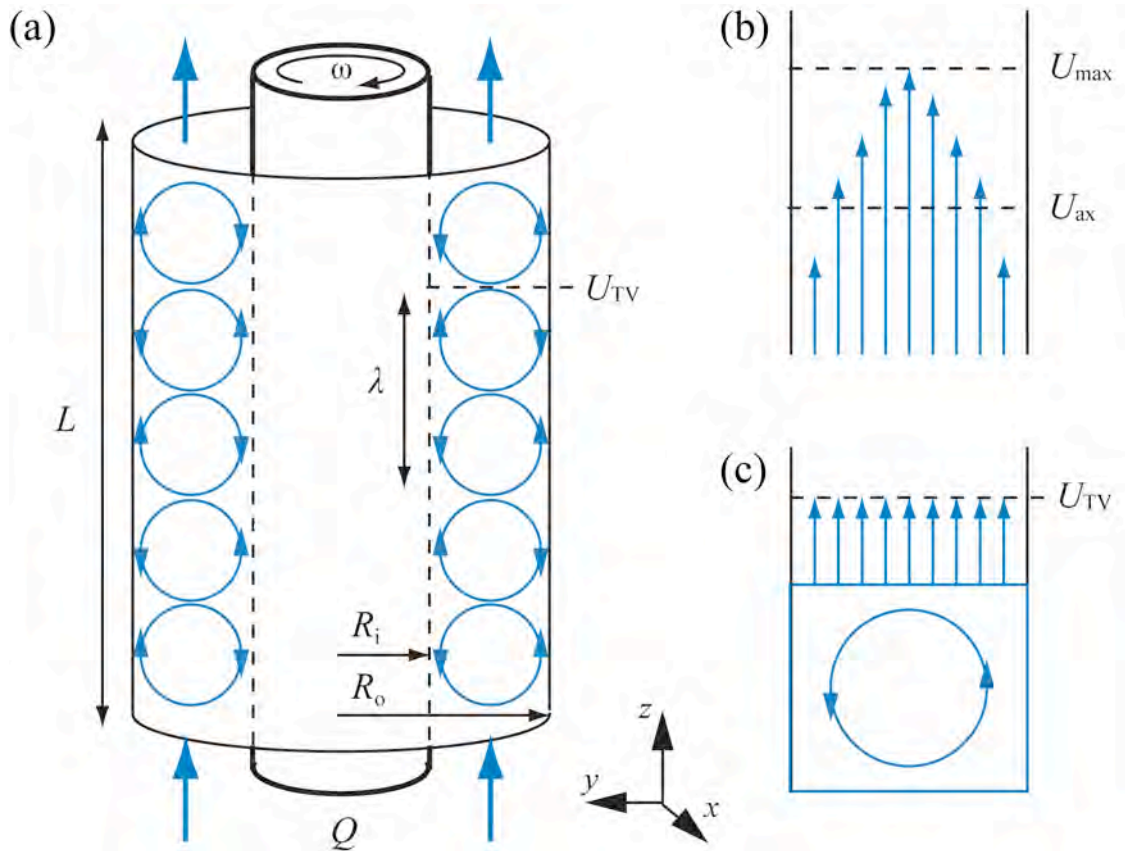
Figure 1.14. (a) The VFR system (b) Pipe flow velocity profile and (c) Plug-flow velocity profile.

Similarly to stationary TVF, this flow can be characterised by the dimensionless numbers η, Γ and *Ta*. But the addition of pipe flow in the Couette cell annulus introduces the need for additional parameters. The Reynolds number (Equation 1.13) gives a measure of the ratio of inertial forces to viscous forces. The velocity drift, V_d, is the ratio of the vortices pair axial velocity to the flow average axial velocity.

$$V_d = \frac{U_{TV}}{U_{ax}} \qquad (1.21)$$

Finally, the ratio of the Reynolds number to the Taylor number, γ_{Re}, gives the importance of the axial flow to the rotational one.

$$\gamma_{Re} = \frac{Re}{Ta} = \frac{U_{ax}}{\omega R_i} \qquad (1.22)$$

1.4.5.1 Structure and stability of the vortices

Until recently, most models and analyses in the literature make the assumption that vortices are square in the travelling vortex flow, stating that $\lambda = 2d$. But several results[63,64] provide clear evidence of a decrease in the wavelength of Taylor vortices with increasing axial flow rate. In 2000, Giordano *et al.*[65] while assuming vortices were square, noticed that there was a wavelength increase at the inlet and a wavelength decrease at the outlet of their reactor. Their Γ value was 18.3, and the effect of boundary conditions is expected to be stronger in systems that have small Γ. The authors considered that boundary conditions do not have any effect on the flow in the middle of the cell, basing themselves on the theoretical (Navier-Stokes equation simulations) and experimental studies made by Buchel *et al.*[66]

Regarding the stability of the flow, Lueptov *et al.*[64] noticed that vortices move with pipe flow but appear unaltered by it. Wereley *et al.*[67] showed that a γ_{Re} decrease (Q decrease and/or ω increase) stabilises the vortices. Also, a transition to the wavy TVF could break the stability and symmetry of the flow. Moser *et al.*[68], quoting Coles[69], say that wavy TVF should only appear for $\eta > 0.714$, making η an important parameter to consider when building a Couette cell.

1.4.5.2   Velocity drift and velocity field

The velocity drift between the average axial flow and the vortex translation speed has been the subject of many controversies. Theoretical results using both linear and non-linear Navier-Stokes equations, predict a V_d close to 1.17 for the axisymmetric regime[70–72]. In 1974, in their paper named "Ideal plug-flow properties of the Taylor vortex flow", Kataoka *et al.*[73] used the assumption that $V_d = 1$ in order to support a translating-tank model for the flow. This assumption has been used until recently[74], despite a widespread literature proving its inaccuracy in many systems[64,67,75]. In the later experimental papers, the velocity drift is found to vary from 1 to 1.4, depending on the flow regime. Giordano *et al.*[55] showed that, by increasing ω, it is possible to decrease the velocity of the Taylor vortices until obtaining stationary vortices with flow passing through them. In their experiments, where $0 < V_d < 1$, they identified two competing effects: firstly, if axial flow is high enough the vortices are transported as a stack; secondly, a lower γ_{Re} will have as a consequence to decrease V_d by lowering U_{TV}. These results brought the necessity for a new understanding of the flow, and, since the velocity of the vortices can be different than that of the flow, the inter-vortex mixing becomes an important parameter.

The model presented by Haim and Pismen[75] introduces a slalom by-pass flow around the vortices, providing a plausible explanation of the phenomenon. Giordano *et al.*[65] used this model to show that the translation velocity can be slowed thanks to this by-pass flow until obtaining stationary vortices. Hence, decreasing V_d could correspond to an increase of the by-pass flow. Wereley *et al.*[67] showed that when the pressure driven axial velocity is removed from the velocity field in a VFR almost pure TVF is obtained (Figure 1.15). This suggests that the velocity field of the travelling vortex flow can be a simple superposition of TVF and pipe flow velocity fields.
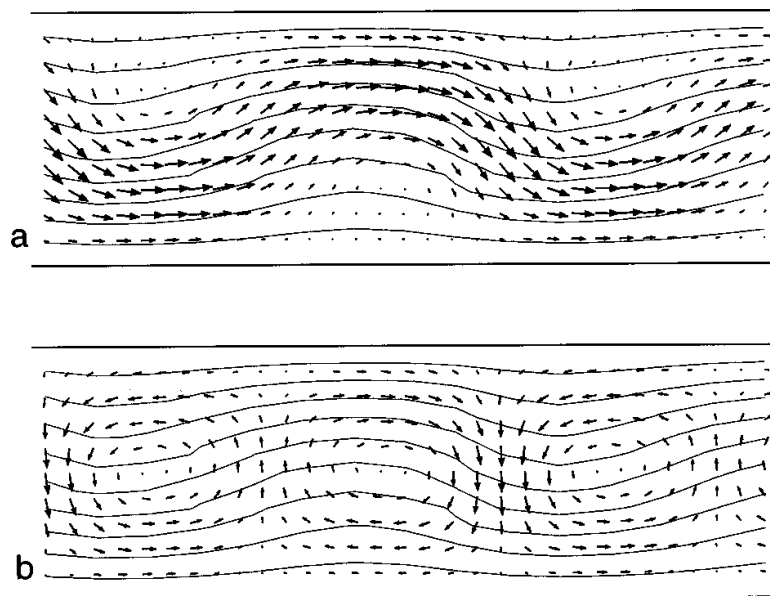
Figure 1.15. Radial and axial 2D velocity vector maps with azimuthal velocity contours obtained by Wereley et al.[67] using particle imaging velocimetry (PIV) at Ta=123 and Re=5.3. The rotating inner cylinder is located at the upper part of each frame. Vectors and contours are normalised to the dimensions of the VFR and the rotation of the inner cylinder. (a) Velocity field including the axial velocity profile. (b) Velocity field with the axial velocity profile removed. Reprinted from ref.67, Copyright 1999 American Institute of Physics.

Travelling vortex flow in a Couette is used for numerous chemical[8,76,77] and biochemical[9,78] applications due to its plug-like flow and mixing properties, but it is particularly those flow properties that are subject to remaining open questions. The way matter passes through the vortices and the mixing properties inside them are subjects that need to be further investigated.

1.4.5.3 Mixing in the VFR: plug-flow and by-pass velocities

Using a sodium chloride solution tracer and benzoic acid dissolution techniques, Kataoka *et al.*[73] determined the amounts of radial and axial mixing and found that their VFR operated as an ideal plug-flow reactor. They noticed deviations at highly turbulent regimes and attributed them to an increase in axial mixing in the reactor due to turbulence. The vortices were shown to provide intense radial mixing, but little axial exchange between them was found, characterising an ideal plug-flow reactor. These statements are also found in Haim *et al.*[75](1994) and Sczechowski *et al.*[79](1995).

In 1996, Desmet *et al.*[56] proposed the first 2-parameter model for the mixing in TVF. This model, supported by most of the experiments, reveals the importance of considering both intra-vortex and inter-vortex mixing. Following this work, Campero *et al.*[80] made a 3-parameter model for VFR flow considering the axial dispersion coefficient, the residence time of an exchange volume inside the vortices and the fraction of the total vortex this exchange volume occupies. Their experiments show that all three parameters increase with *Ta.* Those two papers led to the idea that 1D diffusion models should not be applied to the axisymmetric

regime of a VFR, as each vortex behaves like a well-mixed region connected to an exchange volume.

Giordano *et al.*[55,65] showed that by increasing *Ta* it was possible to transform the plug-like flow in a VFR into a high dispersion flow. For low rotations their system was close to plug-flow but has bad intra-vortex mixing and for higher rotations by-pass flow was enhanced, giving greater intermixing. VFR models developed after this work, are suitable for dealing with the by-pass mode[78,81]. However, the influence of different parameters on the micro and macro mixing properties remain unclear and often seems related to particular devices.

1.4.5.4 MR studies of travelling vortices

Not many MR studies of the unsteady vortex flow are found in the literature. Imaging travelling vortex flow in a VFR represents a serious challenge: the addition of pipe flow generating the periodic motion of the vortices causes imaging artifacts and errors in velocity measurements. Fast imaging sequences were used to obtain velocity measurements of the axisymmetric[68] and helical[82] regimes of the travelling vortex flow (Figure 1.16). Moser *et al.*[68] could observe that in their systems V_d was higher than 1 and that, at higher rotations, additional vortices were appearing. Due to a very low resolution, this MR technique provides a limited insight into the mixing properties of the flow. High-resolution 3D images and non-invasive measures of transport could provide with answers to many open questions concerning these flows, and recent advances in flow MRI[83] have been shown to progressively address the challenges of unsteady flow.
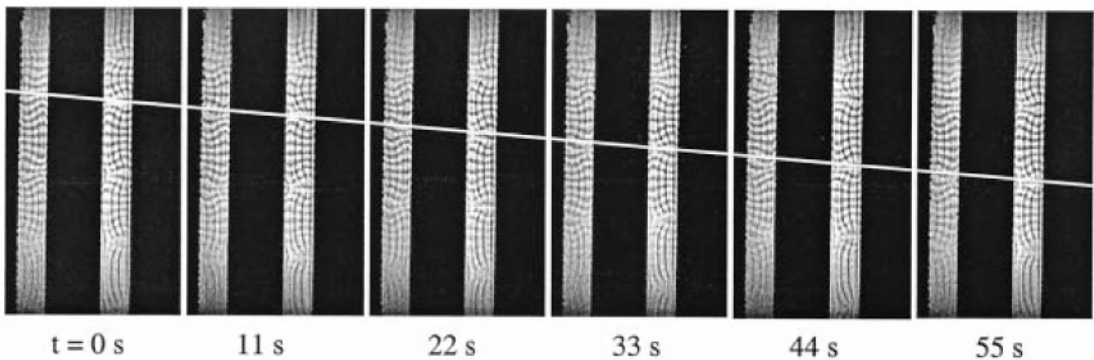
Figure 1.16. MR images of the axisymmetric VFR flow[68]. The vortex pairs can be identified by the repetitive pattern of the deformed grid. The mean axial flow is in the downward direction and the slope of the white line corresponds to U_{TV}. Reprinted from ref.68, Copyright 2000 Elsevier.

1.5 Flow distributed chemical structures

1.5.1 Chemical waves

1.5.1.1 Types of chemical waves

Three main categories of chemical waves are encountered throughout the literature: kinematic, trigger and phase-diffusion waves[84]. Kinematic waves[85] do not involve mass transfer: initial phase gradients in an oscillatory reaction lead to apparent propagation of waves. As soon as large enough concentration differences or significant molecular transport between elements appear, different types of waves known as trigger waves[86] progressively replace kinematic waves. The waves appearing on a thin layer of the BZ reaction (Figure 1.2) are one of the most studied examples of trigger waves. As mentioned before, these waves are generated when concentration inhomogeneities appear in the medium and propagate via the

interplay between reaction and transport processes. The initially localised disturbance is then transported to the neighbouring locations. Unlike kinematic waves, trigger waves are dependant on mass transfer so they annihilate when colliding or get blocked by walls. Finally, phase-diffusion waves[85] can develop during the dissipation of a given perturbation due to diffusion. The distinction between trigger and phase-diffusion waves is delicate and made on the basis of the velocity. The velocity of both waves can be defined by the ratio of phase variation in time to phase variation in space. In the case of simple flows as isotropic diffusion, the presence of a phase-diffusion wave is detected if the velocity exceeds that of a trigger wave.

Kinematic wave properties are only related to the oscillating reaction properties and to the imposed gradient. Trigger waves exhibit very diverse behaviours. Transported by diffusion and velocity, and depending of the geometry of the system, they can produce a large range of shapes. In an isotropic medium, BZ trigger waves propagate with constant shape and amplitude[18]. Their velocity has been shown to exhibit square root dependance on the sulphuric acid and bromate concentrations over a small concentration range[17]. But these waves are also very sensitive to local perturbations. Pojman *et al.*[87] showed the dependence of front velocity on gravity by studying velocity differences in ascending and descending wave fronts in a vertical tube. Menzinger *et al.*[88] showed how the reaction-diffusion description might fail even in a homogeneous medium when the reaction front generates density gradients inducing hydrodynamic flow. These gradients may be due to isothermal density variation or to thermal expansion or contraction linked with the reaction heat[24]. Even small convective effects have been shown to have great influence on BZ wave propagation[89]. In the case of more complex flows, propagating waves become very sensitive to advective mixing. Nugent

et al.[90] showed that BZ reaction waves could mimic the chaotic mixing structures observed by a passive fluorescent tracer.

Recently, there has been an increasing interest in the coupling between oscillating reactions and vortical flow. This is due to the fact that vortical flow provides with a controlled environment for studying the coupling of chemistry with flow properties as vorticity, periodicity or dispersion. Using the stationary Taylor vortex flow and the manganese-catalysed BZ reaction, Thompson *et al.*[23] showed that the propagation of chemical waves in vortices depends on the characteristic times of flow and chemistry.

In the case of time-periodic vortical flows, Paoletti *et al.*[91] showed that synchronisation can occur between the chemical time-scale, defined by the oscillation period of the reaction, and the flow. In their experiments, the ferroin-catalysed BZ reaction was combined with a chain of counter-rotating vortices. The experimental set-up to produce this flow was presented previously (Figure 1.5). The observed patterns (Figure 1.17) were found to be dependant on the relationship between the translation velocity of the vortices, U_{TV}, and the maximum velocity inside the vortices U_{max}. For $U_{TV} < U_{max}$, the BZ reaction formed waves that propagated through the vortices (Figure 1.17a). These waves appeared to reproduce the main features of passive tracer displacements through the same flow (Fig). However, for $U_{TV} > U_{max}$, synchronisation was observed between the BZ reaction and the flow. The authors identified two types of synchronisation phenomena in this system: "corotating synchronisation" (Figure 1.17b), where even and odd vortices were found at different phases of the reaction (oxidised/reduced), and "global synchronisation" (Figure 1.17c), where all the vortices were found to oscillate in unison. In a later study on the same system, Paoletti and

Solomon also identified sychronisation between the chemical and the flow periods in cases were $U_{TV} < U_{max}$. If the time of the wave propagation per vortex corresponded to an integer time the flow period, such synchronisation phenomena could lead to the observation of front mode-locking[48,92]. When mode-locking occurs the front propagation is found to switch to a different velocity, depending on the flow period.
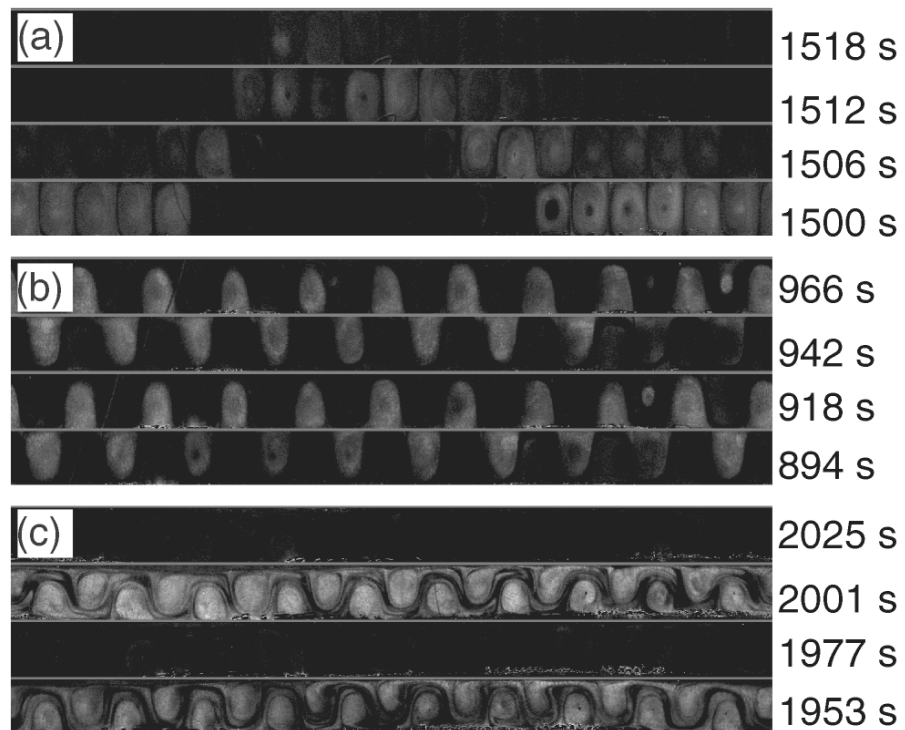
Figure 1.17. Series of decurled images showing the dynamics of the BZ reaction in a vortex chain[91]. The images are taken in the reference frame of the vortices. Time from the start of the experiment is given on the side. (a) Wave behaviour in stationary vortices ($U_{TV} < U_{max}$). (b) Corotating synchronisation for $U_{TV} > U_{max}$. (c) Global synchronisation for $U_{TV} > U_{max}$. Reprinted from ref.91, Copyright 2006 American Physical Society.

Mahoney *et al.*[93] showed that vortical flow could also generate barriers to the chemical wave propagation. Such barriers are similar to passive transport barriers identified in vortical flow[46]

and can play an important role in determining the shape of the propagating wave. The understanding of passive transport within such systems can give a lot of information on the propagation of chemical waves. However, it may not be sufficient to characterise the propagation of autocatalytic chemical waves produced by oscillating reactions, since synchronisation phenomena can occur, leading to behaviours that make it difficult to analyse the interplay between flow and chemistry.

1.5.1.2 Imaging Chemical waves

Due to high visual contrast between the oxidation and reduction phases, ferroin-catalysed BZ reaction has been the most imaged oscillating reaction. Most of the studies concern simple flow systems, since the use of optical techniques is not adapted to study chemical wave propagation through three-dimensional or opaque systems. MRI studies boosted the interest for the coupling between the BZ reaction and flow. In 1981, it was shown that MRI can be used to probe the BZ chemical waves by exploiting the relaxation time difference of ^{1}H protons surrounding the metal ion catalysts[94]. Gao *et al.*[28] showed that in acidic conditions ferroin produces ferric ions, which dominate the MR relaxation time and eliminate image contrast. Because MR relaxation time of water protons is more strongly affected by changes in the oxidative state of manganese (Mn^{2+} / Mn^{3+}), it became the most frequently used catalyst for MR studies of chemical waves. In 1990, Tzalmona *et al.*[95] probed BZ chemical waves in a tube using MRI. In a later work[96], they showed that it is possible to measure velocity of chemical waves using consecutive projections of MR images. While for more viscous solutions containing agarose, the wave velocity was found to be constant, in solutions without agarose, sharp velocity changes were observed. The authors attributed these velocity changes

to convective instabilities, caused by isothermal density decreases occurring while the solution is in the oxidative phase[88].

Cross *et al.*[97] examined the role of phosphates in the manganese catalysed BZ imaging contrast and showed that $Na_4P_2O_7$ and $Na_5P_3O_{10}$ are the most appropriate contrast agents for studying the dynamics of chemical waves, especially in the case of three-dimensional structures in large containers. This allowed them to produce the first three dimensional visualisation of BZ waves[98].

Recently, MR studies of the coupling between the BZ reaction and complex flows started to emerge. Koptyug *et al.*[99,100] and Britton *et al.*[101] imaged BZ reaction waves in a PBR. The later work provides with spatial quantification of the catalyst (Mn) concentration[102]. Taking advantage of the diversity of MRI techniques, Taylor *et al.*[103] probed chemical waves in porous media while determining flow properties. Using the manganese-catalysed BZ reaction, Thompson *et al.*[23] imaged waves in 3D Taylor vortex flow, providing with velocity maps of the same flow. By comparing experimental results with simulation results produced by an Oregonator model for the system, they showed that the propagating wave behaviour depends on the ratio of advective, chemical and diffusive time scales.

1.5.2 Introduction to flow distributed chemical patterns

1.5.2.1 Differential diffusion patterns in RD systems

Since 1975, continuous flow stirred tank reactors (CSTR) are used to study the BZ reaction behaviour far from thermodynamic equilibrium[104]. Progressively, new types of reactors were

introduced to study spatial pattern formation. The disk gel reactor and the linear gel reactor were the first two-dimensional continuously fed unstirred reactors (CFURs) to be used. In these reactors, transport is made by molecular diffusion, and it was soon understood that this property, coupled with an oscillating reaction, provides an ideal environment for the production of stationary Turing patterns.

The Turing instability relies on a diffusion coefficient difference in RD systems involving an autocatalyst species (activator) and an antagonist species that competes with the growth of the autocatalyst (inhibitor). According to Turing's initial work[105], if the diffusion coefficient of the inhibitor exceeds that of the activator, an activated zone could grow locally while lateral inhibition prevents its spreading. This phenomenon can result in the formation of concentration patterns. Experimental evidence of Turing patterns was produced in 1990 by Castets *et al.*[106] by coupling continuous flow of fresh BZ reactants with a permanent differential diffusion environment produced in a gel strip (Figure 1.18).
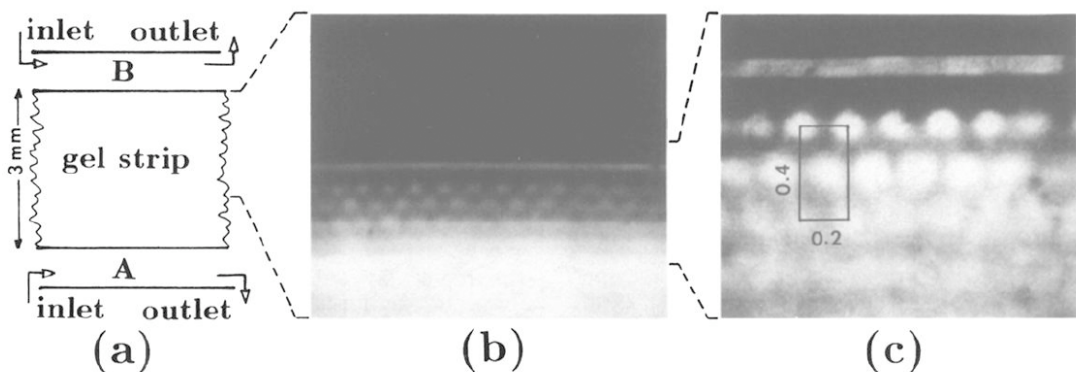
Figure 1.18. Experimental evidence of Turing patterns by Castets et al.[106]. Reprinted from ref.106, Copyright 1990 American Physical Society.

1.5.2.2 Differential dispersion patterns in RDA systems

The requirement of differential diffusion has dominated the field of pattern formation and prevented direct verification in open flow systems for many years[10]. Until 1991, two types of chemical spatial structures have been studied: chemical waves and Turing structures. In that year, Oyang *et al.*[10], examined the chlorite-iodide reaction and the chlorite-iodide-malonic acid reaction (CIMA) in a Couette cell initially used to create a one dimensional RDA system with controllable diffusion rate (Figure 1.19). By changing the concentrations of the reactants in CSTRs on each side of the Couette cell, concentration gradients were generated along the reactor. The rotation rate was used to vary the axial dispersion rate of the reactants. They noticed that the oxidised and reduced states could appear simultaneously in different regions of the reactor.
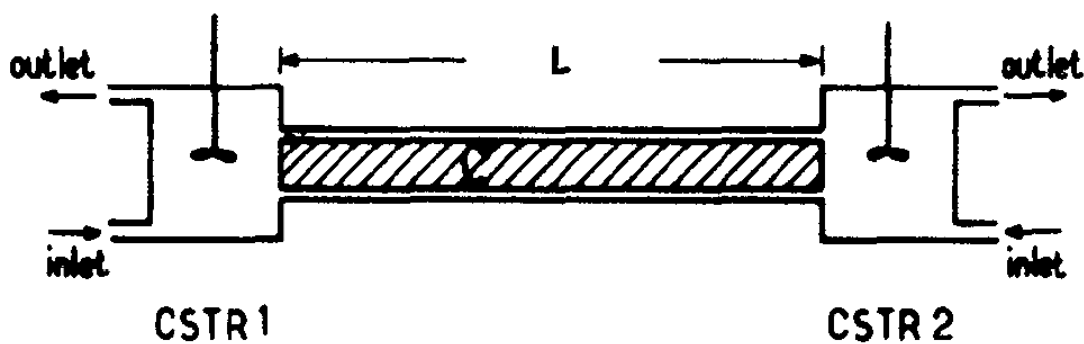
Figure 1.19. Schematic diagram of the Couette reactor experimental used by Ouyang et al.[10].
Reprinted from ref.10, Copyright 1991 American Institute of Physics.

The observed chemical front patterns (Figure 1.20) were different to those previously observed. The spatial distribution of the different BZ phases could be associated with steep concentration gradients that separate the parts of the Couette reactor corresponding to the different steady states. These results showed that the coupling of diffusive transport with local

chemical kinetics in a system where concentration gradients are imposed can generate complex spatiotemporal structures in RDA systems, including the first observed steady patterns with multiple fronts.
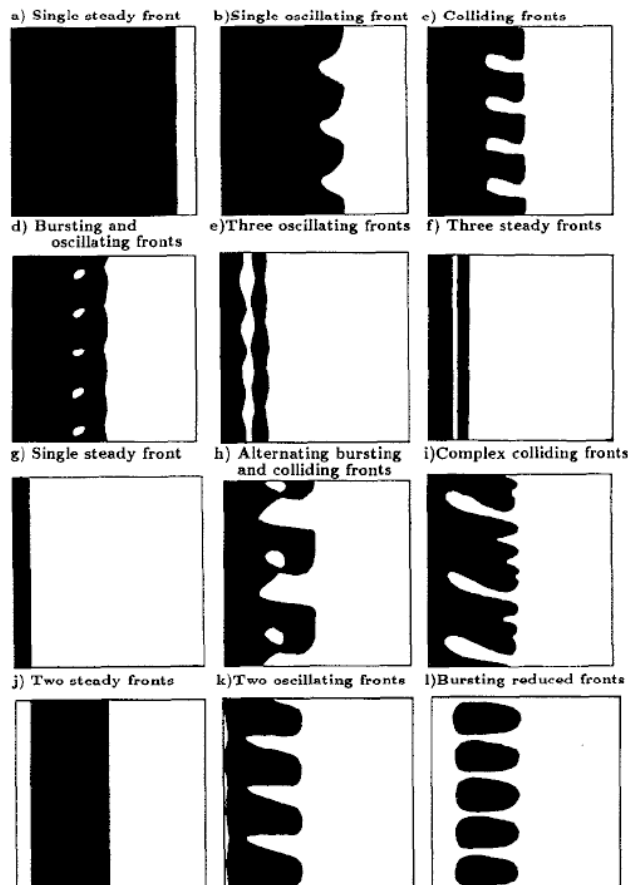
Figure 1.20. Patterns observed by Ouyang et al.[10] at the interface between the reduced and oxidised states of the BZ reaction in a Couette cell. Images were taken from the centre of the Couette cell shown in Figure 1.19. Reprinted from ref.10, Copyright 1991 American Institute of Physics.

Another mechanism for spatiotemporal pattern formation in an RDA systems was developed by Rovinsky *et al.*[107]. This mechanism is based on differential flow of the catalyst species in a homogeneous steady state of an activator-inhibitor system. In their system, the BZ reactants

were pumped through a PBR containing ferroin immobilized on a cation exchanger. The flow generated travelling waves along the length of the tube. Without flow the system was coming back to homogeneity.
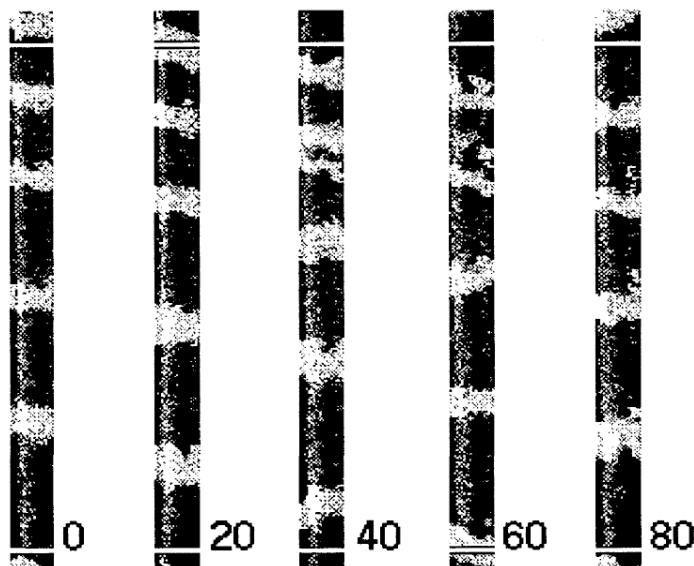
Figure 1.21.The BZ reactants flow passed through ferroin that was immobilized in the tube [107]. The light grey bands correspond to the oxidised state of ferroin (ferriin). The dark bands correspond to the reduced state. Time in seconds for the successive frames is indicated on the figure. Reprinted from ref.107, Copyright 1993 American Physical Society.

1.5.2.3 Equal dispersion patterns in RDA systems

In 1999, Andresen *et al.*[108] modelled the BZ reaction in the presence of a plug-flow and showed that such systems may produce stationary space-periodic patterns even in the case of equal diffusion coefficients and dispersion properties of the main reactants. In their simulations, for flow velocities greater than a critical value, a permanent boundary perturbation could create a global steady periodic pattern. Their novel approach is lying on the distinction between absolute and convective instabilities. Absolute instabilities refer to

trigger waves and are characterised by localised perturbations growing and eventually contaminating the entire system. Convective instabilities refer to kinematic waves and are characterised by localised perturbations advected by the flow in such a way that they grow in the moving reference frame, but decay at any fixed position.

Kaern *et al.*[109] verified experimentally the prediction of stationary waves in open reacting flow. Figure 1.22a shows the first stationary bands in a space-time plot where series of pictures of the reactor are plotted against time. To satisfy the conditions mentioned previously the authors used the BZ oscillating reaction, a PBR for the creation of plug–like flow and realised the boundary condition by feeding the flow tube with the outflow from a CSTR.
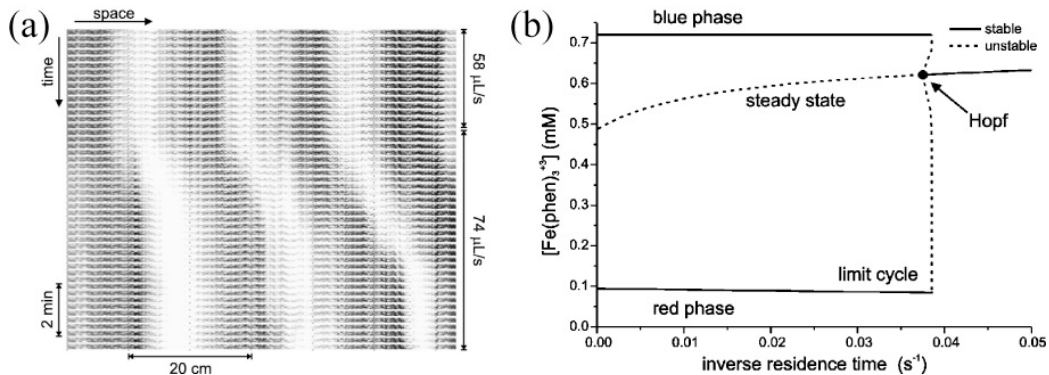
Figure 1.22. (a) Optical images of FDOs in a PBR. White corresponds to high ferriin, black to high ferroin. (b) CSTR bifurcation diagram of the RZ model. Reprinted from ref.109, Copyright 1999 American Physical Society.

Unstable stationary state at the boundary was obtained by choosing a sufficiently high inverse residence time, *k*, in the CSTR. This condition was showed using the bifurcation diagram of the three-variable Rovinsky-Zhabotinsky[110] (RZ) model for the BZ reaction (Figure 1.22b). In

the absence of a flow, the RZ model shows that the CSTR oscillates between the red and blue phases. At a sufficiently high inverse residence time it switches from an oscillating state to a stationary one. This stationary state CSTR output served as the inflow to the PBR.

In this thesis, space-time plots will be presented with time in the horizontal axis, as are the results presented by Bamforth *et al.*[111] (Figure 1.23).
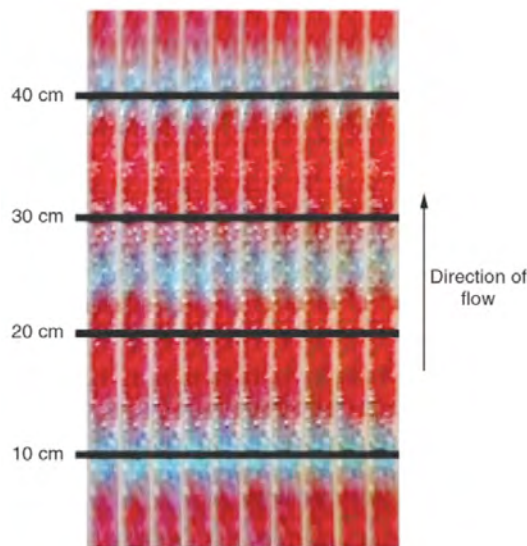
Figure 1.23. Optical images of the FDO patterns in a PBR. Each image interval corresponds to approximately 2 min. Reprinted from ref.111, Copyright 2002 PCCP owner societies.

1.5.3 Flow Distributed Oscillations (FDOs)

1.5.3.1 FDO mechanisms

Kaern *et al.*[109] proposed a simplified model for the FDO formation where the contribution of diffusion/dispersion is negligible and stationary waves are generated through a simple kinematic mechanism where a batch oscillator (undergoing oscillations of period *T*) is

spatially resolved in the presence of a constant flow of velocity U. If the phase of the oscillation is fixed at the inlet, the oscillation phase will be locked in space and stationary waves will emerge with a wavelength, λ_{FDO}, given by:

$$\lambda_{FDO} = U \times T \qquad\qquad (\ 1.23\ )$$

Andresen *et al.*[112] explained that this equation is an oversimplification of the phenomenon, as it is not addressing neither the convective nature of the waves nor the criterion for amplifying waves. In their approach, the perturbation at the inlet is compared to a particle moving at velocity U and emitting waves at frequency $\omega = 1\ /\ T$, where T is the BZ reaction oscillation period. The stationary case arises if the phase velocity of the waves is equal to the flow velocity. To illustrate their point, they used a model[110] describing the system used in the Kaern *et al.*[109] experiments. Their simulations showed that for a constant dispersion coefficient the wavelength grows importantly with the flow velocity for low velocities but relaxes to a linear dependence for high flow velocities. They suggested that a linear relationship between the FDO wavelength and the flow velocity was perceived in the results of Kaern *et al.*[109] because the dispersion coefficient depended linearly on the flow velocity. This reconciled the two models[113]: despite the fact that dispersion is not required for the formation of stationary waves and plays only a secondary role (by altering λ_{FDO}), it has to be sufficiently weak compared to the flow for the system to remain in the FDO domain. Above the critical flow rate, the kinematic model applies when dispersion is negligible or proportional to U. The dependency of λ_{FDO} on U will generally become non-linear in the presence of important flow-induced dispersion.

1.5.3.2 Wave generation mechanism and limit conditions

Following experimental studies of FDOs in PBRs revealed the limitations of the kinematic model proposed by Kaern *et al.*[109] The pattern formation mechanism observed by Taylor *et al.*[114] (Figure 1.24) involves a wave-splitting from successive oxidation pacemaker sites. Once the wave appears, part of it moves in the direction of the flow and disappears, while the other propagates against the flow and settles as a stationary band. Equation 1.23 cannot describe this behaviour. This mechanism was not observed in the work of Kaern *et al.*, probably due to high flow rate.
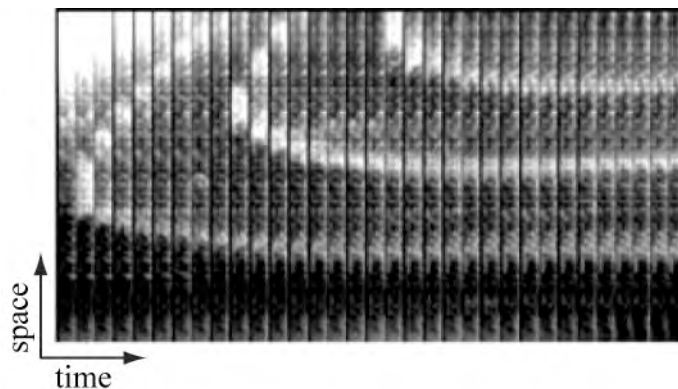
Figure 1.24.Stationary pattern formation mechanism observed by Taylor et al.[114] Reprinted from ref.114, Copyright 2002 PCCP owner societies.

Wave-splitting is only observed at relatively low flow velocities, where dispersion can compete with flow. Of course, depending on the chemical reaction used and the transport properties of the system, the wave-splitting mechanism can be observed even at higher flow rates.

Despite its ability to predict the linear relationship between the FDO wavelength and the flow velocity observed in many experimental set-ups, the kinematic mechanism fails to analyse the

FDO formation. The existence of a minimum flow rate for the observation of stationary patterns was suggesting this limitation[113]. In their seminal paper on FDOs, Kaern and Menzinger[109] observed a linear dependence of λ_{FDO} on flow rate, but did not identify a critical flow rate or observed any non-linear behaviour. The behaviour close to the critical flow rate was to be studied. Bamforth *et al.*[111] analysed theoretically the system dynamics for flow velocities close to the transition from stationary patterns to travelling waves (Figure 1.25a).
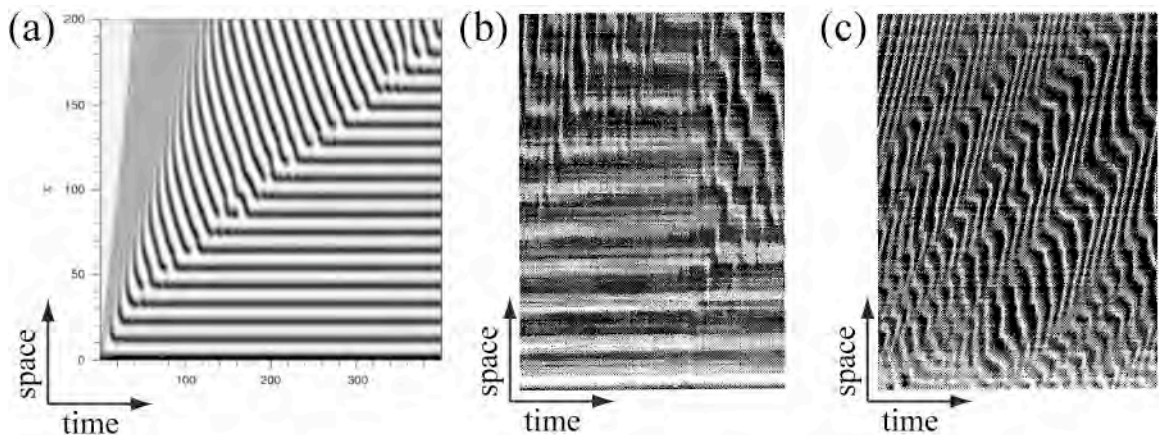
Figure 1.25. (a)Theoretical space–time plots at low flow rate by Bamforth et al.[111] and (b-c) experimental space-time plots at low flow rate by Kaern et al.[115] The flow velocity was of 0.03 cm s^{-1} for (b) and 0.001 cm s^{-1} for (c). (a) is reprinted from ref.111, Copyright 2002 PCCP owner societies. (b) and (c) are reprinted from ref.115, Copyright 2002 American Chemical Society.

In their model one or two bands could fail to stabilise after the wave-splitting before one settles. This phenomenon was observed by Kaern *et al.*[115] (Figure 1.25b). At even lower flow, their results showed an FDO breakdown where the stationary patterns were replaced by irregular travelling waves (Figure 1.25c).

1.5.3.3 FDO wavelength and bands

Both Kaern *et al.*[109] and Bamforth *et al.*[111] noticed that λ_{FDO} was significantly shorter than the wavelength predicted by the kinematic model (Equation 1.23), which they accounted for enhanced dispersion. Hence, λ_{FDO} is shown to increase with flow rate and decrease with dispersion.

The first study of the role of chemistry in the resulting patterns was made by Bamforth *et al.*[111], who added the concentrations of BrO^{3-} and H^+ to the kinematic model. The wavelength of fully-developed patterns was predicted and experimentally verified to scale linearly with the flow rate Q and the inverse square root of BrO^{3-} and H^+ concentrations:

$$\lambda_{FDO} \sim \frac{Q}{\left[BrO_3^-\right]^{1/2}\left[H^+\right]^{1/2}}$$

(1.24)

A better understanding of the interplay between chemistry and flow in these systems was provided by Britton *et al.*[116] who used MRI to probe manganese-catalysed BZ FDOs in a PBR, revealing the 3D shape of the Mn^{3+} bands. A radial concentration gradient was shown to result in a V-shaped wave front (Figure 1.26). The authors related this shape to the hydrodynamic properties of the reactor. The V-shape was explained by the radial variation of the fluid velocity (faster by the walls of the PBR). These results showed that radial mixing is playing an important role in this phenomenon by homogenising the medium and stressed the limitations of 1D models in predicting the evolution of the experimental FDO system behaviour.
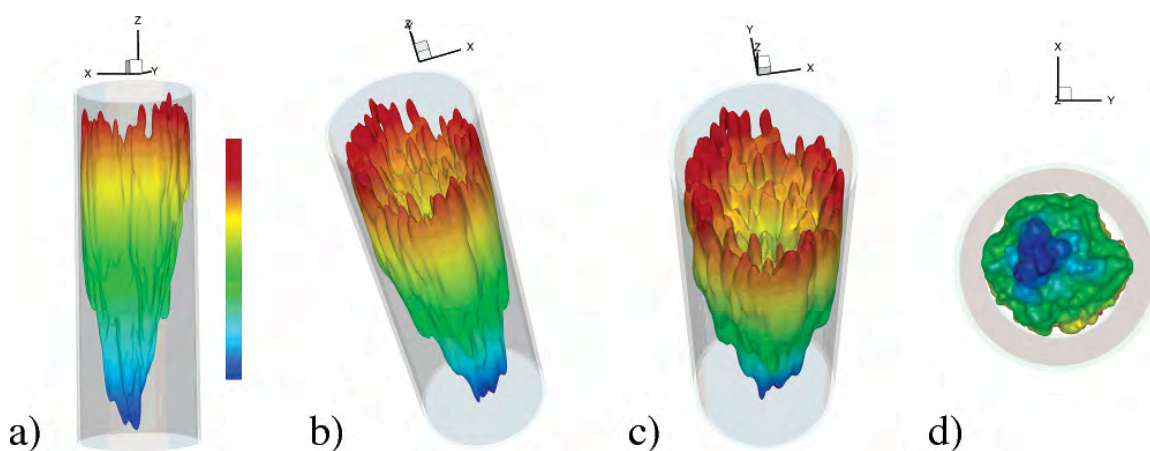
Figure 1.26. 3D renderings of a stationary FDO band in a PBR, at various orientations (a-d). These images were produced using series of 2D MR images. The colour scale indicates the position along the length of the reactor (blue is upstream and red is downstream). Shading highlights the 3D structure of the wave. Reprinted from ref.116, Copyright 2005 American Chemical Society.

1.5.3.4   Influencing parameters

Kaern and Menzinger identified the linear relationship between axial flow rate and wavelength in their first FDO paper[109]. By changing the flow rate, they could observe that the system was readapting its wavelength (Figure 1.22a). Bamforth *et al.*[111] also studied the band readjustment following a change in the flow rate. They observed a simple transition mechanism to the new FDO wavelength. For a flow rate increase, FDO bands move upwards initially keeping their original separation and amplitude. This movement increases the distance separating the first band from the boundary layer that appears unaltered. The amplitude of the first band also increases as it settles at its new stationary position. Following this, the distance between this band and the second band increases. Similarly, the amplitude of the second band increases as it reaches the appropriate separation from the first band and

becomes stationary. This process repeats for all subsequent bands until the new stationary pattern is fully established along the length of the reactor.

At flow velocities close to the critical velocity required for stationary patterns, a new type of complex pattern was observed by Taylor *et al.*[114]. Stationary patterns were found to appear after a transition period (Figure 1.27), the length of which depended sensitively on the flow rate (with higher flow leading to quicker transition). A zigzag pattern observed when the CSTR was close to the bifurcation point was found to depend sensitively on the initial concentrations and flow velocity.
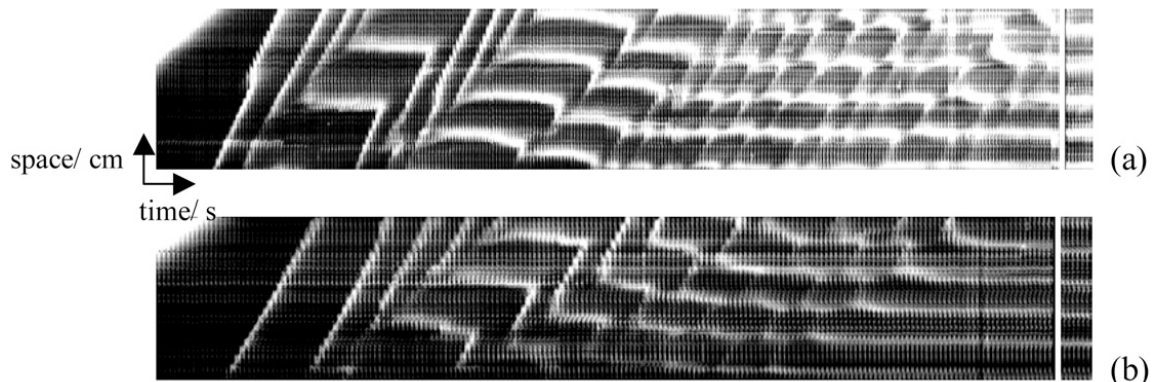
Figure 1.27. Complex pattern development close to the critical flow rate: Experimental images of the BZ FDO in a PBR taken at 10 s intervals. (the vertical white line indicates a break in time of 1 h). (a) Flow rate of 0.09 cm s⁻¹, (b) 0.095 cm s⁻¹. Reprinted from ref.114, Copyright 2002 PCCP owner societies.

The authors discussed possible mechanisms, involving fluid phase fluctuations at the boundary and packing material effects (PBR glass beads). They noticed that once established, the stationary patterns were stable, such that if the flow was switched off and then on again,

the patterns faded and then reappeared. However, if the flow was switched off prior to the establishment of stationary patterns then phase waves propagated through the system from the top of the tube to the bottom. For flow velocities less than a critical value (0.08 cm s^{-1} in their experiments), the CSTR oscillated.

Other flow effects on FDO are related to diffusion and dispersion. At high flow rates, dispersion was shown to play an important role in determining the wavelength of the structure. Kaern *et al.*[115] observed a significant λ_{FDO} decrease with increasing packing material diffusion coefficient. At low flow velocity, where the stationary waves breakdown to irregular wave structures, the critical flow velocity at which this breakdown occured was lowered when the effective diffusion coefficient was decreased. These results confirm that a low ratio of dispersive to advective transport coefficient is favourable to the formation of FDO waves.

Kaern *et al.*[117] studied the influence of the boundary condition by probing travelling waves that arose when the boundary oscillates. Far from the bifurcation point, waves propagate along the reactor with an almost constant velocity. However, when the CSTR residence time lies close to the bifurcation value, the waves propagate with an oscillatory velocity (Figure 1.28).
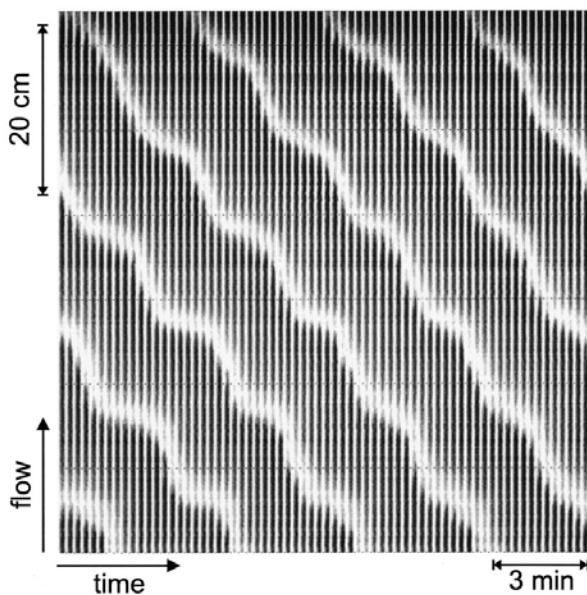
Figure 1.28. Oscillatory wave propagation obtained by Kaern et al.[117] White bands correspond to high ferriin concentrations. The flow tube is fed by an oscillatory CSTR. The residence time in the CSTR is lower than, but close to, the stationary bifurcation one. Reprinted from ref.117, Copyright 2000 American Physical Society.

Novak *et al.*[118] used a temperature sensitive agar gel system to study temperature effects on FDOs. They investigated periodic temperature modulation forcing of FDOs in a tubular reactor and observed synchronisation between the variation of band position and temperature changes. Their results reflect the effect of temperature on both chemical oscillations in batch reactors[33,34] and agar gel.

Taylor *et al.*[114] analysed the possible effect of the PBR glass beads on the FDO patterns. In contact with aqueous solutions, glass beads posses a negative surface charge due to formation of SiO^- groups. Positively charged species in the BZ reaction, such as the metal catalyst $Fe(phen)_3^{2+/3+}$ and $H_2BrO_2^+$, may be affected by the negative surface groups. In this case, the

system can switch from an equal dispersion system to a differential dispersion one. Such a switch may exist when dispersion dominates over turbulent mixing, although this generally occurs under lower flow rates (Re<0.1)[119]. The interactions of positive species with the beads may help to explain the stability of the stationary pulses, once established, by '' locking'' the catalyst in oxidised mode. Also, Kaern *et al.*[115] suggested that stagnant pockets of the fluid could explain similar phenomena.

Finally, less dominant parameters as gravity[36,120] or magnetic fields[121] have been shown to affect the propagation of BZ waves. Also, theoretical work[22] suggests that convectively unstable open flows as in FDO systems can behave as noise amplifiers and lead to the formation of noise-sustained structures.

1.5.4 The general case of flow distributed structures and its applications

The combination of an RDA system with the effect of an initial boundary condition that leads to FDOs can be considered as a specific case of a general category of stationary patterns. Satnoianou *et al.*[122] presented a theoretical study of coupled RDA system instabilities in one-dimensional domains. These instabilities are creating spatially periodic stationary waves that the authors termed flow and diffusion-distributed structures (FDS). FDOs and Turing patterns are presented as particular cases of FDS instability. This work highlights that other FDS should be easier to obtain in chemical systems showing how such structures might have a crucial role in biological pattern formation.

Indeed, FDO mechanisms have already been proposed as a means for explaining biological pattern formation by Kaern *et al.*[123] who applied the FDO kinematic model to the process of somitogenesis. Somitogenesis refers to the formation of spatially repetitive structures along the growth axis of a developing embryo. The authors argued that FDO conditions are satisfied during chick and mouse somitogenesis. Similarly to FDO waves, gene expression waves observed in these species arise from phase dynamics in a growing oscillatory medium. Finally, aside the possible relevance of FDS to biological pattern formation, McGraw *et al.*[124] identified FDS features shared with open flow systems in fluid mechanics and plasma physics (convective instability, role of boundary conditions in the pattern selection).

(1)   Tsuchiya, Y.; Yamazaki, H.; Aoki, T. *Biophys. J.* **1991**, *59*, 249.

(2)   Neufeld, Z. *Chaos* **2012**, *22*.

(3)   Nicolis, G.; Prigogine, I. *Self-Organisation in Non-equilibrium Systems: From Dissipative structures to Order through Fluctuations*; John Wiley and Sons Inc., 1977.

(4)   Haken, H. *Synergetics*; Springer-Verlag Berlin Heidelberg, 1978.

(5)   Prigogine, I.; Stengers, I. *Order out of Chaos: Man's new dialogue with nature*; Flamingo, 1984.

(6)   Taylor, G. I. *Philosophical Transactions of the Royal Society of London Series a-Containing Papers of a Mathematical or Physical Character* **1923**, *223*, 289.

(7)   Tagg, R. A Guide to Literature Related to the Taylor-Couette Problem. In *Ordered and Turbulent Patterns in Taylor-Couette Flow*; Andereck, C. D., Hayot, F., Eds.; Springer US, 1992; pp 303.

(8)   Wolinski, J.; Wronski, S. *Chem. Eng. and Process.* **2009**, *48*, 1061.

(9)   Resende, M. M.; Sousa, R.; Tardioli, P. W.; Giordano, R. L. C.; Giordano, R. C. *AIChE J.* **2005**, *51*, 314.

(10)   Ouyang, Q.; Castets, V.; Boissonade, J.; Roux, J. C.; Dekepper, P.; Swinney, H. L. *J. Chem. Phys.* **1991**, *95*, 351.

(11)   Deng, R. S.; Arifin, D. Y.; Mak, Y. C.; Wang, C. H. *AIChE J.* **2009**, *55*, 3056.

(12)   Dusting, J.; Balabani, S. *Chem. Eng. Sci.* **2009**, *64*, 3103.

(13)   Britton, M. M. *Chem. Soc. Rev.* **2010**, *39*, 4036.

(14)   Haken, H. *Information and self-organization : a macroscopic approach to complex systems*, 3rd enl. ed.; Springer: Berlin ; New York, 2006.

(15)   Vallatos, A.; Wilson, M. C. T.; Taylor, A. F.; Britton, M. M. *Europhys. Lett.* **2012**, *99*.

(16)   Vallatos, A.; Evans, R. D.; Taylor, A. F.; Britton, M. M. *Chaos* **2013**, *23*.

(17)   Scott, S.-K. *Oscillations, Waves, and chaos in Chemical Kinetics* Oxford University Press, 1994.

(18)   Scott, S. K.; Showalter, K. *J. Phys. Chem.* **1992**, *96*, 8702.

(19)   Zhabotinsky, A. M. *Biofizika* **1964**, *9*.

(20)   Noyes, R. M.; Field, R. J.; Koros, E. *J. Am. Chem. Soc.* **1972**, *94*, 1394.

(21)   Field, R. J.; Noyes, R. M.; Koros, E. *J. Am. Chem. Soc.* **1972**, *94*, 8649.

(22)   Kuznetsov, S. P.; Mosekilde, E.; Dewel, G.; Borckmans, P. *J. Chem. Phys.* **1997**, *106*, 7609.

(23)   Thompson, B. W.; Novak, J.; Wilson, M. C. T.; Britton, M. M.; Taylor, A. F. *Phys. Rev. E* **2010**, *81*.

(24)   Field, R. J.; Burger, M. *Oscillations and traveling waves in chemical systems*; Wiley: New York, 1985.

Introduction

(25)   Burger, M.; Koros, E. *J. Phys. Chem.* **1980**, *84*, 496.

(26)   Körös, E.; Murger, M.; Friedrich, V.; Ladányi, L.; Nagy, Z.; Orbán, M. *Faraday Symp. Chem. S.* **1974**, *9.*

(27)   Zhabotinsky, A. M. *Chaos* **1991**, *1*, 8.

(28)   Gao, Y.; Cross, A. R.; Armstrong, R. L. *J. Phys. Chem.* **1996**, *100*, 10159.

(29)   Schlüter, A.; Weiss, A. *Berichte der Bunsengesellschaft für physikalische Chemie* **1981**, *85*, 306

(30)   Hansen, E. W.; Ruoff, P. *J. Phys. Chem.* **1989**, *93*, 264.

(31)   Koros, E.; Orban, M. *Nature* **1978**, *273*, 371.

(32)   Greenwood, N. N.; Earnshaw, A. *Chemistry of the elements*, 2nd ed.; Butterworth-Heinemann: Oxford ; Boston, 1997.

(33)   Dutt, A. K.; Menzinger, M. *J. Phys. Chem.* **1992**, *96*, 8447.

(34)   Dutt, A. K.; Muller, S. C. *J. Phys. Chem.* **1993**, *97*, 10059.

(35)   Treindl, L.; Ruoff, P.; Kvernberg, P. O. *J. Phys. Chem. A* **1997**, *101*, 4606.

(36)   Fujieda, S.; Mori, Y.; Nakazawa, A.; Mogami, Y. *Adv. Space Res.* **2001**, *28*, 8.

(37)   Zaikin, A. N.; Zhabotin.Am. *Nature* **1970**, *225*, 535.

(38)   Epstein, I. R. *P. Natl. Acad. Sci. USA* **2006**, *103*, 15727.

(39)   Noszticzius, Z.; Horsthemke, W.; Mccormick, W. D.; Swinney, H. L.; Tam, W. Y. *Nature* **1987**, *329*, 619.

(40)   Steinbock, O.; Siegert, F.; Muller, S. C.; Weijer, C. J. *P. Natl. Acad. Sci. USA* **1993**, *90*, 7332.

(41)   Zhou, C. S.; Kurths, J. *New Journal of Physics* **2005**, *7.*

(42)   Shlesinger, M. F.; Zaslavsky, G. M.; Klafter, J. *Nature* **1993**, *363*, 31.

(43)   Young, W.; Pumir, A.; Pomeau, Y. *Phys. Fluids a-Fluid* **1989**, *1*, 462.

(44)   Meiss, J. D.; Ott, E. *Phys. Rev. Lett.* **1985**, *55*, 2741.

(45)   Zumofen, G.; Klafter, J.; Shlesinger, M. F. *Anomalous Diffusion: From Basics to Applications* **1999**, *519*, 15.

(46)   Solomon, T. H.; Weeks, E. R.; Swinney, H. L. *Phys. Rev. Lett.* **1993**, *71*, 3975.

(47)   Solomon, T. H.; Tomas, S.; Warner, J. L. *Phys. Rev. Lett.* **1996**, *77*, 2682.

(48)   Paoletti, M. S.; Solomon, T. H. *Phys. Rev. E* **2005**, *72*.

(49)   Solomon, T. H.; Mezic, I. *Nature* **2003**, *425*, 376.

(50)   Frankel, I.; Brenner, H. *J. Fluid Mech.* **1989**, *204*, 97.

(51)   Metcalfe, I. S. *Chemical reaction engineering : a first course*; Oxford University Press: Oxford ; New York, 1997.

(52)   Levenspiel, O. *Chemical reaction engineering*, 3rd ed.; Wiley: New York, 1999.

(53)   Koschmieder, E.-L. *Benard Cells and Taylor Vortices*; Cambridge University Press, 1993.

(54)   Meyer-Spasche, R. *Pattern Formation in Viscous Flows – The Taylor Couette Problem and Rayleigh-Benard Convection*; Birkhauser 1999.

(55)   Giordano, R. C.; Giordano, R. L. C.; Prazeres, D. M. F.; Cooney, C. L. *Chem. Eng. Sci.* **1998**, *53*, 3635.

(56)   Desmet, G.; Verelst, H.; Baron, G. V. *Chem. Eng. Sci.* **1996**, *51*, 1287.

(57)   Desmet, G.; Verelst, H.; Baron, G. V. *Chem. Eng. Sci.* **1996**, *51*, 1299.

(58)   Ohmura, N.; Okamoto, H.; Makino, T.; Kataoka, K. *J. Chem. Eng. Jpn* **2002**, *35*, 692.

(59)   Richter, O.; Menges, M.; Kraushaar-Czarnetzki, B. *Chem. Eng. Sci.* **2009**, *64*, 2384.

(60)   Kose, K. *Phys. Rev. Lett.* **1994**, *72*, 1467.

(61)   Hopkins, J. A.; Santini, R. E.; Grutzner, J. B. *J. Magn. Res. Ser. A* **1995**, *117*, 150.

(62)   Seymour, J. D.; Manz, B.; Callaghan, P. T. *Phys. Fluids* **1999**, *11*, 1104.

(63)   Gu, Z. H.; Fahidy, T. Z. *Can. J. Chem. Eng.* **1985**, *63*, 710.

(64)   Lueptow, R. M.; Docter, A.; Min, K. Y. *Phys. Fluids a-Fluid* **1992**, *4*, 2446.

(65)   Giordano, R. L. C.; Giordano, R. C.; Prazeres, D. M. F.; Cooney, C. L. *Chem. Eng. Sci.* **2000**, *55*, 3611.

(66)   Buchel, P.; Lucke, M.; Roth, D.; Schmitz, R. *Phys. Rev. E* **1996**, *53*, 4764.

(67)   Wereley, S. T.; Lueptow, R. M. *Phys. Fluids* **1999**, *11*, 3637.

(68)   Moser, K. W.; Raguin, L. G.; Harris, A.; Morris, H. D.; Georgiadis, J.; Shannon, M.; Philpott, M. *Magn. Reson. Imaging* **2000**, *18*, 199.

(69)   Coles, D. *J. Fluid Mech.* **1965**, *21*.

(70)   Chandrasekhar, S. *Hydrodynamic and Hydromagnetic Stability*, 1961.

(71)   Recktenwald, A.; Lucke, M.; Muller, H. W. *Phys. Rev. E* **1993**, *48*, 4444.

(72)   Howes, T.; Rudman, M. *AIChE J.* **1998**, *44*, 255.

(73)   Kataoka, K.; Hongo, T.; Futagawa, M. *J. Chem. Eng. Jpn* **1974**, *8*, 4.

(74)   Legrand, J.; Coeuret, F. *Chem. Eng. Sci.* **1986**, *41*, 47.

(75)   Haim, D.; Pismen, L. M. *Chem. Eng. Sci.* **1994**, *49*, 1119.

(76)   Judat, B.; Racina, A.; Kind, M. *Chem. Eng. Technol.* **2004**, *27*, 287.

(77)   Forney, L. J.; Pierson, J. A. *AIChE J.* **2003**, *49*, 727.

(78)   Haut, B.; Ben Amor, H.; Coulon, L.; Jacquet, A.; Halloin, V. *Chem. Eng. Sci.* **2003**, *58*, 777.

(79)   Sczechowski, J. G.; Koval, C. A.; Noble, R. D. *Chem. Eng. Sci.* **1995**, *50*, 3163.

(80)   Campero, R. J.; Vigil, R. D. *Chem. Eng. Sci.* **1997**, *52*, 3303.

(81)   Syed, A.; Fruh, W. G. *J. Chem. Technol. Biot.* **2003**, *78*, 227.

(82)   Raguin, L. G.; Georgiadis, J. G. *J. Fluid Mech.* **2004**, *516*, 125.

(83)   Gladden, L. F.; Sederman, A. J. *Journal of Magnetic Resonance* **2013**, *229*, 2.

(84)   Ross, J.; Muller, S. C.; Vidal, C. *Science* **1988**, *240*, 460.

(85)   Ortoleva, P.; Ross, J. *J. Chem. Phys.* **1974**, *60*, 5090.

(86)   Winfree, A. T. *Science* **1973**, *181*, 937.

(87)   Pojman, J. A.; Epstein, I. R.; Mcmanus, T. J.; Showalter, K. *J. Phys. Chem.* **1991**, *95*, 1299.

(88)   Menzinger, M.; Tzalmona, A.; Armstrong, R. L.; Cross, A.; Lemaire, C. *J. Phys. Chem.* **1992**, *96*, 4725.

(89)   Wu, Y. Q.; Vasquez, D. A.; Edwards, B. F.; Wilder, J. W. *Phys. Rev. E* **1995**, *51*, 1119.

(90)   Nugent, C. R.; Quarles, W. M.; Solomon, T. H. *Phys. Rev. Lett.* **2004**, *93*.

(91)   Paoletti, M. S.; Nugent, C. R.; Solomon, T. H. *Phys. Rev. Lett.* **2006**, *96*.

(92)   Paoletti, M. S.; Solomon, T. H. *Europhys. Lett.* **2005**, *69*, 819.

(93)   Mahoney, J.; Bargteil, D.; Kingsbury, M.; Mitchell, K.; Solomon, T. *Europhys. Lett.* **2012**, *98*.

(94)   Lauffer, R. B. *Chem. Rev.* **1987**, *87*, 901.

(95)   Tzalmona, A.; Armstrong, R. L.; Menzinger, M.; Cross, A.; Lemaire, C. *Chem. Phys. Lett.* **1990**, *174*, 199.

(96)   Tzalmona, A.; Armstrong, R. L.; Menzinger, M.; Cross, A.; Lemaire, C. *Chem. Phys. Lett.* **1992**, *188*, 457.

(97)   Cross, A. R.; Armstrong, R. L.; Reid, A.; Su, S. Y.; Menzinger, M. *J. Phys. Chem.* **1995**, *99*, 16616.

(98)   Cross, A. L.; Armstrong, R. L.; Gobrecht, C.; Paton, M.; Ware, C. *Magn. Reson. Imaging* **1997**, *15*, 719.

(99)   Koptyug, I. V.; Lysova, A. A.; Parmon, V. N.; Sagdeev, R. Z. *Kinet. Catal.* **2003**, *44*, 401.

(100)   Koptyug, I. V.; Lysova, A. A.; Matveev, A. V.; Ilyina, L. Y.; Sagdeev, R. Z.; Parmon, V. N. *Magn. Reson. Imaging* **2003**, *21*, 337.

(101)   Hennig, J.; Nauerth, A.; Friedburg, H. *Magn. Reson. Med.* **1986**, *3*, 823.

(102)   Britton, M. M. *J. Phys. Chem. A* **2006**, *110*, 2579.

(103)   Taylor, A. F.; Britton, M. M. *Chaos* **2006**, *16*.

(104)   Marek, M.; Svobodova, E. *Biophys. Chem.* **1975**, *3*, 263.

(105)   Turing, A. M. *Philos. T. Roy. Soc. B.* **1952**, *237*, 37.

(106)   Castets, V.; Dulos, E.; Boissonade, J.; Dekepper, P. *Phys. Rev. Lett.* **1990**, *64*, 2953.

(107)   Rovinsky, A. B.; Menzinger, M. *Phys. Rev. Lett.* **1993**, *70*, 778.

(108)   Andresen, P.; Bache, M.; Mosekilde, E.; Dewel, G.; Borckmans, P. *Phys. Rev. E* **1999**, *60*, 297.

(109)   Kaern, M.; Menzinger, M. *Phys. Rev. E* **1999**, *60*, R3471.

(110)   Zhabotinsky, A. M.; Rovinsky, A. B. *J. Phys. Chem.* **1990**, *94*, 8001.

(111)   Bamforth, J. R.; Toth, R.; Gaspar, V.; Scott, S. K. *Phys. Chem. Chem. Phys.* **2002**, *4*, 1299.

(112)   Andresen, P.; Mosekilde, E.; Dewel, G.; Borckmans, P. *Phys. Rev. E* **2000**, *62*, 2992.

(113)   Kaern, M.; Menzinger, M. *Phys. Rev. E* **2000**, *62*, 2994.

(114)   Taylor, A. F.; Bamforth, J. R.; Bardsley, P. *Phys. Chem. Chem. Phys.* **2002**, *4*, 5640.

(115)   Kaern, M.; Menzinger, M. *J. Phys. Chem. A* **2002**, *106*, 4897.

(116)   Britton, M. M.; Sederman, A. J.; Taylor, A. F.; Scott, S. K.; Gladden, L. F. *J. Phys. Chem. A* **2005**, *109*, 8306.

(117)   Kaern, M.; Menzinger, M. *Phys. Rev. E* **2000**, *61*, 3334.

(118)   Novak, J.; Thompson, B. W.; Wilson, M. C. T.; Taylor, A. F.; Britton, M. M. *Phys. Chem. Chem. Phys.* **2011**, *13*, 12321.

(119)   Yu, D.; Jackson, K.; Harmon, T. C. *Chem. Eng. Sci.* **1999**, *54*, 357.

(120)   Fujieda, S.; Mogami, Y.; Zhang, W.; Shinohara, H.; Handa, S. *Anal. Sci.* **1999**, *15*, 159.

(121)   Okano, H.; Kitahata, H.; Akai, D. *J. Phys. Chem. A* **2009**, *113*, 3061.

(122)   Satnoianu, R. A.; Maini, P. K.; Menzinger, M. *Physica D* **2001**, *160*, 79.

(123)   Kaern, M.; Menzinger, M.; Hunding, A. *J. Theor. Biol.* **2000**, *207*, 473.

(124)   Mcgraw, P. N.; Menzinger, M. *Phys. Rev. E* **2003**, *68*.

2 Magnetic resonance techniques

2.1 Magnetic resonance principles

Only an overview to the theory behind NMR and MRI will be given in this section. For further information, one may refer to the numerous textbooks on the subject[1-4].

Magnetic resonance (MR) probes the behaviour of nuclei that possess nuclear spin. A spinning nucleus possesses angular momentum, $\boldsymbol{P}$, and charge and it is the motion of this charge that gives rise to an associated magnetic moment, $\boldsymbol{\mu}$ (Figure 2.1a). The magnetic moment and angular momentum of a nucleus are vector quantities related to each other by the magnetogyric ratio, γ, which gives a measure of how 'strongly magnetic' the nucleus is:

$$\boldsymbol{\mu} = \gamma \boldsymbol{P} \qquad\qquad (\,2.1\,)$$

Although several nuclei possess spin property, this thesis will consider only hydrogen, ^{1}H, since it is both the most imaged nucleus in MRI and the only one probed in this work. In the presence of a static magnetic field, the magnetic moment of the ^{1}H nuclei will orient relative to the field. The number of possible orientations, or energy states[5], is determined by the spin quantum number, I. ^{1}H has spin number of 1/2 and can adopt two possible orientations with respect to the field (Figure 2.1b): a low energy one (m = –1/2), where the nuclear spin vector is in the same direction as the field (spin-up), and a high energy one (m = +1/2), where the nuclear spin vector is in the opposite direction (spin-down).

In addition to this alignment, ^{1}H nuclei will precess at a frequency ω, called the Larmor frequency, that will depend on γ, and the field strength, B_0.

$$\omega = -\gamma B_0 \qquad\qquad (\ 2.2\ )$$
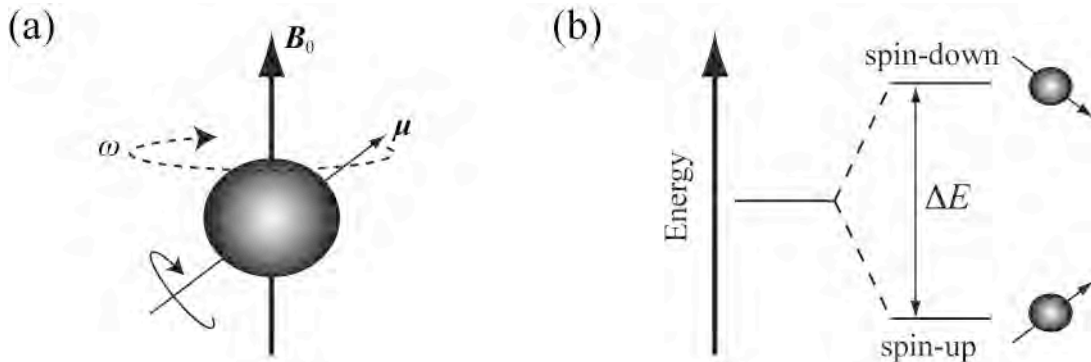
Figure 2.1 (a) The magnetic field causes the nucleus to precess at the Larmor frequency. (b) Schematic diagram showing the degenerate states of ^{1}H.

At thermal equilibrium, there is a Boltzmann distribution of nuclei between the two energy levels with an excess of the lower energy spin-up nuclei. An ensemble average of all the spin magnetic moments produces a macroscopic magnetisation[6], M_0 , along the direction of B_0 (Figure 2.2).
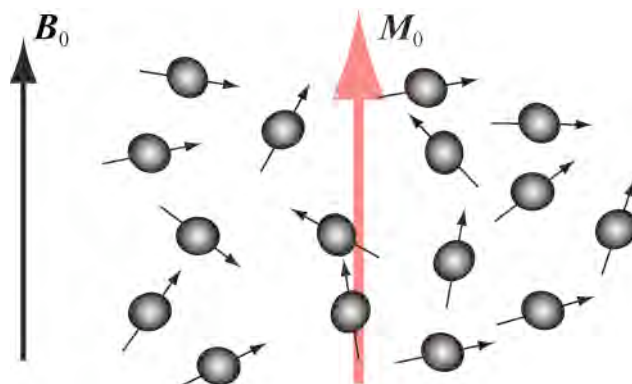
*Figure 2.2. Formation of the magnetisation vector, M_0, at thermal equilibrium.*

Typically, the field is applied in the z direction, $\boldsymbol{B}_z$, and the net magnetisation becomes $\boldsymbol{M}_z$. NMR experiments manipulate $\boldsymbol{M}$ using radiofrequency (rf) pulses to induce transitions between spin states leading to a deflection of the magnetisation. The degree to which the magnetisation is deflected (tip angle, θ) is dependent on the amplitude and duration of the rf pulse. A 90° rf pulse in the y-direction ($90°_y$) will rotate the bulk magnetisation vector from the z axis to the x axis as shown in Figure 2.3a. The magnetisation precesses at the Larmor frequency in the xy-plane and can induce a current in coils. The measured signal is called the free induction decay (FID) and will reduce over time due to spin relaxation processes.
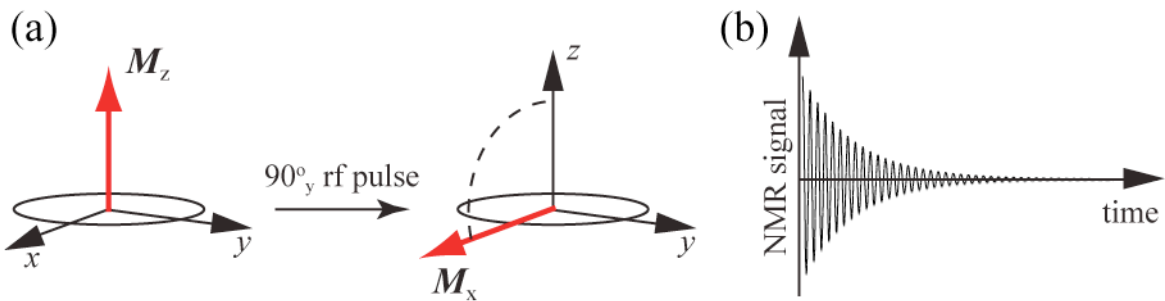

Figure 2.3. (a) Schematic diagram showing a $90°_y$ pulse rotating the net magnetisation vector, $\boldsymbol{M}$, from the z-axis to the x-axis. (b) NMR signal measured by coils as $\boldsymbol{M}$ precesses on the xy-plane.

Magnetic field variations caused by different chemical environments on spins will cause variations in the Larmor frequency. These deviations are called chemical shifts and are the basis of NMR spectroscopy. By using a reference frame rotating at the Larmor frequency, it is possible to resolve frequency deviations related to chemical shift and get an insight regarding the chemistry of the system. The different frequencies at which the FID oscillates can be used to characterise various chemical environments experienced by the spins. Fourier transformation of the FID produces a spectrum, revealing frequency offsets with respect to a

reference. This is the NMR spectrum and probably is one of the most used tools for chemical characterisation. But the relaxation time taken by the spins to regain their equilibrium position after the rf pulse is also characteristic of their chemical environment and can therefore be used for chemical characterisation.

2.2 Magnetic resonance relaxation

MR relaxation is defined by two relaxation times related to two processes that characterise the rate of return to equilibrium after an rf pulse is applied:

- T_1 relaxation time determines the rate at which the ratio of spin-up to spin-down nuclei returns to thermal equilibrium.

- T_2 relaxation time determines the rate at which nuclear spins loose the phase coherence gained by the application of the rf pulse.

2.2.1 T_1 relaxation

T_1 relaxation refers to the return of the magnetisation to the equilibrium value, M_z. The relaxation rate depends on local fluctuations in the magnetic field. T_1 relaxation is an exponential decay process described by:

$$M_z = M_0(1 - 2e^{(-t/T_1)})$$

$$(2.3)$$

Measurement of T_1 relaxation is typically achieved using an inversion recovery experiment[7], the pulse sequence for which is shown in Figure 2.4. In this experiment, the macroscopic magnetisation is inverted by a 180° pulse, so that it resides along the negative z-axis. The

magnetisation starts relaxing towards its thermal equilibrium position. After a time delay, τ, shorter than the relaxation time, a 90° pulse rotates the magnetisation onto the *y*-axis, where an FID is acquired. The maximum intensity of this spectrum gives a measure of M_z. The resulting FID can also be Fourier transformed to produce a spectrum, where the peak intensities are proportional to M_z. Series of experiments are performed at different τ values. The resulting intensity decay with respect to τ is fitted to equation 2.1 to give the time constant T_1.
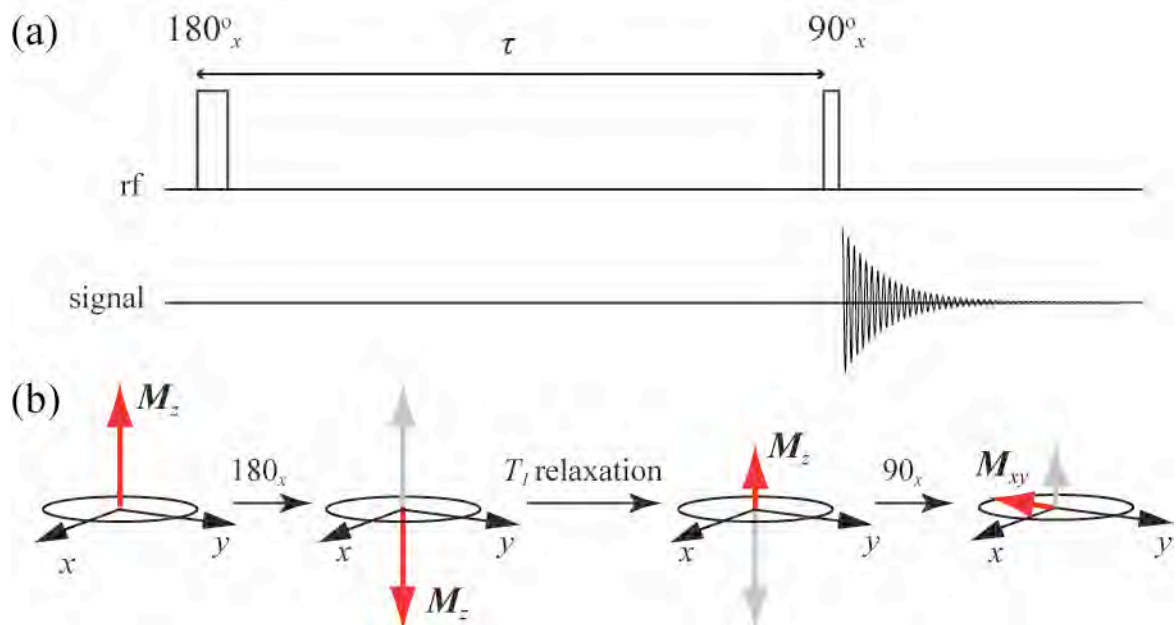
Figure 2.4. (a) Schematic diagram of the inversion recovery pulse sequence and (b) manipulation of the macroscopic magnetisation: The 180° pulse reverses M_z and it starts relaxing back to it equilibrium position. The 180° pulse 'flips' the spins on the xy-plane where an FID is acquired.

2.2.2 T_2 relaxation

T_2 relaxation refers to the relaxation of spins in the transverse plane. This occurs when, following an rf pulse, local magnetic field strength variations cause spins to loose phase coherence in the *xy*-plane, because of the existence of different precession frequencies. This loss of phase coherence is described by an exponential relationship:

$$M_{x,y} = M_0 e^{(-t/T_2)} \qquad\qquad (\ 2.4\ )$$

The Hahn echo, or spin echo, experiment is used for the measurement of transverse relaxation[8]. The pulse sequence producing a Hahn echo and the behaviour of the magnetisation are shown in Figure 2.5.
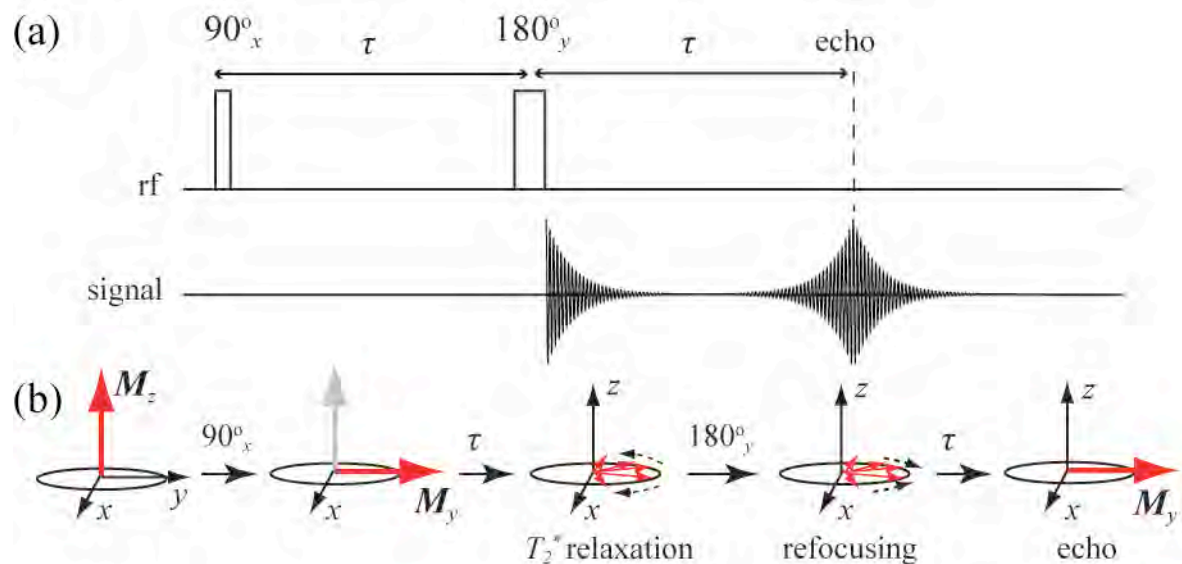
*Figure 2.5. Schematic diagram showing (a) a Hahn echo pulse sequence and (b) manipulation of spins: The 90˚ pulse rotates **M** into the xy-plane and the spins begin to loose phase coherence. The 180˚ pulse 'flips' the spins, which start refocusing until an echo is formed.*

A 90° rf pulse rotates the magnetisation into the *xy*-plane, following which spins begin to loose phase coherence, with some precessing faster and some slower. After a period τ, the spins are inverted by a 180° rf pulse causing them to rotate in the opposite direction until they regain the previously lost phase coherence. An echo occurs when the spins are completely refocussed, after a time τ following the application of the 180° rf. The Hahn echo experiment is, however, very sensitive to magnetic field inhomogeneities and diffusion. If spins diffuse to a region with a slightly different magnetic field, they cannot be fully refocused by the 180° pulse. As a result, in the presence of significant local field inhomogeneities ($\Delta \boldsymbol{B}_0$), the relaxation time of the FID is significantly shorter than T_2. This relaxation time is called T_2*. The relation between T_2 and T_2* is given by:

$$\frac{1}{T_2^*} = \frac{1}{T_{2(\Delta \mathbf{B_0})}} + \frac{1}{T_2} \qquad\qquad (\ 2.5\ )$$

For measuring T_2, and not T_2*, the spins need to be refocused on a timescale where the effects of diffusion are minimal. This is achieved using the Carr-Purcell-Meiboom-Gill (CPMG) experiment[8,9] (Figure 2.6), which repeats the 180° pulse *n* times, acquiring an echo each time and then fitting the decay of the echoes to equation 2.4 to obtain T_2.
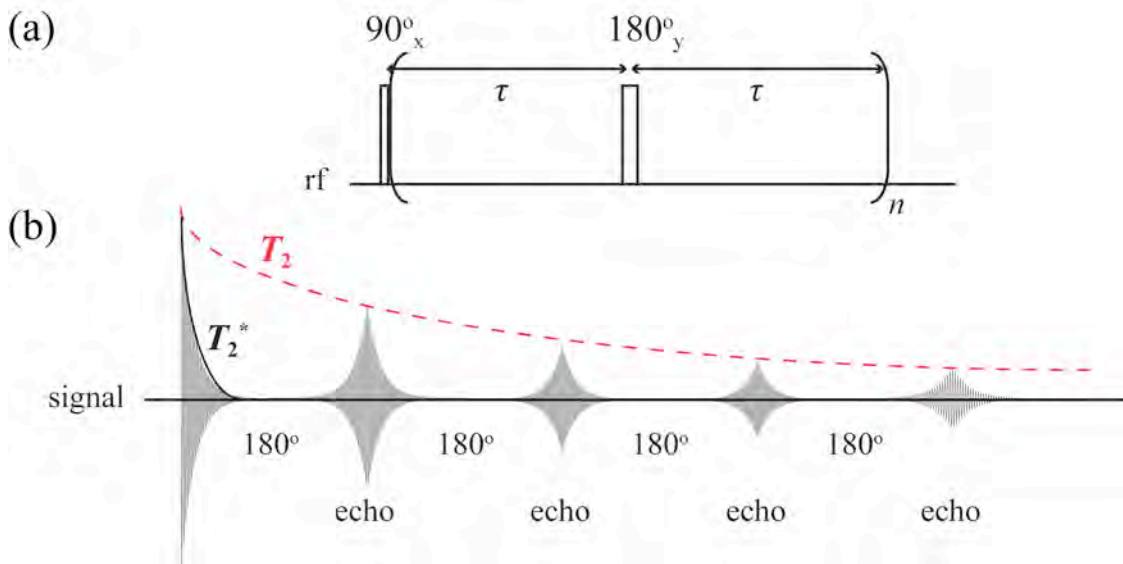
Figure 2.6. (a) Schematic diagram showing the CPMG pulse sequence. The 180˚ pulse is repeated n times with n echoes acquired. (b) Acquired echo train.

T_1 and T_2 relaxation times are characteristic of the chemical and physical environment of the protons in a system and are used to produce contrast in MR images.

2.3 Magnetic Resonance Imaging (MRI)

2.3.1 Using magnetic gradients for spatial encoding

By applying magnetic field gradients, it is possible to obtain spatial information about a sample. The static magnetic field varies linearly in the direction of the applied gradient causing the precessional frequency of nuclei to become spatially dependent:

$$\omega(\boldsymbol{r}) = \gamma B_0 + \gamma \boldsymbol{G} \bullet \boldsymbol{r} \qquad\qquad (\ 2.6\ )$$

where $\boldsymbol{G}$ is the magnetic gradient and $\boldsymbol{r}$ is the position.

Application of a magnetic field gradient generates a helix of phase of the precessing nuclear spin packets (Figure 2.7). To characterise the behavior of the phase of spin packets under the influence of the gradient, one can use the wavelength of this helix, λ, over which a 360° phase shift occurs. λ is dependent on the duration of the gradient, t, and the gradient strength $\mathbf{G}$.

$$\lambda = \frac{2\pi}{\gamma \mathbf{G} t}$$

(2.7)
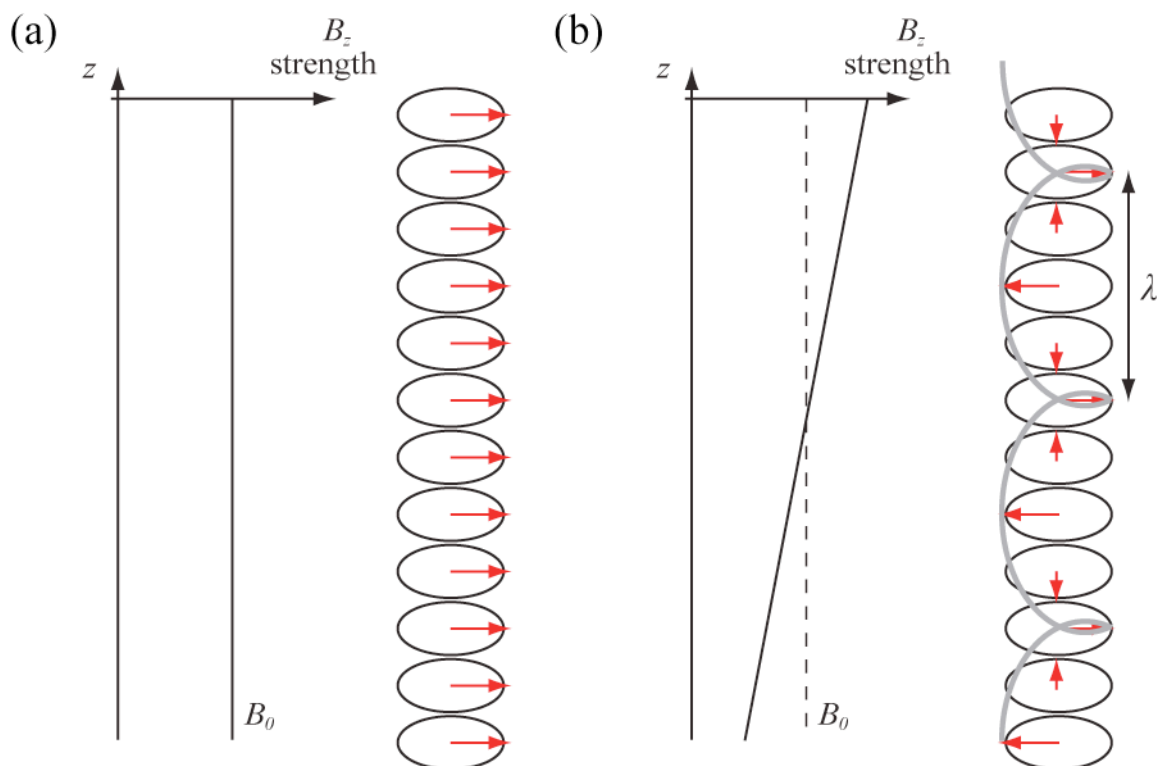
Figure 2.7. (a) Spin packet phase following a 90° pulse without applied magnetic field gradient. (b) Spin packet phase following a 90° pulse with a linear magnetic field gradient applied (here in the z-direction) winding a helix of phase of wavelength λ.

2.3.2 k-space

In 1973, Mansfield[10] introduced the concept of reciprocal space vector k, defined as:

$$k = \frac{\gamma G t}{2\pi} = \lambda^{-1}$$

$$(2.8)$$

The k-space approach introduces a unit that is linearly varying on the experimental parameters G and t in the direction of the gradient. That means that the k-space axes can be traversed either by varying the gradient strength either by varying the duration of the gradient application. This provides with two methods to encode the spatial information in MRI: phase encoding (varying G at constant time) and frequency (or read) encoding (varying t at constant G). In frequency encoding the gradient is switched on during the acquisition. A Fourier transformation of this data produces a spatially dependent intensity plot. The resulting signal intensity is proportional to the number of spins at a particular frequency. For a one-dimensional frequency encoded experiment where a single frequency-encoding gradient is applied along the z-axis, the resultant spectrum is a one-dimensional profile of all the spins in the x and y axes projected onto the z-axis. Figure 2.8 shows an example of a 1D frequency encoding of two tubes of water.
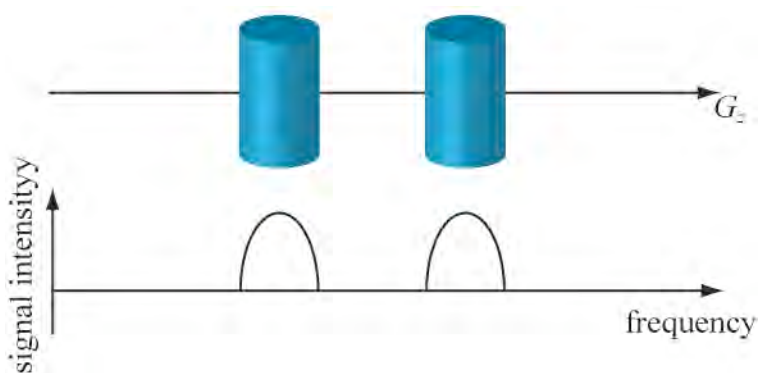

Figure 2.8. Frequency encoding spin density profile of two water tubes obtained when a gradient is applied along z.

For phase encoding, a gradient pulse is used, which is switched on then off, before the signal acquisition. The magnetic field gradient winds a helix of phase of the spin packets along an axis (Figure 2.7b). When the gradient is switched off the spin packets maintain their position-dependent phase.

By combining frequency and phase encoding along different axes it is possible to produce two-dimensional images. Figure 2.9 shows a *k*-space raster with a frequency-encoded *x*-direction and a phase encoded *y*-direction. A *k*-space raster is a representation of the data points acquired for a 2D image and has the same number of points as the number of pixels in the image.
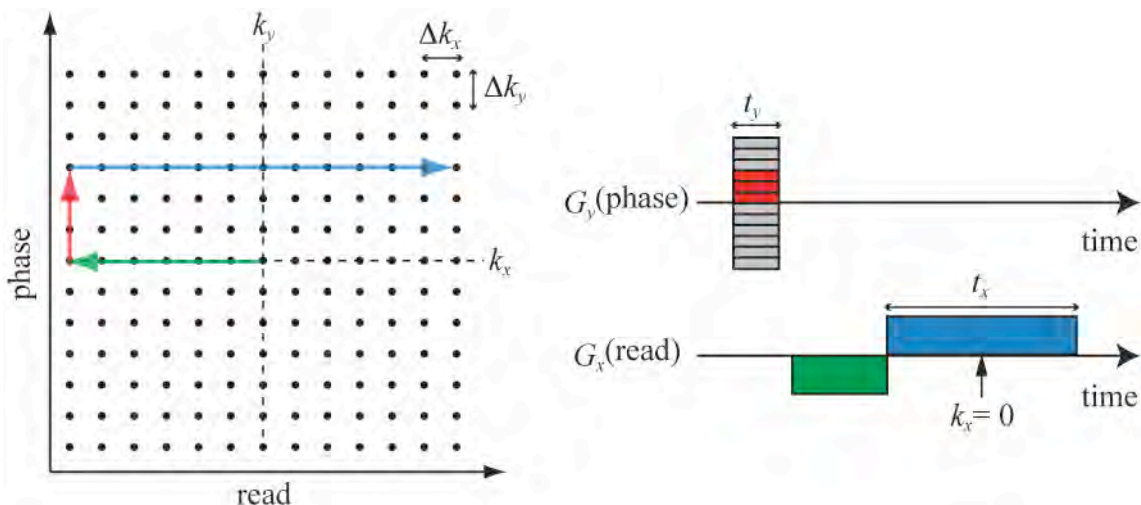
Figure 2.9. Sampling of a k-space raster. The x and y direction gradients are responsible for the frequency(read) and phase encoding respectively.

By applying gradients along the *x* and *y* directions it is possible to traverse this raster in Δk steps. Δk_x is the *x*-direction sampling interval given by $\Delta k_x = \gamma G_x \Delta t_x / 2\pi$, where Δt_x is the sampling interval of the FID. By applying a negative gradient prior to the positive read

gradient it is also possible to traverse negative values of k_x. Δk_y is the y-direction sampling interval given by $\Delta k_y = \gamma \Delta G_y t_y / 2p$, where ΔG_y is the phase encoding step size. k_y is traversed through the application of successive phase encoding gradient steps.

By applying frequency and phase encoding gradients it is possible to produce a 2D data set in *k*-space. A Fourier transformation of *k*-space data in both directions results in a space-domain spectrum where the signal intensity is proportional to the number of spins at a particular location on the *xy*-plane. The resultant real-space data is a 2D profile of all the spins in the third dimension projected onto the encoding plane. To obtain a 2D image, a selection of spins in a plane through the sample of interest, or slice selection, must be performed.

2.3.3 Slice selection

Slice selection[11] along horizontal or vertical planes is achieved by simultaneously applying a magnetic field gradient and a frequency selective rf pulse (Figure 2.10).
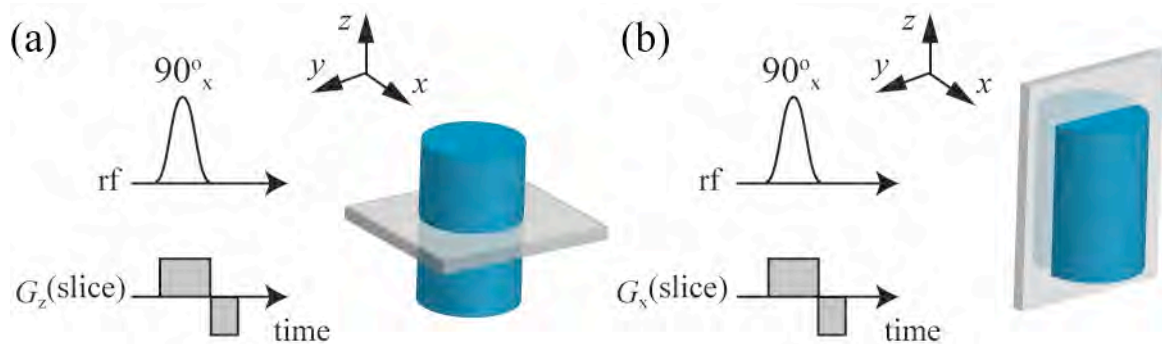

Figure 2.10. Horizontal (a) and vertical (b) slice selection through a cylindrical sample. The grey region is the observable region of the rf coil, or field-of-view.

The magnetic field gradient causes nuclei to precess with different frequencies along the desired direction for the slice selection. Using a soft, frequency-selective, rf pulse (Gaussian or sinc function), it is possible to control the bandwidth of excited frequencies (inversely proportional to the rf pulse duration).

The slice gradient causes an undesirable spread of the magnetisation vectors from different regions of the sample, leading to reduced signal. To cancel out the spread in magnetization, a refocusing gradient needs to be applied after the slice selection. This can be done either with gradient of opposite sign following the slice gradient, either by a gradient of same sign following a 180° rf pulse (Figure 2.10).

2.3.4 Spin echo imaging

Different imaging sequences can be produced by combining frequency encoding, phase encoding and slice selection sequences. A spin echo imaging sequence is based on the use of 90° and 180° rf pulses to form a Hahn echo (Figure 2.11). Initially, a slice-selective pulse is applied. The refocusing gradient produces a gradient echo. One single phase encoding gradient is then applied on the excited spins. In order to refocus the magnetisation, a 180° rf pulse is used to produce a Hahn echo. Following the application of the rf pulse, the spins are frequency-encoded for position. The echo is formed in the middle of the frequency-encoding gradient. The time between the centre of the 90° rf pulse and the centre of the echo is called echo time T_E. The data is acquired during the frequency encoding allowing for a full k-space line to be acquired. The process is repeated for all increasing phase encoding gradients until all k-space lines are acquired. T_R is the repetition time.
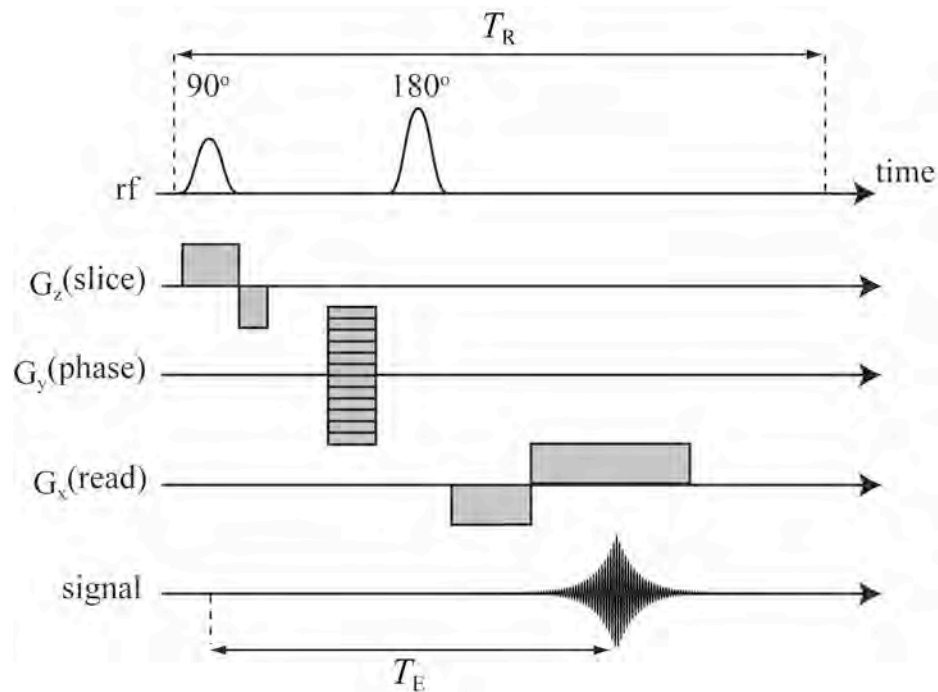
Figure 2.11. Schematic representation of a spin echo imaging sequence.

The imaging experiment time is depending on the number of phase encoding pixels, n_{PE}, the repetition time between experiments, T_R, and the number of image repetitions, n_{REP}. It can be calculated by:

$$\text{Experiment time} = n_{PE} \times T_R \times n_{REP} \qquad (2.9)$$

Two-dimensional Fourrier transformation of the data along the frequency and phase encoding directions allows producing a real space image. Multiple slices can be excited sequentially through different spatial locations of the sample and put together for the generation of 3D images of the sample.

2.3.5 MRI contrast

There are four main ways through which contrast can be achieved in MR imaging: spin density, relaxation times, chemical shift and spin motion. By varying the operating conditions of the pulse sequence it is possible to favour one or another type of contrast.

Equation 2.10 gives a typical expression of the signal intensity at a position r arising from an imaging experiment. In this expression, a_H is the amplitude of the Hahn-echo.

$$a_H(r, T_R, T_E) = M_0(r)\left[1 - \exp\left(-\frac{T_R}{T_1(r)}\right)\right]\exp\left(-\frac{T_E}{T_2(r)}\right)$$ (2.10)

Spin density contrast is obtained by variations of the number of excited spins within a sample. The resulting images are called spin density maps. To eliminate relaxation time contrast and obtain a spin density map, the effects of the exponential terms in Equation 2.10 must be minimised. This can be achieved if the echo time, T_E, is much shorter than T_2 and the repetition time, T_R, is significantly longer than T_1.

Relaxation contrast is obtained when the pulse sequence characteristic times are comparable to the relaxation ones. To obtain T_2 contrast, T_E must be comparable to T_2, in order to achieve significant signal attenuation from the factor $\exp(-T_E / T_2)$. As for spin density contrast, to ensure that T_1 contrast is minimised, T_R needs to be significantly longer than T_1. Contrast on a T_2–weighted image corresponds to relaxation time differences between regions of the sample, with bright regions typically corresponding to high T_2 relaxation regions. Similarly, to obtain T_1 contrast, T_R must be comparable to T_1 in order to achieve significant signal attenuation from the factor $\exp(-T_R / T_1)$. As for spin density contrast, to minimise T_2 contrast on a T_1-

weighted image the echo time must be as close as possible to zero (significantly smaller than T_2). Contrast on a T_1–weighted image corresponds to relaxation time differences between regions of the sample, but contrary to T_2–weighted images, short relaxation times give high signal intensity. Due to this difference, when an image contrast is obtained through a combination of T_1- and T_2-weighted contrast, a parameter region where the two types of contrast cancel out can be observed.

Chemical shift contrast is based on selective excitement of regions that have a particular chemical shift. Exciting a narrow spectral region is obtained in a similar way to the slice selection presented previously. Chemical shift contrast images are formed with signal coming only from the selected regions.

Finally, motional contrast is obtained by combining an imaging sequence with a pulse gradient spin echo sequence (PGSE) that allows encoding for motion. This method that provides with velocity and diffusion/dispersion information within a sample is of particular interest to this work.

2.4 Measurement of molecular motion

2.4.1 Pulsed gradient spin echo principles

In order to measure transport processes such as velocity or diffusion, a technique based on the use of spin echoes is applied. The formation of an echo is based on the cancellation of precessional phase shifts by reversing the phase evolution using a magnetic field gradient.

Over the time scale of the echo, molecular movements will produce additional phase shifts that will not be refocused. The phase shifts in the resulting signal can be used to quantify molecular movements.

The measure of translational motion can be obtained using a pulsed gradient spin echo (PGSE) experiment[6,12] (Figure 2.12).
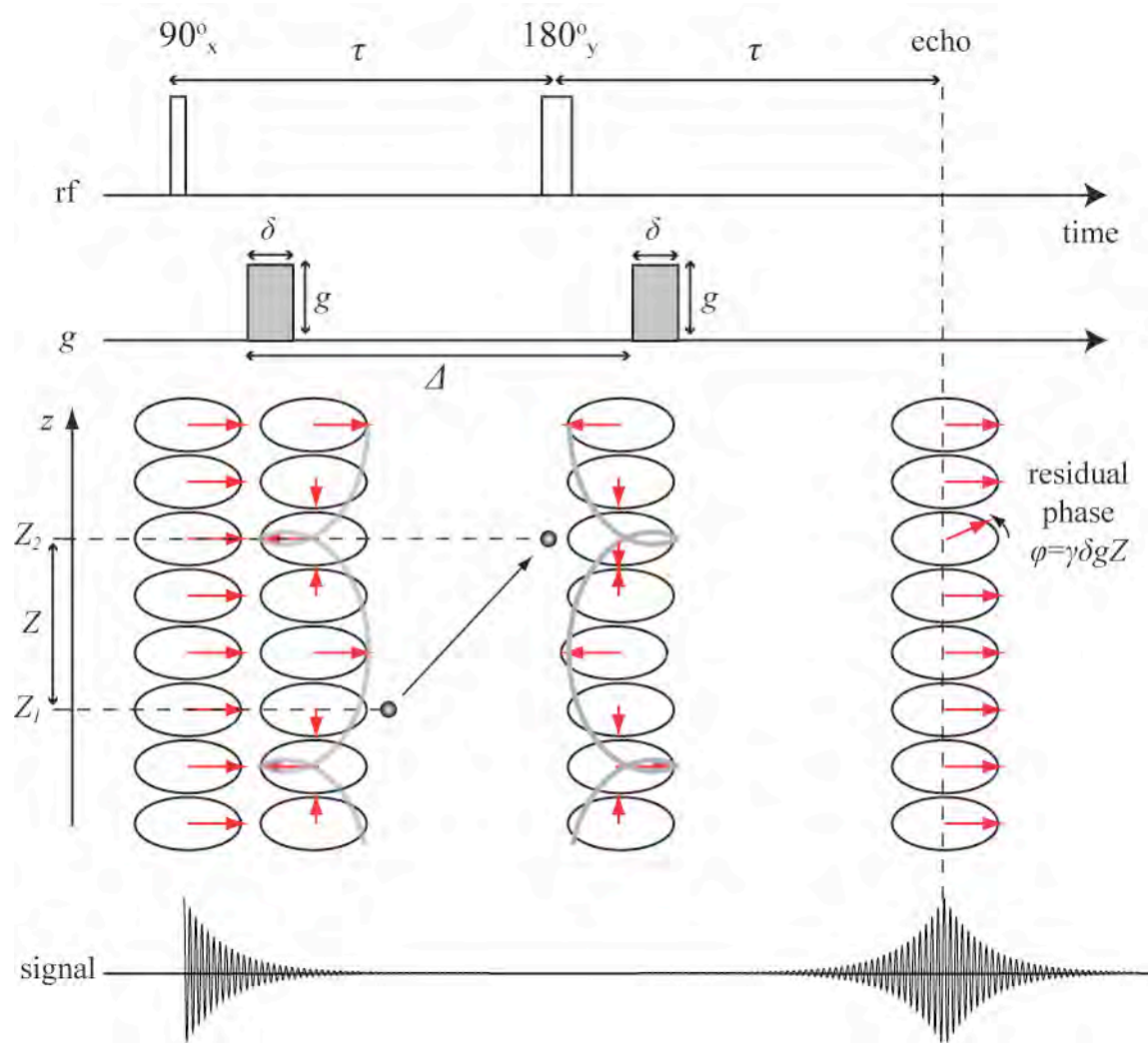

Figure 2.12. PGSE experiment. During Δ, a spin packet migrates by Z, resulting in a phase shift φ = γδgZ.

A 90° rf pulse bringing the net magnetisation in the transverse plane is followed by a short duration gradient that winds a helix of phase of the spin packet magnetisation vectors. A 180° rf pulse flips the vectors before a second gradient unwinds the helix of phase, refocusing all the vectors. Any motion of the molecules during the time Δ between the two gradients will result in a phase shift φ depending on the experiment parameters and the displacement of the molecules. As for the imaging experiments, a reciprocal q-space representing spatial frequency can be introduced. Similarly to the concept of reciprocal k-space, q-space has an inverse relation to the spatial wavelength of the helix phase, allowing to link distances to the gradient strength:

$$q = \frac{\gamma \delta g}{2\pi} \qquad (2.11)$$

Stejskal[13] showed that if the approximation of narrow δ pulses is valid ($\delta << \Delta$), so that we can neglect motion occurring during their duration, it becomes possible to characterise molecular displacements using the propagator formalism introduced in Chapter 1. To do this, one has to define $\rho(r)$ as the molecular density and $\rho(r)P(r'|r, \Delta)$ as the probability for an individual spin to start from r and finish at r' during Δ. For each molecule, the phase shift after the second gradient pulse would be equal to $\Delta\varphi = \gamma g \delta \cdot (r' - r) = q \cdot (r' - r)$ and its contribution to the echo signal E(q,Δ) - defined as the amplitude of the echo at its centre - would be given by the term $\exp(i\gamma g \delta \cdot [r' - r])$. Considering an ensemble of molecules one can then write:

$$E(q, \Delta) = \int \rho(r) \int P(r|r', \Delta) \exp(iq \cdot [r' - r]) dr' dr \qquad (2.12)$$

This equation shows that there is a Fourier relation between the echo amplitude E(q,Δ) and the conditional probability density of molecular displacements P($r'|r, \Delta$). The nature of the motion will determine the effect on the echo amplitude.

In the case of diffusion, where molecular motion is incoherent, there is a distribution of phase shifts, resulting in an attenuation of the magnetic resonance amplitude depending on γ, δ, Δ, **g**, and the diffusion coefficient of the molecules, D. In practice the MR signal is acquired over a range of **g** values, keeping δ and Δ constant, and D is then calculated using the Stejskal-Tanner relation[14]:

$$\frac{E(\boldsymbol{g})}{E(0)} = \exp(-\gamma^2\delta^2\boldsymbol{g}^2 D(\Delta - \frac{\delta}{3})) \qquad (\textit{2.13})$$

where $E(0)$ is the signal intensity when $g = 0$.

In the case of flow, coherent molecular motion will displace entire spin packets producing residual phase shifts on the echo signal. These phase shifts are dependent on γ, δ, Δ, **g**, and the spin packet velocity v in the direction of the gradient. For a z direction gradient (Figure 2.12), $v = Z / \Delta$, where Z is the displacement of the spin packet along z over the time Δ and the phase shift φ (in radians) is given by:

$$\varphi = \gamma g \delta Z = \gamma g \delta \Delta v \qquad (\textit{2.14})$$

Also, since there is an inverse relation between **q** and the displacements along a gradient axis, a Fourier transformation of E(q,Δ) produces the signal distribution as a function of

displacements. By normalising this signal one obtains a propagator giving the probability of molecular displacements along this axis (Figure 2.13).
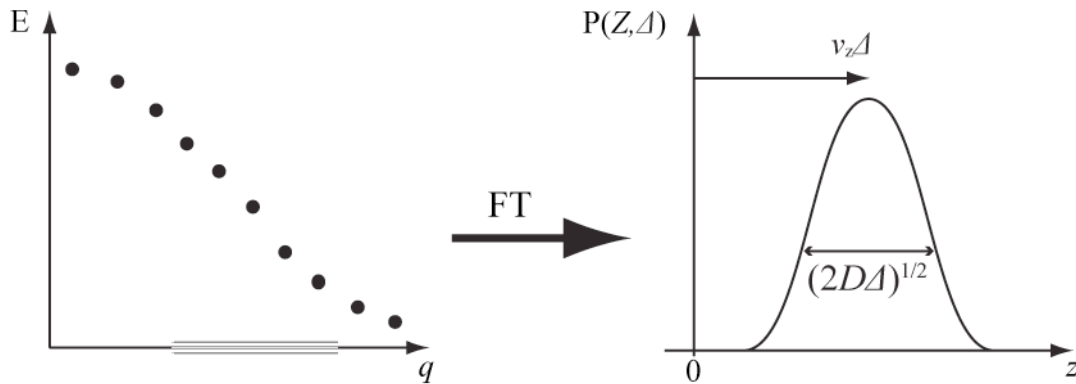

*Figure 2.13. A Fourier transformation of E(**q**), followed by a normalisation, gives a propagator P(Z,Δ) representing the average probability of molecular displacements along z. The propagator showed corresponds to molecules diffusing (D) and flowing at constant average velocity (v$_z$) along the gradient axis z.*

To obtain an accurate measurement of the propagator it is necessary to increase the gradient strength until the echo attenuation is less than 1%. As discussed in 1.4.1, the broadening of the propagator depends on both diffusion and dispersion, while its shifting along the axis depends on velocity (coherent flow). This allows deducing diffusion/dispersion by computing the width of the propagator and mean velocity by computing the offset of the propagator. When velocity gradients in the system are sufficiently high, as Δ increases, the effects of diffusion on the molecular displacements become negligible and the broadening of the propagator is dominated by flow-induced dispersion.

2.4.2 PGSE and PGSTE

Two pulsed gradient pulse sequences will be used in this thesis, the pulsed gradient spin echo (PGSE) and the pulsed gradient stimulated echo (PGSTE) (Figure 2.14).
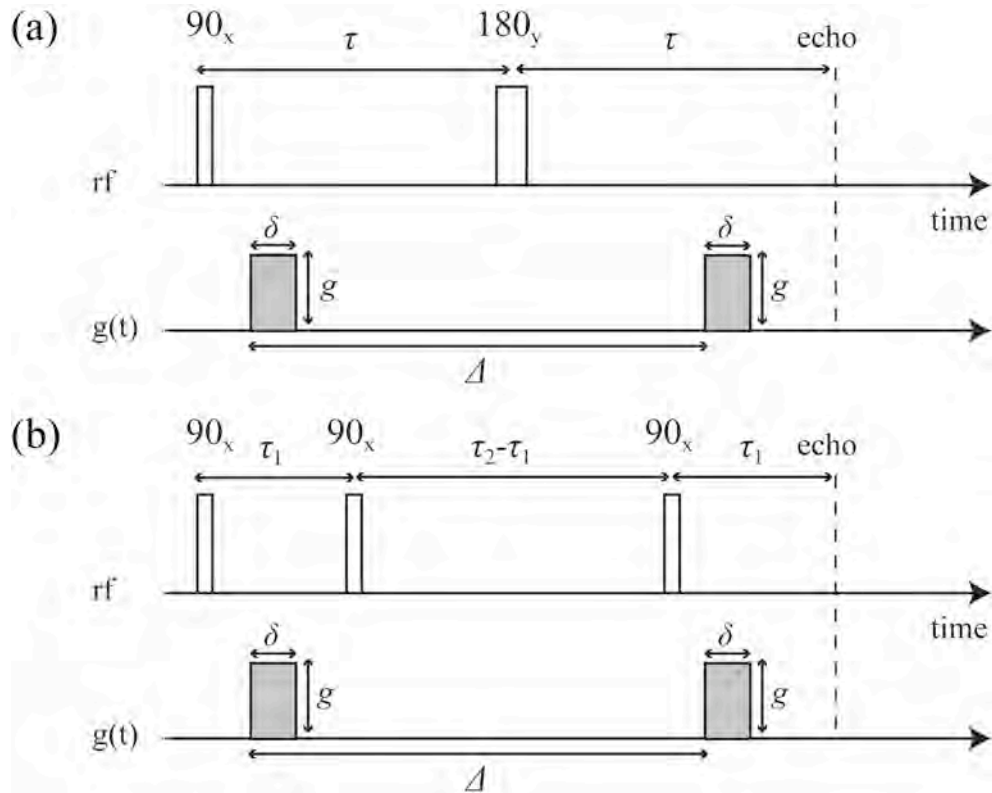

Figure 2.14. PGSE (a) and PGSTE (b) pulse sequences.

In terms of motion encoding, both sequences are equivalent, their difference lying only in the way the signal relaxes. With the PGSE sequence the magnetisation vector evolves in the transverse plane, experiencing T_2 relaxation. In the case of PGSTE, the second 90° pulse flips the magnetisation along the longitudinal axis, thus experiencing the slower T_1 relaxation during its evolution.

2.4.3 Magnetic resonance imaging of velocity, diffusion and dispersion

By integrating an imaging sequence into the PGSE or PGSTE one can obtain information on spatially heterogeneous motion within a sample. A typical pulse sequence used for measuring velocity and diffusion/dispersion images is shown in Figure 2.15.
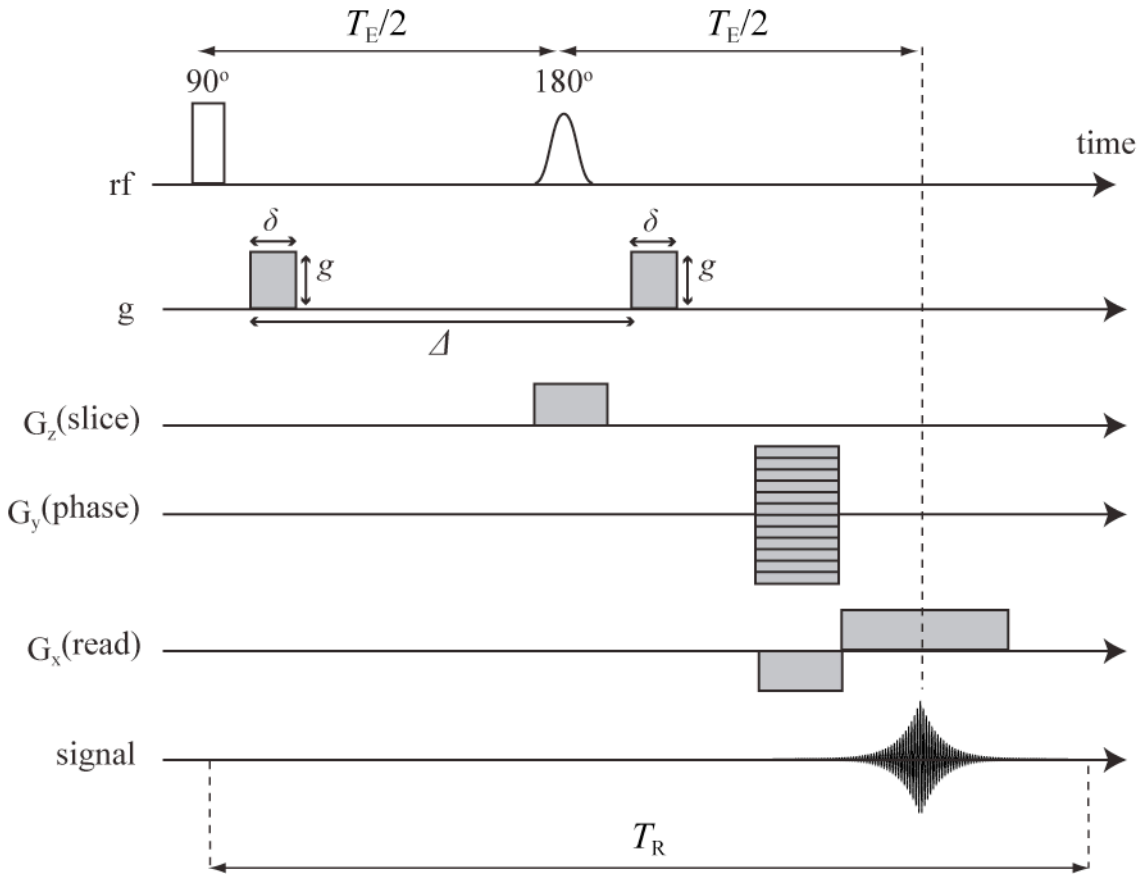
Figure 2.15. Pulse sequence including $\mathbf{k}$-space (imaging sequence) and $\mathbf{q}$-space (PGSE sequence) encoding.

The combination of q-space and k-space allows to simultaneously image spin density and the average propagator. The modulation of the signal in k-space and q-space is described by:

$$S(\boldsymbol{k},\boldsymbol{q}) = \int \rho(\boldsymbol{r})\exp(i2\pi\boldsymbol{k}\cdot\boldsymbol{r})\int P(\boldsymbol{R},\Delta)\exp(i\boldsymbol{q}\cdot\boldsymbol{R})\mathrm{d}\boldsymbol{r}\mathrm{d}\boldsymbol{R} \qquad (\ 2.15\ )$$

where $\boldsymbol{r}$ is the pixel position and $\boldsymbol{R}$ the displacement vector.

The resulting contrast c($\boldsymbol{q},\boldsymbol{r}$) for each pixel is given by:

$$c(\boldsymbol{q},\boldsymbol{r}) = \int P(\boldsymbol{R},\Delta)\exp(i2\pi\boldsymbol{q}\cdot\boldsymbol{R})\mathrm{d}\boldsymbol{r}\mathrm{d}\boldsymbol{R} \qquad (\ 2.16\ )$$

The combination of q-space and k-space allows to simultaneously image spin density and the average propagator. The modulation of the signal in k-space and q-space is described by:

$$S(\boldsymbol{k},\boldsymbol{q}) = \int \rho(\boldsymbol{r})\exp(i2\pi\boldsymbol{k}\cdot\boldsymbol{r})\int P(\boldsymbol{R},\Delta)\exp(i\boldsymbol{q}\cdot\boldsymbol{R})\mathrm{d}\boldsymbol{r}\mathrm{d}\boldsymbol{R} \qquad (\ 2.17\ )$$

where $\boldsymbol{r}$ is the pixel position and $\boldsymbol{R}$ the displacement vector.

The resulting contrast c($\boldsymbol{q},\boldsymbol{r}$) for each pixel is given by:

$$c(\boldsymbol{q},\boldsymbol{r}) = \int P(\boldsymbol{R},\Delta)\exp(i2\pi\boldsymbol{q}\cdot\boldsymbol{R})\mathrm{d}\boldsymbol{r}\mathrm{d}\boldsymbol{R} \qquad (\ 2.18\ )$$

The overall imaging process is four-dimensional, where three dimensions correspond to space and one to molecular motion. The direction in which motion is measured is determined by the direction of the motion-encoding gradient. The measurement of diffusion/dispersion and velocity requires the acquisition of several images, or q-slices, for different motion encoding gradient amplitudes. Increasing the number of q-slices increases the accuracy of the measurement. Before calculating a diffusion/dispersion coefficient and average velocity for

each pixel, a Fourier transformation of these images must be performed with respect to $\boldsymbol{k}$-space. In order to get velocity information the Fourier transformation is performed with a phase correction rather than a magnitude calculation. This produces complex data for the signal intensity for each pixel. A Fourier transformation of the echo decay curves for each pixel provides with an average propagator for each pixel. It allows to deduce individual pixel average diffusion/dispersion coefficient and velocity and to produce a spatially resolved velocity and diffusion/dispersion maps. An alternative way of producing velocity maps is to measure the phase shift between two q-slices. This approach reduces the experiment time but does not allow detecting velocity fluctuations.

(1)   Levitt, M. H. *Spin Dynamics; Basics of Nuclear Magnetic Resonance*; Wiley, 2001.

(2)   Callaghan, P. T. *Principles of Nuclear Magnetic Resonance Microscopy*; Oxford University Press: Oxford, 1991.

(3)   Freeman, R. *Magnetic Resonance in Chemistry and Medicine*; Oxford University Press, 2003.

(4)   Hore, P.-J. *Nuclear Magnetic Resonance*; Oxford University Press, 1995.

(5)   Atkins, P.; De Paula, J. *Physical Chemistry*; Oxford University Press, 2002.

(6)   Callaghan, P.-T. *Translational dynamics and magnetic resonance : principles of pulsed gradient spin echo NMR*; Oxford University Press, 2011.

(7)   Vold, R. L.; Waugh, J. S.; Klein, M. P.; Phelps, D. E. *J. Chem. Phys.* **1968**, *48*, 3831.

(8)   Hahn, E. L. *Physical Review* **1950**, *80*, 580.

(9)   Carr, H. Y.; Purcell, E. M. *Physical Review* **1954**, *94*, 630.

(10)   Mansfield, P.; Grannell, P. K. *J. Phys. C Solid State* **1973**, *6*, L422.

(11)   Edelstein, W. A.; Hutchison, J. M. S.; Johnson, G.; Redpath, T. *Phys. Med. Biol.* **1980**, *25*, 751.

(12)   Fukushima, E. *Annu. Rev. Fluid Mech.* **1999**, *31*, 95.

(13)   Stejskal, E. O. *J. Chem. Phys.* **1965**, *43*, 3597.

(14)   Stejskal, E. O.; Tanner, J. E. *J. Chem. Phys.* **1965**, *42*, 288.

3 MR characterisation of stationary vortex flow

3.1 Introduction

An investigation on Taylor Vortex Flow (TVF) structure and mixing properties is presented in this chapter. The flow environment produced within stationary Taylor vortices finds diverse applications in chemistry[1], chemical engineering[2] and biochemistry[3-5]. These applications require a good understanding of flow properties and mixing. But despite the numerous research publications on vortical flows within a Couette cell (more than 1400 published studies over the last 90 years[6]), there are many open questions remaining. Experimental results are not easy to generalise, since besides the fluid viscosity and the rotation rate, the flow properties have been shown to be very sensitive to the cell specifications (dimensions and materials). Therefore it becomes very difficult to predict with accuracy the flow pattern of a given experimental setup and even more difficult to predict mixing properties as intra-and inter-vortex mixing.

MR velocimetry has provided with 3 dimensional data in TVF revealing the ability of velocity encoding to characterise flow structure and spatio-temporal phenomena in vortical flow[7,8]. In the present study, magnetic resonance techniques were used to investigate the laminar Taylor Vortex Flow regime[9]. The aim is to characterise both structure and mixing properties of TVF flow, while examining the potential of MR techniques in analysing complex vortical flows. Working in the laminar regimes allows to have a steady-state flow, facilitating chemistry-flow coupling studies (chapter 6,7), but also to take complete advantage of the MR resonance techniques that, despite the advances on fast imaging[10], present several

limitations in probing unsteady or turbulent flow systems.

Velocity and diffusion/dispersion maps of TVF flow were produced and used to characterise the flow structure. The study focuses on the effect of rotation on the velocity field and the dimension of the vortex pairs. On the basis of these results, conclusions are drawn on the rotation effects on mixing within TVF. Velocity and diffusion/dispersion mapping alone are shown to provide with a limited insight to the intra- and inter-vortex mixing properties. To overcome these limitations, non-spatially resolved measurements are performed in order to measure global propagators for the flow and provide information on overall molecular displacements along a given direction. The probabilities of displacement obtained may come either from advection (resulting in a propagator offset along the displacement axis) or from dispersion (resulting in a broadening of the propagator)[11]. Several studies have shown the possibility to compare the average propagator with spatially resolved velocity image data[12,13] but its use has been limited to the study of flows in porous materials. It is shown that TVF propagator analysis provides with both qualitative and quantitative information on mixing inside this flow, giving a direct measure inter-vortex mixing.

3.2 Experimental

3.2.1 Couette cell dimensions and set-up

The Couette cell was constructed from an outer glass tube of radius R_o = 8.25 mm and an inner PEEK rod of radius R_i = 4.1 mm, resulting in a gap, d, of 4.15 mm. The experimental setup is shown in Figure 3.1. The length of the gap, L, was of 896 mm, giving a length to gap

ratio Γ of 216 and a radius ratio η of 0.5. PTFE guides were placed at the top and bottom of the cell in order to reduce the inner cylinder movements during the rotation. To rotate the inner cylinder, a stepper motor (Bruker NMR Rheokit) was used. To reduce vibrations in the system that could cause artifacts and errors in velocity measurements, the connection between the motor and the inner cylinder was made with a rubber connection absorbing vibration transmission and shocks due to alignment errors. The Couette cell was placed into the magnet and the MRI field of view (rf coil) was situated 13 cm above the lower PTFE guide.
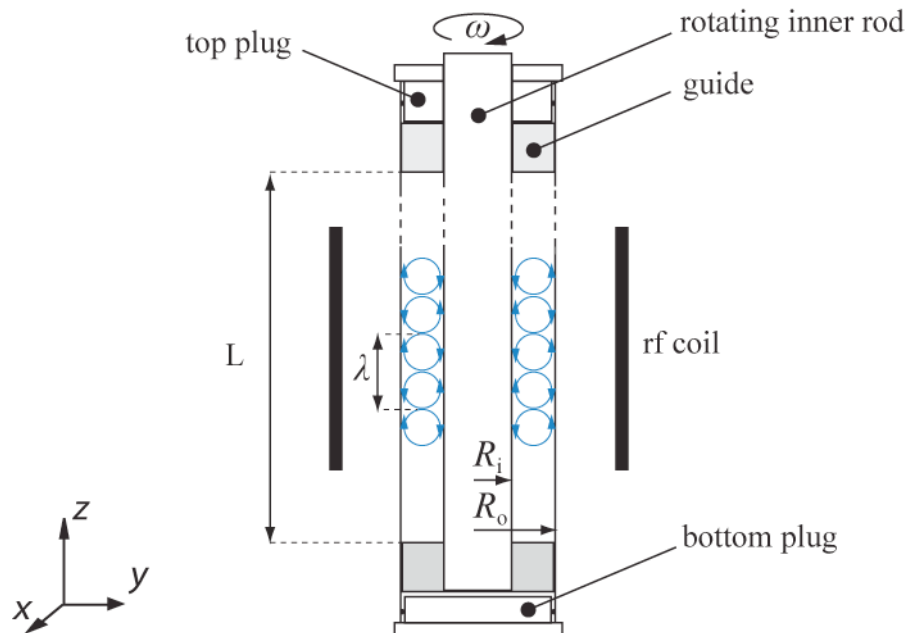
Figure 3.1. Schematic diagram of the Couette cell set-up, showing series of counter-rotating vortex pairs of wavelength λ. The field of view of the MR experiments is situated in the area within the rf coil.

3.2.2 Parameter ranges

Tap water was used for all the experiments. The viscosity ν, measured with a calibrated Ubbelohde Viscometer, was of 0.979 mm^2 s^{-1} at 22 ± 0.5 ˚C. Five rotation rate values, ω,

were used: 0.5 Hz, 1 Hz, 1.5 Hz, 2 Hz and 2.5 Hz. The respective $Ta = \omega R_i d / \nu$ values were of: 8.5, 17, 25.5, 34 and 42.5. To ensure flow steady state, each series of measurements was performed 5 minutes after setting the rotation rate of the inner cylinder.

3.2.3 Velocity and dispersion imaging

All NMR measurements in this thesis were performed on a Bruker DMX 300 spectrometer operating at a proton resonance frequency of 300 MHz. The probe diameter was of 25 mm and the temperature of the bore was 289.4 K $\pm$ 1 K.

A Pulsed Gradient Spin Echo (PGSE) sequence was used for the velocity and dispersion imaging (Figure 2.15). The PGSE parameters used during these experiments were in the following ranges: $\Delta = 10 - 30$ ms, $\delta = 1 - 2$ ms and $G = 0.1 - 0.8$ T m^{-1}. A hard 90° excitation pulse was used, in a range of 43-45 µs. A soft 180° Gaussian pulse of 1000 µs was used for slice selection, with an attenuation range of 16-16.8 dB. Imaging slices had a thickness of 1 mm. The field of view was of 50 × 25 mm, with a matrix size of 256 × 128 pixels resulting in a pixel size of 0.196 × 0.196 mm. The spectral width was of 100 kHz. 4 *q*-slices were acquired for velocity maps and 8 *q*-slices for diffusion/dispersion maps, with 2 signal averages. By positioning the phase encoding gradient as close as possible to the readout, artifacts that could be created by spins travelling in an oblique direction to the phase and read orientations[10] were minimised. The data was analysed using Prospa software.

3.2.4 Propagator measurements

A Pulsed Gradient Stimulated Spin Echo (PGSTE) sequence was used for the propagator measurements[14] (Figure 2.14). The PGSTE parameters used were in the following ranges: $\Delta =$ 20 - 1000 ms, $\delta = 1$ ms and $G = $ -0.2 - 0.2 T m^{-1}. The data were obtained using 64 and 128 $\boldsymbol{q}$-slices with 4 and 16 averages respectively. More $\boldsymbol{q}$-slices and averages could improve the quality of the measurements but they were avoided due to the fact that the experiments were becoming very long (i.g $\sim$ 5hrs for 64 averages and 128 $\boldsymbol{q}$-slices), causing wear of the inner cylinder PTFE stabilisers, heating of the water and bubbles stagnating in the gap. The data was analysed using Prospa software.

3.3 Results and discussion

3.3.1 TVF velocity and dispersion imaging

3.3.1.1   Velocity maps

Figure 3.2 shows axial (a), radial (b) and azimuthal (c) velocity maps of stationary TVF vortices at $\omega = 1$ Hz. For each map, the positive velocities in the axis direction are shown in orange, while the negative ones are shown in blue.
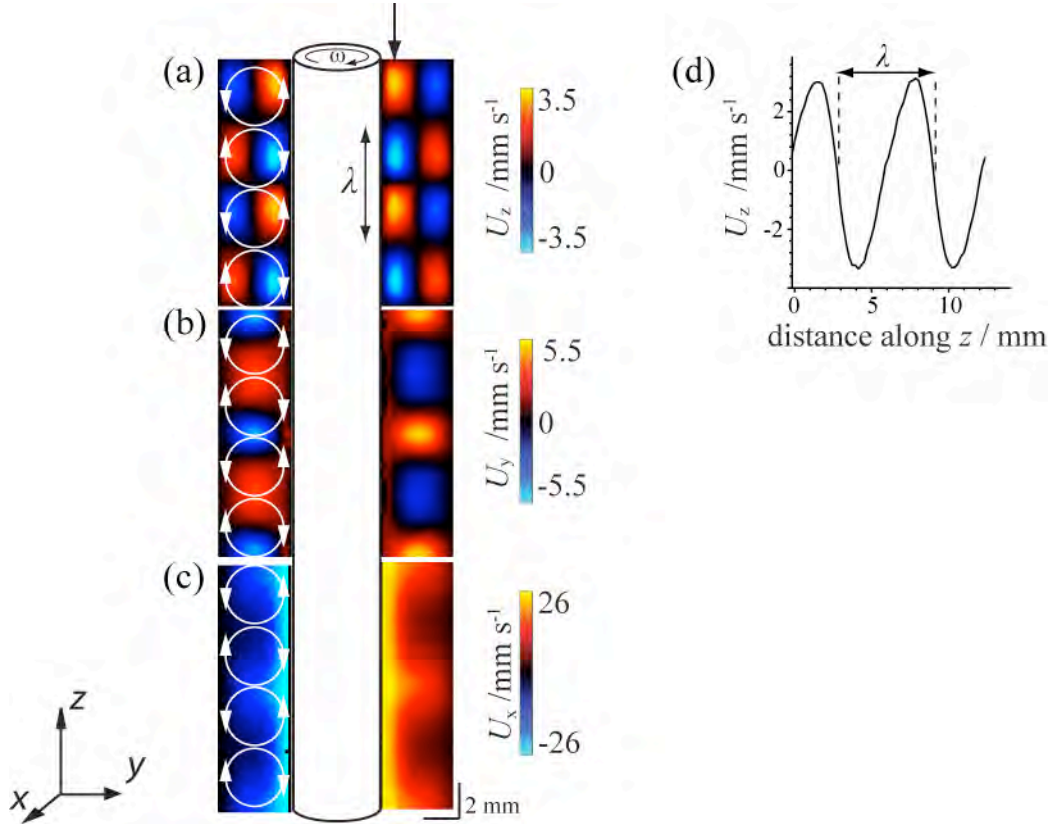

Figure 3.2. (a)–(c) MR velocity maps of TVF flow in the axial, U_z (a), radial, U_y (b), and azimuthal, U_x (c), directions at $\omega = 1$ Hz. The left hand side schematic diagram of the vortices allows identifying the main features of the flow. (d) Plot of a velocity vector from the area indicated by the arrow on the axial direction velocity map.

Main structural features of TVF flow[9] can be easily identified on these maps. The U_z map shows the circulating motion of the vortices, with series of alternating positive and negative velocities. In the inter-vortex regions the velocities in this direction are several times smaller than in the vortex core revealing the low inter-vortex mixing properties of this flow. The periodic variation of velocity with respect to space corresponds to the vortex pair wavelength. Figure 3.2d shows how the plot of a velocity vector line allows measuring the wavelength. The radial velocity map, U_y (Figure 3.2b), also highlights the vortex pair wavelength, with the high positive velocities marking the outer edges of each vortex pair where the secondary flow towards the outer cylinder is formed. This secondary flow appears in positive velocities on the left hand side of the Couette gap, where the outflow is in the direction of the *y*-axis, and in negative velocities on the left hand side. Velocities are positive all along the inner cylinder side, with some pixels missing probably due to slight wobbling during the acquisition. The U_x map (Figure 3.2c) shows velocities in-between vortex pairs that are an order of magnitude higher compared to those inside the vortex pairs. Again, the velocities in the right hand side, where the direction of rotation of the inner cylinder is the same as the direction of the *x*-axis, appear in positive while the velocities in the left hand side appear in negative. The high radial and azimuthal velocities in the outflow region of the vortex pairs dominate molecular displacements. Their interplay with the vortical recirculation in the axial direction explains the reduced inter-vortex exchanges observed at these regimes.

3.3.1.2 Diffusion/dispersion maps

Prior to the analysis of the diffusion/dispersion maps produced from the PGSE imaging experiments it is important to understand the nature of the results obtained by the PGSE sequence. The calculation of a diffusion/dispersion coefficient is based on the measurement of the propagator broadening caused by phase spreading. This measurement is therefore very sensitive to any effect that can introduce additional phase spread[15]. In the absence of flow, and assuming that phase spread caused by the experimental setup and the spectrometer is minimised, the phase spread arises mainly from Brownian motion. However, in most propagator experiments presented in this thesis velocity shear is present in the system and contributes to the phase spread measured during the PGSE experiment. This causes the broadening of the propagator to be generated by both diffusion and velocity shear. In the case of a PGSE imaging sequence this broadening is found to be proportional to velocity differences between adjacent voxels[16]. This means that the dimension of the voxels will affect the phase spread. Hence, despite the fact that the diffusion/dispersion maps allow to identify regions of high and low dispersion, the quantitative nature of the coefficients obtained has to be considered with precaution since they include the effects of flow inhomogeneities. In order to measure only stochastic motion such as diffusion or dispersion in a system in the presence of flow, and produce a quantitative diffusion or dispersion map, the voxel size would have to be small enough so that the velocity shear contribution, caused by velocity inhomogeineities, can be neglected. This is not always achievable, especially in systems were high shear is present. An alternative method consists in exploiting the fact that, contrary to Brownian motion, velocity shear is coherent and its effects can therefore be reversed using an appropriate pulse sequence, such as the double PGSE pulse sequence[17,18].

Figure 3.3 shows axial (d), radial (e) and azimuthal (f) diffusion/dispersion maps at the same rotation rate as the velocity maps (ω = 1 Hz). Diffusion/dispersion maps for this flow have not been previously reported in the literature.
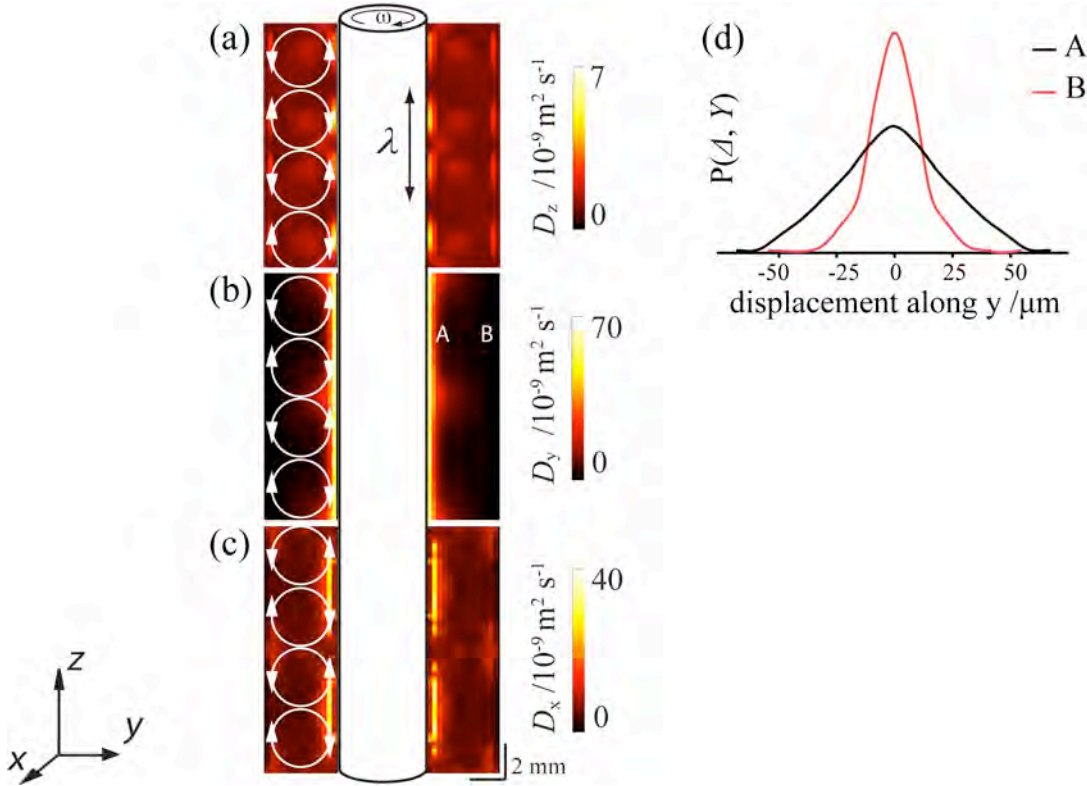
Figure 3.3. (a)–(c) MR diffusion/dispersion maps of TVF flow in the axial, D_z (a), radial, D_y (b), and azimuthal, D_x (c), directions at ω = 1 Hz. The observation time was of 20 ms. The left hand side schematic diagram of the vortices allows identifying the main features of the flow. (d) Plot of propagators for the positions A and B shown on the radial direction diffusion/dispersion map.

The higher dispersion regions are identified close to the inner cylinder where the velocity gradients are higher. Between vortex pairs, where the radial and azimuthal direction velocity profiles are less sharp, reduced dispersion is observed. Despite the fact that it presents one

order of magnitude lower dispersion rates, the axial direction diffusion/dispersion map is of particular interest, since it is linked with inter-vortex exchanges and can help us analyse axial dispersion in the system. Note that a map of this system with a stable inner cylinder (no flow) gives a uniform coefficient of 2×10^{-9} m^2 s^{-1}, in this case it can be called a diffusion map since no dispersion effects are measured. The values obtained in the diffusion/dispersion maps (Figure 3.3) are varying from 2×10^{-9} m^2 s^{-1} to 70×10^{-9} m^2 s^{-1} indicating the dominant role of flow-induced dispersion in determining the molecular displacements measured.

The high dispersion regions in the axial direction (Figure 3.3a) are situated in the regions of friction between the vortices' higher velocities and the wall. The vortex core region, where higher dispersion is observed, can be clearly seen in the middle of each vortex. Finally, in the area between the vortex pairs, dispersion seems low, except from a point near the inner cylinder, where high velocities of opposed direction are adjacent. In this region, enhanced molecular exchanges between vortex pairs might be occurring. These results are in agreement with previous studies[19] showing higher inter-vortex mixing near the inner wall region and the inflow boundaries. In the radial direction, the secondary flow generates additional dispersion increase in between vortex pairs. For each pixel of the diffusion/dispersion maps a propagator can be obtained by Fourier transformation of the signal decay against the gradient increase. Figure 3.3d shows propagators from two pixels A and B shown in the radial direction diffusion/dispersion map. These propagators give the probability distribution of molecular displacements along the *y*-axis during the observation time $\Delta = 20$ ms. The propagators are centred around zero displacement, due to the fact that the velocities in both regions are equal to zero. Coherent flow would lead to an offset of the propagator along the displacement axis. In this case, the propagators are mainly affected by incoherent flow

(dispersion and self-diffusion). A wider propagator corresponds to a higher dispersion coefficient within a given pixel. The width at the average height is equal to $(4D_y\Delta)^{1/2}$, where D_y is the average diffusion/dispersion coefficient. For low velocity gradient regions (B) the propagator seems more affected by self-diffusion and is similar to a typical Gaussian distribution of molecular displacements. The main difference is the presence of high displacement side lobes. At higher velocity gradient regions (A), the shape of the propagator is modified towards a more triangular shape, with a linear distribution of molecular displacements. Finally, in the azimuthal direction (Figure 3.3c), the higher dispersion is observed along the length of the vortex pairs, where the sharper velocity profiles in the azimuthal direction are generated. High dispersion is also found in the region of the outer cylinder where the secondary flow is formed.

3.3.2 The effect of rotation on TVF flow structure

The effect of ω on the flow within a Couette cell was investigated. The axial direction velocity maps are shown in Figure 3.4. Below the critical rotation rate for the TVF instability onset is applied, no coherent flow can be measured in the axial direction (Figure 3.4a). Measurements show that the TVF instability arises at around 0.7 Hz. At $\omega = 1$ Hz (Figure 3.4b), the series of alternating positive and negative velocities indicate the presence of vortices stacked along the length of the cell. For this rotation rate range, the velocities increase for increasing rotation rates, with the part of the vortices situated near the inner cylinder presenting always higher velocities than the ones measured near the outer cylinder. The opposed negative and positive velocities at the secondary flow regions are coming closer as rotation increases, and the vortical regions close to the inner cylinder are expanding taking

more and more space in the gap centre (Figure 3.4c-d). Also, the interface between the positive and negative regions is reduced before becoming unstable at $\omega = 2.5$ Hz (Figure 3.4e).
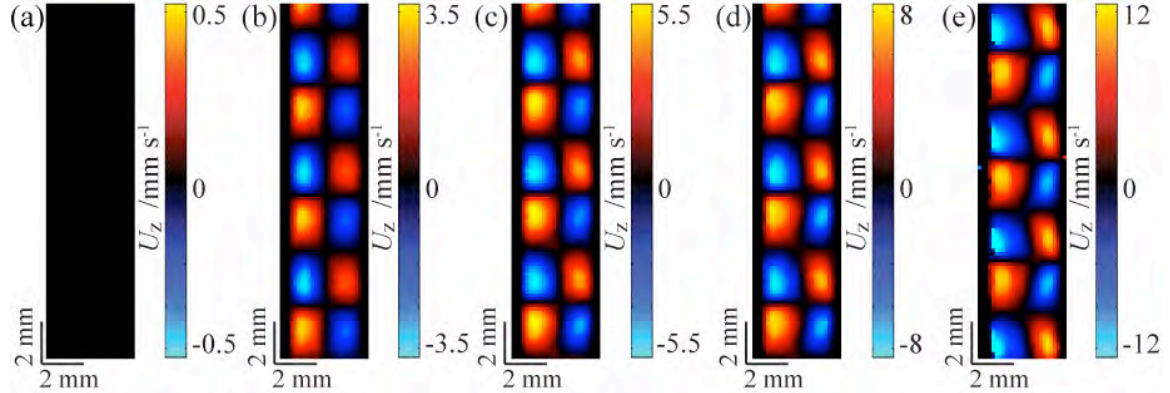

Figure 3.4. Axial direction (z) velocity maps at increasing ω: (a) 0.5 Hz, (b) 1 Hz, (c) 1.5 Hz, (d) 2 Hz and (e) 2.5 Hz. The rotating inner cylinder is situated on the left hand side of each image.

In the radial direction, below the critical rotation rate (Figure 3.5a) a velocity gradient is observed with the higher velocities close to the inner wall. Above the critical rotation rate (Figure 3.5b-e) secondary flow can be observed in orange. This flow is always at higher velocities than the inflow towards the inner cylinder (in blue). For low rotation rates, this region is symmetric with respect to the *y*-axis (Figure 3.5b). As the rotation rate is increased, both direction velocities are increased. The secondary flow velocity gradients are steeper and the region situated near the rotating cylinder is narrower (Figure 3.5d-e). At $\omega = 2.5$ Hz (Figure 3.5e) the region corresponding to the secondary flow is unstable and not symmetric with respect to the *y*-axis, indicating a possible state transition.
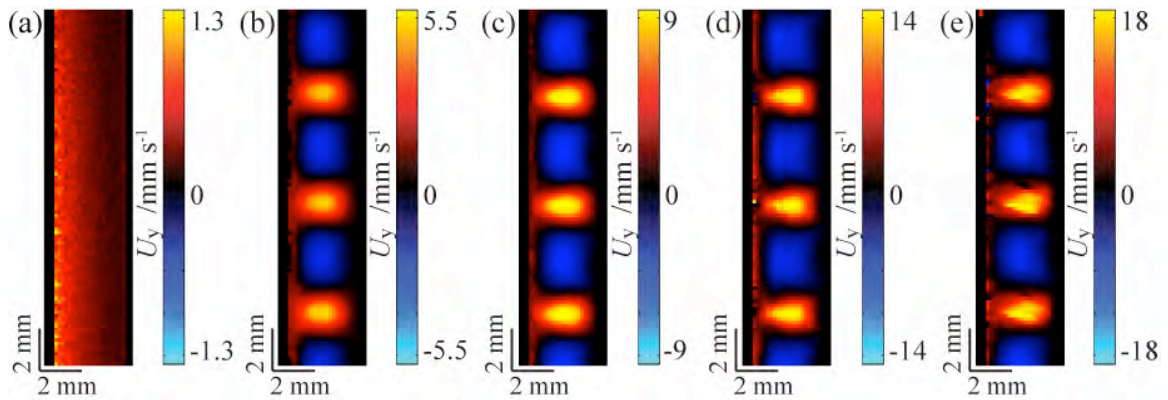
Figure 3.5. Radial direction (y) velocity maps at increasing ω: (a) 0.5 Hz, (b) 1 Hz, (c) 1.5 Hz, (d) 2 Hz and (e) 2.5 Hz. The rotating inner cylinder is situated on the left hand side of each image.

The azimuthal direction velocity maps (Figure 3.6a-e) present the higher velocities. The product between the rotation rate and the perimeter of the cylinder gives the velocity on the inner cylinder. At ω = 0.5 Hz (Figure 3.6a) higher velocities are observed near the inner wall but no instability is seen. As the rotation increases the velocity gradient between the rotation inner cylinder and the stationary outer cylinder becomes steeper. This velocity gradient generates an opposition between centrifugal forces towards the outer cylinder and pressure gradients toward the inner cylinder. Above the critical rotation rate, secondary flow arises, characterised by periodic velocity increases along the length of the cell (Figure 3.6b). The outflow regions have less steep profiles in the radial direction than the neighbouring regions. Further increase in rotation makes this secondary flow velocity profiles steeper, both in the axial and radial direction. At ω = 2.5 Hz these regions become unstable and the system seems to switch to wavy TVF[9].
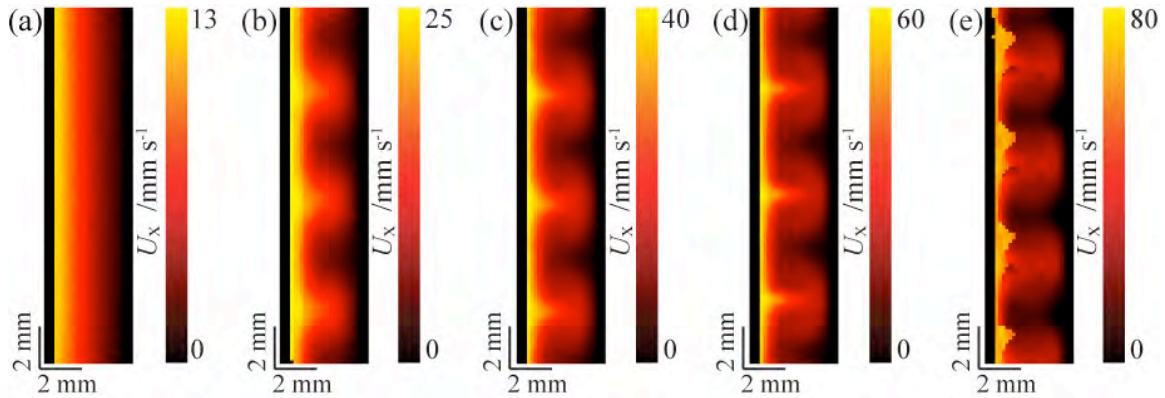
Figure 3.6. Azimuthal direction (x) velocity maps at increasing ω: (a) 0.5 Hz, (b) 1 Hz, (c) 1.5 Hz, (d) 2 Hz and (e) 2.5 Hz. The observation time was of 20ms. The rotating inner cylinder is situated on the left hand side of each image.

Figure 3.7 shows a plot of the evolution of the maximum velocity for each direction against the rotation rate. For all these experiments, the maximum velocities have been found to increase linearly with the rotation rate. The non-slip boundary condition at the inner cylinder surface allows to calculate the maximum velocities in this direction: $U_{max} = 2\pi R_i \omega \approx 26\omega$. As we see from the *x* direction plot this trend is found in our experimental data where $U_{max} \approx 26\omega$. In the axial and radial directions, the maximum velocity increase with rotation follows a linear trend of smaller slope ($U_{max} \approx 10\omega$ in the y direction and $U_{max} \approx 5\omega$ In the z direction). The fact that the maximum velocities in the radial direction are two times higher than the ones in the axial direction indicates that the circulation in the vortices is not done at uniform speed. This is probably due to the presence of helical streamlines wrapping around the torroidal vortices[20].
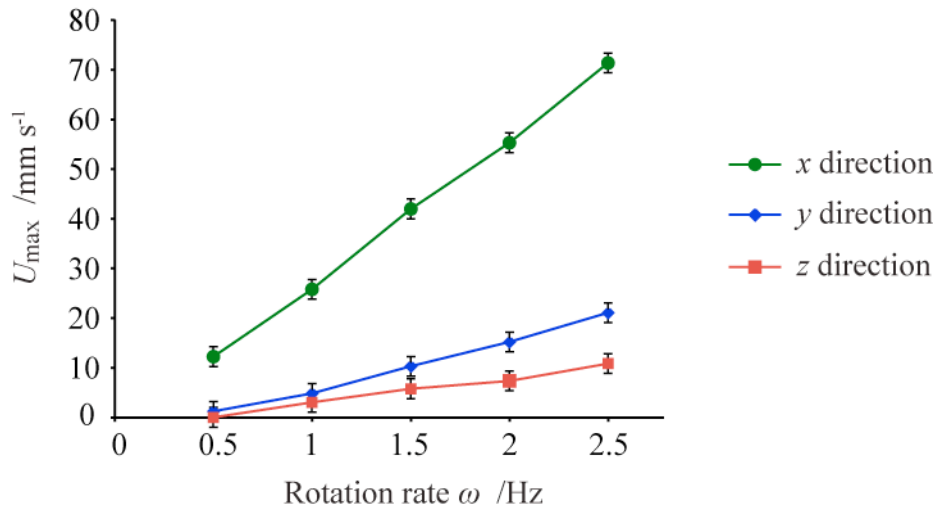
Figure 3.7. Maximum velocities, U_{max}, against rotation rate for velocity maps in the azimuthal (x), radial (y) and axial (z) direction.

One other important parameter that can be extracted from the velocity maps is the vortex pair wavelength, λ. The spatial periodicity within this flow was measured by plotting velocity vectors along the axial direction as shown previously (Figure 3.2d). Velocity vectors were selected from the middle of the gap of the velocity maps. Figure 3.8 shows plots of the measured wavelength in each direction, for different rotation rates. For low rotation rates, similar wavelength is measured in every direction velocity map. For ω ≥ 2 Hz, there is more spread in the measurements, and the wavelength in the azimuthal direction is found to be shorter than the ones in the axial and radial directions. The wavelength in the axial direction is also reduced at ω = 2.5 Hz, but in the radial direction the wavelength increases. As the difference between wavelengths in different directions is increased, the shape of the vortices is expected to change. The difference of wavelength between flow in different directions might give information on the flow structure transition to wavy TVF and has to be further investigated.
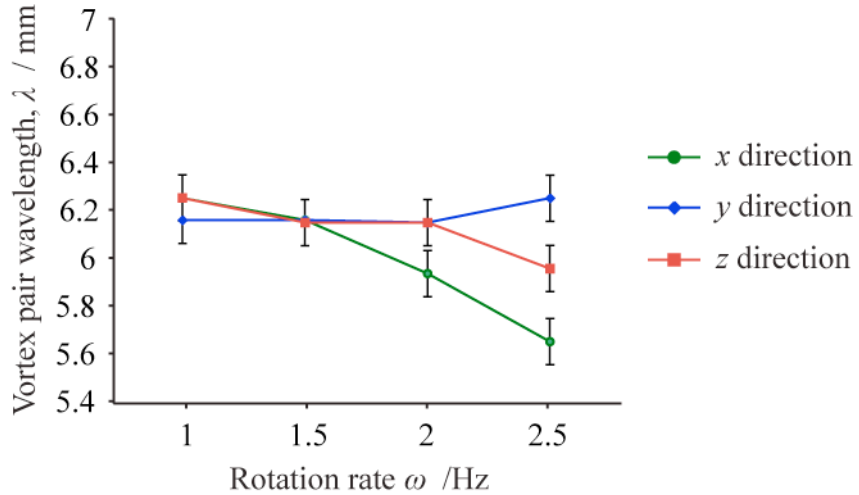
Figure 3.8. Vortex pair wavelength against rotation rate obtained from a velocity vector selection from the x, y and z direction velocity maps. The velocity vectors were selected in the higher velocity regions of each map.

The structure change with increased rotation rates is also expected to affect mixing within the flow. The diffusion/dispersion maps can help getting an insight into the mixing properties within and between vortices.

3.3.2.1   Axial dispersion

Figure 3.9 shows diffusion/dispersion maps in the axial direction for increasing rotation rates. Dispersion maps in the axial direction are of particular interest when studying inter-vortex mixing since they can probe incoherent molecular displacements in between vortices. Below the critical rotation rate enhanced but spatially homogeneous dispersion coefficients are measured. At the onset of the TVF instability, high dispersion regions are situated between the inner cylinder and the vortex outer regions. The flow-induced dispersion rates seem to

increase rapidly with rotation rate until reaching an order of magnitude higher values for ω = 1.5 Hz. For ω ≥ 1.5 Hz, dispersion rate increase with rotation is less important, but there is a more homogeneous distribution of high dispersion regions within the vortices. The region of higher dispersion has now moved from the areas between the inner cylinder and the vortices to the inter-vortex area where the secondary flow is directed towards the outer cylinder. That is expected to increase intra-vortex relative to inter-vortex dispersion related mixing.
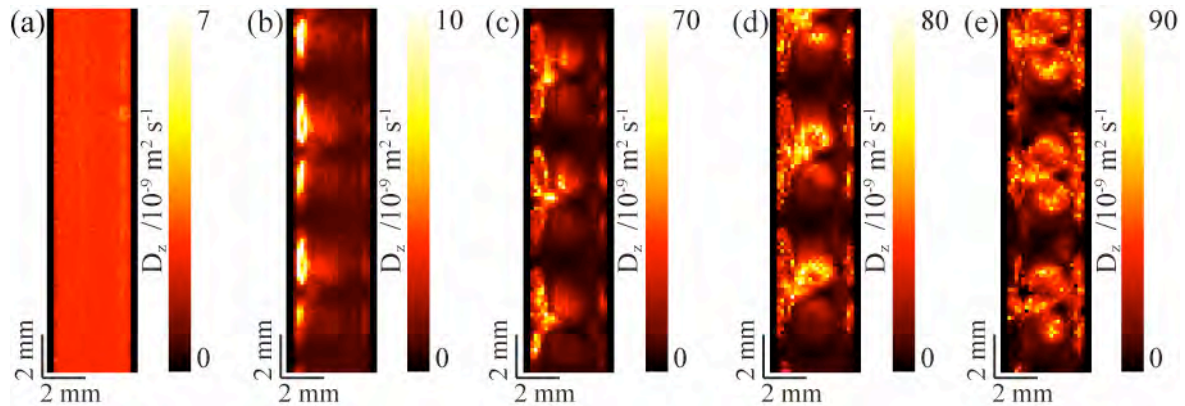
Figure 3.9. Axial direction (z) diffusion/dispersion maps at increasing ω: (a) 0.5 Hz, (b) 1 Hz, (c) 1.5 Hz, (d) 2 Hz and (e) 2.5 Hz. The observation time was of 20 ms. The rotating inner cylinder is situated on the left hand side of each image.

Note that the inter-vortex areas, where flow is coming towards the inner cylinder, maintain low dispersion rates relative to the vortex centres, indicating poor dispersion induced inter-vortex exchanges. This is in agreement with dye measurement studies showing that local mixing intensity increase is not followed by similar axial dispersion increase[21].

The analysis of velocity and diffusion/dispersion maps gives good insight into TVF flow structure, but presents limitations when studying mixing. This is because it is not possible to get a direct measure of intra or inter-vortex mixing using these maps. However, this information could be gathered using bulk propagators measurements.

3.3.3 Molecular displacements and mixing in TVF

Figure 3.10 shows conditional probability of molecular displacement plots, propagators, for TVF at $\omega = 1$ Hz, over a range of observation times Δ. As expected, the maximum displacement in P(Z, Δ) increases with increasing mixing time. The propagators are centred about zero displacement with a symmetrical structure, consistent with flow recirculation in a vortex pair. The peak at zero displacement reveals that a large number of molecules are not moving along the z direction during this observation time. This peak corresponds to both molecules of the outer wall and to molecules travelling perpendicular to the z direction, as the ones that are caught by the strong inter-vortex velocities in the radial and azimuthal directions.
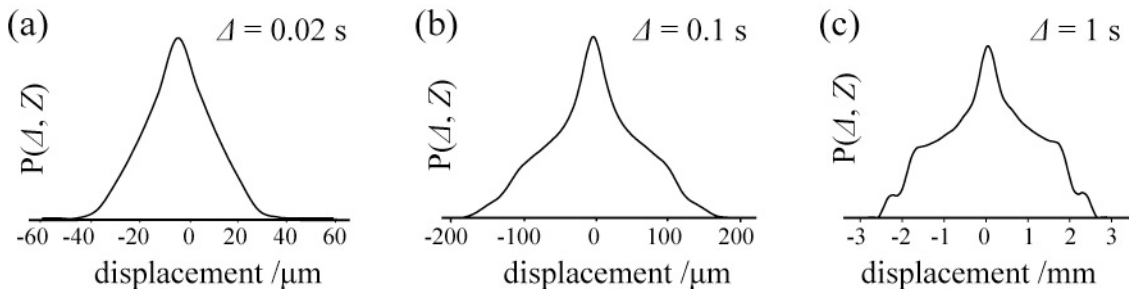
Figure 3.10. Normalised propagators for TVF flow with $\omega = 1$ Hz at increasing mixing times Δ: 20ms (a), 100 ms (b), and 1 s (c). 64 q-slices and 4 averages were used for these experiments.

The symmetry of the propagators with respect to zero displacements is showing that the flow imposes even molecular displacements in both directions along the Couette cell axis. For $\Delta = 20$ ms (Figure 3.10), the propagators have a triangular shape. As the mixing time is increased, the molecular displacements get more and more affected by the flow as molecules have had the time to sample a greater area of the vortices. Small side lobes appearing for $\Delta = 0.1$ s are clearly formed at $\Delta = 1$ s. These lobes correspond to high-circulation regions within the flow and could possibly be linked with inter-vortex displacements[16]. This cannot be verified experimentally at this regime because not enough molecules travel the distance of a vortex in the z direction (≈ 3.1 mm) during 1 s. Molecular-displacement measurements at higher observation times would have helped characterising inter-vortex mixing at this regime, but MR relaxation limits PGSTE experiments to $\Delta \leq 1$ s. Nevertheless, the possibility to distinguish high and low circulation zones is in adequacy with previously proposed models of the TVF vortices[16], where a low mixing vortex core and a high circulation outer zone are considered.

For higher rotation rates the displacements where expected to cover the distance corresponding to one vortex and help with the analysis of inter-vortex exchanges in the system. Figure 3.11 shows propagators at $\Delta = 1$ s for increasing rotation rates. Comparison between propagators ($\omega = 1$ Hz - $\Delta = 1$ s) obtained with 64 q-slices / 4 averages (Figure 3.10a) and 128 q-slices / 16 averages (Figure 3.11a) shows that a higher number of q-slices allowed for more details to be probed, but that the propagators lost their smooth shape. For $\omega \geq 1.5$ Hz (Figure 3.11b-d), the propagator side lobes are reduced and expand over more than one vortex in both directions along z. The peak at zero displacement does not seem to change a lot for $\omega = 1.5$ Hz and $\omega = 2$ Hz. At $\omega = 2.5$ Hz the side lobes have almost disappeared and

the propagator starts having a triangular shape. The broadening of the central peak at this rotation rate indicates a more homogeneous distribution of molecular displacements. This homogenisation suggests a more uniform mixing within the vortices, and is in agreement with the analysis of the diffusion/dispersion map results (Figure 3.9) where more homogeneous dispersion coefficients were found in the vortex core region. These propagators allow to quantitatively verify these results. Inter-vortex mixing can be estimated using the molecular displacements that are found to exceed the vortex dimension (Figure 3.11).
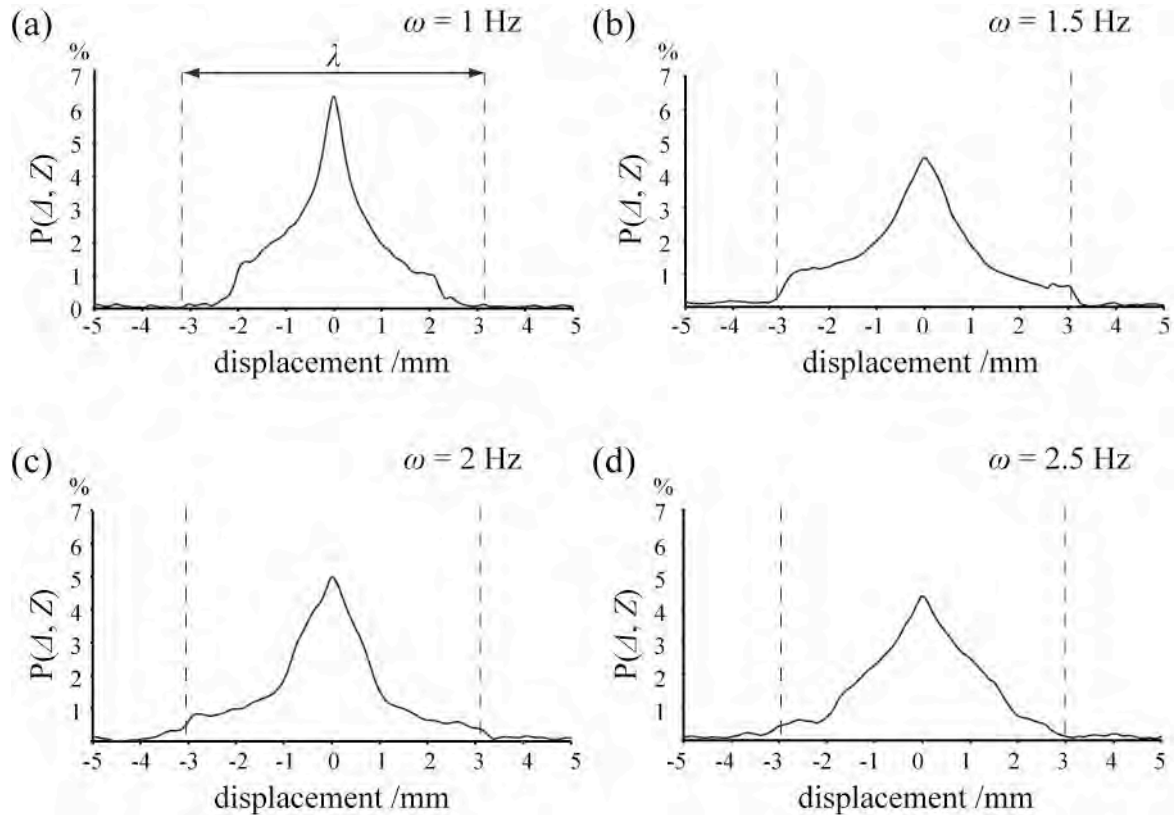
Figure 3.11. Normalised propagators for TVF flow at Δ = 1 s for increasing rotation rates ω: 1 Hz (a), 1.5 Hz (b), 2 Hz (c) and 2.5 Hz (d). 128 q-slices and 16 averages were used for these experiments. The distance between the doted lines correspond to one vortex pair wavelength.

Figure 3.12 shows the percentage of molecules that had displacements out of the region corresponding to one vortex pair (regions within doted lines in Figure 3.11). The percentages obtained correspond to a measure of inter-vortex pair mixing for counter-rotating vortex pairs over Δ. Inter-vortex mixing seems to increase linearly with rotation rate for $\omega \leq 2$ Hz. As expected from the propagator results, at $\omega = 2.5$ Hz there is a decrease of inter-vortex mixing. This can be clearly linked with the flow phase transition that seems to occur at this rotation rate. Despite the fact that at this regime TVF flow has higher velocities in all directions, less molecular displacements between vortex pairs are found than for the lower rotation rate regimes.
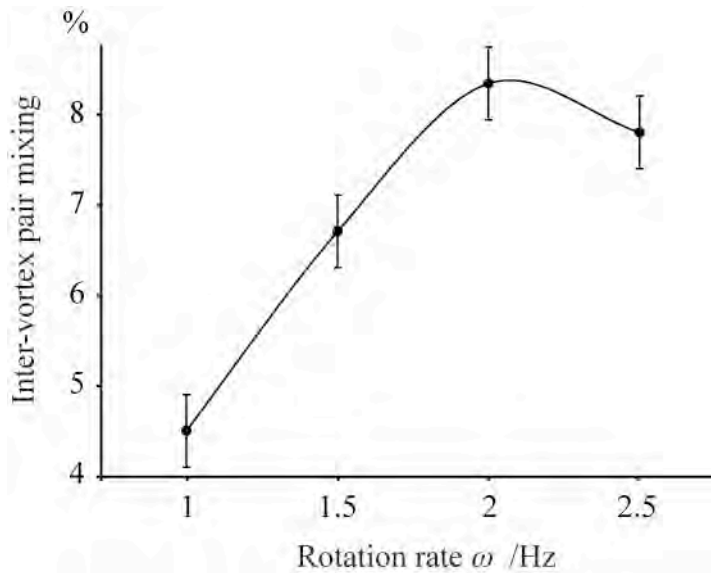
Figure 3.12. Plot showing the percentage of displacements out of the region corresponding to one vortex pair against rotation rate.

The quantitative nature of these inter-vortex mixing measurements has to be considered with caution. Part of the signal that leads to these small percentages of molecular displacements might come from noise or truncation artifacts. Comparison with other techniques and further

experiments on reactors presenting higher inter-vortex mixing might help establishing this technique providing with quantitative measurements of inter-vortex mixing.

3.4 Conclusions

Magnetic resonance techniques were used to characterise Taylor vortex flow. The combination of MR velocity and diffusion/dispersion mapping with propagator measurements was shown to provide with means, not only to characterise velocity and dispersion fields, but also to obtain quantitative information on micro-mixing within the studied flows.

Velocity maps of TVF in all directions helped analysing the structure of TVF flow and identify how the interplay between velocity fields can produce the stationary vortex structure. Velocities in all direction were shown to depend linearly on the rotation rate. Critical rotation rates for the onset of the instability (0.5 Hz < ω < 1 Hz) and transition to unsteady TVF regimes (2 Hz < ω < 2.5 Hz) were determined. At these unsteady regime, the vortex-pair wavelength was found to vary in the different directions, providing with possible explanations so as to the nature of the transition. The first produced diffusion/dispersion maps of TVF in all directions gave an insight into the dispersion properties of the flow. As rotation was increased a more uniform diffusion/dispersion coefficient in the vortex core was identified, probably related to better intra-vortex mixing.

Propagator experiments were shown to address the limitations of velocity and diffusion/dispersion mapping in characterising micro-mixing within TVF. Propagators were shown to provide with insight into both intra and inter-vortex mixing. Low and high

displacement molecular paths within the vortices were identified, supporting a two-zone model for the analysis of TVF. Quantitative inter-vortex mixing measurements were provided for increasing rotation rates. For the laminar TVF regimes in this system ($\omega \leq 2$ Hz) inter-vortex mixing increased linearly while the TVF regime change that occurs at $\omega = 2.5$ Hz is followed by an increase of intra-vortex mixing and a decrease of inter-vortex mixing. Note that propagator experiments overcome the limitations of MR imaging at high *Ta* numbers (unsteady and turbulent flows), allowing probing molecular displacements at all flow regimes within a Couette cell. Although the quantitative nature of these measurements has to be confirmed by future studies, the ability of propagators to probe mixing in vortical flow is indubitable.

(1)   Kataoka, K.; Ohmura, N.; Kouzu, M.; Simamura, Y.; Okubo, M. *Chem. Eng. Sci.* **1995**, *50*, 1409.

(2)   Holeschovsky, U. B.; Cooney, C. L. *AIChE J.* **1991**, *37*, 1219.

(3)   Haut, B.; Ben Amor, H.; Coulon, L.; Jacquet, A.; Halloin, V. *Chem. Eng. Sci.* **2003**, *58*, 777.

(4)   Ameer, G. A.; Grovender, E. A.; Obradovic, B.; Cooney, C. L.; Langer, R. *AIChE J.* **1999**, *45*, 633.

(5)   Hill, E. K.; Krebs, B.; Goodall, D. G.; Howlett, G. J.; Dunstan, D. E. *Biomacromolecules* **2006**, *7*, 10.

(6)   Tagg, R. A Guide to Literature Related to the Taylor-Couette Problem. In *Ordered and Turbulent Patterns in Taylor-Couette Flow*; Andereck, C. D., Hayot, F., Eds.; Springer US, 1992; pp 303.

(7)   Kose, K. *Phys. Rev. Lett.* **1994**, *72*, 1467.

(8)   Seymour, J. D.; Manz, B.; Callaghan, P. T. *Phys. Fluids* **1999**, *11*, 1104.

(9)   Koschmieder, E. L. *Bénard cells and Taylor vortices*; Cambridge University Press: Cambridge [England] ; New York, 1993.

(10)   Elkins, C. J.; Alley, M. T. *Experiments in Fluids* **2007**, *43*, 823.

(11)   Packer, K. J.; Stapf, S.; Tessier, J. J.; Damion, R. A. *Magn. Reson. Imaging* **1998**, *16*, 463.

(12)   Waggoner, R. A.; Fukushima, E. *Magn. Reson. Imaging* **1996**, *14*, 1085.

(13)   Kutsovsky, Y. E.; Scriven, L. E.; Davis, H. T.; Hammer, B. E. *Phys. Fluids* **1996**, *8*, 863.

(14)   Seymour, J. D.; Callaghan, P. T. *AIChE J.* **1997**, *43*, 2096.

(15)   Callaghan, P. T.; Trotter, C. M.; Jolley, K. W. *J. Magn. Res.* **1980**, *37*, 247.

(16)   Xia, Y.; Callaghan, P. T. J. *Magn. Res.* **1991**, *91*, 326.

(17)   Khrapitchev, A. A.; Callaghan, P. T. J. *Magn. Res.* **2003**, *21*, 373.

(18)   Callaghan, P.-T. *Translational dynamics and magnetic resonance : principles of pulsed gradient spin echo NMR*; Oxford University Press, 2011.

(19)   Dusting, J.; Balabani, S. *Chem. Eng. Sci.* **2009**, *64*, 3103.

(20)   Desmet, G.; Verelst, H.; Baron, G. V. *Chem. Eng. Sci.* **1996**, *51*, 1287.

(21)   Desmet, G.; Verelst, H.; Baron, G. V. *Chem. Eng. Sci.* **1996**, *51*, 1299.

4 MR characterisation of translating vortex flow

4.1 Introduction

The combination of MR velocity and diffusion/dispersion mapping with MR propagator measurements was shown to provide with rich information on the stationary Taylor vortex flow (TVF). This section expands this approach to the translating vortex flow produced in a Vortex Flow Reactor (VFR). A VFR is obtained by superimposing pipe flow on steady Taylor Vortex Flow. The resulting flow consists of a series of counter-rotating vortex pairs travelling along the length of the Couette cell. Plug flow properties and non-agitative mixing inside the translating vortices make the axi-symmetric, laminar flow regime of a VFR an ideal candidate for numerous chemical[1–3] and biochemical[4,5] applications. However, the literature reveals that open questions still remain for important flow properties as inter-vortex and intra-vortex mixing. In particular, the emergence of by-pass flow, where fluid is able to flow at a different velocity to the translating vortices, is a topic of much debate[6,7]. One of the most commonly used parameters for the analysis of the VFR flow properties is the velocity drift, V_d, given by the ratio of the translation velocity of the vortices, U_{TV}, to the axial flow average velocity, U_{ax}.

$$V_d = \frac{U_{TV}}{U_{ax}} \qquad\qquad (\ 4.1\ )$$

Several authors have assumed that $V_d = 1$ in order to support the "translating tanks" model for the flow, where the VFR is considered to be ideal an plug flow reactor[6,8,9]. This assumption has been widely adopted despite a growing literature highlighting its inaccuracy in many systems[10–12], where the velocity drift is found to vary from 1 to 1.4. Desmet *et al.*[13,14]

demonstrated the existence of a significant inter-vortex flux for the stationary vortices, which refutes the generally-accepted concept of zero intermixing between vortex units. These results also further questioned the plug-flow hypothesis for a VFR. Later, Giordano *et al.*[7] showed that, by increasing ω, it is possible to decrease the velocity of the Taylor vortices until obtaining stacked vortices with a flow passing through them. In their experiments, V_d was found to vary between 0 and 1. Haim and Pismen[11] considered the role of the strong secondary flow in transforming pipe flow into a slalom by-pass around the vortices that could be completely suppressed at higher rotation rates. Giordano *et al.*[7,15] used this model to explain how an increase in rotation could decrease U_{TV} by increasing the by-pass flow. VFR models developed after this work were suitable for dealing with the by-pass flow[4,16]. In 1999, Wereley *et al.*[12], by removing the pressure driven axial velocity field from the overall velocity field in their VFR, obtained a flow field very similar to the linear TVF one. Their results suggest that VFR flow could be a linear superposition of pipe flow and TVF. These results, in addition with studies demonstrating that vortical flows can generate Levy flights and resonant mixing, are revealing the limitations of the translating tank and by-pass models in addressing the flow complexity. A new understanding of VFR flow is necessary in order to reflect the dependence of the mixing properties on the system parameters and the role of V_d in characterising flow properties.

MRI velocity and diffusion/dispersion maps of this flow could provide answers for these questions, but the VFR flow has properties that make it difficult to image. The main challenge lies in the periodic motion of the translating vortices, causing imaging artifacts and errors in velocity measurements. Periodic flow makes pixel signal magnitude and/or phase to change during motion encoding and acquisition, leading to inconsistencies between acquisitions[17]. An

increase in phase dispersion inside voxels can lead to multi-lobe propagators generating velocity disparities inside pixels and errors in the velocity calculation[17]. Phase-encoding is more affected by velocity field fluctuations[18]. If the motion is periodic, artifacts appear as discrete replicates (ghosts) of the moving structures. In the case of periodically fluctuating Poiseuille flow[19], the amplitude of ghosts has been shown to increase with the amplitude and frequency of the fluctuations but also with several imaging parameters (δ, $\varDelta$, g). On the other hand, a repetition time increase leads to a ghost intensity reduction. Most common approaches to reduce artifacts consist in reducing δ, $\varDelta$ and g. By decreasing the pixel size it is also possible to avoid big velocity ranges within spins in each voxel, but this necessitates a gradient increase that is also source of artifacts. Finally, the reduction of amplitude and frequency of velocity fluctuations in the sample is also reducing the observed artifacts. In the case of VFR flow this will consist in working at lower rotation and flow rates.

Previous attempts to characterise VFR flow using MRI by Moser *et al.*[20], have relied on a 2D imaging method combining DANTE spatial tagging with a fast imaging sequence. The vortical structure within the VFR was identified and the translation velocity U_{TV} was measured. However, these measurements were not able to provide 3D characterisation of the flow and the images were restricted to low resolution, in order to reduce the imaging time and hence artifacts. Producing high-resolution 3D images in a VFR requires longer experimental times and/or faster imaging sequences.

In this study, in order to remove the effects of periodic flow, the PGSE imaging sequence was synchronised with the flow period, T_{TV}. Data was acquired when the successive vortices were at the same spatial point. A similar method was successfully employed by Han *et al.*[21] who

mapped the velocity of fluid inside a falling droplet by gating the acquisitions to the droplet dispenser. Unlike their system, VFR flow is continuous and T_{TV} is not a directly controllable parameter. Hence, optical experiments using dye visualisation were performed on the VFR system in order to measure the flow periodicity at different flow and rotation ranges. These measurements were also used for comparison with the existing literature and for helping with the analysis of the MR data.

MR velocity imaging using a pulse sequence timed to the flow period allowed producing the first three-dimensional velocity maps of the VFR flow[22]. These velocity maps are used to characterise the velocity field structure and get a better understanding of the respective roles of axial and TVF flow in the resulting VFR flow. Maps obtained by superposition of axial and TVF flow velocity maps were compared with VFR maps in order to test the linear superposition hypothesis[12]. The role of V_d in characterising the plug flow properties of the reactor is discussed.

Finally, molecular transport in pipe flow, TVF and VFR flow was investigated by performing propagator measurements. The propagator analysis is shown to provide with quantitative information on molecular mixing within these systems. The effect on mixing of each of the two superposed flows (axial and TVF) that form the VFR flow is discussed. The effects of rotation and flow rate on molecular displacement within a VFR are investigated.

4.2 Experimental

4.2.1 Vortex Flow Reactor dimensions and set-up

The Couette cell used in this study is the same as the one used for the TVF studies (Chapter 3). The VFR reactor (Figure 4.1) was obtained by superimposing pipe flow to the TVF and constructed from an outer glass tube of radius R_o = 8.25 mm and an inner PEEK rod of radius R_i = 4.1 mm, resulting in a gap, d, of 4.15 mm.
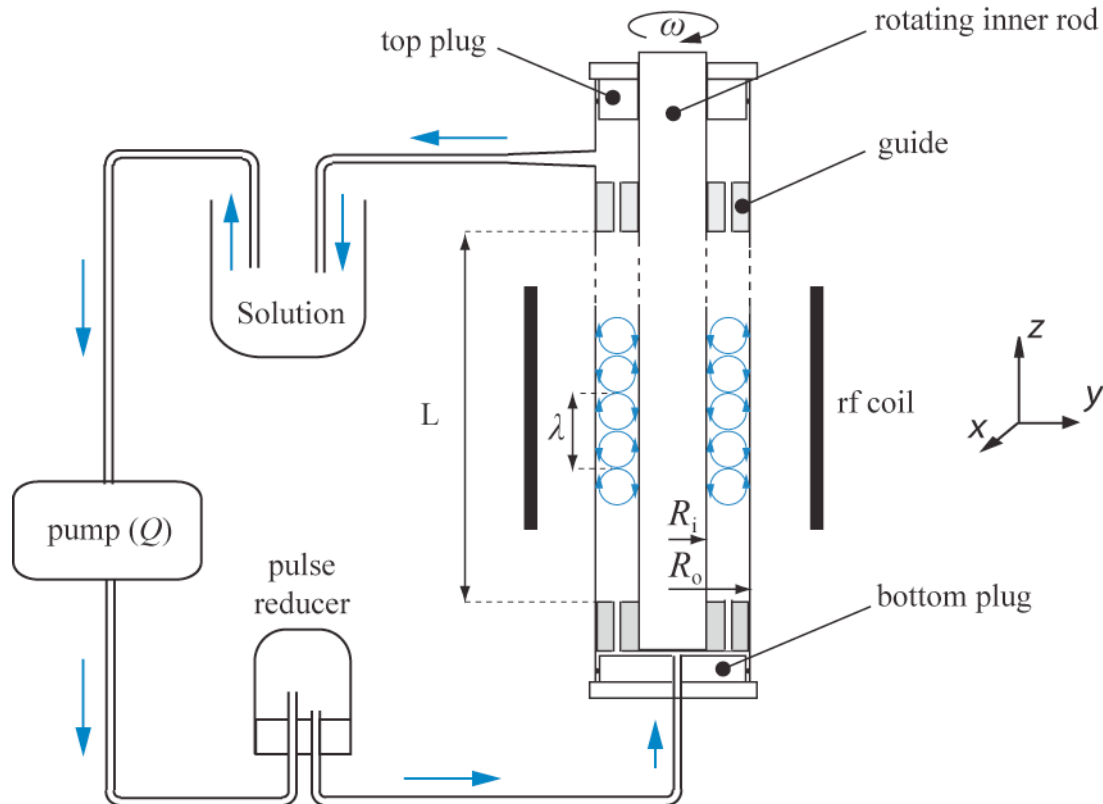
Figure 4.1. Schematic diagram of the VFR. The arrows show the flow circulation within the system. The area within the rf coil corresponds to the field of view for both dye and MR experiments.

The effective length of the Couette cell, *L*, was of 896 mm, giving a length to gap ratio Γ of 216 and a radius ratio η of 0.5. PTFE guides were placed at the top and bottom of the cell, to reduce wobble from the inner cylinder. The inner cylinder was rotated using a stepper motor (Bruker NMR Rheokit). The connection between the motor and the inner cylinder was made with a rubber connection absorbing vibration transmission and shocks due to alignment errors. The VFR was placed in the magnet with the MRI field of view of the rf coil situated 11 cm above the lower inner cylinder guide. An Ismatec pump was used to pump solution through the VFR. A pulsation reducer was placed at the pump outlet in order to reduce the pump pulse effects.

In previous VFR studies[7,9,10,12,20,23–29], η was found to vary between 0.5 and 0.9, and Γ between 12 and 120. The VFR used in this work has one of the smallest radius ratios in the literature and the larger characteristic length. This is mainly due to the constraints linked with MR imaging: the VFR had to be thin enough to fit the in the probe and long enough to connect the stepper motor at the top and the pump at the bottom. To avoid the unsteady wavy vortex regimes, both for better MR results and for ensuring better plug-flow properties, a large gap VFR was used[30], leading to a small radius ratio η.

4.2.2 Parameter ranges

Tap water was used for all the experiments presented in this chapter. The viscosity ν, measured with a calibrated Ubbelohde viscometer, was of 0.979 mm^2 s^{-1} at 22 ± 0.5 ˚C. Five evenly spaced rotation rate values, ω, were used, from 1 Hz to 2.5 Hz. The respective *Ta* values varied from 17 to 42.5. Four flow rate values, *Q*, were used: 4 cm^3 min^{-1}, 7.2 cm^3 min$^-$

[1], 10.4 cm^3 min^{-1} and 13.6 cm^3 min^{-1}. The respective *Re* values varied from 1.7 to 5.3 and γ_{Re} = U_{ax} / $R_i\omega$ varied from 0.03 to 0.29. The velocity of translation of the vortices varied between 0.45 mm s^{-1} and 1.51 mm s^{-1} and the velocity drift, V_d, between 1.02 and 1.21. Measurements were performed 5 min after setting the rotation and flow rates. Each experiment was repeated a minimum of three times.

4.2.3 Optical and timing measurements

Optical images were acquired using a digital CCD camera Canon EOS 1000 and transferred to a PC using the remote capture utility of the EOS software. To follow the evolution of the system over time, images were acquired every 5 s using the remote control option of the software.

The visualisation of the vortices was done by injecting 0.2 ml of a dye (ferroin solution, [ferroin] = 3.74 mM) with a syringe at the inlet of the pump. The vortex pair wavelength, λ, was measured on photographic material. Each value of λ corresponds to an average over a minimum of three measurements. The speed of the translating vortices, U_{TV}, was obtained by measuring the time *t* taken by the vortices to travel a given distance. The time necessary for one vortex pair to travel one wavelength corresponds to the flow period, T_{TV}. The velocity drift, V_d, is given by the ratio of Taylor vortices velocity, U_{TV}, to the axial average velocity, U_{ax}. The value deviation was of 5%. All optical measurements were taken for the region of the Couette cell that was positioned inside the rf coil in the MR measurements.

4.2.4 Velocity imaging of steady flow

A Pulsed Gradient Spin Echo (PGSE) velocity imaging sequence was used (Figure 2.15). The PGSE parameters used for these experiments were in the following ranges: $\Delta = 10 - 30$ ms, $\delta = 1 - 2$ ms and $G = 0.1 - 0.6$ T m^{-1}. The hard 90° excitation pulse was typically of 43-45 µs. A soft 180° Gaussian pulse of 1000 µs was used for slice selection, with an attenuation range of 16 - 16.8 dB. A slice thickness of 1 mm was used, with a field of view of 50 × 25 mm and a matrix size of 256 × 128 pixels resulting in a pixel size of 0.196 × 0.196 mm. The spectral width was of 100 kHz. 4 q-slices were acquired with 2 signal averages.

4.2.5 Velocity imaging of periodic flow

For velocity imaging of periodic flow most PGSE and imaging sequence parameters were similar to the steady flow experiments. Phase pixels were reduced to 64 pixels giving a matrix size of 256 × 64 pixels. Also, the field of view was reduced to 40 × 20 mm, resulting in a pixels size of 0.156 × 0.313 mm. The three loops defining the PGSE pulse sequence were adapted to the flow period (T_{TV}) (Figure 4.2): the acquisition loop, repeated 64 times (n_{ph} phase points) to acquire all the blocks of time domain size, the experiment average loop (n_{avg} averages), repeated twice and the gradient encoding loop (n_q q-slices), repeated 2 or 8 times depending on the experiment. Flow and rotation rate were kept constant and series of 2 q-slice experiments were performed, varying the loop period by 20 ms steps. The period range was defined by the experimental T_{TV} values obtained by optical measurements. The loop time varied from $T_{TV} - 500$ms to $T_{TV} + 500$ms. For each one of the imaging series with increasing T_{TV}, one single measurement was giving an intensity map with no appearing artifacts (no

signal outside the gap region and no signal loss inside the gap region). The data acquired during this measurement were post-treated to produce a velocity map of the measured flow.
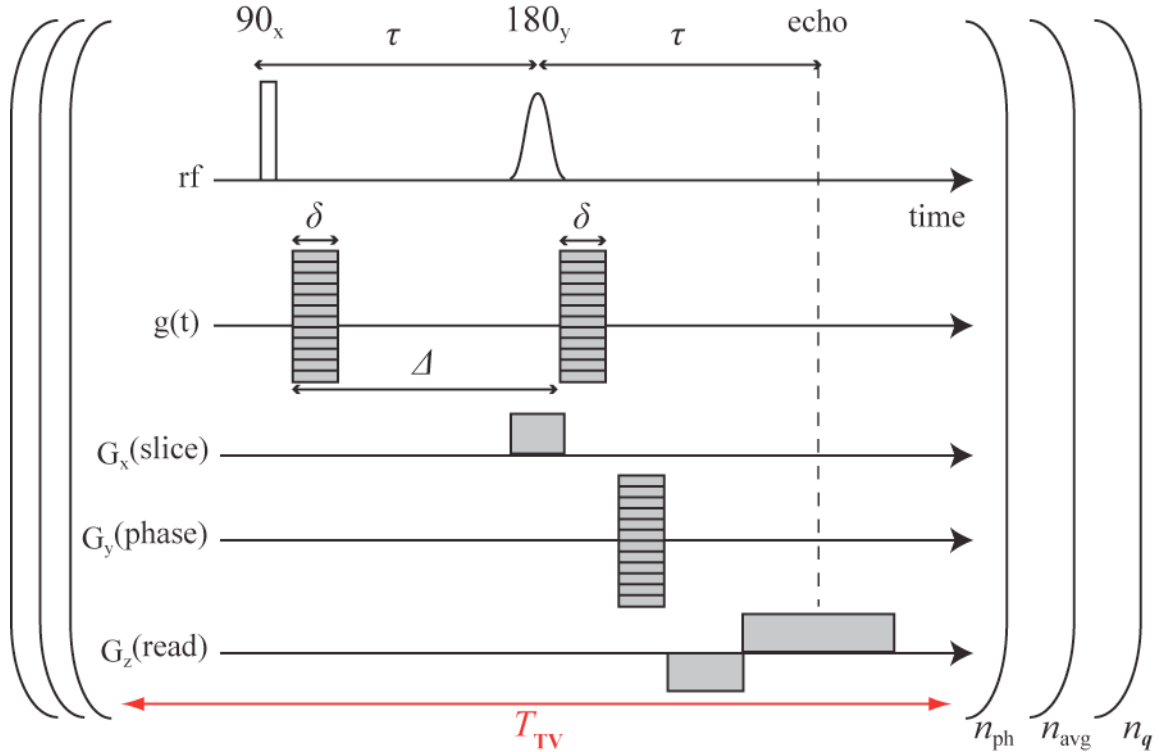
Figure 4.2. The 3 loops defining the PGSE pulse sequence had to be adapted to the period of the translating vortices (T_{TV}).

4.2.6 Propagator measurements

A Pulsed Gradient Stimulated Spin Echo (PGSTE) sequence was used for the propagator measurements[31] (Figure 2.14). Either 64 or 128 q-steps were collected with 4 and 16 averages respectively. The PGSTE parameters used were in the following ranges: $\Delta = 20 - 1000$ ms, $\delta = 1 - 2$ ms and $G = -0.6 - 0.6$ T m^{-1}.

4.3 Results and discussion

4.3.1 Optical visualisation of travelling vortices

Dye injection experiments allowed a clear identification of the vortical structures in VFR flow. Figure 4.3 shows of photos taken in the region of the VFR that contained the rf coil during the MR experiments.
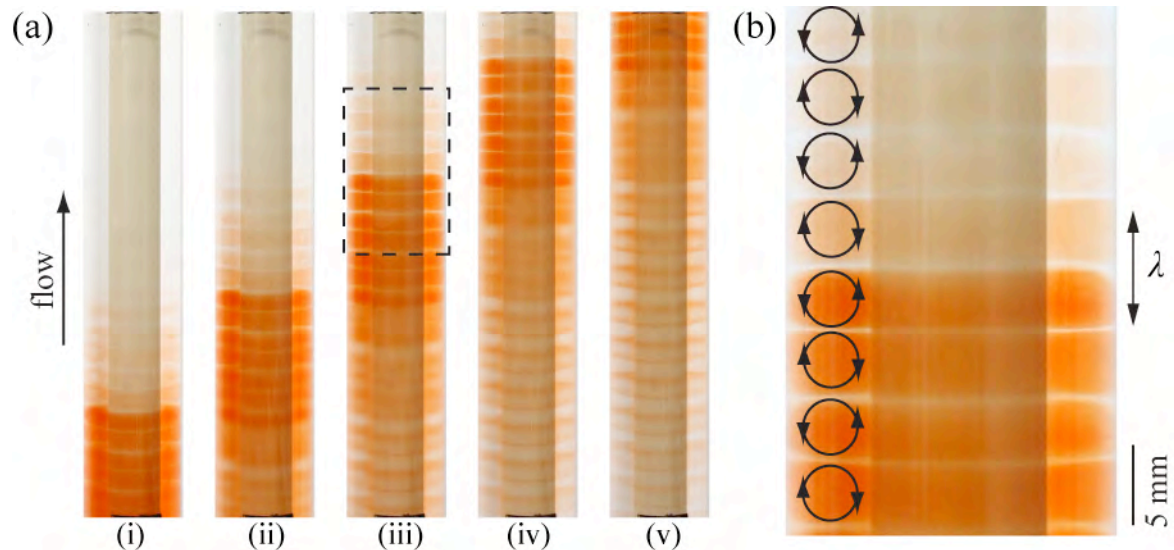
Figure 4.3. (a) Photographs of translating vortices in a 10 cm region of the VFR system at ω = 1 Hz and Q = 7.2 cm^3 min^{-1}. Photographs were taken with an interval of 5 s. Vortices are visualised using ferroin. (b) Close-up of the region highlighted in the doted square with a schematic of the counter-rotating vortices.

Figure 4.3a shows time series of the propagation of the dye front. The dye spreads over several vortex pairs, with the major part concentrated in 4 vortex pairs. This spread of the dye into successive vortices gives insight into the by-pass and drag properties of the flow, where molecules go faster or slower than the translating vortices. Figure 4.3b shows a close-up of

the propagation front. The schematic of the vortex pairs allows understanding the observed dye distribution. Each vortex pair is formed of two counter-rotating vortices separated by secondary flow in the radial direction. For one over two vortices the outer part is colourless while the core remains red, suggesting a heterogeneous dye distribution into successive vortices. At the rear part of the high concentration dye region (Figure 4.3a(v)) the vortex cores are colourless and the inter-vortex areas red. This indicates that the drag within this flow is mainly occurring within the inter-vortex and outer-vortex areas.

Figure 4.4 shows plots of the measured wavelength, λ, against flow and rotation rate.
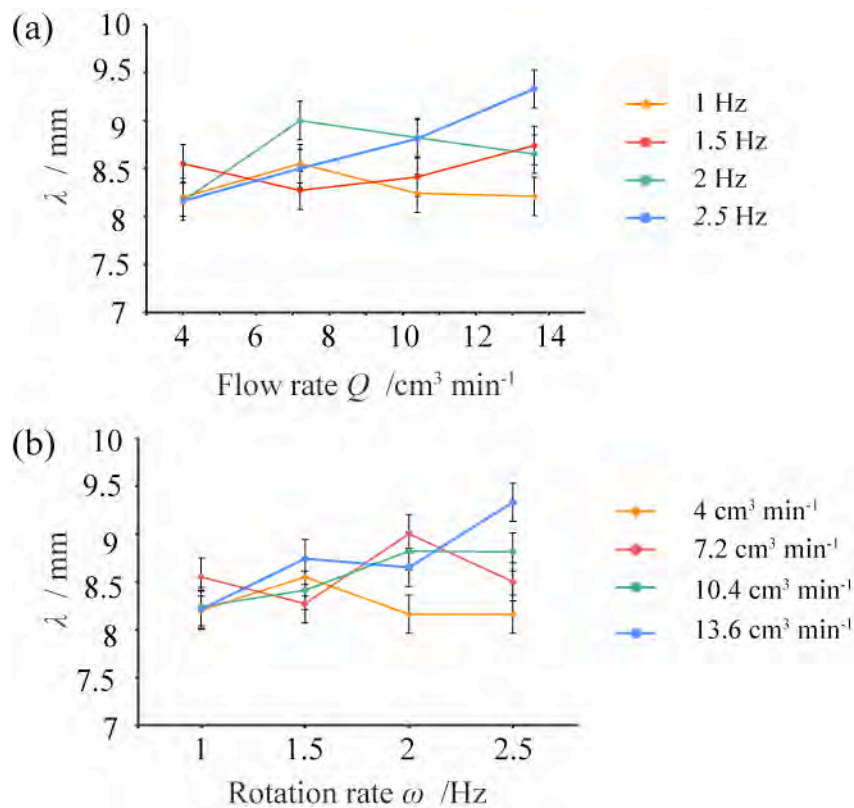
Figure 4.4. Plots of vortex pair wavelength against flow rate (a) and rotation rate (b).

λ varied between 8.16 mm and 9.33 mm, but no clear trend with the experiment parameters could be identified, except the fact that higher rotation and flow rates systematically lead to a bigger spread of λ values. These results are close to the "square vortices" approximation, $\lambda = 2d$, often made in literature[12,15] since $1.96d < \lambda < 2.25d$, where d is the gap between the inner and outer cylinder.

Figure 4.5 shows plots of U_{TV} and T_{TV} against flow rate at different rotation rates. At this range, U_{TV} is found to increase linearly with the flow rate, while T_{TV} is decreasing. The rate of decrease of T_{TV} is higher for lower flow rates.
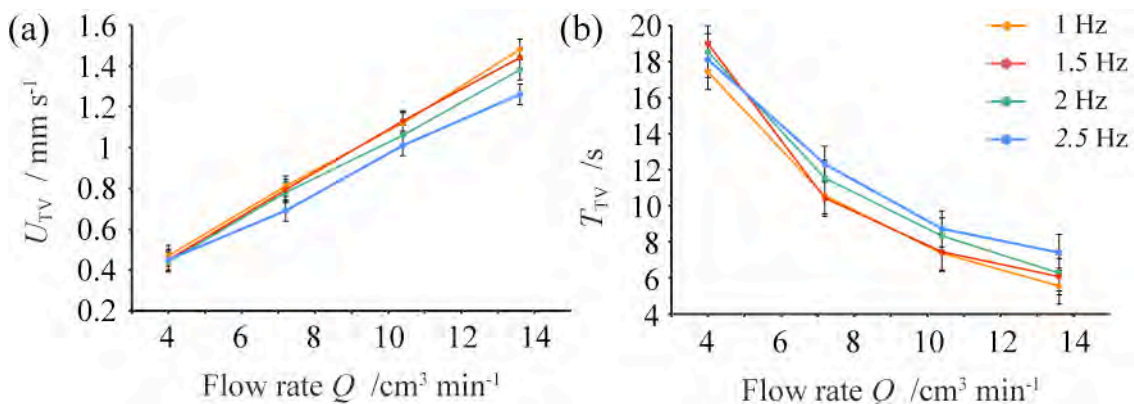
Figure 4.5. Plots of vortex translation velocity (a) and flow period (b) against flow rate.

Figure 4.6 shows plots of U_{TV} and T_{TV} against rotation rate for different flow rates. For $Q > 4$ cm³ min⁻¹, U_{TV} is found to decrease linearly and T_{TV} to increase with rotation rate. These results are in agreement with previous works where an increase in rotation rate was shown to decrease the translation velocity of the vortices[7]. A different behaviour is observed only for the lower flow rate (4 cm³ min⁻¹) at high rotation rates, where U_{TV} is increasing and T_{TV} is decreasing. Imposed pipe flow has been shown to delay the onset of the Taylor vortex

instability and to stabilise the flow[12], but below a critical flow rate the instable regime observed at high rotation rates in TVF without axial flow ($\omega = 2.5$ Hz) is expected to appear (ref. chapter 3). These results suggest that 4 cm^3 min^{-1} is below this critical flow rate.
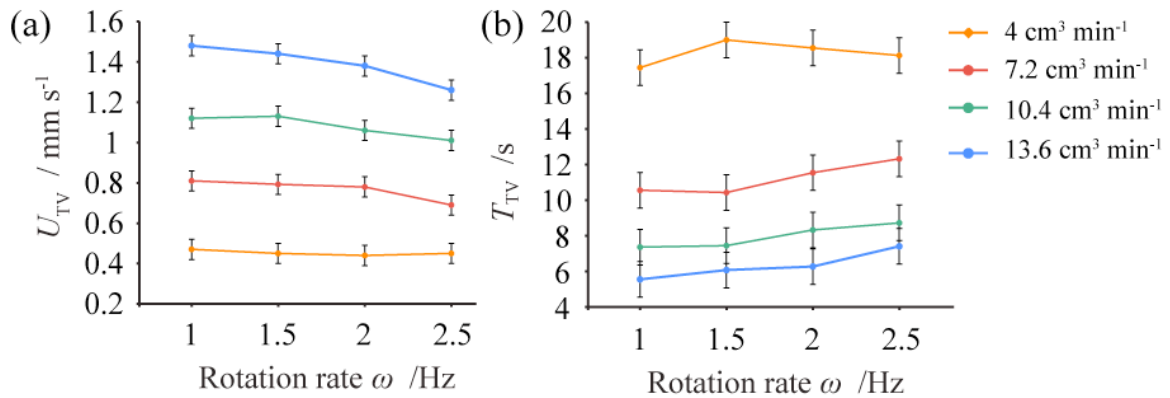
Figure 4.6. Plots of vortex translation velocity (a) and flow period (b) against rotation rate.

To evaluate the velocity drift, V_d, and understand the importance of the pipe flow into the resulting VFR flow, pipe flow was investigated using MR velocity imaging.

4.3.2 Pipe flow properties

Figure 4.7a shows a velocity map in the *z*-axis direction of pipe flow in the Couette cell with stationary inner cylinder, at $Q = 7.2$ cm^3 min^{-1}. The dark part in the middle of the image corresponds to the inner cylinder. An average over 50 cross-section lines of this velocity map shows the typical Poiseuille velocity profile (Figure 4.7b). Due to the shape of the Couette cell, the maximum velocities on the profile are found closer to the inner than the outer cylinder[32]. The inner surface of the outer cylinder being larger than the surface of the inner cylinder, higher friction is experienced on the outer side. The right-hand part of the velocity

profile is slightly higher than the left hand-side. This symmetry break, probably caused by inhomogeneous distribution at the inlet or a gap irregularity, has to be considered when studying the VFR flow.
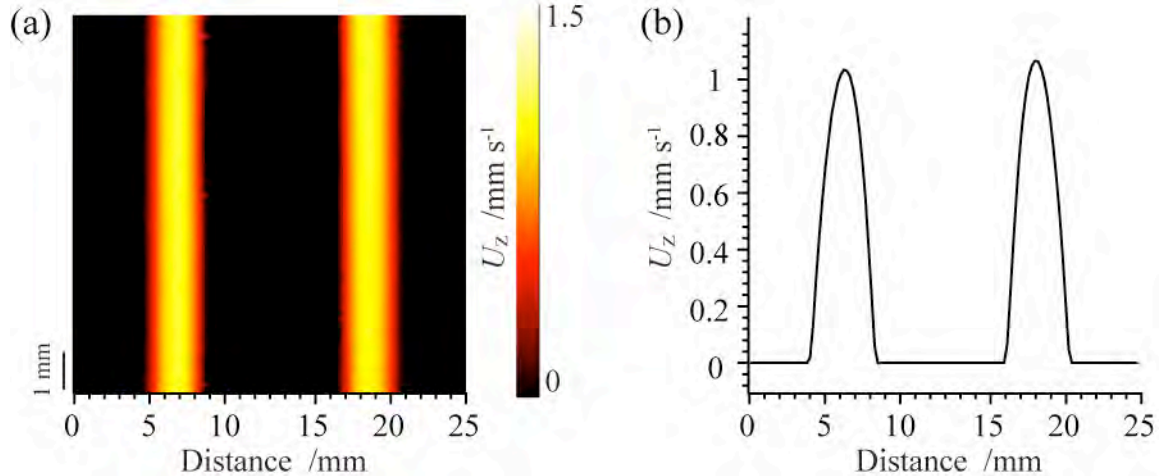
Figure 4.7. (a) Velocity map in the z direction of pipe flow at Q = 7.2 cm³ min⁻¹. (b) Average velocity profile in the radial direction.

Figure 4.8 shows a plot of average (U_{ax}) and maximum (U_{max}) velocities for different flow rates. As expected, there is a linear relation between the average velocity and the pump flow rate. Due to the Couette cell shape, the measured pipe flow profile is lying between Poiseuille profile in a tube and Poiseuille profile between two parallel planes[32]. For low radii ratio, η, the Couette cell looks more like a tube where typically $U_{ax} = 1/2\ U_{max}$, while for high η values the TC cell gap is similar to the gap between two parallel planes where $U_{ax} = 2/3\ U_{max}$. So, the ratio $U_{ax}\ /\ U_{max}$ is characteristic of each VFR device. In these results, $U_{ax}\ /\ U_{max}$ is found to be constant at 0.64 ± 1 (Note that $1/2 < 0.64 < 2/3$).
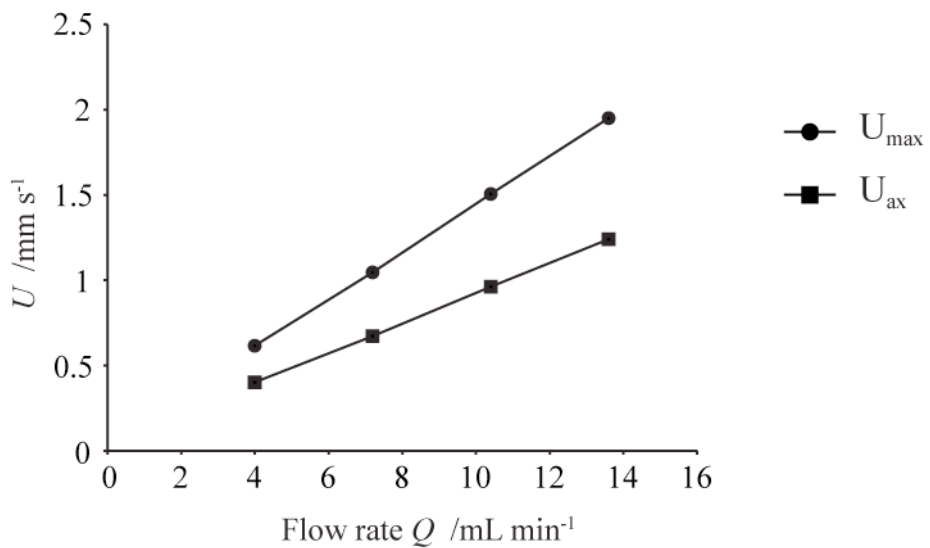
Figure 4.8. Plot showing U_{max} and U_{ax} velocities of pipe flow in the Couette cell against the applied flow rate.

U_{ax} measurements were also used to calculate the Reynolds numbers for this range of flow rates. *Re* was found to vary between 1.7 and 5.3. Also, since the average axial velocity is the same for pipe and VFR flows at the same Q, knowing U_{ax} allows calculating the velocity drift for the VFR.

4.3.3 Velocity drift

Figure 4.9 shows the evolution of the velocity drift, $V_d = U_{TV} / U_{ax}$, with flow and rotation rate. V_d was found to vary between 1.02 and 1.21. $V_d > 1$ indicates that the vortices move faster than the axial flow rate. $V_d \sim 1$, where the vortices travel at approximately the same velocity as the axial flow, is considered as an important condition for good plug-flow properties of a VFR. If the vortices move at a different speed than the average velocity, inter-vortex mixing is expected to occur, compromising the plug-flow properties.
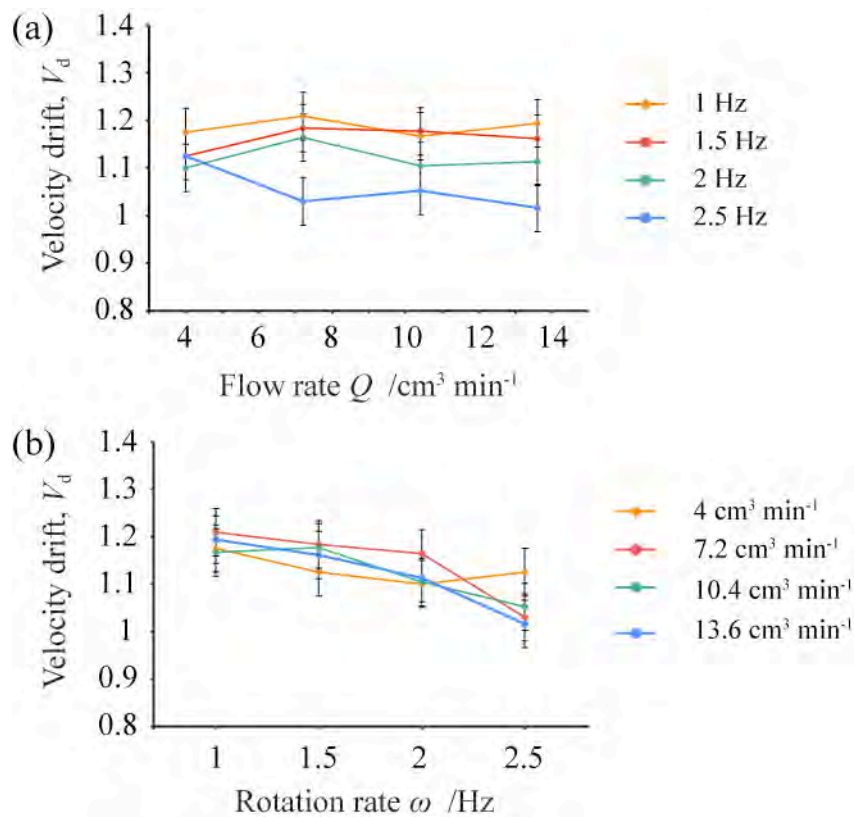
Figure 4.9 Plots of the velocity drift against flow (a) and rotation (b) rate.

For $Q > 4$ cm^3 min^{-1}, V_d does not seem significantly influenced by the flow rate (Figure 4.9a). In fact, as both U_{TV} and U_{ax} were found to have a linear dependence on the flow rate, $V_d = U_{TV} / U_{ax}$ is expected to be constant at this range of parameters. V_d is found to be limited so as to the characterisation of flow properties for increasing flow rates. An increase in rotation rate causes a V_d decrease for $Q > 4$ cm^3 min^{-1}. The lower V_d values, where the most plug-like flow properties are expected, are found for $\omega = 2.5$ Hz. The only exception is found for $Q = 4$ cm^3 min^{-1} and $\omega = 2.5$ Hz, where a higher vortex pair velocity is observed, leading to a V_d increase. Notice that despite $V_d > 1$ for all our experiments, images obtained from dye injection experiments (Figure 4.3) give the impression of plug-flow, indicating that the vortices are being pushed as a stack. The dye experiments might indeed provide misleading

information about the properties of the reactor. MR velocity imaging was performed to get a better understanding of the VFR system.

4.3.4 MR Velocity imaging of travelling vortices

The travelling vortex period values, T_{TV}, measured in the dye experiments (Figure 4.5 and Figure 4.6) were used to time the PGSE velocity imaging sequence. Series of 2 q-slice MR experiments were performed, where the triggering time of the pulse sequence varied from T_{TV} – 500ms to T_{TV} + 500ms, with 20 ms steps. The experimental time for each image acquired was of 18 to 40 minutes, depending on T_{TV}. Figure 4.10 shows intensity maps obtained at different loop time periods.
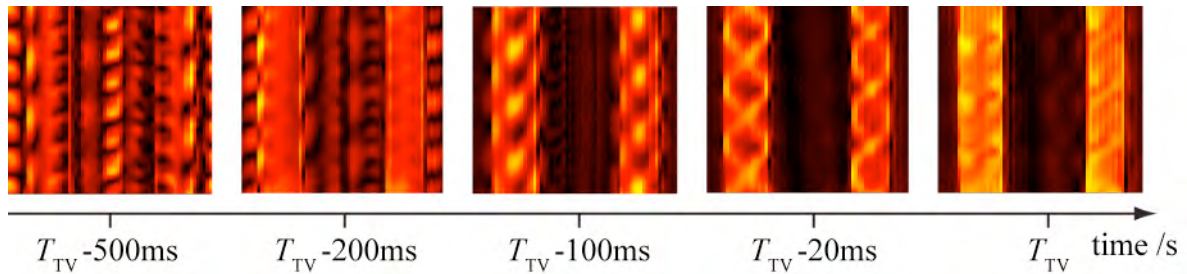
Figure 4.10. Intensity maps of VFR flow at ω = 1 Hz and Q = 7.2 cm³ min⁻¹, obtained at different PGSE loop times. The loop that eliminated artifacts had a period of 8.16 s (= T_TV).

When the loop period of the sequence is different from T_{TV} ± 20ms, several phase artifacts are observed, with high signal observed in the region corresponding to the inner cylinder and low signal regions in the gap area. This behaviour was observed for all direction experiments on this VFR. As the PGSE loop period is approaching the estimated T_{TV} value, less artifacts appear on the intensity maps. For each one of the imaging series, only one measurement gives

an intensity map with no apparant artifacts (no signal outside the gap region and no signal loss inside the gap region). The loop time producing this intensity map corresponds to T_{TV}. Similar experiments were conducted on a second VFR, giving the same results (Appendix A). The data acquired during this measurement were post-treated to produce a velocity map of the measured flow.

Figure 4.11 shows axial (b), radial (c) and azimuthal (d) MR velocity maps at $\omega = 1$ Hz and $Q = 7.2$ cm^3 min^{-1}, in comparison with a dye visualisation picture at the same regime (a). The vortex pair wavelength measured on the velocity maps is in agreement with the dye experiment results ($\lambda \sim 85$ mm). These velocity maps present also several similar features with the TVF velocity maps at $\omega = 1$ Hz (cf. 3.3.1). In fact, the addition of pipe flow does not seem to have a strong effect on the velocity field. The velocity map in the direction of the translating vortices, Uz, is more affected, since pipe flow does not have radial and azimuthal components at this range. Figure 4.10b shows a slalom-like, high-velocity region, suggesting the presence of by-pass flow. The higher velocities in the axial direction are found in the parts of the vortices situated close to the inner cylinder. This can be explained by the fact that both TVF and pipe flow exhibit enhanced velocities in this region. The radial direction velocity map shows the secondary flow jets towards the outer cylinder.
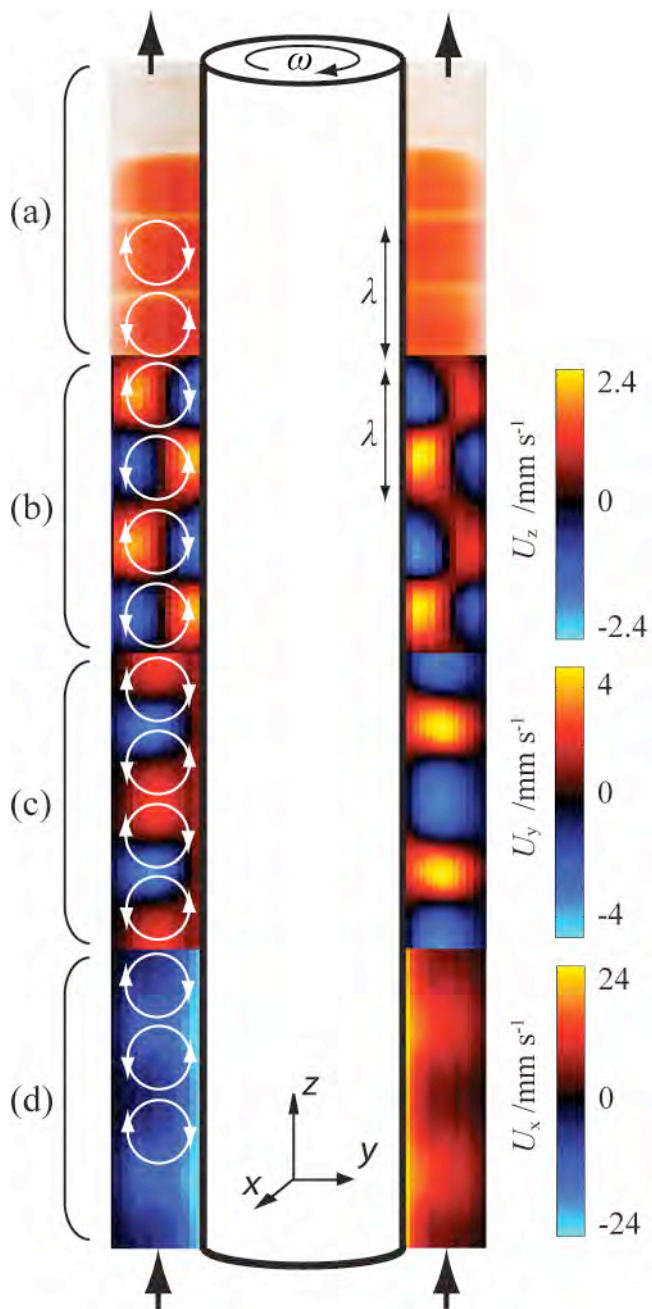
Figure 4.11. (a) Digital photo of translating vortices in the VFR system at ω = 1 Hz and Q = 7.2 cm³ min⁻¹. (b)–(d) MR velocity maps of VFR flow in the axial, U_z (b), radial, U_y (c) and azimuthal, U_x (d), directions.

These jets are not oriented perpendicularly to the inner cylinder as for TVF. The outer part of the jet (on the outer cylinder) is positioned slightly lower than the inner part. This "bending"

of the secondary flow is probably due to the higher axial velocities found close to the inner cylinder. As with TVF, velocities in-between vortex pairs in the azimuthal direction (Figure 4.10d) are an order of magnitude higher compared to those inside the vortex pairs, so they are not noticeably deformed. These strong inter-vortex flows, in combination with the periodic outwards flow structures in the radial direction, create the sharp interfaces observed in the dye-injection experiments. Despite the fact that the vortices move faster than the average axial velocity ($V_d \sim 1.2$) and the observed high-velocity slalom-like region in the axial direction velocity maps, these interfaces give the misleading impression of plug-flow, where vortices appear as non inter-mixing translating reactors.

To compare with other studies of travelling vortex flow in a VFR, several approaches can be used. A contour plot obtained using the axial direction map (Figure 4.12a) allows better comparison with contour plots found in theoretical studies of the travelling vortex flow, where streamlines are found to slalom around the vortex cores[33]. A 2D velocity vector map, produced using the MR velocity maps (Figure 4.12b), facilitates comparison with particle imaging velocimetry measurements[12], typically used to study this flow. Moreover, a 2D map can give a better visualisation of the vortical structures within a VFR. In this map, the MR velocity maps (U_z and U_y) were used to define the magnitude of each vector in the axial and radial directions. In the resulting 2D velocity vector map, the centre of the successive vortices can be easily identified, as well as the slight distortions caused by the secondary inflows and outflows in the radial direction.
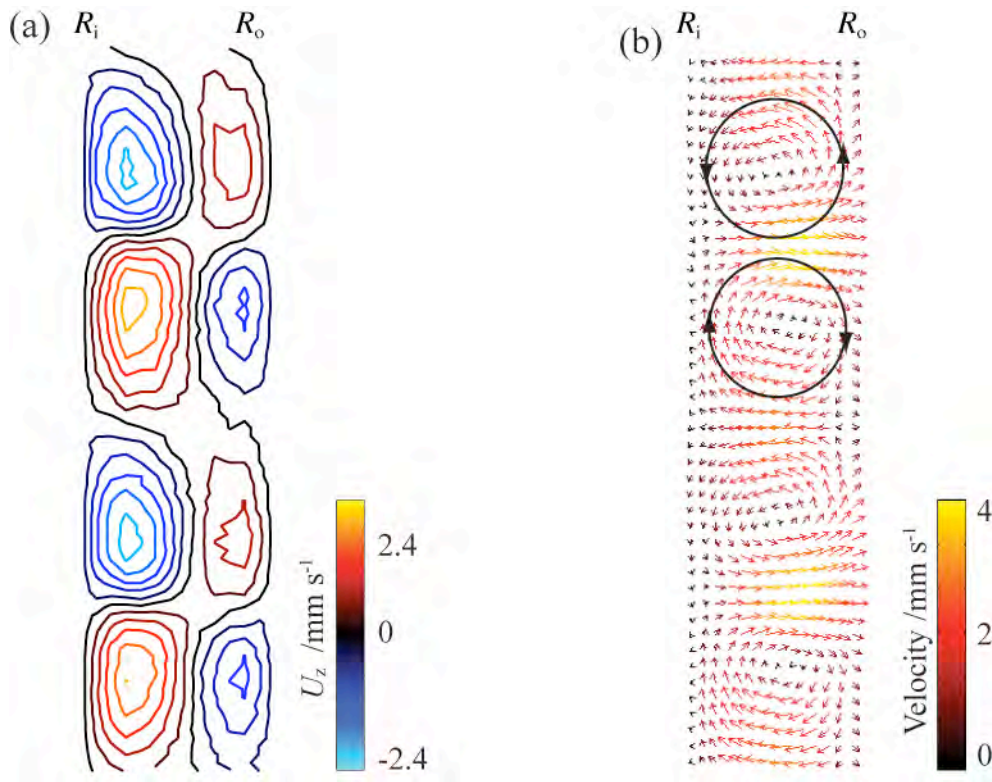
Figure 4.12. (a) Contour representation of the left part of the axial direction velocity map (U_z) and (b) 2D velocity vector map obtained by combining the axial and radial direction velocity maps.

MR experiments using 8 *q*-slices were also performed to obtain more accurate measurements. The experimental time for each image to be acquired with the pulse sequence timed to the flow period was of 2 - 3 hours. The main challenge in performing these experiments was to maintain the vortex translation stable over the course of the 8 *q*-slice experiments. As mentioned before, the precision required for the data synchronisation to eliminate motion artifacts was of the order of 20 ms, and small axial flow rate variations (of the order of 0.05 cm^3 min^{-1}) tended to desynchronise the pulse sequence timing, resulting in motion artifacts. Figure 4.13 shows a velocity map of VFR flow in the axial direction obtained with an 8 *q*-

slice PGSE experiment. Artifacts can be noticed outside the gap (right-hand side) but also in the inter-vortex regions where opposed direction velocities are found.
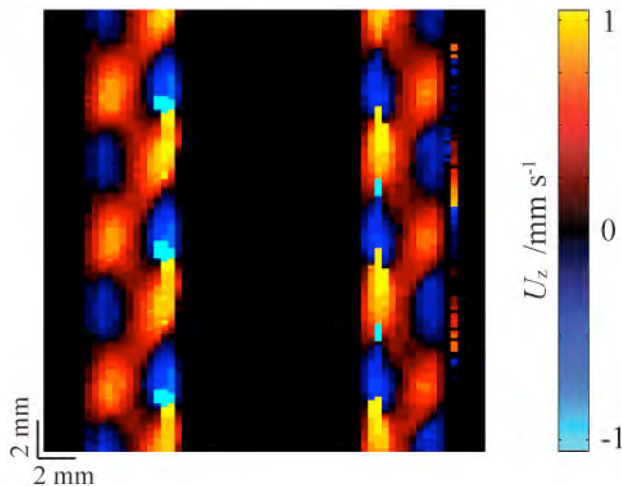
Figure 4.13. MR velocity map of VFR flow (at ω = 1 Hz and Q = 7.2 cm3 min-1) in the axial direction obtained with an 8 q-slice PGSE experiment.

Despite the vortical shape being clearly identifiable and the wavelength in agreement with the 2 *q*-slice experiments, the overall velocities are found to be much lower, probably due to disparities in the successive slices. Hence, 2 *q*-slice experiments were used to study the relative effects of pipe flow and TVF in the resulting VFR flow.

4.3.5 VFR flow as a superposition between pipe flow and TVF

VFR flow is obtained by imposing pipe flow to TVF. As discussed earlier, several authors assumed that the introduction of pipe flow was simply causing the vortices to translate along the length of the reactor[6]. But the slalom high-velocity regions on the axial direction velocity maps in a VFR (Figure 4.11b) show that the vortices are not simply "pushed" by the addition

of pipe flow. In fact, the velocity field in a VFR appears as a combination between the velocity fields of TVF and pipe flow. These results seem to support the assumption made by Wereley *et al.*[12], that the VFR velocity field could be modelled by an addition of pipe flow and TVF velocity fields. MRI maps offer a simple way of testing this hypothesis, since model VFR maps can be obtained by a pixel-to-pixel addition of pipe flow and TVF velocity maps. Figure 4.14 shows experimental and modelled VFR velocity maps at the same flow and rotation rates.
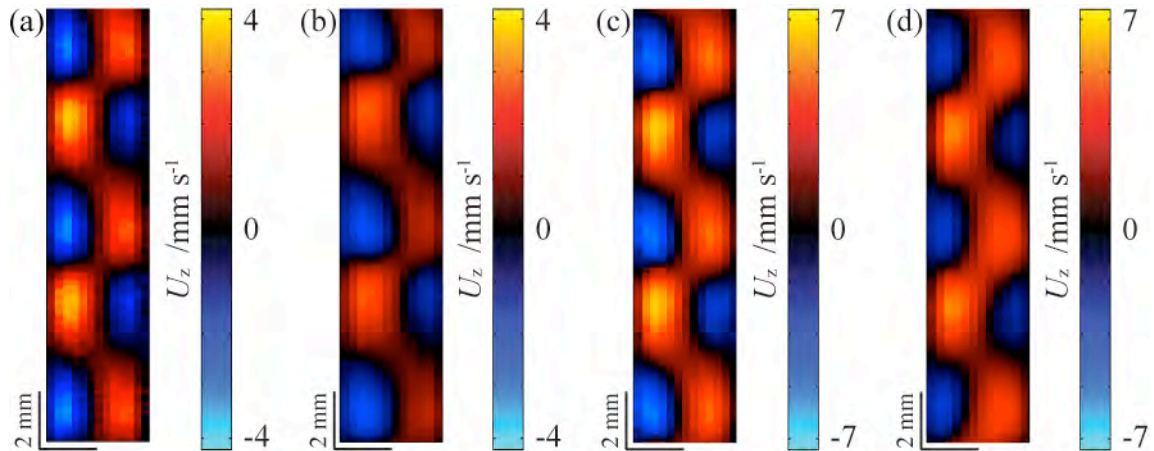
Figure 4.14. (a) Axial velocity map obtained by linear addition of experimental pipe flow (Q =7.2 cm³ min⁻¹) and TVF (ω =1 Hz) velocity maps. (b) Experimental velocity map of VFR flow at ω =1 Hz and Q = 7.2 cm³ min⁻¹. (c) Axial velocity map obtained by linear addition of experimental pipe flow (Q =13.6 cm³ min⁻¹) and TVF (ω =1 Hz) velocity maps. (d) Experimental velocity maps of VFR flow at ω =1 Hz and Q =13.6 cm³ min⁻¹.

The velocity maps obtained by linear addition show good agreement with the experimental VFR flow ones. The main difference is that the model velocity maps have about 30% higher velocities. Also, by removing the average axial map from the experimental VFR map one

obtains a typical TVF map corresponding to a lower rotation rate[12]. This could be explained by head loss occurring via the combination of the two flows. The strong TVF flow in azimuthal direction possibly transforms a part of the coherent motion in the z direction into dispersion, not detected by the velocity mapping experiments. Decrease in velocity in the VFR maps is in agreement with experimental results[12] showing that the addition of pipe flow increases the critical rotation rate necessary for the formation of the vortices. Also, this phenomenon could explain the possibility of stopping the moving vortices by increasing the rotation rate[7].

The properties of the slalom high-velocity region seem closely related to the pipe flow properties. Comparison between VFR velocity maps at $Q = 7.2$ cm^3 min^{-1} (Figure 4.14b) and $Q = 13.6$ cm^3 min^{-1} (Figure 4.14d) shows that for higher flow rates, this region is increased. However, the velocity drift, V_d, typically used for analysing the VFR flow properties, was found to be constant for all flow rates at a given rotation rate. These results highlight the limitation of V_d in characterising flow properties in a VFR and in particular the presence and properties of the slalom velocity region. The results presented here, could allow identifying more appropriate parameters for predicting VFR velocity field properties such as the importance of the slalom velocity field. One of these parameters is the pipe flow velocity profile (*Figure 4.7*a). For a given flow rate, this profile depends mainly on the value of the gap (d), the radii ratio (η), the viscosity (v) and the material properties of the inner walls. Two reactors with different d would exhibit different profiles and therefore have different VFR flow properties. At equal axial flow rates, a smaller gap VFR device made of high friction coefficient materials will exhibit a steeper pipe flow velocity profile, and hence, tend to have higher velocity deviations from U_{ax}. In that case, the $V_d = 1$ condition would not be sufficient

to predict plug flow, because of the presence of an important by-pass flow suggested by the *z* direction velocity maps. A review of the literature reveals that the studies that used the bigger gap VFR reactors and low axial flow rates (flat pipe flow profiles) tend to use the plug-flow approximation[6,8,9], whereas studies that used smaller gap reactors (steep pipe flow velocity profiles) tend to study the by-pass flow[7,12,24]. For plug-flow applications of the VFR, the parameters affecting the shape of the axial velocity profile have to be considered as much as V_d to analyse the quality of the plug-flow.

Diffusion/dispersion maps of the flow could give a measure of the extent of dispersion caused by the superposition of pipe flow and TVF. But diffusion/dispersion imaging typically requires a minimum of 8 q-slices encoding rather than the 2 used for velocity imaging. As discussed earlier, it is difficult to maintain a constant flow rate over the course of an 8 q-slice experiment (2-3 hours). Hence, while diffusion/dispersion mapping within the VFR should also be possible with the pulse sequence timing method, it was not possible to produce VFR diffusion/dispersion maps for this work. An estimation of diffusion/dispersion within the system could be obtained using the 2 q-slice experimental data. These experiments provide with the initial signal and one attenuated signal value, which allow getting information on the signal attenuation for each pixel. Signal attenuation is caused both by incoherent flow (diffusion/dispersion) and velocity shear, generating a spread of phases within the spin packets. The normalisation of the signal attenuation per pixel provides with a diffusion/dispersion variation map but no accurate diffusion/dispersion value can be obtained. Average propagator measurements could provide additional information on molecular displacements.

4.3.6 Molecular displacements and mixing

Average propagator experiments were performed to provide with information on molecular displacements and mixing. Figure 4.15 shows propagators for pipe flow in the axial direction. Where no flow is imposed on the system, the propagator has a Gaussian shape, characteristic of a diffusion propagator (Figure 1.4). The addition of flow causes a spread of this Gaussian along the displacements axis. The propagator maximum peak is found to decrease and shift to the positive displacements. This peak corresponds to molecules moving in the centre of the Couette cell gap. They have higher displacements because they experience higher velocities in the flow direction (Figure 4.7). The molecules situated closer to the Couette cell walls (inner and outer cylinder) are travelling smaller distances over this observation time, and have a more uniform distribution along the displacements axis.
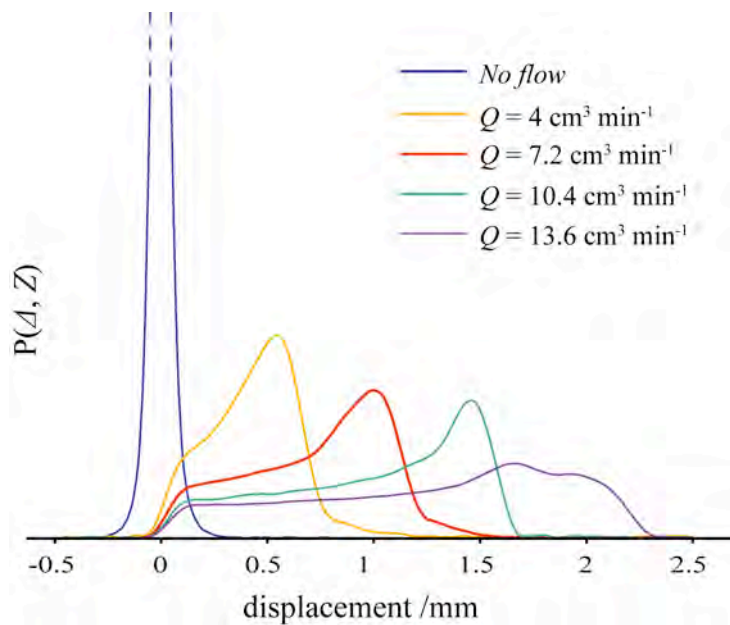
Figure 4.15. Normalised average propagators for pipe flow in the z direction, at an observation time $\Delta = 1$ s and for different flow rates. 128 q-slices and 16 averages were used.

An increase in the flow rate is causing a reduction of the high displacement peak and a more uniform distribution of displacements. For $Q = 13.6$ cm^3 min^{-1}, two lower peaks are produced and the molecular distribution becomes more uniform along the displacement axis, indicating a more homogeneous molecule distribution. This propagator has a shape similar to the rectangular function shape that is typically obtained in tubular Poiseuille flow propagator measurements[34].

Figure 4.16 shows propagators for VFR flow in the axial direction, at increasing observation times. As expected, the maximum displacement in P(Z , Δ) increases with increasing Δ. For $\Delta = 20$ ms, the maximum of the propagator is found on the positive displacements along the axis, similarly to the pipe flow propagators. As the observation time is increased, molecules sample a greater area of the vortices and the propagators get more affected by the flow. For $\Delta > 0.1$ s, the propagators have two maxima peaks. Also, small side lobes can be seen for $\Delta = 0.1$ s and become clearly formed at $\Delta = 1$ s.
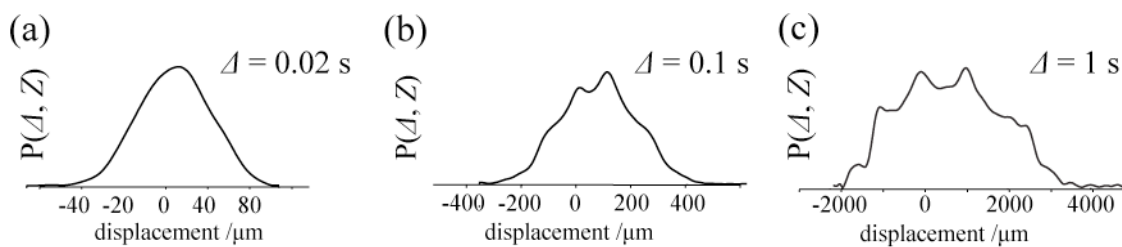
Figure 4.16. Normalised propagators for VFR flow (Q =7.2 cm^3 min^{-1} and ω =1 Hz) at increasing observation times Δ: 20ms (a), 100 ms (b), and 1 s(c). 64 q-slices and 4 averages were used.

Comparison with propagators of pipe flow and TVF can give a better understanding of the features observed on the VFR propagators. Figure 4.17 displays propagators for pipe flow, TVF and VFR flow. Propagators of TVF flow were analysed previously (cf. 3.3.3). The combination of pipe flow and TVF is clearly reflected on the VFR flow propagator. The left hand-peak of the VFR propagator and its overall broadening shape are characteristic of molecular circulation within vortices and are clearly resulting from the vortical movement as the same peak and shape is found for the TVF propagator. However, the VFR propagator is not symmetric, and the right hand-side part, corresponding to displacements in the direction of the flow is spreading over a longer distance along the axis.
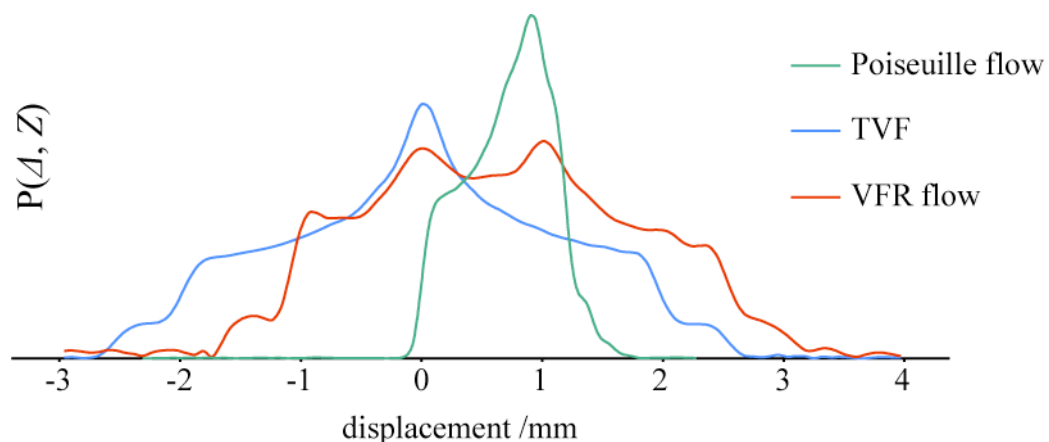
Figure 4.17. Normalised average propagators for displacements in the z direction at Q =7.2 cm³ min⁻¹ (pipe flow), ω =1 Hz (TVF) and Q =7.2 cm³ min⁻¹ - ω =1 Hz (VFR flow). The observation time Δ was of 1 s. 64 q-slices and 4 averages were used.

The pronounced peak that persists at zero displacement for both TVF and VFR propagators is not found on the pipe flow propagator. This peak reveals the presence of low axial displacement regions in the vortical flows. Such regions could be generated by the strong

secondary flow in the radial and azimuthal directions, constraining the molecular displacement in the axial direction. This is in agreement with previous studies showing that low molecular displacement regions (or "sticking regions") can be found in both vortical[35] and time-dependant[36] flows.

The influence of pipe flow on the VFR flow displacements is to be found on the right-hand maximum of the VFR propagator (at ~ 1.1 mm), situated almost at the same position as the pipe flow maximum (at ~ 1 mm). The fact that the VFR maximum is slightly advanced is probably due to axial flow enhancement by the vortical movement in the flow direction. As the position of the pipe flow propagator maximum depends on U_{ax}, the position of the VFR propagator maximum could be a function of U_{ax} and U_{TV}. The deviation between the two peaks could be related to the velocity drift and the VFR maximum position advance explained by the fact $V_d > 1$ (the vortex translation velocity is higher than the average flow velocity).

These results show that VFR propagators provide with a unique insight into the molecular displacement properties within this complex flow. Studies of the effect of flow and rotation rate on the VFR propagators were performed in order to obtain information on the short time-scale mixing properties of the VFR.

4.3.7 Flow and rotation rate effect on molecular displacements

Figure 4.18 shows propagators for increasing flow rates at a constant rotation rate ($\omega = 1$ Hz). Previously (cf. 4.3.5), the right-hand maximum on the VFR propagator was related to the pipe flow. Comparison with pipe flow propagators at the same flow rates (Figure 4.15), shows that

this maximum is always situated at a similar position as the pipe flow propagator maximum. Also, similarly to the pipe flow propagator observations, this maximum is decreasing with a flow rate increase. On the other hand, pipe flow does not have any effect on the peak at zero displacement, showing that both its position and intensity depend on the vortical flow. An increase in flow rate is to be related with a shift of the left-hand side of the propagator towards the positive displacements. Except for $Q = 10.4$ cm^3 min^{-1}, this width reduction is followed by an increase in intensity giving the impression that molecules are "pushed" towards the positive displacements.
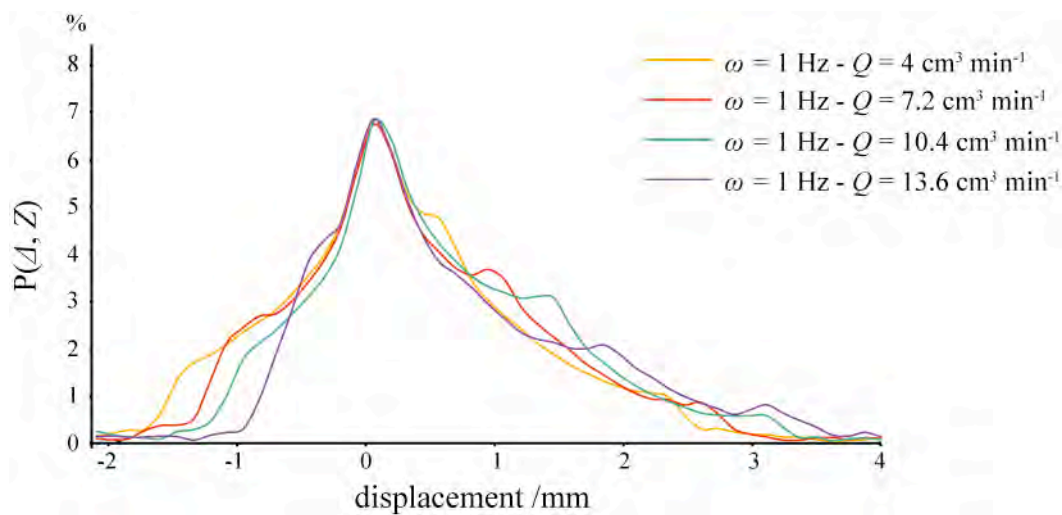
Figure 4.18. Normalised propagators for axial displacements in VFR flow at ω = 1 Hz for different flow rates. The observation time Δ was of 1 s. 128 q-slices and 16 averages were used.

The shape of the propagator at low flow rates is more similar to the TVF propagator shape, showing that higher flow rates tend to reduce the vortical flow. The overall width of the propagators is reduced at higher flow rates, suggesting a possible reduction in axial dispersion

with axial flow rate increase. The analysis of these results shows that the translating tank model for the VFR flow is not able to address the complexity of the observed phenomena, while a simple superposition approach as the one suggested by Wereley *et al.*[12] provides with means for analysing these propagators.

Figure 4.19 shows VFR flow propagators for increasing rotation rates at a constant flow rate ($Q = 7.2$ cm^3 min^{-1}), in comparison with TVF propagators at the same rotation rates.
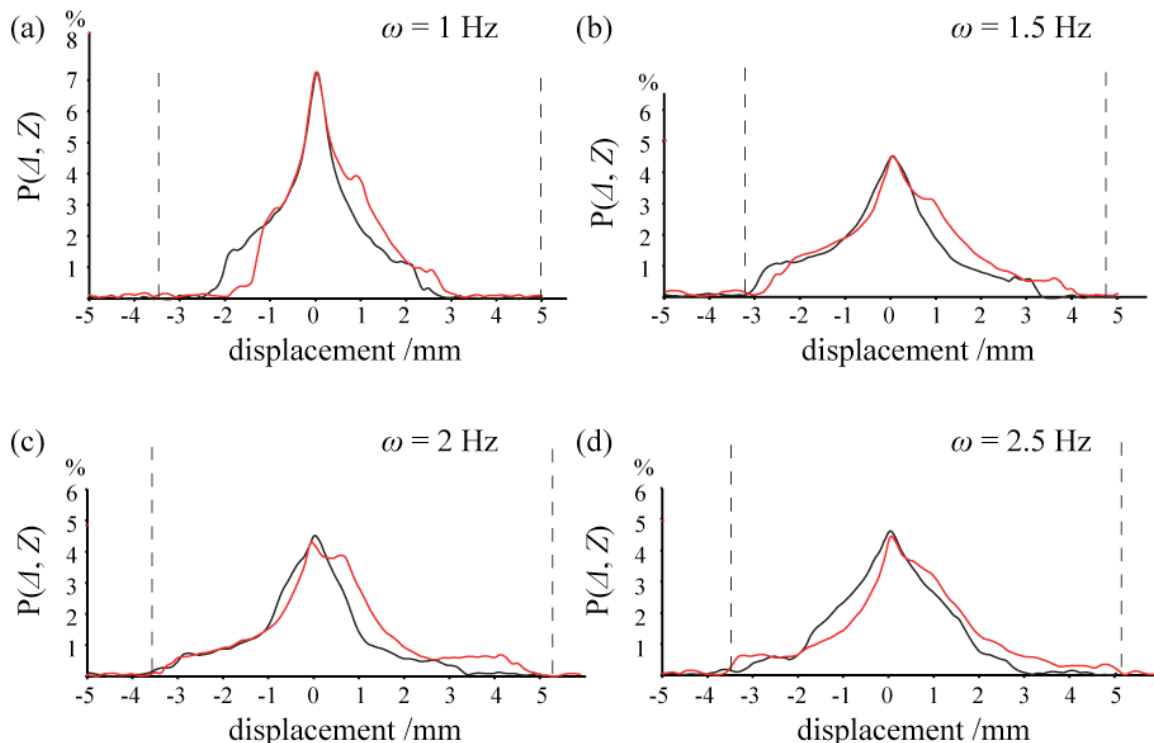
Figure 4.19. Normalised propagators for VFR flow (red) at Q = 7.2 cm^3 min^{-1} and in TVF flow (black) for different rotation rates ω: (a) 1 Hz, (b) 1.5 Hz, (c) 2 Hz and (d) 2.5 Hz. Δ was of 1 s. 128 q-slices and 16 averages were used. The area between doted lines indicates the wavelength of the vortex pair including a shift corresponding to the translation of the vortices during Δ.

Again, the centre peak height does not seem influenced by the flow rate at any rotation rate in this range. As expected, for higher rotation rates the flow effect is less important and the shape of the VFR propagator is more similar to the TVF one. An increase in rotation rate is followed by an increase of the propagator width in the negative displacements. For $\omega = 2.5$ Hz (Figure 4.18d) the negative displacements are higher than for the TVF propagator at the same rotation rate. This might be due to the fact that the flow rate increases displacements in the high-circulation outer zone of the vortices. This phenomenon at higher rotation rates seems to support the model[11] where the vortical flow is transforming the pipe flow into a slalom by-pass winding around the vortices. The rotation rate increase is also causing a slight shift in the position of the flow related right hand side peak. For higher rotation rates, this peak is found at lower displacements along the axis. This is related to a rotation rate increase reducing the travelling speed of the vortices (Figure 4.6). For $\omega = 2.5$ Hz, no right-hand maximum can be seen. This suggests a more homogeneous mixing at these regimes as the presence of the peak at low rotation rates is causing a more heterogeneous distribution of molecular displacements along the axis. In fact, the velocities within the vortices have been shown to increase linearly with rotation rate (cf. chapter 3) while the maximal displacements on the propagators do not follow the same trend. For an increase of rotation from $\omega = 1$ Hz to $\omega = 2$ Hz, the increase in the maximal displacements is of 60% (going from 3 mm to 4.8 mm). At $\omega = 2.5$ Hz the maximal displacements are the same as for $\omega = 2$ Hz while the velocities are 25% higher. Enhanced molecular displacements seem to be constrained within the vortical structure at higher rotation rates, suggesting that better intra-vortex mixing is occurring. Due to the vortical translation, inter-vortex mixing is more difficult to study using these propagators, but the overall width of the propagators for $\omega \geq 2$ Hz is found to be equal to the

wavelength of the vortex pairs measured at the same regime, suggesting limited mixing between vortices.

Propagators at higher flow rates can give a better visualisation of this homogenising effect of rotation. Figure 4.20 shows propagators at $Q = 13.6$ cm^3 min^{-1} for $\omega = 1$ Hz and $\omega = 2.5$ Hz. At $\omega = 1$ Hz, the molecular distribution is very heterogeneous, with two peaks in the positive displacements and a small percentage of molecules travelling over long distances, while the majority of them is restricted to small displacements At the higher rotation rates the distribution within the vortex pair is more homogeneous and the molecular displacements are confined within the distance corresponding to a vortex pair.
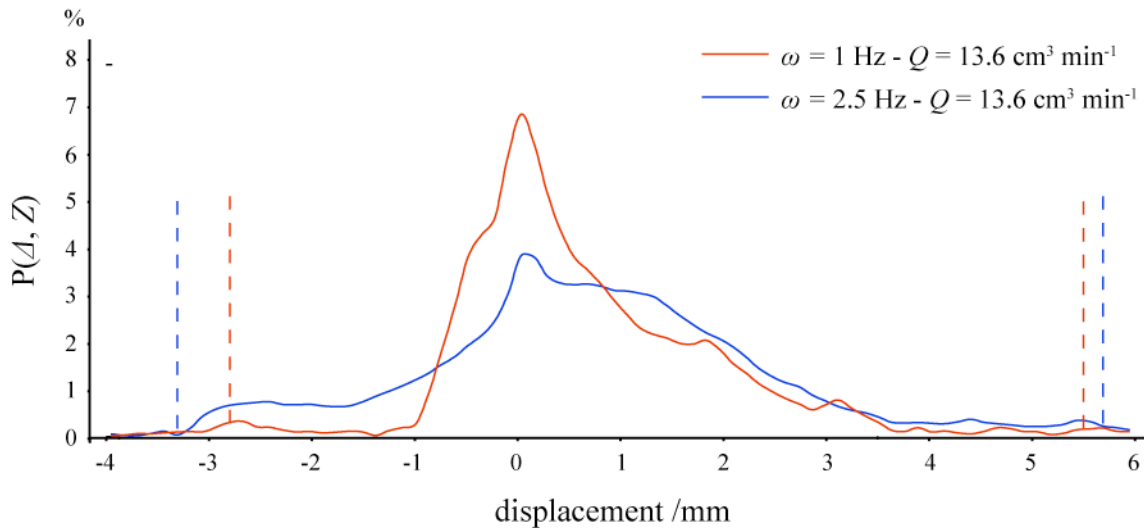
Figure 4.20. Normalised propagators for displacements in the z direction for VFR flow at Q =13.6 cm^3 min^{-1} for ω =1 Hz (red) and ω =2.5 Hz. Δ was of 1 s. 128 q-slices and 16 averages where used for these experiments. The area between doted lines indicates the wavelength of the vortex pair including a shift corresponding to the translation of the vortices during the observation time.

4.4 Conclusions

The combination of dye experiments, MR velocity mapping and propagator studies was shown to allow a unique flow characterisation, relating macroscopic flow properties, as the vortex pair dimension, with the vortex velocity field and the intra-vortex mixing that is of particular interest for chemical and biochemical applications of the reactor.

By providing three-dimensional velocity maps of the VFR flow, the present work demonstrated the ability of MRI to produce velocity maps of complex periodic flows. The velocity maps in the axial direction showed that the addition of pipe flow to the steady TVF generates a slalom high velocity region linking successive vortices on the velocity map. The possibility to model VFR flow by linear addition of the velocity maps of the two steady flows composing it (axial and TVF) gave very encouraging results, supported both by comparison with literature and by propagator experiments. The results of velocity map linear addition in combination with dye experiments allowed addressing the question of the by-pass flow nature and its dependence on the system parameters. They revealed the important role of the pipe flow profile and the limitations of the velocity drift V_d in characterising flow properties within a VFR. Modelling based on velocity map addition has to be further investigated and optimised, since it can provide with a fast and effective way of obtaining good behaviour predictions for VFR flow properties. It can also provide with high-resolution velocity field approximations for other unsteady flows obtained by superposition of steady flows.

Propagator measurements provided with insight into the micro-mixing behaviour related to particle displacements in a VFR. The propagators of the VFR flow were shown to be a

combination of the pipe flow and TVF propagators, revealing the limitations of the simplistic translating tank model for the VFR flow. The effects of flow and rotation on the micro-mixing properties of the VFR were studied using propagator analysis. At low rotations, high flows were shown to generate a heterogeneous distribution of molecular displacements along the reactors length, while an increase in rotation was linked with better intra-vortex mixing.

(1)   Judat, B.; Racina, A.; Kind, M. *Chem. Eng. Technol.* **2004**, *27*, 287.

(2)   Forney, L. J.; Pierson, J. A. *AIChE J.* **2003**, *49*, 727.

(3)   Wolinski, J.; Wronski, S. *Chem. Eng. and Process.* **2009**, *48*, 1061.

(4)   Haut, B.; Ben Amor, H.; Coulon, L.; Jacquet, A.; Halloin, V. *Chem. Eng. Sci.* **2003**, *58*, 777.

(5)   Resende, M. M.; Sousa, R.; Tardioli, P. W.; Giordano, R. L. C.; Giordano, R. C. *AIChE J.* **2005**, *51*, 314.

(6)   Kataoka, K.; Hongo, T.; Futagawa, M. *J. Chem. Eng. Jpn* **1974**, *8*, 4.

(7)   Giordano, R. C.; Giordano, R. L. C.; Prazeres, D. M. F.; Cooney, C. L. *Chem. Eng. Sci.* **1998**, *53*, 3635.

(8)   Legrand, J.; Coeuret, F. *Chem. Eng. Sci.* **1986**, *41*, 47.

(9)   Cohen, S.; Marom, D. M. *Chem. Eng. J. and Biochem. Eng.* **1983**, *27*, 87.

(10)   Lueptow, R. M.; Docter, A.; Min, K. Y. *Phys. Fluids a-Fluid* **1992**, *4*, 2446.

(11)   Haim, D.; Pismen, L. M. *Chem. Eng. Sci.* **1994**, *49*, 1119.

(12)   Wereley, S. T.; Lueptow, R. M. *Phys. Fluids* **1999**, *11*, 3637.

(13)   Desmet, G.; Verelst, H.; Baron, G. V. *Chem. Eng. Sci.* **1996**, *51*, 1287.

(14)   Desmet, G.; Verelst, H.; Baron, G. V. *Chem. Eng. Sci.* **1996**, *51*, 1299.

(15)   Giordano, R. L. C.; Giordano, R. C.; Prazeres, D. M. F.; Cooney, C. L. *Chem. Eng. Sci.* **2000**, *55*, 3611.

(16)   Syed, A.; Fruh, W. G. *J. Chem. Technol. Biot.* **2003**, *78*, 227.

(17)   Elkins, C. J.; Alley, M. T. *Exp. Fluids* **2007**, *43*, 823.

(18)   Henkelman, R. M.; Bronskill, M. J. *Med. Phys.* **1987**, *14*, 506.

(19)   Uludag, Y.; Powell, R. L.; McCarthy, M. J. *AIChE J.* **2004**, *50*, 1662.

(20)   Moser, K. W.; Raguin, L. G.; Harris, A.; Morris, H. D.; Georgiadis, J.; Shannon, M.; Philpott, M. *Magn. Reson. Imaging* **2000**, *18*, 199.

(21)   Han, S. I.; Stapf, S.; Blumich, B. *Phys. Rev. Lett.* **2001**, *8714*.

(22)   Vallatos, A.; Wilson, M. C. T.; Taylor, A. F.; Britton, M. M. *Europhys. Lett.* **2012**.

(23)   Sczechowski, J. G.; Koval, C. A.; Noble, R. D. *Chem. Eng. Sci.* **1995**, *50*, 3163.

(24)   Campero, R. J.; Vigil, R. D. *Chem. Eng. Sci.* **1997**, *52*, 3303.

(25)   Resende, M. M.; Tardioli, P. W.; Fernandez, V. M.; Ferreira, A. L. O.; Giordano, R. L. C.; Giordano, R. C. *Chem. Eng. Sci.* **2001**, *56*, 755.

(26)   Raguin, L. G.; Georgiadis, J. G. *J. Fluid Mech.* **2004**, *516*, 125.

(27)   Resende, M. M.; Vieira, P. G.; Sousa, R.; Giordano, R. L. C.; Giordano, R. C. *Braz. J. Chem. Eng.* **2004**, *21*, 175.

(28)   Richter, O.; Hoffmann, H.; Kraushaar-Czarnetzki, B. *Chem. Eng. Sci.* **2008**, *63*, 3504.

(29)   Richter, O.; Menges, M.; Kraushaar-Czarnetzki, B. *Chem. Eng. Sci.* **2009**, *64*, 2384.

(30)   Coles, D. *J. Fluid Mech.* **1965**, *21*.

(31)   Seymour, J. D.; Callaghan, P. T. *AIChE J.* **1997**, *43*, 2096.

(32)   Bird, R. B.; Stewart, W. E.; Lightfoot, E. N. *Transport phenomena*, 2nd, Wiley international ed.; J. Wiley: New York, 2002.

(33)   Howes, T.; Rudman, M. *AIChE J.* **1998**, *44*, 255.

(34)   Callaghan, P. T.; Xia, Y. *J. Magn. Res.* **1991**, *91*, 326.

(35)   Young, W.; Pumir, A.; Pomeau, Y. *Phys. Fluids a-Fluid* **1989**, *1*, 462.

(36)   Meiss, J. D.; Ott, E. *Phys. Rev. Lett.* **1985**, *55*, 2741.

5 Molecular displacement simulations using MR data

5.1 Introduction

Theoretical studies of axial dispersion in TVF and VFR flow[1] have been made using models that lead to transport equations including a dispersion tensor[2]. These studies provided with good estimates of axial dispersion for stationary vortex flow (TVF) but not for translating vortex flow (VFR). Most theoretical studies of flow patterns in Couette cells focus on the Eulerian properties of the flow, and present limitations in addressing micro-mixing properties that necessitate a Lagrangian analysis[3]. Similarly, the results presented in the previous chapters show that MR velocity and diffusion/dispersion mapping cannot give quantitative information on molecular displacements and that this information could be assessed by propagator measurements. In particular, knowing the molecular displacements in a VFR could allow characterisation of the axial dispersion while providing quantitative information on plug-flow properties, by probing the extent of inter-vortex mixing. In the context of chemical engineering, information on molecular displacements and mixing is often more crucial in characterising the properties of a reactor than the velocity field. For example, when flow is coupled with autocatalysis, quantitative information on molecular displacements can provide a means to evaluate the relative input of transport and reaction into the propagation of autocatalytic waves and fronts [4,5].

However, propagator measurements are constrained to short observation times ($\Delta \leq 1$ s), due to MR relaxation. Previous studies[6] have addressed this limitation by producing simulated propagators for longer times using molecular displacement models. Similar models, based on

fluid particle tracking, were also used for studying mixing and dispersion in wavy TVF[3,7]. In such particle-tracking simulations the velocity field is calculated using the NS equation. In the case of complex vortical flows, velocity field simplifications are required, limiting the quantitative nature of the results. The present work overcomes this limitation by using experimental MR velocity and diffusion/dispersion maps. Velocity distribution histograms have been shown to reproduce the molecular distribution features in propagator measurements[8,9]. Here, molecular displacements are simulated using the pixel average velocity and diffusion/dispersion coefficient provided by experimental maps. Considering the symmetry of the studied flows in the azimuthal direction, two-dimensional simulations were performed, where two-dimensional coordinates identified each molecule's position. By using a sufficiently large number of molecules in the simulation, the percentage distribution of displacements along an axis can be plotted as a propagator along this axis.

Initially, simulations for short observation times were performed ($\Delta \leq$ 1s). The obtained simulated propagators for pipe flow, TVF and VFR flow were compared with experimental propagators presented in the previous chapter. This comparison allowed the verification of the method. Following this, simulations for observation times that are not accessible experimentally were performed. These simulations enable molecular transport and mixing to be assessed over longer-time scales, allowing plug-flow, by-pass flow and inter-vortex mixing to be quantified[10]. Also, since two-dimensional coordinates identify the molecular trajectories, the simulations allow for molecular pathways on the map surface to be predicted. These results provide with quantitative and qualitative spatially resolved information on the mixing properties within each flow.

Propagator simulations can show the transport of molecules. Molecular trajectories can also be observed experimentally using a chemical front. Where an autocatalytic reaction is used, it is possible to detect the transport of even small numbers of molecules. The simulation results are compared with experimental studies of chemical front propagation in TVF and VFR flow. Chemical waves are obtained using the bromate-sulfite pH clock reaction[11]. The reaction is followed by a sharp drop in pH that is used to visualise the propagation of chemical fronts[12]. These fronts have been shown to be sensitive to convection effects and can be particularly useful in the study of transport processes within flow systems. This study shows how molecular displacement simulations based on experimental MR data allow to understand and predict the shape of chemical fronts propagating through stationary and translating vortical flow. The VFR simulations allow prediction of the effects of small numbers of molecules travelling faster (by-pass flow) or slower (drag flow) than the translating vortices.

5.2 Experimental

5.2.1 Molecular displacement simulations

Simulations were performed using Matlab on a PC. The velocity and diffusion/dispersion fields were created using experimental velocity (U_y, U_z) and diffusion/dispersion (D_y, D_z) maps for axial flow at $Q = 7.2$ cm^3 min^{-1}, Taylor vortex flow at $\omega = 1$ Hz and VFR flow at $Q = 7.2$ cm^3 min^{-1} and $\omega = 1$ Hz. A more detailed analysis of the properties of these flows is provided in chapters 3 and 4. Molecular displacements in the azimuthal direction were assumed to be symmetric. Also the flow fields present symmetry with respect to the inner cylinder. This allowed considering only the velocity and diffusion/dispersion fields obtained

on one side of the Couette cell gap.

As discussed earlier, diffusion/dispersion maps do not provide with quantitative values of diffusion and dispersion within each voxel (cf. 3.3.1.2). This is due to the fact that the measured values are affected by both velocity shear and the pixel size. An alternative to the use of these maps would have been to use a constant self-diffusion coefficient for these simulations. But for sufficiently long mixing times, the effect of diffusion-dispersion on overall molecular displacements was expected to be negligible compared to the effect of the velocity field. In fact, for all the simulations with mixing times $\Delta > 100$ ms presented in this chapter, replacing the diffusion/dispersion maps with a constant diffusion coefficient gave similar molecular distribution results. Hence, the errors coming from the use of the experimental diffusion/dispersion maps were only expected to play a role for short simulation times. Moreover, using these maps allowed accounting for effects related to spatial inhomogeneity of dispersion.

The simulations used n molecules identified by their two-dimensional coordinates in the velocity field plan. For simulations of stationary and translating vortices, the molecules were evenly distributed throughout several vortex pairs within the velocity maps. The same distribution was used in axial flow simulations. The dimensions of the experimental velocity and diffusion/dispersion maps do not allow simulating displacements over more than a distance corresponding to five vortex pairs. For pipe flow, where velocity is constant along the axial direction, an average velocity profile was considered over longer distances. For the vortical flows, spatial periodicity allowed for longer velocity maps to be constructed by juxtaposition of series of an experimental map region corresponding to one vortex pair. For

the VFR flow, as experimental diffusion/dispersion maps were not available, an estimation of the dispersion field was made. Regions of high and low dispersion could be identified from the diffusive attenuation produced by the PGSE velocity imaging experiments[13]. The estimated diffusion/dispersion maps were then obtained by scaling the diffusive attenuation field to the TVF diffusion/dispersion map. Also, an additional modification was required in order to take the observed translation of the vortices into account, which allowed the velocity and diffusion/dispersion fields to translate at a velocity U_{TV}.

Time steps, dt, were considered for these simulations. The total number of steps, N, was given by $N = \Delta / dt$, where Δ is the observation time to be simulated. At every time step, dt, the displacement of each molecule n_i of coordinates (y_i, z_i) was defined by a velocity and a diffusion/dispersion step. The velocity step was determined using the experimental velocity maps U_y and U_z. For the diffusive step, the direction was determined by a randomly generated angle θ and the magnitude was calculated using the diffusion/dispersion maps D_y and D_z. Displacements due to velocity and diffusion in each direction where then added to the initial coordinates to define the final coordinates $y_i(t+dt)$ and $z_i(t+dt)$.

A bounce-back boundary condition was employed for molecules near the reactor walls. If the distance to the wall was found to be smaller than the distance d_{dt} to be traveled during dt, the molecule was simply considered to travel until the wall and perform the rest of d_{dt} in the reverse direction. A minimum of three repetitions for each set of parameters was performed. The Maltab code used for these simulations is included in Appendix B.

After $N \times dt$ steps, the overall displacement for each molecule n_i along the z-axis was determined by comparing the z_i coordinates of the initial and final positions. The displacement

axis was separated in bins and the number of molecules to attain each bin at the end of the simulation was counted. Simulated normalised propagators for a given observation time Δ were obtained by plotting the proportion of molecules at each displacement bin against displacements.

Molecular paths were tracked either by calculations of molecular density per pixel at different observation times, either by calculation of the residence time of molecules per pixel. In this second approach, a matrix counting how many molecules attend each pixel during the simulation was produced to give information on molecular displacements over time. A 2D plot of theses matrices shows high and low circulation pathways within the flow. Because the attendance in some pixels was orders of magnitude higher than in others, a logarithmic scale was used to reveal minor paths taken by molecules.

500 000 molecules were used for all the simulations. The observation times Δ were of 20 ms, 100 ms, 1 s and 1 min. For simulations with $\Delta < 1$ s, dt was of 0.1 ms and 40 bins were used for the displacement axis. For simulations with $\Delta \geq 1$ s, dt was of 1 ms and 60 bins were used for the displacement axis. For the VFR simulations the velocity and diffusion/dispersion fields were translating at a velocity $U_{TV} = 0.81$ mm s^{-1}, in accordance with experimental results obtained in chapter 4.

5.2.2 Chemical front propagation in vortical flow

A bromate-sulfite reaction mixture was obtained by mixing two separate reagent solutions. Solution A contained sodium bromate (0.1 M), while solution B contained sodium sulfite

(0.26 M) and a colour pH-indicator (0.5 g in 1L) both in deionised water. Two pH-indicators were used for obtaining contrast between the reactants and the more acidic products: bromocresol purple (yellow product front in purple reactant solution) and methyl red (red product front in orange reactant solution). The solutions were mixed and then pumped into the Couette cell. The waves were initiated using a 0.5 mL injection of 1 M sulphuric acid at the inlet of the reactor. The Couette cell used for these experiments is described in previous sections (cf. 3.2.1 and 4.2.1). The viscosity ν of the solutions was on the order of 1 mm^2 s^{-1} at 22 ± 0.5 °C, similar to the viscosity of the solutions used for the velocity and diffusion/dispersion imaging experiments (Chapters 3 and 4). A rotation rate of $\omega = 1$ Hz and a flow rate $Q = 7.2$ cm^3 min^{-1} were used for these experiments. Each experiment was repeated a minimum of three times. Optical images of the reactor were acquired every 5 s. The optical imaging technique is described in previous sections (cf. 4.2.3).

5.3 Results and discussion

5.3.1 Molecular displacements and propagator simulations

Figure 5.1 shows experimental (a - c) and simulated (d - f) propagators for pipe flow at the same observation times Δ. Simulated propagators are shown to reproduce the main features of the experimental ones (positive displacements and formation of a maximum). Also, both the position of the maximum peak and the overall displacements are found to be in quantitative agreement.
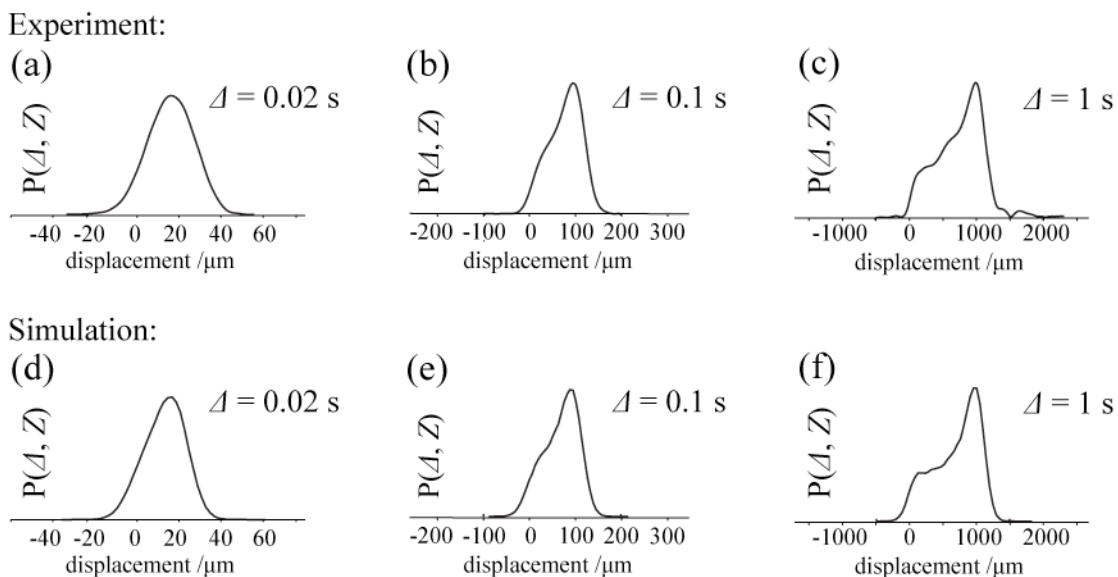
Figure 5.1. (a)–(c) Experimental propagators and (d)–(f) simulated propagators at increasing observation times, for pipe flow at Q=7.2 cm³ min⁻¹.

Figure 5.2 shows experimental (a - c) and simulated (d - f) propagators for TVF flow at the same observation times Δ. At low observation times ($\Delta \leq 100$ ms), the simulated propagators have less clear structural features than the experimental ones, but for $\Delta = 1$ s all the features of

the measured propagator can be identified (centre maximum and side lobes). Again quantitative agreement is found both for the overall displacements and the position of the main features.
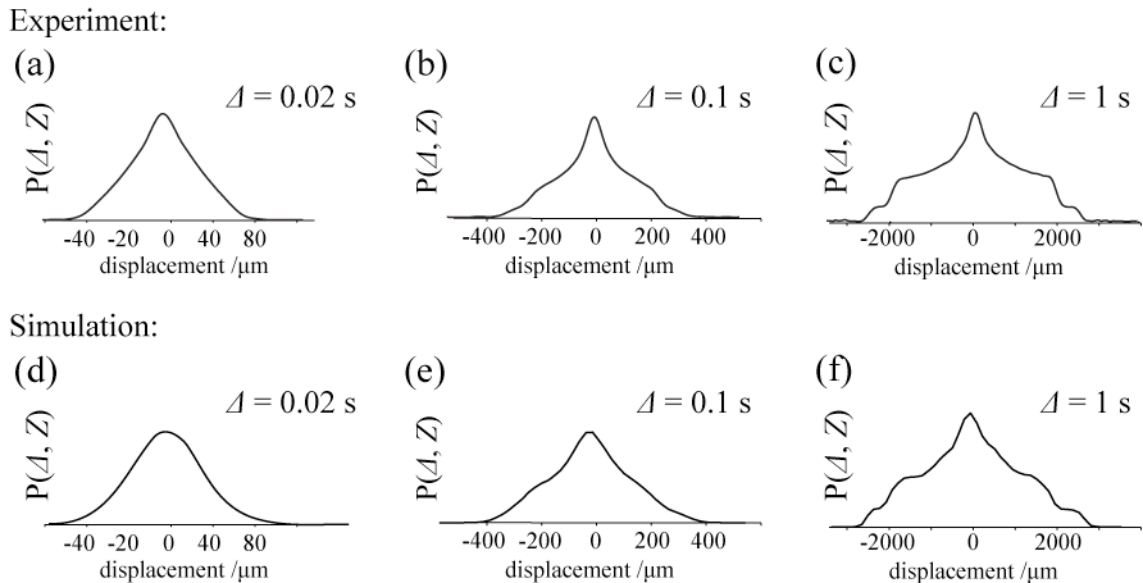
Experiment:

Figure 5.2. (a)–(c) Experimental propagators and (d)–(f) simulated propagators at increasing observation times, for Taylor vortex flow at ω =1 Hz.

Figure 5.3 shows experimental (a - c) and simulated (d - f) propagators for VFR flow at the same observation times Δ. Although the agreement is not as good as for pipe fow or TVF, the simulation reproduces all the structural features of measured molecular displacements in the VFR. Discrepancies in the overall broadening of the VFR propagators may be related with the use of an estimated diffusion/dispersion map for the simulated ones. The main difference arises from a shift in position of the maximum associated with the pipe flow (right-hand maximum on the propagators). There seems to be a delay for the formation and the overall displacement of this maximum in the case of the simulation. In the experimental propagator,

this maximum is always found at higher displacement compared to the pipe flow maximum, while for the simulated propagators it is found at a lower displacement.
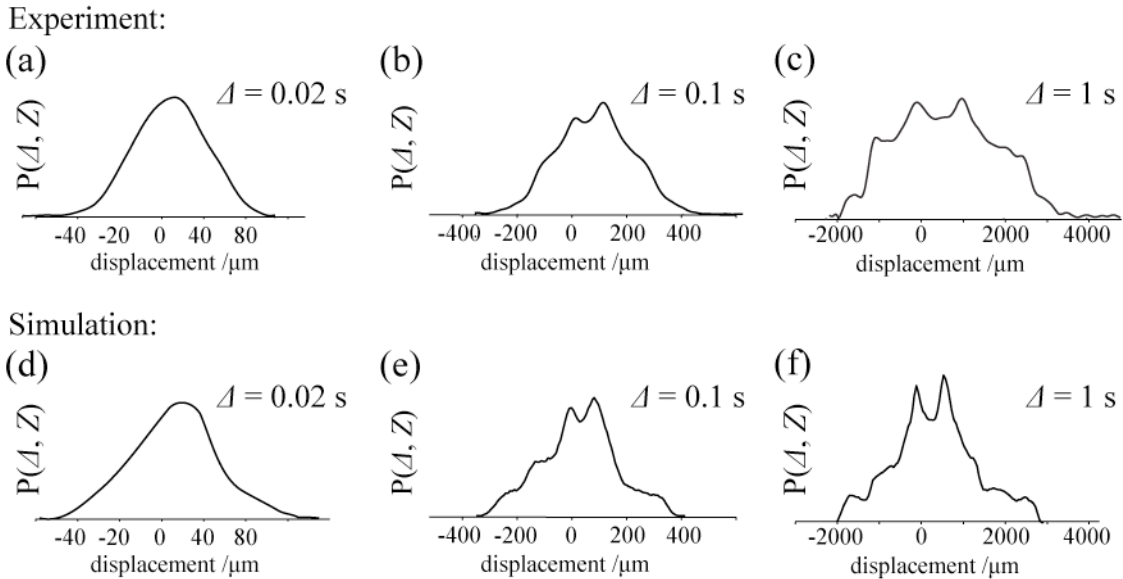
Figure 5.3. (a)–(c) Experimental propagators and (d)–(f) simulated propagators at increasing observation times, for VFR flow at ω = 1 Hz and Q = 7.2 cm³ min⁻¹.

This difference could be attributed to dispersion enhancement between vortex pairs, which is not taken into account in our model. In fact, the translational movement of the vortex pairs could give rise to Taylor dispersion[14] as measurements in TVF and VFR show that the addition of pipe flow is followed by an increase in axial dispersion[15]. In their theoretical study on axial dispersion within VFR flow, Howes and Rudman[1] suggested that discrepancies between their results and experimental data could be explained by the existence of a further mechanism for axial dispersion caused by the difference in velocity between the vortex translation and the average axial velocity ($U_{TV} - U_{ax}$). Comparison between simulated and

experimental propagator data could provide with information on dispersion linked with such molecular displacements.

As it has also been observed in TVF, the structural features of experimental propagators (two peaks, middle and side lobes) become clear in the simulated propagators for VFR flow as the observation time increases. At higher Δ, coherent molecular displacements such as the ones imposed by the velocity maps, play a dominant role in determining the overall molecular displacements. Therefore, it is expected that discrepancies related to diffusion/dispersion are reduced, and simulated propagators tend to be in better agreement with experimental ones. To confirm the secondary role of dispersion, longer time-scale simulations were performed on pipe flow and TVF. These simulations showed that diffusion/dispersion map effects on the overall molecular distribution are minimal at high observation times (Δ). Thus, even though the VFR simulated propagators do not completely capture the displacement characteristics of flow in the VFR for low observation times, they do allow us to probe molecule trajectories and explore displacements in excess of what can be measured experimentally, where Δ is typically limited to $\leq$ 1s.

5.3.2 Long time scale displacements and axial dispersion

Figure 5.4 shows simulated propagators for pipe and VFR flows at an observation time of $\Delta =$ 1 min. As expected, pipe flow spreads the molecules along the axial direction with a maximum close to the higher displacements (at 60 mm). In the case of the VFR propagator simulation, the molecular spread along the axial direction is reduced both on high and low displacements. Hence, at the same flow rate the vortical flow is shown to reduce axial

dispersion. This reduction of molecular spread reflects the plug-flow properties of the translating vortices.
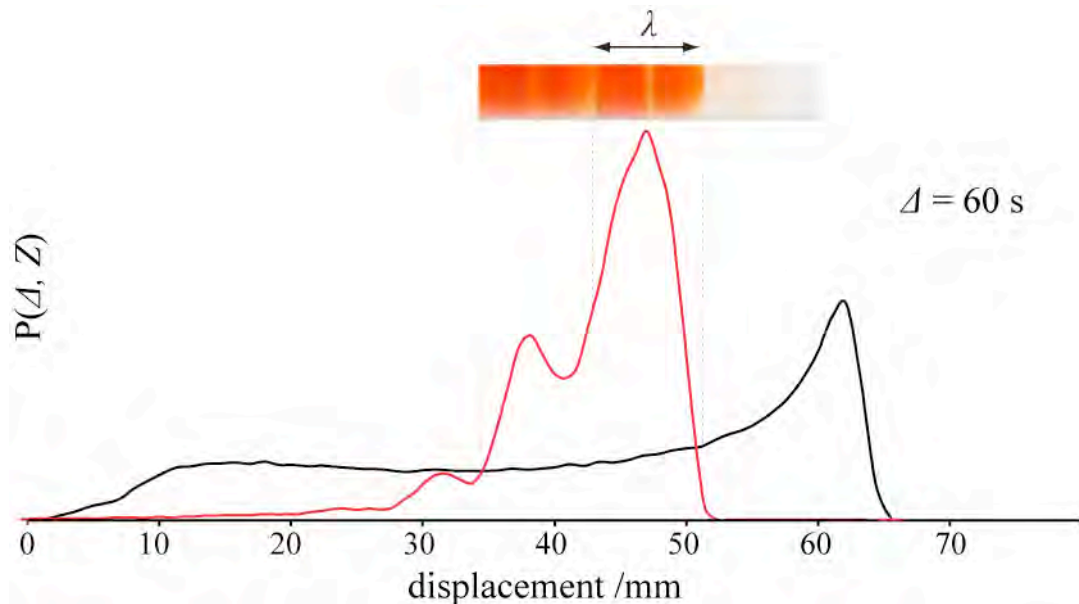
Figure 5.4. Simulated propagators at Δ = 1 min, for pipe flow (black line) at Q =7.2 cm³ min⁻¹ and VFR flow (red line) at ω =1 Hz and Q = 7.2 cm³ min⁻¹, with dye injection photograph inlay.

The simulated propagators can provide with quantitative information of the mixing properties within the VFR. Over the time of the simulation, vortices translate up to 49 mm (approximately the length of 6 vortex pairs). What this propagator reveals is partial plug-flow, with 95% of molecular displacements limited to three vortex pairs.

A surprising feature of the VFR propagator is the presence of peaks and troughs. The distance between the peaks corresponds to approximately one vortex pair wavelength, λ. At the end of the simulation, each vortex pair on the velocity map was situated between a peak and a trough on the propagator, indicating that higher molecular concentration is expected in one over two

vortices. These results are in agreement with the dye experiment results (cf. 4.3.1) where heterogeneous distribution of molecules into successive vortices was suggested. (Figure 5.4).

These simulations allow, for the first time, to predict residence times and quantify inter-vortex mixing and plug-flow. In the case of the $\Delta = 1$ min simulation, 72 ± 10 % of the molecules remained in the vortex pair in which they started, while 26 ± 10 % mixed with the vortices behind and 2 ± 1 % mixed with the vortices ahead. This indicates that the plug-flow properties of the reactor are more affected by molecules moving slower than the vortices (drag) than by ones moving faster (by-pass). This was expected, as the vortices move faster than the average axial velocity ($V_d > 1$), and was also suggested by the dye experiments, where the dye front was sharp while the back was spreading over several vortex-pairs. To get a better insight into the mechanisms that underlie the molecular distribution within these flows spatial information is required in order to identify molecular pathways and regions of high and low mixing.

5.3.3 Molecular paths in pipe flow

Molecular paths in the pipe flow simulation for molecules starting from a region corresponding to two vortex pairs are shown in Figure 5.5a. At $t \geq 10$ s, the shape of the molecular pathways reflects the typical parabolic shape of Poiseuille flow velocity profiles. The longer displacements are found in the middle of the gap, in the region of the velocity maxima. Similarly to the velocity profile for pipe flow (Figure 4.7), the maximum is situated slightly towards the inner cylinder. This effect can be noticed more clearly at higher observation times where the molecules are found at higher displacements on the inner

cylinder part, causing a dissymmetry of the parabolic shape. While the friction at the walls causes a dispersion of the molecules depopulating the sides, the middle part of the front stays densely populated during the simulation. This explains the presence of the peak at high displacements observed in the pipe flow propagators (Figure 5.1c and Figure 5.4). The use of a logarithmic scale (Figure 5.5b) reveals less populated areas of the map. In the case of vortical flows, where the spread of the molecules is expected to be greater, a logarithmic scale can allow identifying low-density molecular paths.
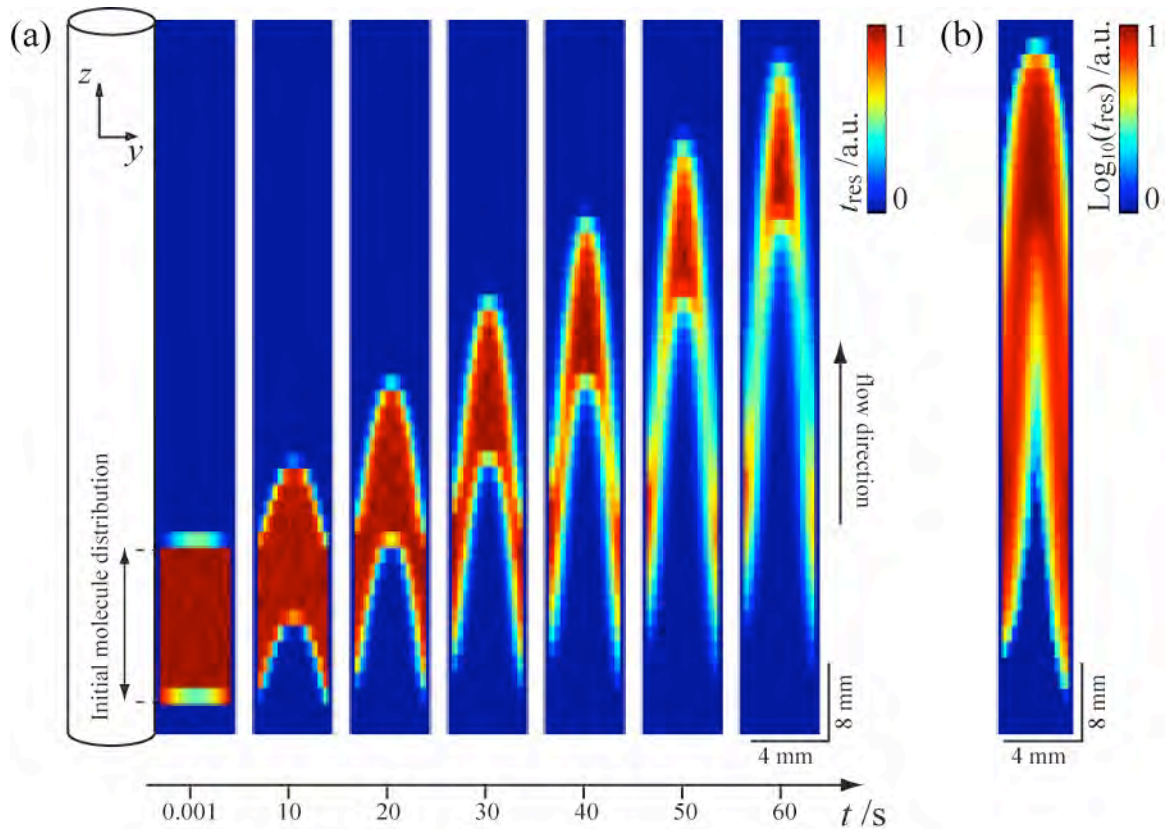
Figure 5.5. (a) Maps showing the molecular density per pixel in a simulation of molecular displacements in pipe flow at different observation times. (b) Map at t = 60 s plotted on a log10 scale.

5.3.4 Molecular paths in TVF

The velocity maps used for the simulation of molecular displacements in TVF at $\omega = 1$ Hz are shown in Figure 5.6a. These maps were obtained by juxtaposing a region of the experimental velocity maps corresponding to one vortex pair. The region of the maps corresponding to the initial molecule distribution covers four vortex pairs. Molecular paths for molecules starting from this region are shown in Figure 5.6b for observation times of 30 s and 60 s.
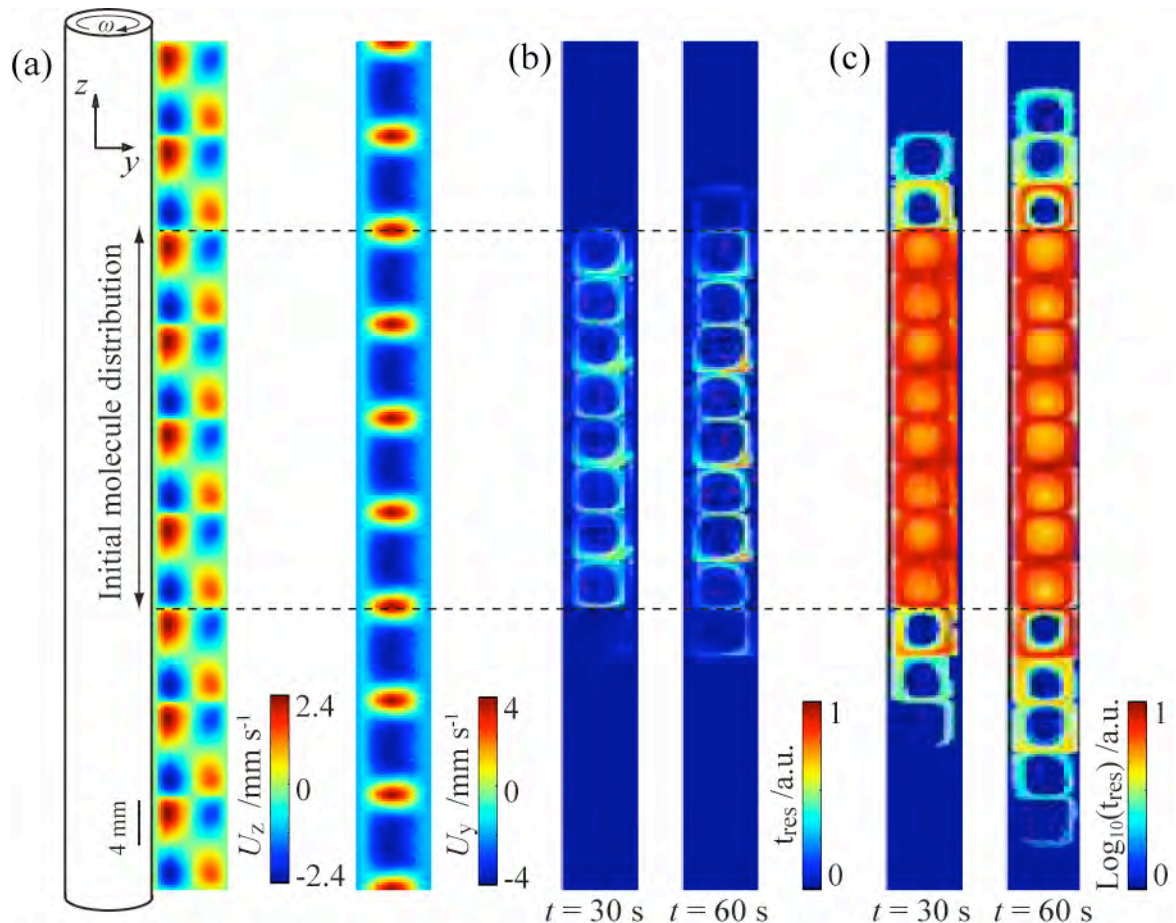
Figure 5.6. (a) Velocity maps of TVF flow at $\omega = 1$ Hz. (b-c) Maps showing the residence time (t_{res}) per pixel, over 30 s and 60 s, for molecules starting from the region indicated in part (a). The maps are plotted on linear (b) and log_{10} (c) scale.

Contrary to the pipe flow simulations, molecular spread was very important during the TVF simulations, making it difficult to identify the paths followed by the molecules on molecular density maps. To address this issue, pixel intensity in these maps corresponds to the number of times molecules were found in each pixel during the simulation, or molecular residence time (t_{res}). Figure 5.6b shows the presence of high-movement square pathways on the outer region of the vortices. Molecules seem trapped in these pathways as very low movements are seen in the vortex core region. Molecular displacement in these high-movement regions can help explaining the features of the TVF propagators (Figure 5.2). Molecules moving in the axial direction (z) correspond to the high displacement side lobes seen in TVF propagators. Molecules moving in the radial direction can probably explain the maxima of the TVF propagator at zero displacement: despite the fact that these molecules make big displacements along the radial direction, they are not moving along the axial direction. In these secondary flow areas in the radial direction, the paths are larger when the flow is coming towards the inner cylinder and narrower when it is leaving it.

As discussed, the use of a logarithmic scale for the molecular path map allows probing lower circulation paths. Figure 5.6c reveals that enhanced displacements are performed by a relatively small number of molecules that travel in the outer region. These paths seem to go further in one direction (lower part of the image). This might be due either to gravity effects reflected in the velocity and diffusion/dispersion maps, either to small errors in the reconstruction of the long maps by addition of successive bits of the experimental maps. In the latter case, an overlapping of the velocity maps of the order of a pixel size might favour one direction rather than the other. These displacements may be seemingly negligible, however they may play an important role in transmitting a chemical signal thus helping to

explain features of chemical front propagation through these systems. This is particularly the case when the flow is coupled with autocatalytic chemistry, where only a small amount of autocatalyst is required to carry the chemical wave[16].

5.3.5 Molecular paths in VFR flow

The z-direction velocity map used for the simulation of molecular displacements in VFR flow at ω = 1 Hz and Q = 7.2 cm^3 min^{-1} is shown in Figure 5.7a. Similarly to TVF, this map was obtained by juxtaposition of a region of the experimental velocity maps corresponding to one vortex pair. The molecules were seeded uniformly in a region corresponding to a single vortex pair highlighted by the doted rectangle.

Molecular path simulations in VFR flow for an observation time of 60 s are shown in Figure 5.7b. These paths correspond to molecular displacements in translating vortices from the point of view of a stationary observer. As the vortices are translating by a distance corresponding to 6 vortex pairs during this observation time, the vortical structure is not reflected in these paths as for the TVF flow. The highest circulation regions are observed on the walls of the reactor (red colour) and correspond to the flow generated in the outer region of the vortices. More circulation (higher intensity) is found in the outer cylinder region than the inner cylinder one. The middle of the reactor is less densely populated, probably due to the lower circulation in the vortex core regions.
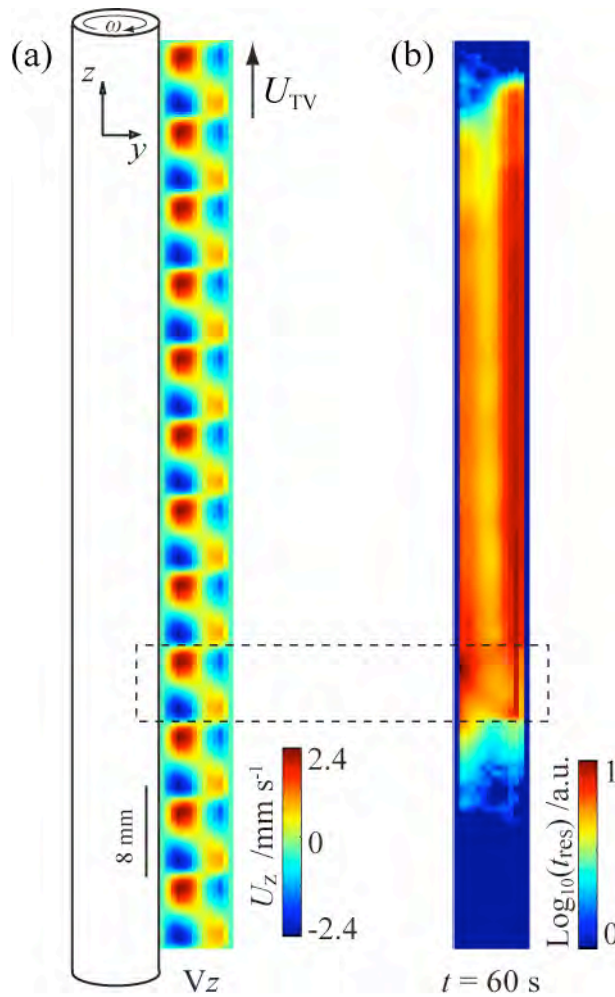
Figure 5.7. Velocity map of VFR flow at ω =1 Hz and Q = 7.2 cm³ min⁻¹ (the arrow shows the direction of the travelling vortices) and map showing the residence time (t_{res}) per pixel, over Δ = 60 s, for molecules starting from the single vortex pair highlighted in the doted rectangle. The residence times are plotted on a log10 scale.

Contrary to TVF simulation results (Figure 5.6), circulation in the centre of the VFR gap (yellow colour) is shown to be homogeneous. The translation of the vortices causes the pixel attendance along the axial direction to be averaged. An average of the TVF map along the z direction gives similar results, with the walls being highly populated and the attendance at the centre of the gap corresponding to an average between the vortex core circulation and the

outer region circulation along the radial direction. Close to the initial molecular distribution region this averaging is not well performed and two high circulation paths going from one wall to the other can be seen. In fact, at the initial stages of the simulation, the vortical flow dominates the molecular pathways since its velocities are three to five times greater than the vortex translation velocity U_{TV}. This causes the initial paths in the middle of the gap to be more noticeable.

This simulation provides with poor insight into the mixing properties of the vortical flow. In this stationary reference frame, molecular paths do not coincide with the velocity streamlines of the vortices. This explains why velocity field features, as the slalom high velocity regions, are not reflected on the molecular paths. In order to facilitate the comparison between the molecular paths and velocity fields both must be on the same reference frame. This can be obtained by tracking the molecules in the reference frame of the translating vortices. To get a better understanding of the role of the vortices in the molecular displacements within this flow and characterise by-pass and drag flow within the system, the same simulations were performed with molecular displacements tracked on a map translating at the same speed as the velocity and diffusion/dispersion maps, U_{TV}.

 Figure 5.8 shows these molecular displacements in comparison with the velocity maps in the axial and radial direction. The velocity field features can be identified on the molecular paths. As the propagator simulations suggest (Figure 5.4), the majority of the molecules remain within the vortex pair they were initially seeded. The highest molecular attendance in this map (red colour) is identified at the interface of opposite direction velocities between the vortex pairs. The circulation paths out of the initial vortex pair correspond to by-pass if they

are situated downstream (above the vortex pair), or drag if they are situated upstream (below the vortex pair).
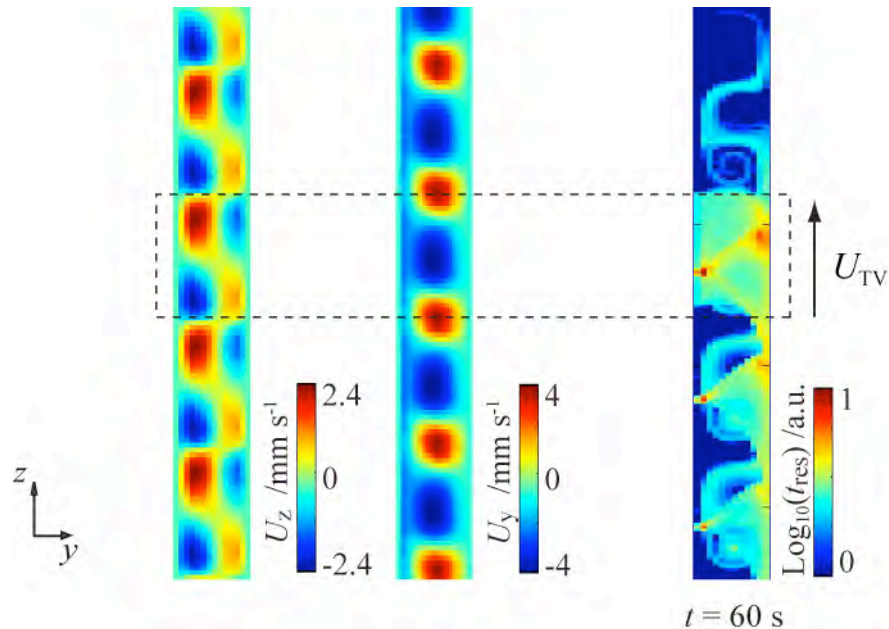
Figure 5.8. Velocity maps of VFR flow in the axial and radial directions at $\omega = 1$ Hz and $Q = 7.2$ cm^3 min^{-1} and map showing the residence time (t_{res}) per pixel, over $\Delta = 60s$ s, for molecules starting from the single vortex pair highlighted in the doted square. All maps are translating with a velocity U_{TV} so the molecular paths are shown in the reference frame of the translating vortices. The residence times are plotted on a log10 scale.

This map shows the importance of drag in this system where the vortices travel faster than the average axial velocity ($V_d > 1$). The drag is mainly situated on the outer cylinder side. The molecules leave the vortex pair attracted by the negative velocities along z in the following vortex pair. As soon as they enter the following vortex pair, these molecules follow the path in the high circulation outer vortex zone. Some of them are transported by the secondary flow

169

in the middle of the vortex pair and start wrapping around the vortices. Notice that due to the fact that the high circulation path brings the molecules in the middle of the vortex pair, the lower vortex tends to by populated before the upper one. This is probably the cause of the heterogeneous distribution observed in the simulated propagators (Figure 5.4).

Heterogeneous distribution can also be noticed in the by-pass flow identified at the top of the image. Long time-scale propagators showed that by-pass molecular paths represent a very small percentage of molecules. As for drag, the by-pass molecules are leaving from the outer cylinder side and wrap around the outer region of the preceding vortex. Some of these molecules seem to reach the vortex core after following the high circulation path in the outer region that leads them in the inter-vortex area. Those that do not mix with the first vortex seem to wrap around the second vortex without reaching its inner core, and when arrived at the outer cylinder wall, they follow the circulation path leading to the following vortex pair. The percentage of these molecules is small, however, where a chemical system is coupled to VFR flow, this by-pass flow can play a substantial role in the propagation of chemical waves and fronts.

5.3.6 Chemical wave propagation in TVF

Figure 5.9 shows bromate-sulfite chemical fronts (in yellow), visualised with bromocressol purple pH indicator, propagating upwards and downwards through TVF at $\omega = 1$ Hz. The front shape seems similar for upwards and downwards propagating waves. The chemical wave propagates through the successive vortices until it consumes the entire Couette cell. It initially reaches the outer part of the vortices and the inter-vortex areas.
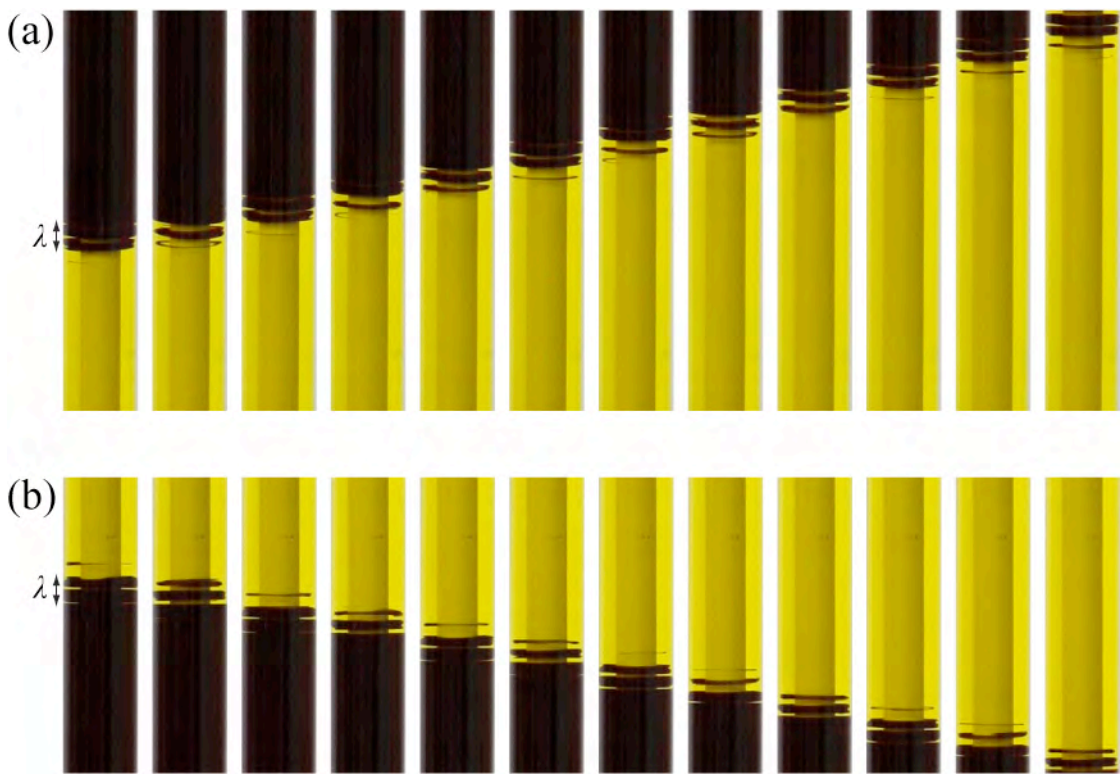
Figure 5.9 Upwards (a) and downwards (b) propagating wave front in TVF at ω = 1 Hz. Each picture was taken at 5 s intervals.

As the yellow front spreads through the outer vortex region, the vortex core can be distinguished as a region in purple in these images. The chemical front propagation in the outer regions has an advance of 2-3 vortices compared to its propagation in the core regions. This is a clear indication of the existence of high-circulation paths in the vortex outer zones. These results are in agreement with previous studies of chemical front propagation through TVF vortices[5,16,17], probing the high-circulation outer zone. The molecular path simulations for TVF (Figure 5.6) also reproduced these zones. In the simulations, molecular displacements in the outer vortex regions were found to have 3-4 vortices of advance. A more detailed comparison, between the simulations and the experiments could allow identifying the relative inputs of reaction and transport in the propagation of this wave.

5.3.7 Chemical wave propagation in VFR flow

Although chemical reactions are often used to characterise transport properties of the travelling vortices produced in a VFR[18], no published studies of autocatalytic front propagation in this system has been identified in the literature. Figure 5.10 shows chemical waves propagating through translating vortices in a VFR (Q = 7.2 cm^3 min^{-1}, ω = 1 Hz) visualised wit bromocressol purple (yellow) and methyl red (red). The chemical waves, initiated at the inlet of the reactor, propagate in the same direction as the travelling vortices until reaching the outlet of the reactor. As fresh reactants keep on entering the reactor, after the wave passes, the solution switches back to its steady state. That means that each wave can be characterised both by its front and backside.

In Figure 5.10a bromocressol purple is used to visualise the chemical front. The yellow front is not uniform and the inter-vortex regions are maintained in the purple state much longer than the vortex core. This reveals the two mixing regions (inner and outer) identified for TVF. At this regime the vortices travel faster than the axial flow (V_d > 1). Molecular simulations showed the presence of important drag at this regime, which means that matter is left behind the travelling vortex pairs. This drag seems to be mostly concentrated in the inter-vortex areas where the purple colour is located. In fact, as the front is yellow and the drag purple the latter is easier to characterise with this chemical system.

In Figure 5.10b methyl red is used to visualise the front. Methyl red gave a better contrast for the front (red front in orange background). Aso, the transition from the reactants to the products seems less sharp than for the bromocressol purple, allowing different information on

mixing to be gained. These images reveal a heterogeneous distribution of the waves into successive vortices. One vortex of each pair "switches" to red before the other, showing that non-uniform mixing occurs in the axial direction. The vortices in the red state seem smaller, probably because the inter-vortex area is in orange state. Note that simulated VFR propagators showed a similar distribution of molecular displacements into successive vortices (Figure 5.4).
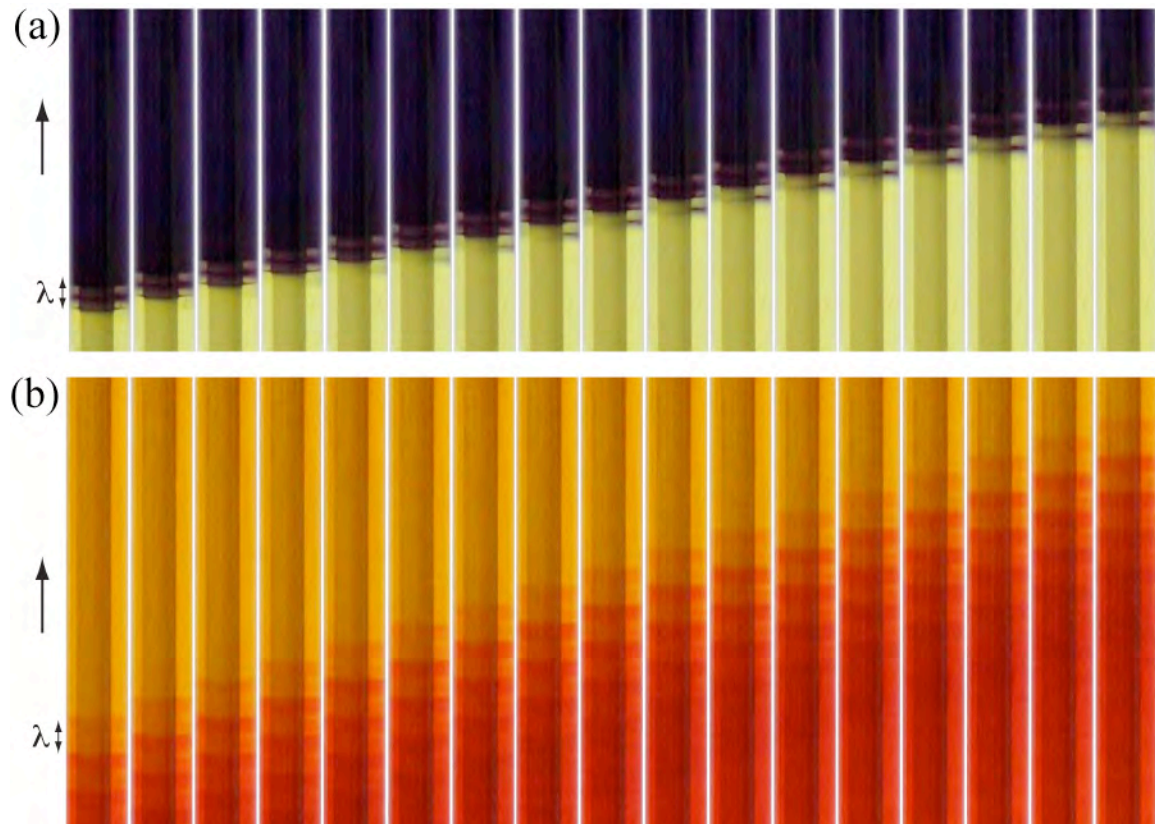
Figure 5.10. Downstream front of (a) bromocressol purple and (b) methyl red waves in VFR flow at $\omega = 1$ Hz and $Q = 7.2$ cm^3 min^{-1}. Each picture was taken at 5 s intervals. The arrow indicates the flow direction.

Figure 5.11 shows the upstream part of this propagating wave. Bromocressol purple is now more adapted to visualise by-pass effects (Figure 5.11a). The drag of the propagating wave appears in yellow. The sharper transition of the bromocressol purple system makes that less heterogeneous distribution can be seen and only a single vortex pair seems detached from the others in the downstream direction (in purple). Progressively, the detached vortex pair is mixed with the wave (in yellow) and faints before a new vortex in the purple state gets detached. These successive detachments reflect the heterogeneous distribution of by-pass flow molecules suggested by the molecular path simulations (top of *Figure 5.8*).
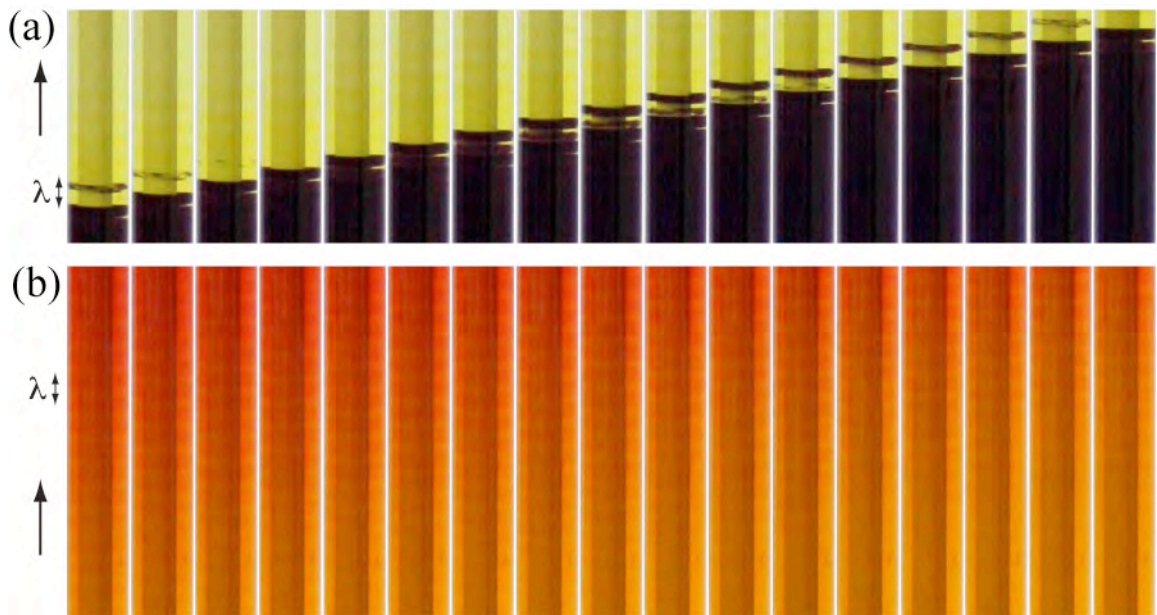
Figure 5.11. Upstream front of (a) bromocressol purple and (b) methyl red waves in VFR flow at ω = 1 Hz and Q = 7.2 cm³ min⁻¹.The arrow indicates the flow direction.

For the methyl red system (Figure 5.11b) the transition from the product wave (red) to the steady reagent state (orange) covers several pairs of vortices where heterogeneous distribution can be noticed as alternating darker and lighter colour vortices. Again, this heterogeneous

distribution of molecules seems to be explained by the molecular path simulations, where drag is found to affect differently one over two vortices of each pair (bottom of Figure 5.8). This suggests that comparison with propagator simulations over similar observation times can allow a quantification of this heterogeneous distribution in the axial direction.

5.4 Conclusions

Taking the examples of pipe flow, TVF and VFR flow in a Couette cell, the study presented in this chapter demonstrates that the combination between magnetic resonance techniques (MR flow imaging - propagator measurements) and molecular displacement simulations is able to uniquely characterise mixing properties in complex laminar flows[10]. Comparison with experiments of autocatalytic wave propagation showed that molecular pathway simulations can also provide with a way to analyse the coupling between reaction and transport in complex flows.

For small observation times these simulations produced propagators in good agreement with experimental ones. Increasing the simulation observation time allowed obtaining information on molecular transport over longer time scales. The simulated propagators provided with quantitative information regarding molecular dispersion, mixing and residence times.

Simulated molecular path maps provided with a deeper insight into the micro-mixing properties of the flows. They allowed understanding the features of experimental propagators, linking molecular displacement measurements with mixing properties. In the case of travelling vortex flow, the simulations enabled a quantitative analysis of drag and by-pass

effects, showing how these can co-exist with the plug-like flow properties of the system. These results can be of particular interest in chemical engineering applications for analysing the mixing properties of chemical reactors.

Molecular displacement simulations reproduced the main features of autocatalytic bromate-sulfite waves propagating through vortical flow. Simulated VFR propagators provided insight into the surprising phenomenon of segmented chemical fronts by showing that heterogeneous molecular distribution within successive vortices is occurring. Also, statistically insignificant molecular displacements, that may not compromise the plug-like flow properties of the reactor, were shown to play crucial role in the chemical wave propagation and shape. Comparison between simulations and systems where autocatalytic chemistry is coupled with vortical flow could allow a quantitative analysis of how flow and chemistry affect the propagation of chemical waves.

(1)   Howes, T.; Rudman, M. *AIChE J.* **1998**, *44*, 255.

(2)   Carbonell, R. G.; Whitaker, S. *Chem. Eng. Sci.* **1983**, *38*, 1795.

(3)   Ashwin, P.; King, G. P. *J. Fluid Mech.* **1997**, *338*, 341.

(4)   Edwards, B. F. *Phys. Rev. Lett.* **2002**, *89*.

(5)   Thompson, B. W.; Novak, J.; Wilson, M. C. T.; Britton, M. M.; Taylor, A. F. *Phys. Rev. E* **2010**, *81*.

(6)   Britton, M. M.; Graham, R. G.; Packer, K. J. *J. Magn. Res.* **2004**, *169*, 203.

(7)   Rudman, M. *AIChE J.* **1998**, *44*, 1015.

(8)   Waggoner, R. A.; Fukushima, E. *Magn. Reson. Imaging* **1996**, *14*, 1085.

(9)   Kutsovsky, Y. E.; Scriven, L. E.; Davis, H. T.; Hammer, B. E. *Phys. Fluids* **1996**, *8*, 863.

(10)   Vallatos, A.; Wilson, M. C. T.; Taylor, A. F.; Britton, M. M. *Europhys. Lett.* **2012**.

(11)   Edblom, E. C.; Luo, Y.; Orban, M.; Kustin, K.; Epstein, I. R. *J. Phys. Chem.* **1989**, *93*, 2722.

(12)   Keresztessy, A.; Nagy, I. P.; Bazsa, G.; Pojman, J. A. *J. Phys. Chem.* **1995**, *99*, 5379.

(13)   Azer, K. *Int. J. Heat Mass Tran.* **2005**, *48*, 2735.

(14)   Frankel, I.; Brenner, H. *J. Fluid Mech.* **1989**, *204*, 97.

(15)   Moore, C. M. V.; Cooney, C. L. *AIChE J.* **1995**, *41*, 723.

(16)   Pocheau, A.; Harambat, F. *Phys. Rev. E* **2006**, *73*.

(17)   Pocheau, A.; Harambat, F. *Phys. Rev. E* **2008**, *77*.

(18)   Cohen, S.; Marom, D. M. *Chem. Eng. J. and Biochem. Eng.* **1983**, *27*, 87.

6 Chemical patterns in translating vortices: intra- and inter-vortex mixing effects

6.1 Introduction

In the previous chapter, autocatalytic fronts were shown to be very sensitive to transport (advection and mixing). Such Reaction – Diffusion – Advection (RDA) systems, which combine autocatalytic chemical reactions with flow and diffusion, can be used to explain mechanisms of pattern formation that are important in numerous engineering, chemical and biological environments[1,2]. In particular, the interplay between long-range axial dispersion and micro-mixing has an important role in defining the nature and stability of spatial self-organisation in combustion[3,4], plankton blooming[5,6] and biological morphogenesis[7,8].

Chemical patterns with well-defined spatial wavelength rouse a particular interest[9], both due to their similarities with biological processes and because they are more accessible to experimental studies. One simple mechanism for such spatial patterns arises from considering the constant plug-flow velocity advection of an oscillating chemical reaction[10,11]. If the phase of the oscillation is set at the boundary, then the temporal oscillation is simply spatially distributed onto the flow axis resulting in flow-distributed oscillations (FDOs). Most experimental works on FDO formation has typically exploited the oscillating, ferroin-catalyzed Belousov-Zhabotinsky reaction in the plug-like flow formed in packed bed reactors [12–14] (PBRs). In these experiments, a Continuous Stirred Tank Reactor (CSTR) is placed at the inlet of the PBR in order to achieve a constant boundary condition. A critical flow velocity is

required for the observation of FDOs, where at lower velocities patterns tend to become unstable resulting in absolute instabilities (AI) where chemical waves travel across the reactor.

Studying FDOs in PBRs presents limitations, as PBRs offer poor reproducibility of conditions and smaller scale mixing properties are very dependent on the experimental setup. Other methods for creating plug-flow have been investigated, such as using agar gel[15], and found to also produce FDOs. Most of FDO studies mainly focus on the effect of flow rate on the wavelength distance between FDO bands (λ_{FDO}) and only a few systematic studies of chemistry-flow coupling have been made in these systems. Better understanding of this coupling has been provided by magnetic resonance imaging (MRI)[16], which is able to visualise the stationary chemical waves and determine flow properties.

Recently, there has been interest in the interaction between vortical flow and BZ chemical waves[17–19]. As shown in the previous chapter, vortex flow, such as that obtained in vortical flow, provides a controlled environment for studying the effects of flow and dispersion on chemical wave propagation, where the transport properties can be characterised using simple models[20]. Also, previous work has shown that the plug-flow properties of travelling vortices enable FDO formation[15].

This chapter presents a study on chemical patterns in travelling vortices produced in a Couette cell. The ability of the VFR to produce FDOs and the effect of complex flow properties identified in the Chapter 5 are examined. In particular, the study focuses on the influence of inter- and intra-vortex mixing on the formation and stability of the macroscopic chemical

patterns. The ferroin-catalysed BZ reaction is used, to enable comparison with previous FDO studies. The effect of inner rotation rate and flow rate on the structure, stability and wavelength of patterns produced are investigated for two VFR systems presenting different mixing properties.

Initially, FDO studies are performed on the VFR studied in Chapters 3-5, at similar flow and rotation rates. As seen in chapter 4, this VFR presents high inter-vortex mixing and reduced plug-flow properties, as the vortex pairs were travelling faster than the average axial velocity ($V_d \sim 1.3$). To investigate the effect of inter-vortex mixing on the patterns, further studies are performed on a VFR that is shown to have $V_d \sim 1$ at the studied rotation rate range. This second reactor is therefore exhibiting lower inter-vortex mixing, resulting in better plug-flow properties. The effects of rotation and flow rate on the pattern formation are analysed both on the experimental space-time plots of the chemical pattern formation and on close-up pictures of vortices. Throughout this section, the high inter-vortex mixing reactor is called VFR_H while the low inter-vortex mixing one is called VFR_L.

In order to relate the pattern formation with the flow mixing properties, simulation results are compared with experimental results. An Oregonator-type model consisting of two-zone reaction cells connected in series is used to analyse the role of intra- and inter-vortex mixing on the pattern formation. These results show that inter-vortex and intra-vortex mixing in the VFR can be characterised by FDO properties as wavelength, stability and band structure. Conclusions are drawn on the relationship between experimental parameters (rotation and flow rate) and flow properties (intra- and inter-vortex mixing).

6.2 Experimental

6.2.1 The ferroin-catalysed BZ reaction

The ferroin-catalyzed BZ reaction was prepared immediately before each experiment using reactants dissolved in deionized water. Solution A contained malonic acid (MA) and sodium bromate. Solution B contained sulfuric acid and the ferroin catalyst. Initial concentrations in solution A were: $[MA] = 0.52$ M (Alfa Aesar, 99 %), $[BrO_3^-] = 0.4$ M (Alfa Aesar, 99.5 %). Initial concentrations in solution B were: $[H_2SO_4] = 0.26$ M (Fisher, 98 %) and $[ferroin] = 9.35 \times 10^{-4}$ M. The ferroin catalyst was prepared using a 3:1 ratio of 1,10-phenanthroline (Sigma, 99 %) to iron (II) sulphate heptahydrate (Acros Organics, 99 %) in deionized water. Solutions A and B were degassed prior to experimentation.

6.2.2 Pt-electrode measurements of BZ temporal oscillations

Temporal oscillations were monitored in a well-stirred batch reactor using a Pt-combination redox electrode connected to a Picoscope Oscilloscope (Picotech). The reaction temperature was maintained at 22 °C ± 0.5 °C by a water jacket, which was controlled by a water bath. The experimental set-up is shown in Figure 6.1.
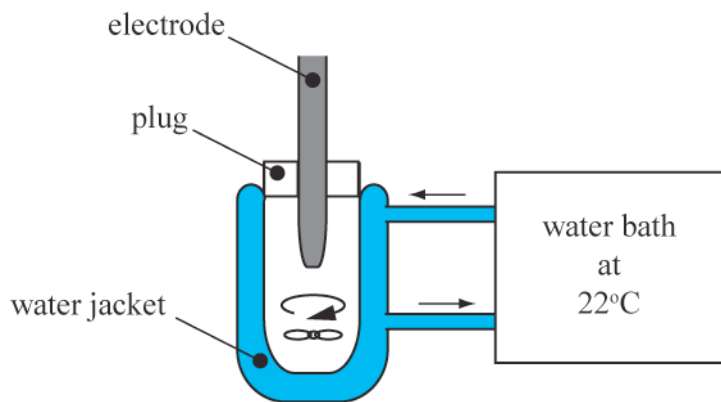
Figure 6.1. Set-up for Pt-electrode measurements.

6.2.3 Experimental set-up for chemical patterns in a VFR

Two VFR reactors were used for these experiments. For both reactors, the Couette cell was constructed from an outer glass tube of radius R_o = 8.25 mm. For VFR$_H$, a PEEK inner cylinder of radius R_i = 4.1 mm was used, resulting in a gap, d, of 4.15 mm. For VFR$_L$, a glass inner cylinder of radius R_i = 3.5 mm was used, resulting in a gap of 4.75 mm. The length of the gap, L, was of 896 mm for both VFRs. The length to gap ratio, Γ, was of 216 for VFR$_H$ and 189 for VFR$_L$. The radius ratio, η, was of 0.5 for VFR$_H$ and 0.42 for VFR$_L$. Further details on the VFR set-up have been given previously (cf. 4.2.1). Figure 6.2 shows the experimental set-up used for producing flow distributed chemical patterns in a VFR. Solutions A and B were pumped into a continuously stirred tank reactor (CSTR) of volume 3 cm^3 using a peristaltic pump (Ismatec, Glattbrugg, Switzerland). From the CSTR, the mixture was passed, via capillary tube (1.3 mm inner diameter and 30 cm long) into the reaction tube. The residence time in both the capillary tube and the CSTR was less than 30 s. The experiments were performed at a room temperature of 22 ± 0.5 ˚C.
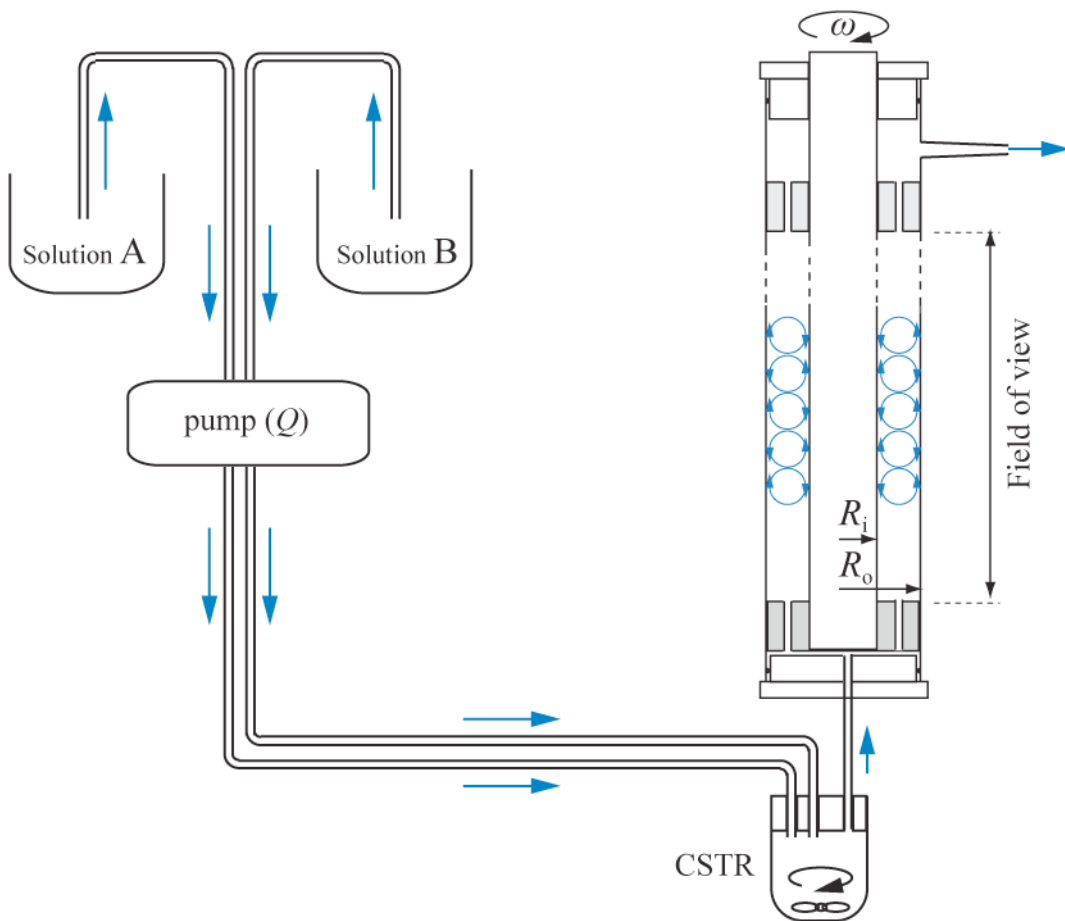
Figure 6.2. Experimental setup for the observation of BZ patterns in a VFR.

6.2.4 Optical measurements of chemical patterns

Chemical patterns were recorded using a digital camera (Cannon DS1000). Photographs were acquired at an interval of 10 s. Adobe Photoshop was used to enhance contrast and colour intensities, before passing the images to grey scale. A region, 6-pixels wide, along the length of the reactor, was selected from the centre of the Couette cell annulus and averaged into a single profile using Matlab. Compiling these profiles as a function of time produced the space-time plots. In these plots, the dark regions correspond to the reduced state (high [ferroin] - red) and bright regions to the oxidised state (high [ferriin] - blue).

6.2.5 Parameter ranges

The viscosity of the solution, ν, was of 1.04 mm^2 s^{-1} at 22 ± 0.5 ˚C, measured using a calibrated Ubbelohde viscometer. Four evenly spaced rotation rate values, ω, were used, from 1 Hz to 2.5 Hz. The *Ta* values varied from 17 to 43 for VFR$_H$ and between 16 and 41 for VFR$_L$. The flow rate varied between 4 cm^3 min^{-1} and 13.6 cm^3 min^{-1} for VFR$_H$ and between 11.6 cm^3 min^{-1} and 13.6 cm^3 min^{-1} for VFR$_L$. The *Re* values varied from 1.7 to 5.3 for VFR$_H$ and from 5.2 to 6.2 for VFR$_L$. $\gamma_{Re} = U_{ax} / R_i \omega$ varied from 0.03 to 0.29 for VFR$_H$ and from 0.13 to 0.39 for VFR$_L$. Each experiment was repeated a minimum of three times.

For VFR$_L$, the translational velocity of the vortices, U_{TV}, was measured using a dye-visualisation method. A sulphuric acid solution ([H$_2$SO$_4$] = 0.13 M) having the same viscosity as the ferroin-catalyzed BZ reaction was pumped into the reactor. Using the same viscosity as the ferroin-catalysed BZ reaction enabled obtaining similar flow properties. Visualisation of the vortices was achieved by injecting 0.5 ml of 25 mM ferroin solution at the inlet of the pump. U_{TV} was obtained by measuring the time taken by the vortices to travel a given distance. U_{ax} was measured during the filling of the reactor.

6.2.6 Modelling chemical pattern formation in travelling vortices

A model has been developed[21] in collaboration with the group of Annette Taylor (School of Chemistry, University of Leeds), to simulate the formation of chemical patterns in translating vortex flow in a system where V_d ~1. The BZ reaction was modelled using a 2-variable Oregonator model[18,22]. This model retains the dominant reactions of the FKN reaction mechanism (cf. 1.3.2) and their rate constants k_n. The model reactions can be expressed by a

set of differential equations describing the kinetic behaviour of the main reactants. Under certain conditions, this model can be reduced to a two-variable one, with $u = 2k_4U / k_5A$ and $v = k_ck_4BV(k_5A)^2$; where $U = $ [HBrO$_2$] (autocatalyst), $V = $ [Fe(III)] (oxidised form of the ferroin catalyst), B = [MA], A = [BrO$_3^-$] and k_n are rate constants. Combining the BZ reaction model with a model for the VFR flow allows analysing the spatial behaviour of the pattern forming system.

Simulations of molecular pathways in vortical flow (cf. Chapter 5) suggested that a two-zone model, distinguishing the outer from the core zone of each vortex, could describe the main features of VFR flow. Desmet *et al.*[20] and Giordano *et al.*[23] have shown that the vortices can be considered as reaction cells split into two zones, with an external zone E and a core zone C. In this work, a similar model was used to model the VFR flow (Figure 6.3a). The external zone E of the *i* cell undergoes mass transfer with $i - 1$ and $i + 1$ cells (k_o, inter-vortex exchange /axial dispersion) and mass transfer with the core zone C (k_e, intra-vortex exchange). To approximate the vortex translation leading to axial plug-flow at constant velocity $U_{TV} = U_{ax}$ ($V_d=1$), both zones of the *i* cell are connected in series to the $i - 1$ cell. The scaled time for these simulations is given by $\tau = k_cBt$, where k_cB is the chemical relaxation time.

The chemical parameters used lead to a dimensionless oscillatory period of $\tau = 9$ for the BZ reaction. The simulated temporal oscillations of the ferroin catalyst, *V*, can be seen in Figure 6.3b. The vortex cells were made of 3×3 pixels with the centre pixel representing the core zone C. Simulated space-time plots were constructed from 50 stacked cells at time intervals of $\tau = 1$.
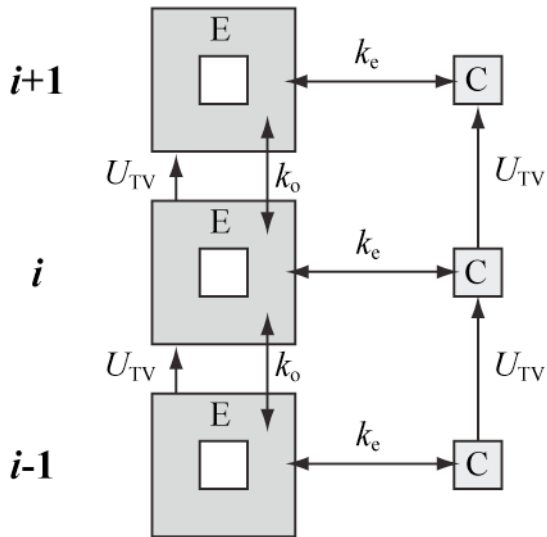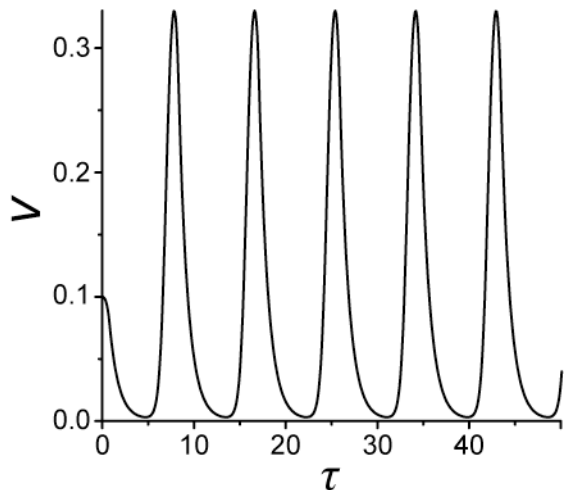
Figure 6.3. (a) Sketch of two-zone reaction cells (E = outer zone and C = core zone) and processes used in the model. (b) Model of temporal oscillations in a cell in the absence of flow/dispersion.

Development of this model required the introduction of additional dimensionless numbers that characterised the chemistry and transport properties of the system. The Dakömhler number, relating the BZ reaction timescale with the characteristic flow time, is given by $Da = k_c B d / U_{TV}$, where d is the annular gap width (m) and U_{TV} is the velocity of the translating cells (m s^{-1}). The scaled axial flow rate is given by $1 / Da = U_{TV} / (k_c B d)$. The Péclet number, relating the rate of advection to the rate of dispersion, is given by $Pe = U_{TV} d / k_o$, where k_o is the inter-vortex exchange coefficient (m^2 s^{-1}). The inter-vortex exchange rate is given by $1 / (PeDa) = k_o / (k_c B d^2)$. The scaled intra-vortex exchange rate $K_e = k_e / k_c B$ where k_e is the intra-vortex exchange rate (s^{-1}). By introducing these parameters, the model allows to investigate the effects of intra- and inter-vortex exchanges on the resulting patterns.

6.3 Results and discussion

6.3.1 Temporal oscillations in the BZ reaction

Figure 6.4 shows a plot of temporal oscillations in the ferroin-catalysed BZ reaction in a batch reactor, observed over time. The periodic increase in potential indicates a switch of the catalyst from red (Fe^{2+}) to blue (Fe^{3+}). For all experiments, the first five oscillations had an average period of 185 ± 3 s at 22 ± 0.5 ˚C. By introducing the BZ reaction into the travelling vortex flow of a VFR, these temporal oscillations are spatially distributed along the length of the reactor, giving rise to chemical patterns.
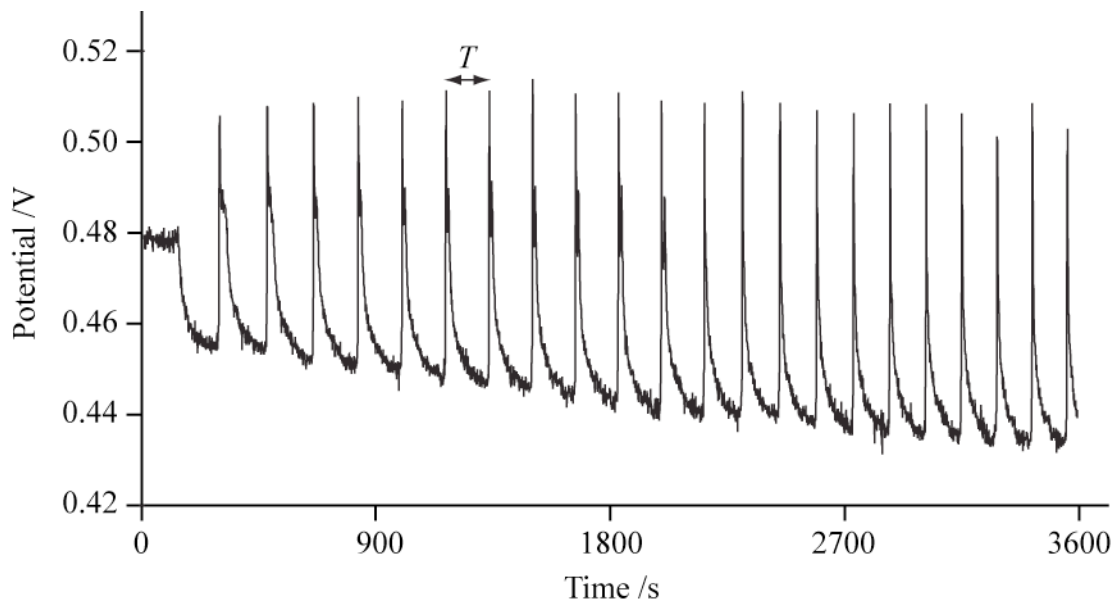
Figure 6.4. Temporal oscillations of the redox potential in the BZ reaction.

6.3.2 Chemical patterns in a high inter-vortex exchange system

The BZ reactants were pumped into VFR_H ($V_d \sim 1.3$) and images of chemical patterns were acquired. The plug-like properties of the translating vortices distributed the chemical oscillations along the length of the reactor leading to the formation of flow-distributed oscillation (FDO) bands. Figure 6.5 shows a schematic diagram of a series of translating vortices (a) in comparison with close-up pictures of a single FDO band appearing in blue (b).
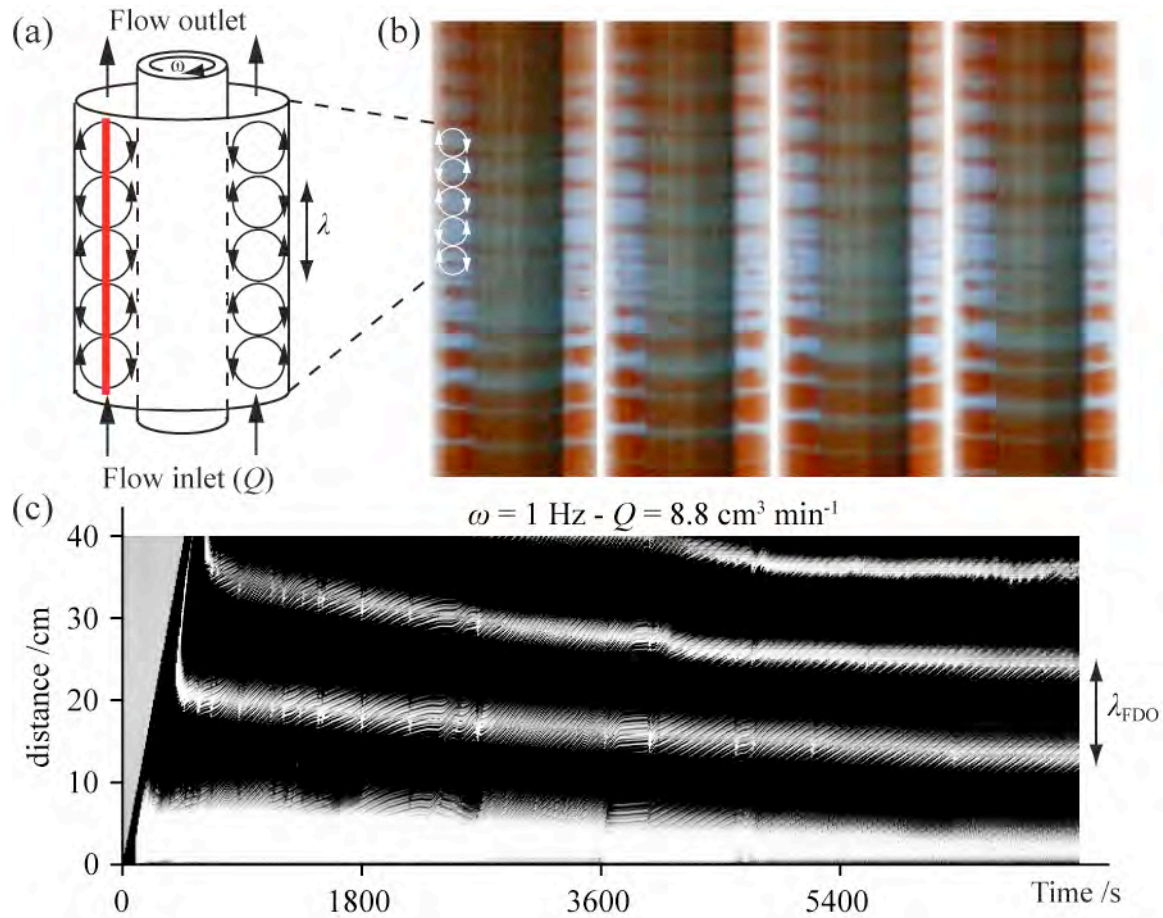
Figure 6.5. (a) Schematic diagram of the VFR with translating vortices. The thick red line represents a pixel slice selection for the creation of space-time plots. (b) close-up on the complete width of the VFR for the first FDO band of the space-time plot between 900 s and 940 s and (c) complete space-time plot of FDO patterns for $Q = 8.8 \ cm^3 \ min^{-1}$ and $\omega = 1Hz$.

Plotting the evolution of an averaged profile taken along the entire length of the reactor (Figure 6.5a) allows observing the long-time behaviour of the system in a space-time plot (Figure 6.5c). The blue bands, corresponding to high ferriin concentration regions, appear in white on this plot.

The bands are formed via wave-splitting mechanism, where a part of the wave leaves the reactor while the other settles at stationary position[13]. The average distance between the centres of successive bands corresponds to wavelength of the FDO bands, λ_{FDO}. The segmentation of the bands observed in the close-up pictures is also reflected in the space-time plot, where stripes can be seen within each band. This segmentation is mainly due to phase inhomogeneities between the core of the vortices and the high circulation outer-zones. Information on the transport properties within VFR_H can help understanding the resulting chemical patterns. Hence, the chemical pattern formation in this system was studied at the same flow and rotation rates as for the previous sections, so as to compare with previously obtained results on the flow properties of VFR_H (Chapters 4 and 5).

Figure 6.6 shows three space-time plots of chemical pattern formation at $Q = 7.2 \text{ cm}^3 \text{ min}^{-1}$ and $\omega = 1$ Hz. At this regime, the system was unstable and repetitions gave a range of outcomes. Figure 6.6a shows stationary FDOs maintained over 2 hours. In Figure 6.6b FDOs are initially formed but the bands fail to settle at their steady position and the system switches to travelling waves (TW). In Figure 6.6c the reverse phenomenon is observed, where travelling waves are produced initially before the system reaches equilibrium, with successive bands settling at a fixed position. For each repetition, when stationary bands are formed, λ_{FDO} was found to be constant ($\lambda_{FDO} \sim 8$ cm).
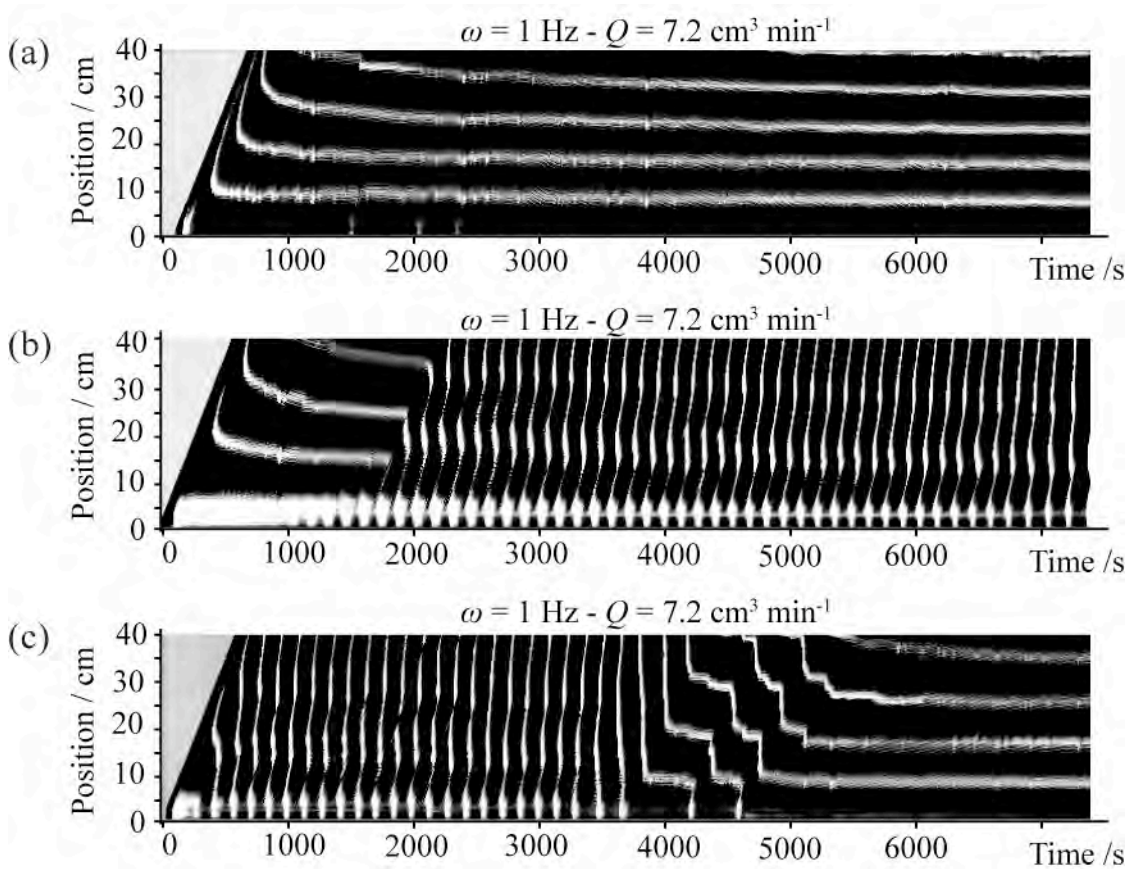
Figure 6.6. Space-time plots at $Q = 7.2 \text{ cm}^3 \text{ min}^{-1}$ and $\omega = 1 \text{ Hz}$

The presence of travelling waves in this system could be related to several factors[10] as boundary conditions, critical flow rate or poor plug-flow properties. Changes in BZ phase at the inlet of the reactor (0 cm) indicate an unstable boundary condition (Figure 6.6). This could explain the observation of TW, as a stationary boundary is an important requirement for the production of stationary FDOs. Oscillating boundary conditions were previously shown to produce TW[24]. Note that stationary waves in this system coincide with a stationary boundary condition at the reactor inlet, while travelling waves are preceded by an oscillating boundary. On the other hand, TW could also be caused by the poor plug-flow properties for this regime of the VFR_H, presented in the previous chapter. Finally, observation of TW can be related to

the flow rate. Kinematic models show that unstable bands can be generated bellow a critical flow rate value where the flow velocity is not high enough to resolve spatially the BZ temporal oscillation[12].

The complexity of the system and the low reproducibility of the experiments make it impossible, at this stage, to draw conclusions so as to the conditions that generate travelling waves. Studying the effect of the main flow parameters (flow, rotation and boundary) on the resulting patterns could provide with a better understanding of the mechanisms involved in the pattern formation and with answers concerning the nature of the observed bands.

6.3.2.1 Flow rate effect on the pattern formation

Space-time plots for different flow rates at $\omega = 1$ Hz (Figure 6.7) provide with some insight into the effect of flow rate on the pattern formation. At $Q = 4$ cm^3 min^{-1} (Figure 6.7a) the chemical patterns remain unstable with no stationary bands observed. At $Q = 8.8$ cm^3 min^{-1} (Figure 6.7b) no travelling waves were observed over this experimental time and the boundary was maintained at a fixed phase. However, after 2 hours, the position of the bands is still decreasing, indicating that they are not settled at a stationary position. Considering the instabilities observed at $Q = 7.2$ cm^3 min^{-1} and the dynamic behaviour of the bands, no conclusions should be drawn so as to the long-term stability of these chemical patterns. At $Q = 10.4$ cm^3 min^{-1} (Figure 6.7c) the bands systematically reach their equilibrium position after approximately 500-700 s.
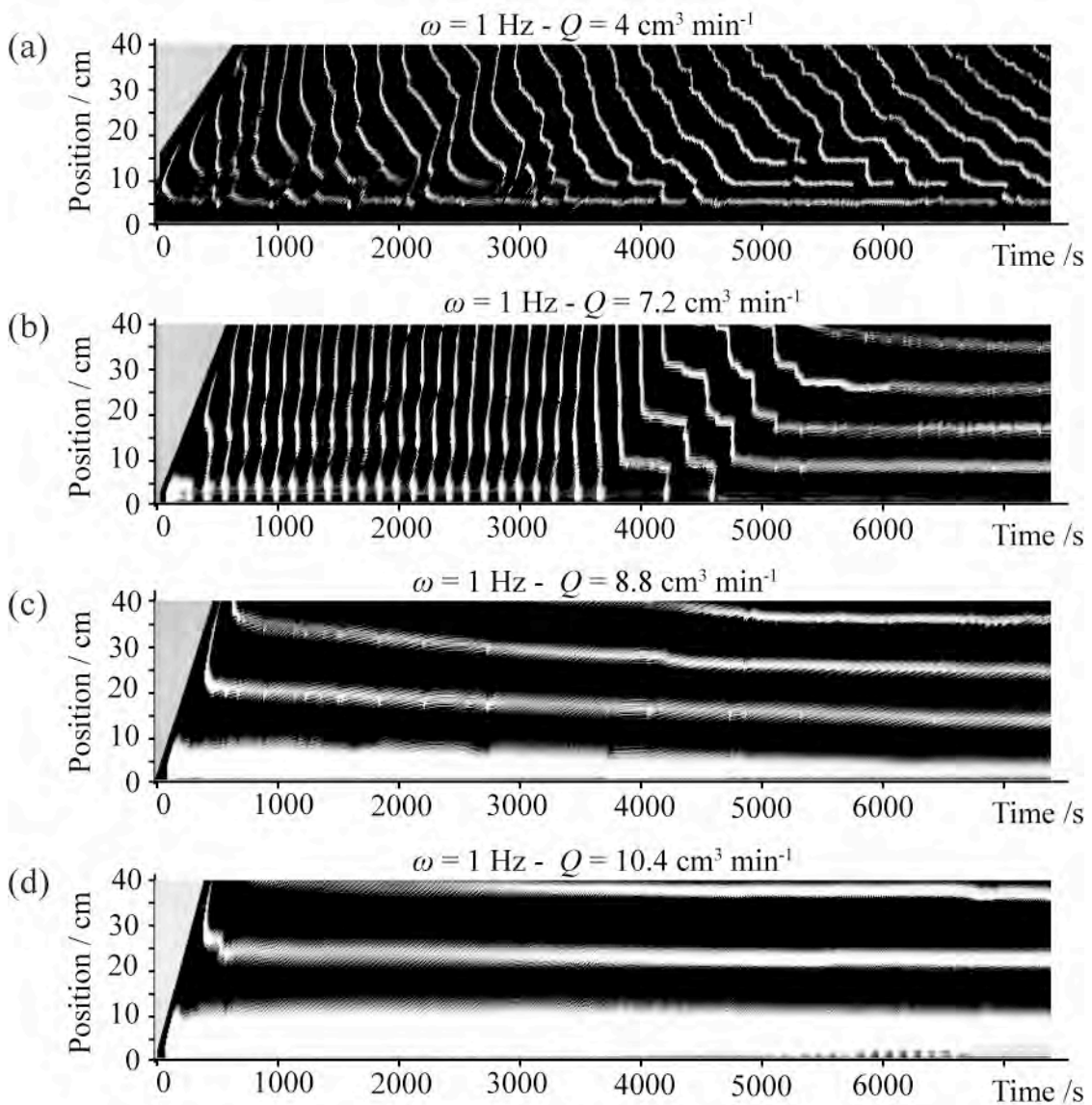
Figure 6.7. Space-time plots for ω = 1 Hz at a range of flow rates.

These results suggest that by increasing the flow rate the bands become stationary resulting in FDOs. The flow rate also has an important effect on the FDO wavelength. As with FDOs formed in a PBR[11] the distance between bands (λ_{FDO}) and the dimension of the bands is shown to increase with flow rate. Another feature of these patterns is associated with the evolution of the shape of stationary bands, producing a variety of structures at fixed Q. Figure 6.8 shows the dynamic behaviour of a band at $Q = 10.4$ cm^3 min^{-1}. At 1000 s, the band is

segmented, due to inhomogeneities between the core and the outer region of the vortices. As the experiment advances, the band is progressively becoming more continuous. At 5000s the band is uniform, with discontinuities only in the interface regions where the phase transition occurs. At this stage, CO_2 bubbles produced by the BZ reaction can be seen on the reactor walls. This bubble production could not account for the dynamic behaviour of the band as it is also a feature of lower flow rates, where different dynamic behaviour of the bands is observed.
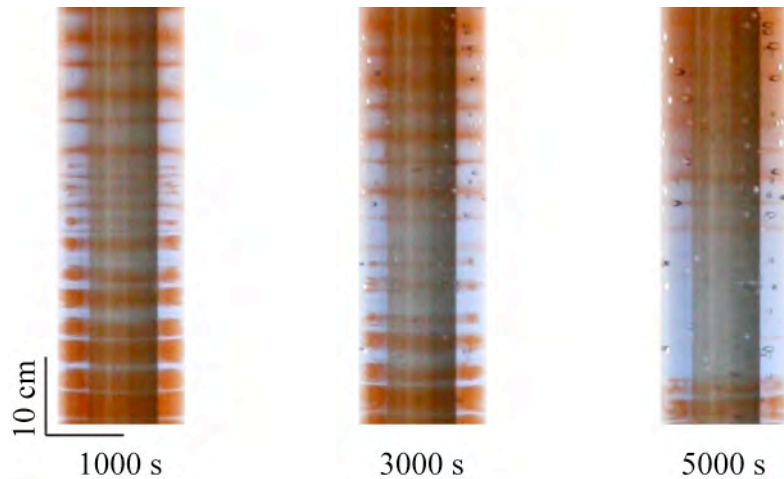
Figure 6.8. Close-up on the complete width of the VFR at different times for the first FDO band of the space-time plot for Q = 10.4 cm^3 min^{-1} and ω= 1Hz.

6.3.2.2 The role of the CSTR on the pattern formation

An investigation was performed on the role of the CSTR on the pattern formation. The use of a CSTR is a standard feature of all experimental studies on FDOs using PBRs. It ensures that a uniformly mixed solution is penetrating the reactor while maintaining a constant boundary condition. However, the CSTR introduces additional parameters to the study of FDOs making

the analysis of the resulting pattern more complicated. A VFR flow provides with constant mixing within the vortices, so the mixing of the reactants prior to the inlet of the reactor provided by the CSTR becomes redundant. This was tested in a series of experiments at low flow rates without CSTR.

At $Q = 7.2$ cm^3 min^{-1}, where travelling waves were observed in the presence of a CSTR (Figure 6.6), all repetitions without CSTR produced stationary FDOs (Figure 6.9a).
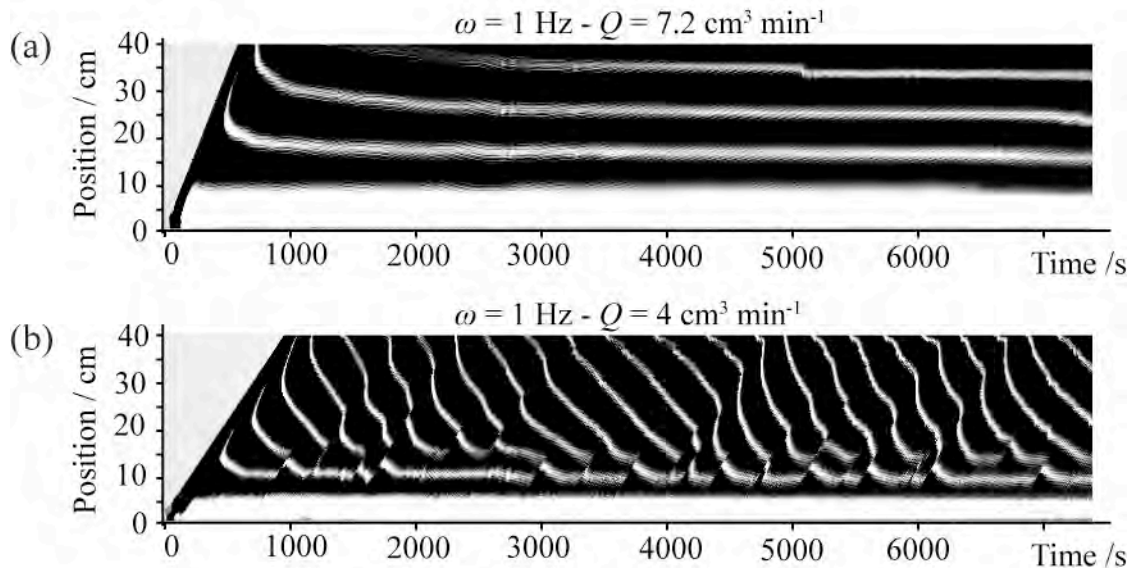
Figure 6.9. Space-time plots of a system without CSTR for $\omega = 1$ Hz at $Q = 7.2$ cm^3 min^{-1} (a) and $Q = 4$ cm^3 min^{-1}(b).

This suggests that the instabilities observed in the experiments with CSTR were caused by the CSTR oscillations. At $Q = 4$ cm^3 min^{-1}, despite the stationary boundary, no stationary bands were observed. It can be concluded that the critical flow rate for the formation of FDOs is found between 4 cm^3 min^{-1} and 7.2 cm^3 min^{-1}. These results demonstrate that the presence of

the CSTR might play a crucial role in determining the resulting patterns at low flow rates. It can introduce difficulties in the analysis of the system, where instabilities of the CSTR might be confounded with a critical flow rate regime. Note that previous experimental studies of pattern formation[13,25], used CSTRs of different dimensions, and probably different mixing properties.

6.3.2.3   Rotation rate effect on the pattern formation

The rotation rate is the new parameter in the study of chemical pattern formation that is introduced by the use of the VFR. In the previous chapters, the rotation rate was found to play an important role in determining the mixing properties of the reactor, with an increase in rotation leading to higher mixing.

Figure 6.10 shows space-time plots for increasing rotation rates.
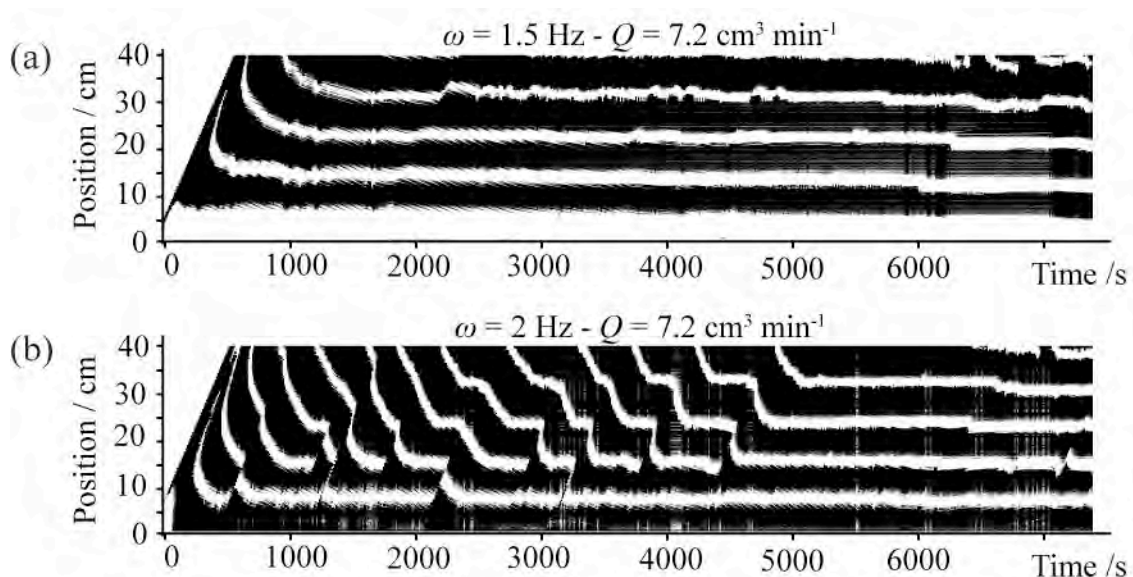
Figure 6.10 Space-time plots for Q = 7.2 cm³ min⁻¹ at ω = 1.5 Hz (a) and ω = 2 Hz (b).

At ω = 1.5 Hz, stable FDOs are formed but the bands close to the outlet are found to be thinner and more unstable. At ω = 2 Hz, FDOs seem to form via convective instability (CI-FDOs), where series of bands fail to stabilise before one of them settles at a stationary position. Note that contrary to the travelling waves observed at ω = 1 Hz (Figure 6.6b,c), these CI-FDO are reproducible and always lead to the formation of stationary bands. Also, the unstable bands in CI-FDO are generated at the top of the reactor while TW were linked with instabilities at the inlet.

Figure 6.11 shows space-time plots for experiments at Q = 13.6 cm^3 min^{-1} for different ω.
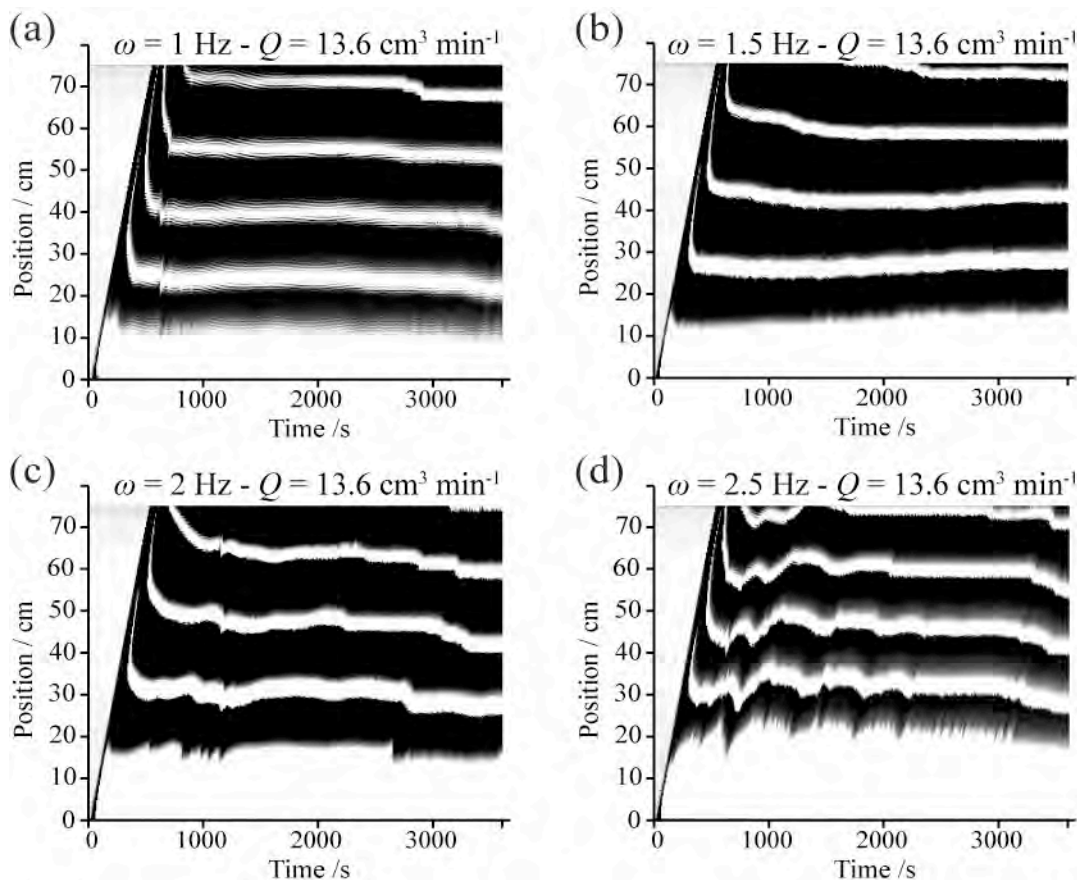
Figure 6.11 Space-time plots for Q = 13.6 cm^3 min^{-1} at a range of rotation rates.

At this flow rate, boundary conditions are stable, allowing to study the effect of rotation on stable FDOs. Stable FDO bands were obtained for this range of rotation rates. At $\omega = 1$ Hz (Figure 6.11a) the bands appear segmented while for $\omega > 1$ Hz continuous bands are observed. As the rotation rate increases the bands become unstable but no travelling waves are observed. This instability could be attributed to increasing mixing or possibly enhanced wobbling of the inner cylinder observed for $\omega > 2$ Hz.

Care is required in interpreting the space-time plots at high rotation rates due to the wobbling of the inner cylinder. Nevertheless, these results confirm that stable FDOs could be obtained in a high inter-vortex mixing VFR for a significant range of parameters. The relative roles of rotation and flow rate need to be further studied. The chemical patterns resulting from each set of parameters ω and Q were shown to be strongly dependant on the flow properties. The observation of CI-FDOs at high rotation rates shows that inter- and intra-vortex mixing effects play a crucial role in determining the features of the resulting chemical patterns. A systematic study of intra- and inter-vortex mixing effects of chemical pattern formation in a VFR was conducted using a second reactor, VFR$_\mathrm{L}$, that has better plug flow properties (V_d ~ 1) and exhibits reduced wobbling at higher rotation rates.

6.3.3 Chemical patterns in a low inter-vortex exchange system

The dye experiments were used to probe the plug-flow properties of VFR$_\mathrm{L}$. The velocity drift, $V_\mathrm{d} = U_\mathrm{TV} / U_\mathrm{ax}$, was found to vary between 1 and 1.1, suggesting low inter-vortex mixing. As for previous results (cf. 4.3.3), higher V_d values were obtained at lower rotation rates. Chemical pattern formation in this system was studied at the same range of parameters as the dye experiments. In order to study the relative effect of flow and rotation rates on the

chemical patterns, the parameter $\gamma_{Re} = U_{ax} / R_i\omega$, indicating the balance between axial and rotational flow[26], was introduced for the analysis of these results.

Figure 6.12 shows space-time plots of chemical pattern formation for different flow and rotation rates. For these experiments, γ_{Re} varied from 0.13 to 0.39. Stationary FDOs were observed in between two limiting values of γ_{Re}. At $\gamma_{Re} \geq 0.35$, all the bands were found to be unstable (Figure 6.12b,c), with complex patterns produced by travelling waves (TW) along the length of the reactor. In the case of PBR FDOs, similar instabilities were observed when a packing material providing enhance diffusive mixing was used[13]. At $\gamma_{Re} \leq 0.13$ (Figure 6.12j), bands at the outlet of the VFR failed to settle at the steady-state position and vanished. These were then replaced by bands from above, which moved down to replace them. Such patterns display convective instabilities (CI-FDOs) similar to the ones observed at high rotations in VFR_H (Figure 6.10b).
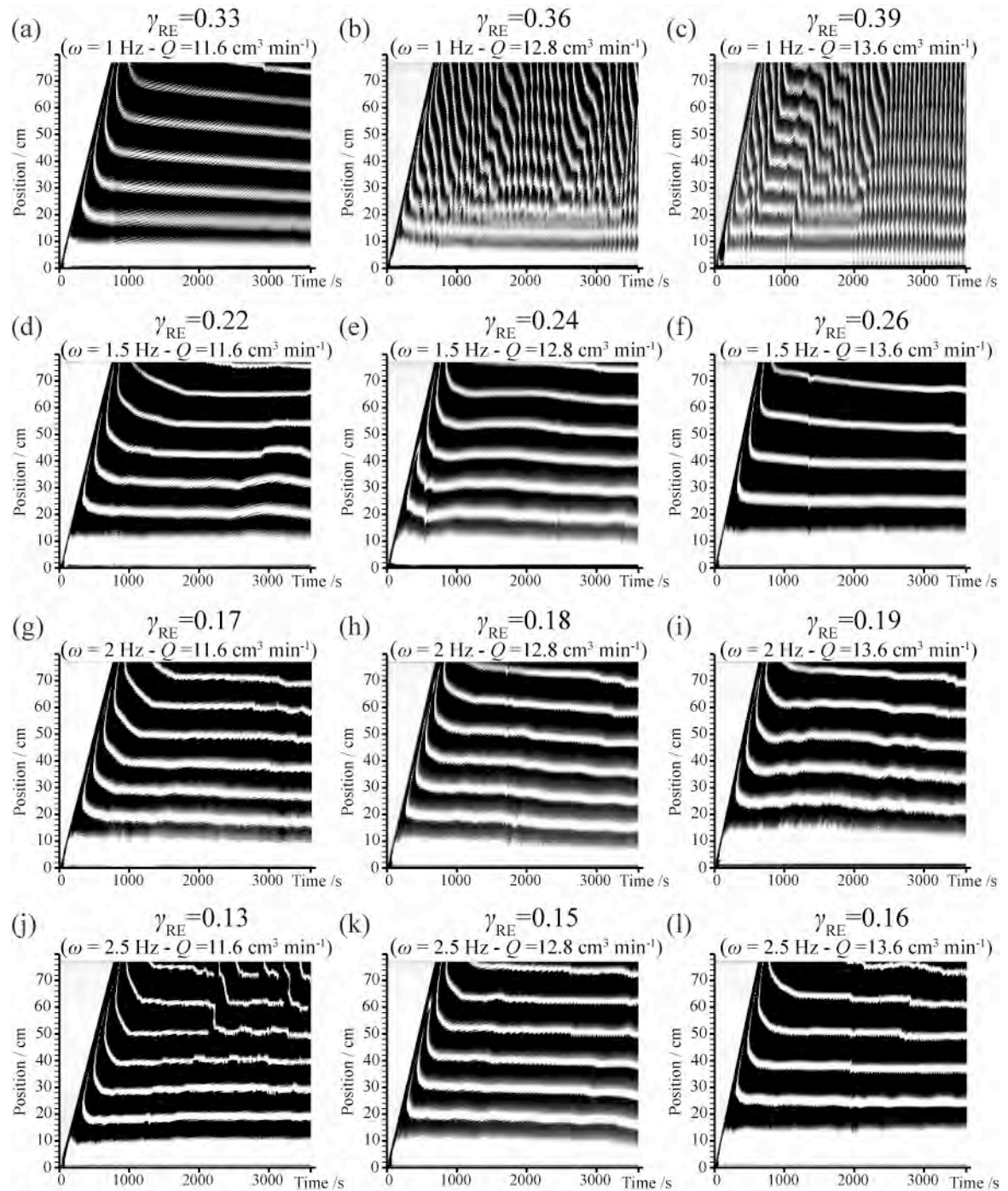
Figure 6.12. (a-l) Space-time plots at a range of flow and rotation rates.

The phase diagram in Figure 6.13 summarises the variety of patterns observed in this system, as a function of Q and ω.
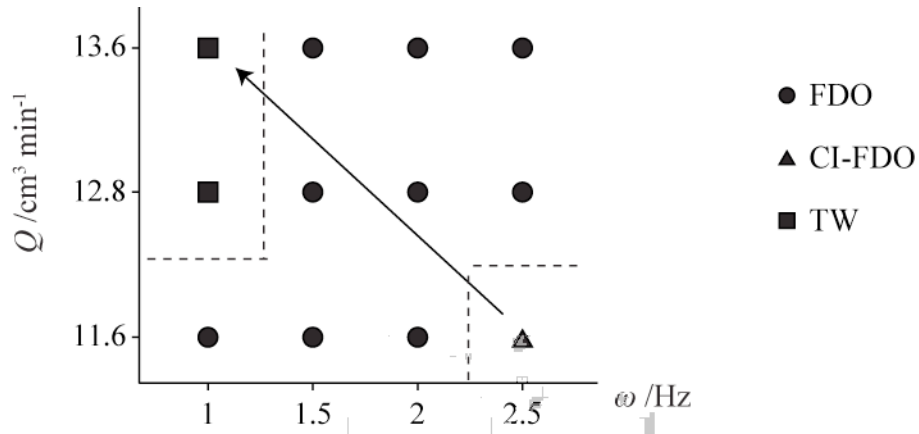
Figure 6.13. Phase diagram of patterns observed as function of flow and rotation rates. The arrow indicates the transition from lower to higher γ_{Re} values. Doted lines indicate phase transitions.

For all stable FDOs, λ_{FDO} was found to increase with flow rate (Figure 6.14) and the rotation rate only seems to have an effect on λ_{FDO} at higher flow rates. These results are similar to those observer in FDO studies in a PBR[12–14], where the distance between bands increases with the flow rate. At lower γ_{Re} the bands are found to be solid (Figure 6.12j-l), while at higher γ_{Re} they have a segmented structure, appearing as stripes within a band on the space-time plot (Figure 6.12a-c). Segmentation of the bands seems to be related to the poor mixing properties of the reactor, since it has been a common feature of the chemical patterns in the high inter-vortex mixing VFR (Figure 6.5, Figure 6.6, Figure 6.7).
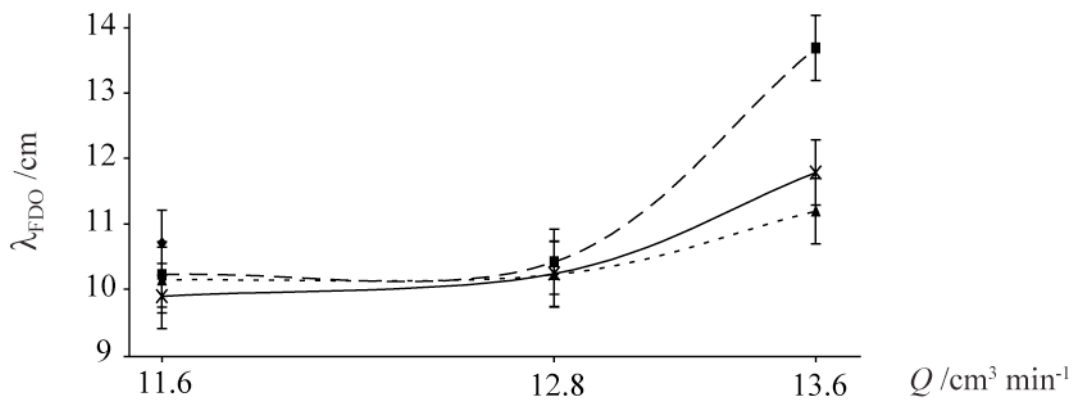
Figure 6.14. Plot of the average distance between stable FDO bands against flow rate for ω= 1.5 Hz (---), ω = 2 Hz (···) and ω = 2.5 Hz (—).

Closer inspection of the chemical bands provides insight into the structure and possible formation mechanisms. Figure 6.15 shows close-up photos of a FDO band at $Q = 11.6$ cm^3 min^{-1}, for different rotation rates.
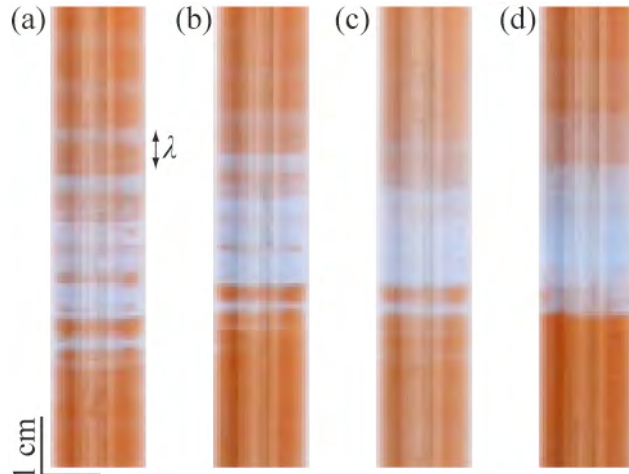
Figure 6.15. Digital photographs of the second FDO band from the inlet at $Q = 11.6$ cm^3 min$^-$
^{1} and for increasing rotation rate: ω = 1 Hz (a), ω = 1.5 Hz (b), ω = 2 Hz (c) and ω = 2.5 Hz (d). The dimension of one vortex pair, λ, is indicated in (a).

At low ω (Figure 6.15a,b), there appears to be a heterogeneous distribution of the oxidised state between neighbouring vortices, as well as between the centre region of the vortices and the outside region. This heterogeneous distribution gives rise to the segmented bands observed on the space-time plots (Figure 6.12a). At constant flow rate, an increase in rotation rate was found to lead to the progressive disappearance of the segmented bands (Figure 6.15c,d) and the formation of a homogeneous distribution of oxidised and reduced states, with narrower and more clearly defined bands.

The resulting chemical patterns are shown to depend strongly on the interplay between chemistry and inter- and intra-vortex mixing. Comparison of the experimental chemical pattern features with simulations combining the Oregonator model for the BZ reaction with a VFR flow model were performed to get a better understanding of the mechanisms underlying the coupling between oscillating reactions and vortical flow.

6.3.4 Inter- and intra-vortex mixing effects

Simulations were used to explore the effects of flow rate, inter-vortex exchange rate and intra-vortex exchange rate on the resulting patterns. In order for the model to provide some illumination regarding the experimental results it was necessary to link the parameters used in each case. The increase of the rotation rate (ω) in a VFR has been shown to increase both intra-vortex mixing (k_e) and inter-vortex mixing (k_o) through dispersion[23,27]. For relatively low rotation rates, an increase of the flow rate (Q) has also been shown to increase inter-vortex mixing[28]. Flow-induced inter-vortex mixing is linked with the formation of high circulation paths on the outer zones of successive vortices. For low intra-vortex mixing, these

paths can lead to uneven molecular distribution into successive cells[29]. The increase of the flow rate was also linked with a stabilisation of the vortical instability[28], thus the vortices form better at lower flow rates.

The effect of the scaled inter-vortex exchange rate, or axial dispersion rate, $1 / PeDa$, on the simulated chemical patterns is shown in Figure 6.16.
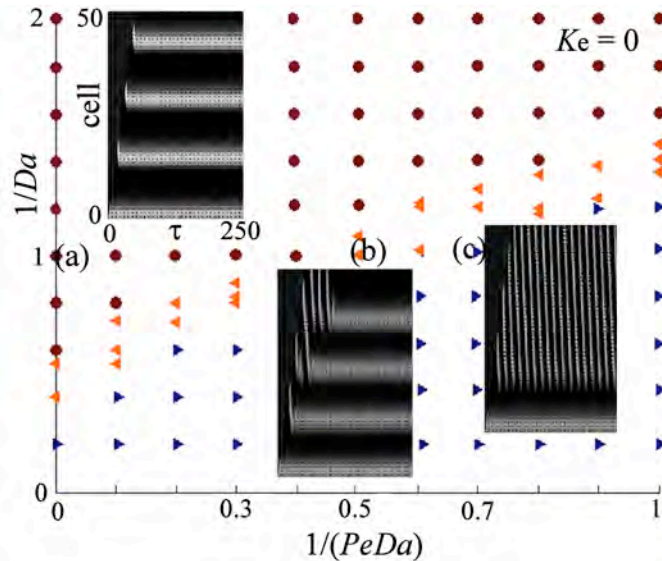
Figure 6.16. Phase diagram of chemical patterns with scaled flow rate (1 / Da) and scaled inter-vortex exchange rate (1 / PeDa) when there is no intra-vortex exchange. Red circle = FDOs, left-pointing triangle = CI-FDO and right-pointing triangle = absolute instability (AI). The space-time plots (50 cells × 250) show pattern formation when 1 / Da = 1 and 1 / PeDa = (a) 0 (FDO); (b) 0.5 (CI-FDO) and (c) 0.7 (AI). The greyscale corresponds to concentration of v with white = 0.35.

The intra-vortex exchange rate K_e was 0. For a scaled flow rate of $1 / Da = 1$ and $1 / PeDa = 0$, flow distributed oscillations (FDOs) formed (Figure 6.16a). When $1 / PeDa$ was increased,

the FDOs formed via a convective instability, where initial perturbations were amplified with the flow (Figure 6.16b). Above a critical value of 1 / *PeDa*, absolute instabilities (AI) were observed, where the spatial oscillation transformed into a temporal one (Figure 6.16c). AI appear as travelling waves along the length of the reactor.

These simulations reproduce the main features of the experimental chemical pattern observation (FDOs, CI-FDOs and TW). The simulation results suggest that the instabilities obtained experimentally at low and high γ_{Re} values are generated by enhanced inter-vortex mixing. Inter-vortex mixing at low rotation rates, where travelling waves were observed (Figure 6.12b,c), seems to be higher than inter-vortex mixing at high rotation rates, where CI-FDOs are observed (Figure 6.12j).

Simulation results at a fixed flow rate, illustrate the influence of intra-vortex exchange on the patterns (Figure 6.17). With a scaled intra-vortex exchange rate of $K_e = 0.2$, there was a phase lag between the outer zone and core zone of the vortices with the FDO band beginning in the outer region. The critical inter-vortex exchange rate for the CI-FDO and the AI was increased compared to in the absence of intra-vortex exchange. When K_e was increased to 1.2, the phase lag between the outer and core zone disappeared and narrower bands were observed. Also, the transition to CI-FDO and AI occurred at even higher values of 1 / *PeDa*. These results are in good agreement with experimental chemical pattern formation observations. The segmented bands observed at low rotation rates both for high and low inter-vortex exchange systems (Figure 6.6 and Figure 6.12a respectively) can be attributed to low intra-vortex exchange cases. At the higher rotation rates, where increased intra-vortex mixing occurs, the bands were also found to be narrower (Figure 6.15). In the simulations, when the dispersion in the outer-

region is sufficient to cause absolute instabilities, coupling with the inner core can lead to convective instabilities and then back to stable FDOs. In the experiment, the travelling waves observed at $\omega = 1$ Hz at high flow rates (Figure 6.12b,c) can be stabilized by increasing the rotation rate and, hence, the intra-vortex mixing (Figure 6.12e,f). But in this case, rotation also affects the inter-vortex mixing, so no conclusions can be drawn.
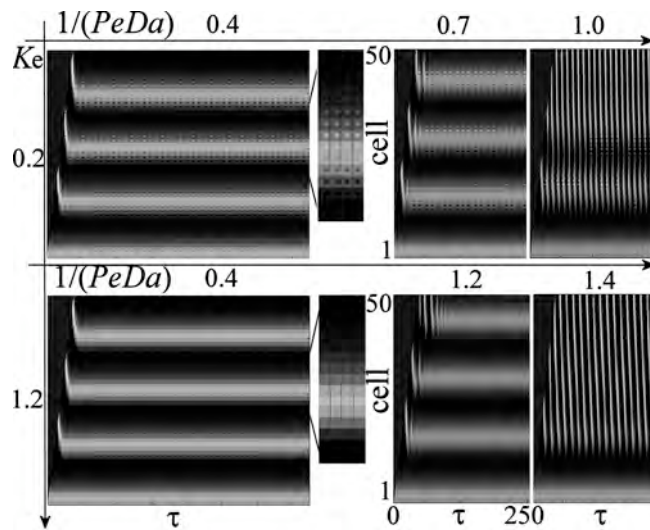
Figure 6.17. Simulated space-time plots showing the critical dispersion rate 1 / PeDa for the appearance of convective and absolute instabilities at different intra-vortex exchange rates, K_e. The scaled flow rate, 1 / Da, was 1.

Additional information on the stabilising role of intra-vortex mixing is provided by simulation results where the flow and the inter-vortex exchange rate are increased simultaneously (Figure. 6.18). For low intra-vortex exchange rates, the increase of flow and inter-vortex exchange is followed by a transition from FDOs to travelling waves (AI). An increase in the intra-vortex-exchange rate, K_e, led to the re-emergence of stable FDO. These results can also be related to the experimental ones. An increase of flow rate (inter-vortex mixing) between

Figure 6.12a and Figure 6.12b led to TW, while an increase in rotation (intra-vortex mixing) between Figure 6.12b and Figure 6.12e led to the formation of stable FDOs.
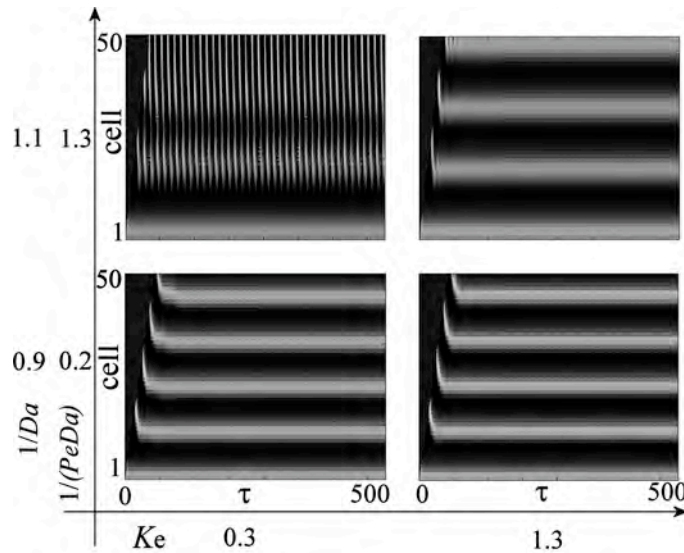
Figure. 6.18. Simulated space-time plots showing the effect of increasing flow rate and inter-vortex exchange rate on the patterns at two different intra-vortex exchange rates.

6.4 Conclusions

The results shown in this chapter demonstrate that flow distributed oscillations (FDOs) can form over a significant range of parameters, despite the travelling vortex flow complexity and high inter-vortex mixing.

Similarities with FDOs observed in PBRs[12–14] were identified, as the band distance increase with flow rate and the existence of a critical flow rate for the stabilisation of the bands. In a VFR, high mixing inside the vortices was shown to make the CSTR redundant. Removing it allowed reducing the minimum flow rate for stable FDO observation. FDOs in a VFR become

unstable as the flow rate Q is increased at low rotation rates, with the observation of complex patterns and travelling waves. This was attributed to increased inter-vortex mixing. In the PBR, similar instabilities were observed when the packing material was changed to enhance diffusive mixing[13]. At high rotation rates, FDOs in a VFR were shown to form via convective instability, where successive bands fail to settle at equilibrium position before the stationary pattern is observed. Similar structures were observed at low flow rates in the PBR[13] and increasing the flow rate could stabilise the FDO bands.

Simulations combining the Oregonator model for the BZ reaction with a model considering cells with an inner vortex core coupled to an outer zone reproduced the main features of the system. Comparison between experimental and simulated results of pattern formation allowed the effect of inter-vortex and intra-vortex mixing of to be studied. The simulations showed that above a critical inter-vortex exchange rate, $1/PeDa$, the FDO bands tend to become unstable and absolute instabilities (AI) appear forming travelling waves similar to the ones observed in the experiments. The disappearance of bands observed at high rotation and low flow rates appears to be related to the convective instabilities observed in the simulations as the inter-vortex exchange rate is increased: the perturbations are amplified upstream resulting in the loss of FDO band stability. Flow or rotation induced inter-vortex mixing can destabilise stationary FDO patterns because of dispersive mixing. However, the coupling of the vortex core with the outer zone can lead to the re-appearance of stable FDOs. The agreement of experimental and simulated results suggests that exploring the interplay between modes of pattern formation in a VFR for bigger ranges of parameters may provide insight into more complex instabilities observed in networks of coupled cellular systems[30–33].

207

(1)   De Wit, A.; Eckert, K.; Kalliadasis, S. *Chaos* **2012**, *22*.

(2)   Tel, T.; de Moura, A.; Grebogi, C.; Karolyi, G. *Phys. Rep.* **2005**, *413*, 91.

(3)   Vladimirova, N.; Constantin, P.; Kiselev, A.; Ruchayskiy, O.; Ryzhik, L. *Combust. Theor. Model.* **2003**, *7*, 487.

(4)   Kiss, I. Z.; Merkin, J. H.; Scott, S. K.; Simon, P. L.; Kalliadasis, S.; Neufeld, Z. *Physica D* **2003**, *176*, 67.

(5)   Medvinsky, A. B.; Petrovskii, S. V.; Tikhonova, I. A.; Malchow, H.; Li, B. L. *Siam Rev.* **2002**, *44*, 311.

(6)   Neufeld, Z. *Chaos* **2012**, *22*.

(7)   Steinbock, O.; Siegert, F.; Muller, S. C.; Weijer, C. J. *P. Natl. Acad. Sci. USA* **1993**, *90*, 7332.

(8)   Perumpanani, A. J.; Sherratt, J. A.; Maini, P. K. *Ima J. Appl. Math.* **1995**, *55*, 19.

(9)   Mcgraw, P. N.; Menzinger, M. *Phys. Rev. E* **2003**, *68*.

(10)   Andresen, P.; Bache, M.; Mosekilde, E.; Dewel, G.; Borckmans, P. *Phys. Rev. E* **1999**, *60*, 297.

(11)   Kaern, M.; Menzinger, M. *Phys. Rev. E* **1999**, *60*, R3471.

(12)   Bamforth, J. R.; Toth, R.; Gaspar, V.; Scott, S. K. *Phys. Chem. Chem. Phys.* **2002**, *4*, 1299.

(13)   Taylor, A. F.; Bamforth, J. R.; Bardsley, P. *Phys. Chem. Chem. Phys.* **2002**, *4*, 5640.

(14)   Britton, M. M.; Sederman, A. J.; Taylor, A. F.; Scott, S. K.; Gladden, L. F. *J. Phys. Chem. A* **2005**, *109*, 8306.

(15)   Novak, J. Visualisation of Chemistry in Flow, University of Birmingham, 2010.

(16)   Taylor, A. F.; Britton, M. M. *Chaos* **2006**, *16*.

(17)   Pocheau, A.; Harambat, F. *Phys. Rev. E* **2006**, *73*.

(18)   Thompson, B. W.; Novak, J.; Wilson, M. C. T.; Britton, M. M.; Taylor, A. F. *Phys. Rev. E* **2010**, *81*.

(19)   Paoletti, M. S.; Solomon, T. H. *Phys. Rev. E* **2005**, *72*.

(20)   Desmet, G.; Verelst, H.; Baron, G. V. *Chem. Eng. Sci.* **1996**, *51*, 1287.

(21)   Vallatos, A.; Evans, R. D.; Taylor, A. F.; Britton, M. M. *Chaos* **2013**, *23*.

(22)   Bamforth, J. R.; Merkin, J. H.; Scott, S. K.; Toth, R.; Gaspar, V. *Phys. Chem. Chem. Phys.* **2001**, *3*, 1435.

(23)   Giordano, R. L. C.; Giordano, R. C.; Prazeres, D. M. F.; Cooney, C. L. *Chem. Eng. Sci.* **2000**, *55*, 3611.

(24)   Kaern, M.; Menzinger, M. *Phys. Rev. E* **2000**, *61*, 3334.

(25)   Kaern, M.; Menzinger, M. *J. Phys. Chem. A* **2002**, *106*, 4897.

(26)   Gu, Z. H.; Fahidy, T. Z. *Can. J. Chem. Eng.* **1985**, *63*, 710.

(27)   Giordano, R. C.; Giordano, R. L. C.; Prazeres, D. M. F.; Cooney, C. L. *Chem. Eng. Sci.* **1998**, *53*, 3635.

(28)   Wereley, S. T.; Lueptow, R. M. *Phys. Fluids* **1999**, *11*, 3637.

(29)   Vallatos, A.; Wilson, M. C. T.; Taylor, A. F.; Britton, M. M. *Europhys. Lett.* **2012**.

(30)   Votrubova, V.; Hasal, P.; Schreiberova, L.; Marek, M. *J. Phys. Chem. A* **1998**, *102*, 1318.

(31)   Yoshimoto, M.; Yoshikawa, K.; Mori, Y. *Phys. Rev. E* **1993**, *47*, 864.

(32)   Nevoral, V.; Votrubova, V.; Hasal, P.; Schreiberova, L.; Marek, M. *J. Phys. Chem. A* **1997**, *101*, 4954.

(33)   Laplante, J. P.; Erneux, T. *Physica A* **1992**, *188*, 89.

7 MR Imaging of chemical waves in vortical flow

7.1 Introduction

In the previous chapter, the analysis of chemical pattern formation arising from the coupling of oscillating reactions and vortical flow was shown to provide information on flow properties, such as inter- and intra-vortex mixing. Molecular displacements within the flow are expected to play an important role in determining the features of the propagating chemical waves.

MRI studies of BZ waves in stationary and travelling vortex flow were performed to get a better understanding of the interplay between reaction and transport in these systems. The characteristics of the chemical waves were analysed in the light of previously presented results on the molecular transport properties of the flows. Three types of systems presenting different features were investigated: travelling waves in stationary vortices, travelling waves in travelling vortices and stationary waves in travelling vortices (FDOs). This work demonstrates how magnetic resonance experiments can provide deeper insight into underpinning mechanisms behind pattern forming RDA systems, particularly those involving vortical flows.

In order to image chemical waves using MRI, the manganese-catalysed BZ reaction was used. Contrary to the ferroin catalyst[1] used in the previous chapter, manganese has been shown to provide good MR contrast[2] between the two oxidative states (Mn^{3+} and Mn^{2+}). On the other hand, poor optical contrast is obtained with manganese-catalysed BZ systems[3]. But optical

contrast was necessary in order to visualise the overall chemical pattern formation and make sure that stationary waves formed within the MRI rf coil, in a region of about 4 cm. Also, in order to obtain stationary waves within the VFR, the oscillation period of the manganese catalysed BZ reaction had to be similar to the one of the ferroin-catalysed BZ reaction used in the previous chapter.

In initial publications[4,5] on MRI of the manganese-catalysed BZ reaction, high concentrations of phosphoric acid (H_3PO_4) were used (> 1 M). The phosphate group (PO_4^{3-}) of phosphoric acid was shown to improve MR contrast by stabilising the Mn^{3+} ions[6]. In previous MR studies of FDOs in a PBR, Britton *et al.*[7] also used a version of the manganese-catalysed BZ reaction involving high concentrations of sulphuric and phosphoric acid. Thompson *et al.*[8] used the same reaction to visualise BZ waves propagating in stationary vortices. But high acid concentrations lead to high-viscosity solutions[9], which are significantly higher than those used in the previous chapters of this thesis to characterise vortical flows. Thus, a manganese-catalysed BZ reaction of similar viscosity had to be used, so as to ensure similar flow properties. In order to obtain lower viscosity solutions, the phosphoric acid was replaced with $Na_5P_3O_{10}$, which has been shown[6] to also stabilise Mn^{3+}. Moreover, $Na_5P_3O_{10}$ allows to produce a reaction of adaptable oscillation period without changing the flow properties of the system[10].

The MR contrast properties of oscillating chemistry and vortical flow were analysed separately, prior to the imaging of chemical waves in vortical flow. Chemical contrast was studied using MRI of phantom samples containing an oxidised and a reduced form of the BZ reaction[6], in order to evaluate the maximum contrast expected for each set of parameters. The

imaging parameter ranges were restricted to values leading to short sequence times, in order to take into account the transient nature of the chemical waves and the effects of flow. MR imaging sequences have been shown to be subject to flow artifacts[11,12]. Also, T_1 and T_2 relaxation times used for MRI contrast are sensitive to molecular motion and flow properties[13]. Experiments were conducted to study the effects of stationary and travelling vortex flow on both MR relaxation and MR imaging.

The optimised manganese-catalysed BZ reaction and MR parameters were used to produce images of chemical waves in vortical flow. Particular attention was given to the role of flow properties, as intra- and inter-vortex mixing, on the propagation of the chemical waves. Trying to separate flow- from chemistry-induced effects, the chemical wave images were compared with molecular displacement simulations obtained in Chapter 5, at the same flow regimes. The use of BZ reactions with different concentrations of manganese allowed analysing the role of the catalyst into the wave propagation and opening a discussion on the role of chemistry in the resulting pattern formation.

7.2 Experimental

7.2.1 The manganese-catalysed BZ reaction

The manganese-catalyzed BZ reaction was prepared immediately before each experiment using reactants dissolved in deionized water. Solution A contained malonic acid ([MA] = 0.5 M, Alfa Aesar, 99 %) and sodium bromate ([BrO$_3^-$] = 0.14 M, Alfa Aesar, 99.5 %). Solution B contained sulfuric acid ([H$_2$SO$_4$] = 1 M, Fisher, 98 %), penta-sodium triphosphate

([Na$_5$P$_3$O$_{10}$] = 4 mM, Sigma Aldrich, 98%) and the manganese catalyst (Sigma Aldrich, 98%). [MnSO$_4$] varied from 0.5 mM to 8 mM. Solutions A and B were degassed prior to experimentation.

Control solutions of either the oxidised or reduced state of the BZ reaction were obtained by removing one of the main reactants (MA or BrO$_3^-$) of the mixed BZ solution[6]. The oxidised state solution contained sodium bromate ([BrO$_3^-$] = 0.07 M), sulfuric acid ([H$_2$SO$_4$] = 0.5 M), penta-sodium triphosphate ([Na$_5$P$_3$O$_{10}$] = 2 mM) and the manganese catalyst. The reduced state solution contained malonic acid ([MA] = 0.25 M), sulfuric acid ([H$_2$SO$_4$] = 0.5 M), penta-sodium triphosphate ([Na$_5$P$_3$O$_{10}$] = 2 mM) and the manganese catalyst. For both solutions [MnSO$_4$] varied from 0.25 mM to 4 mM.

7.2.2 Pt-electrode measurements of BZ temporal oscillations

Temporal oscillations were monitored in a well-stirred batch reactor using a Pt-combination redox electrode connected to a Picoscope Oscilloscope (Picotech). The reaction temperature was maintained at 22 ˚C ± 0.5 ˚C. The experimental set-up was the same as the one described in section 6.2.2.

7.2.3 Experimental set-up for chemical waves in vortical flow

The Couette cell used was the same as the one described in the previous chapters, and constructed from an outer glass tube of radius R_o = 8.25 mm and an inner PEEK rod of radius R_i = 4.1 mm. Description of the experimental set-up for the observation of chemical patterns

is detailled in Chapter 6 (cf. 6.2.3). For MR imaging experiments, the Couette cell was placed in the MRI magnet, inside the rf coil. The coil was situated 11 cm above the lower PTFE guide (cf. 4.2.1).

7.2.4 Flow parameter ranges

Tap water, of viscosity $v = 0.979$ mm^2 s^{-1} at 22 ± 0.5 ˚C, was used for the investigation into flow artifacts. The manganese-catalysed BZ reaction was used for all the other experiments, and had a viscosity of $v = 1.05$ mm^2 s^{-1} at 22 ± 0.5 ˚C. Viscosities were measured using a calibrated Ubbelohde Viscometer. Four rotation rate values, ω, were used: 1 Hz, 1.5 Hz, 2 Hz and 2.5 Hz. The respective Ta values varied from 17 to 43. For the pipe flow and translating vortex flow experiments, two flow rate values, Q, were used: 7.2 cm^3 min^{-1} and 13.6 cm^3 min^{-1}. The respective Re values were of 2.51 and 5.3. The velocity of translation of the vortices, U_{TV}, varied between 0.45 mm s^{-1} and 1.51 mm s^{-1} and the velocity drift, V_d, between 1.02 and 1.21. γ_{Re} varied from 0.06 to 0.29. Each experiment was repeated a minimum of three times.

7.2.5 Optical measurements

Optical images were acquired using a digital CCD camera (Canon Power Shot A520). Adobe Photoshop was used to enhance colour contrast. The pink colour component of each image was saturated, so that the pink solutions, where Mn^{3+} predominated, could be distinguished from the colourless solutions, where Mn^{2+} predominated. Chemical pattern formation images were passed to grey scale with the pink components (Mn^{3+}) appearing in black and the

colourless components (Mn^{2+}) in white. Space-time plots of chemical pattern formation were produced using the method presented in Chapter 6 (cf. 6.2.4).

7.2.6 T_1 and T_2 relaxation measurements

T_1 and T_2 relaxation times of both oxidised and reduced solutions were measured for [Mn] values of 0.25 mM, 0.5 mM, 1 mM, 2 mM and 4 mM. T_1 relaxation times were measured using an inversion-recovery sequence (Figure 2.4). Variable delay lists with 20 exponentially spaced τ values were used (from 5×10^{-6} s to 1 s, 2 s, 5 s or 10 s). T_2 relaxation times were measured using a CPMG sequence (Figure 2.6). A series of 17 spectra were collected, acquired using a range of echoes. A variable count list was used with values ranging from 0 to 1500. The echo time, τ, was varied between 0.5 ms and 3 ms.

For both inversion recovery and CPMG experiments, the spectral width was 10 kHz and 16 k complex data points were acquired. Four signal averages were acquired for each τ value. The hard rf pulse length was of 45 µs for the 90° r.f. pulse and 90 µs for the 180° r.f. pulse. The data was analysed using Prospa and Kaleidagraph software.

Both experiments produced two-dimensional data sets of spectral data against points in the variable delay (inversion recovery) or variable counter (CPMG) lists. For the inversion recovery experiment data, the signal intensity against time was fitted to a single-exponential recovery function (equation 2.1) to obtain the T_1 value. For the CPMG data, the signal intensity against time was fitted to a single-exponential decay function (equation 2.2) to obtain the T_2 value.

7.2.7 Relaxation-weighted imaging

A phantom sample made from the oxidised and reduced state solutions of the BZ reaction was used to determine the imaging parameters that produce the higher contrast. These parameters were used to image chemical waves in the Couette cell.

For the phantom sample experiments, a 5 mm o.d. NMR tube filled with the oxidised state solution (Mn^{3+}) was placed inside a 10 mm o.d. tube filled with the reduced state BZ solution (Mn^{2+}) (Figure 7.1a). The tubes were then placed inside the probe, in the MRI magnet. Images were acquired in the transversal plane so as to visualise the cross section of the tubes (Figure 7.1b). For this experiments, the field of view was of 2 cm^2 with a matrix size of 128 × 128 pixels.
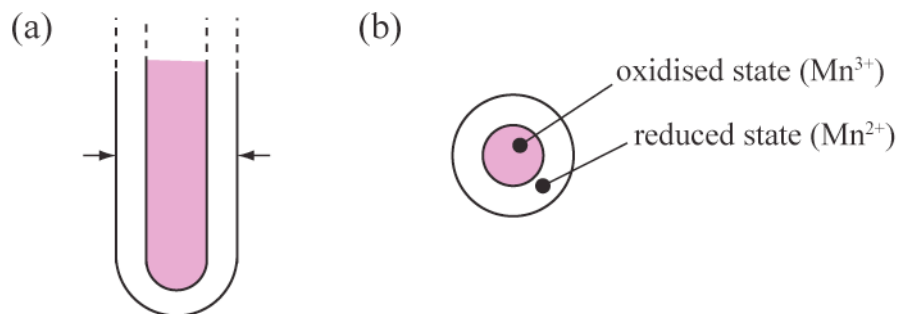
Figure 7.1. (a) Schematic diagram of the experimental set-up for phantom experiments. (b) Transverse section of the image in (a) at the level indicated by the arrows.

For imaging chemical waves within the Couette cell, the field of view was 40 × 20 mm with a matrix size of 128 × 64 pixels resulting in a pixel size of 0.3125 mm^2. The cell was placed into the magnet and the MRI field of view (rf coil) was situated 11 cm above the lower PTFE

guide. The same set-up and parameters were used for studying flow-induced contrast in imaging of tap water.

A spin echo imaging pulse sequence was used for all MR imaging experiments (Figure 2.11). The soft rf pulse length was of 1 ms with attenuations of 8 - 13 dB for the 90° pulse and 2 - 7 dB for the 180° pulse. Spectral widths of 50 kHz and 100 kHz were used. A slice thickness of 1 mm was used. Recovery time, T_R, between 100 ms and 300 ms. The echo time, T_E, varied between 3 ms and 35 ms. At this range of T_R and T_E, MR contrast was obtained with a combination of T_1- and T_2-weighted contrast, with T_1 contrast dominating at low T_E and T_2 contrast dominating at high T_E.

7.3 Results and discussion

7.3.1 Optical imaging of chemical patterns in translating vortices

In order to visualise optically the waves produced by the manganese-catalysed BZ reaction one has to be able to distinguish between the oxidised and reduced states. In the Mn^{2+} / Mn^{3+} system, the reduced state (Mn^{2+}) is colourless and the oxidised (Mn^{3+}) is pink. The contrast between the two states depends on [Mn]. But even if the manganese concentration is sufficient to produce optical contrast in bulk solutions, when the solution layer is thin, poor contrast is observed between the two states. However, it is possible to enhance optical contrast either by changing the composition (increasing [Mn]) or by enhancing the image, using an image-editing software. Figure 7.2a shows pictures of BZ solutions in 20 mm tubes with increasing Mn^{3+} concentrations. For $[Mn^{3+}] = 0$ the solution is colourless like the reduced state solutions. The pink colour intensity is increasing with $[Mn^{3+}]$.
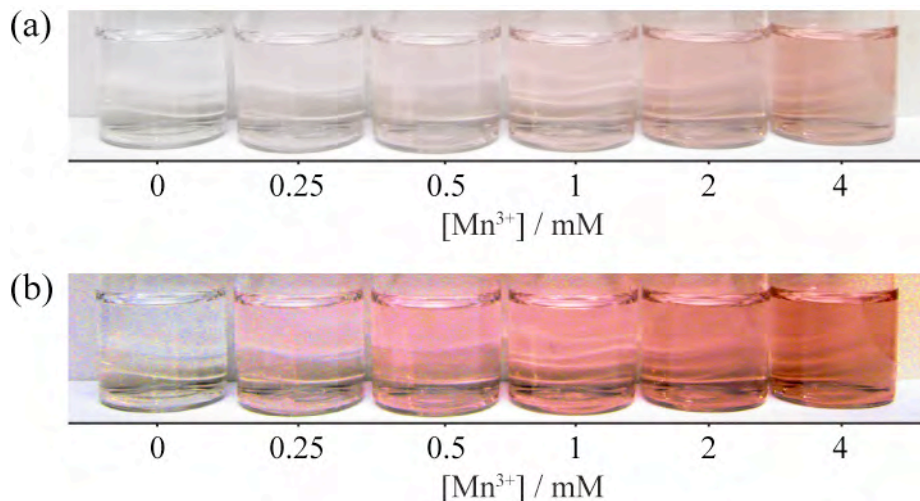
Figure 7.2 (a) Optical contrast at increasing [Mn^{3+}] and (b) Photoshop enhanced optical contrast for the same picture.

In the Couette cell, where the gap (and the fluid column thickness) is of only 4.15 mm, the contrast is poorer and the pink colouration is visible only for $[Mn^{3+}] \geq 2$ mM. To visualise BZ contrast for $[Mn^{3+}] < 2$ mM, Photoshop was used to saturate the pink component in the images (Figure 7.2b). Using the BZ reaction in a Couette cell, no good contrast was obtained for $[Mn^{3+}] = 0.25$ mM. Very good contrast was obtained for $[Mn^{3+}] = 4$ mM, but at this manganese concentration, the BZ oscillations were producing a lot of CO_2, perturbing the pattern formation and reducing the imaging quality. Therefore, only BZ reactions with 0.5 mM $\leq [Mn^{3+}] \leq 2$ mM were used for optical imaging experiments of chemical pattern formation in translating vortex flow.

While changing [Mn] can improve the visualisation of the waves, there are also effects on the BZ reaction. Pt-electrode measurements were performed to determine the oscillation period of the BZ reaction for increasing $[Mn^{3+}]$. Figure 7.2 shows plots of temporal oscillations in the BZ reaction for three [Mn] observed over 30 minutes using the Pt-electrode. As the potential oscillates, there is an oscillatory conversion between Mn^{2+} and Mn^{3+}, with Mn^{2+} at low potential and Mn^{3+} at high potential. The sharp increases in potential correspond to the autocatalytic steps where the system switches from colourless (Mn^{2+}) to pink (Mn^{3+}). Each potential maximum is followed by a slower decay that brings the system back to the reduced state. Where [Mn] = 2 mM, there is an additional shoulder after each peak, indicating a possible change in the behaviour of the BZ oscillation.

The average oscillation period was of 100 s for [Mn] = 0.5 mM, 170 s for [Mn] = 1 mM and 200 s for [Mn] = 2 mM. For comparison, the oscillation period of the ferroin-catalysed BZ reaction studied in the previous chapter was of 185 s (Figure 6.3).
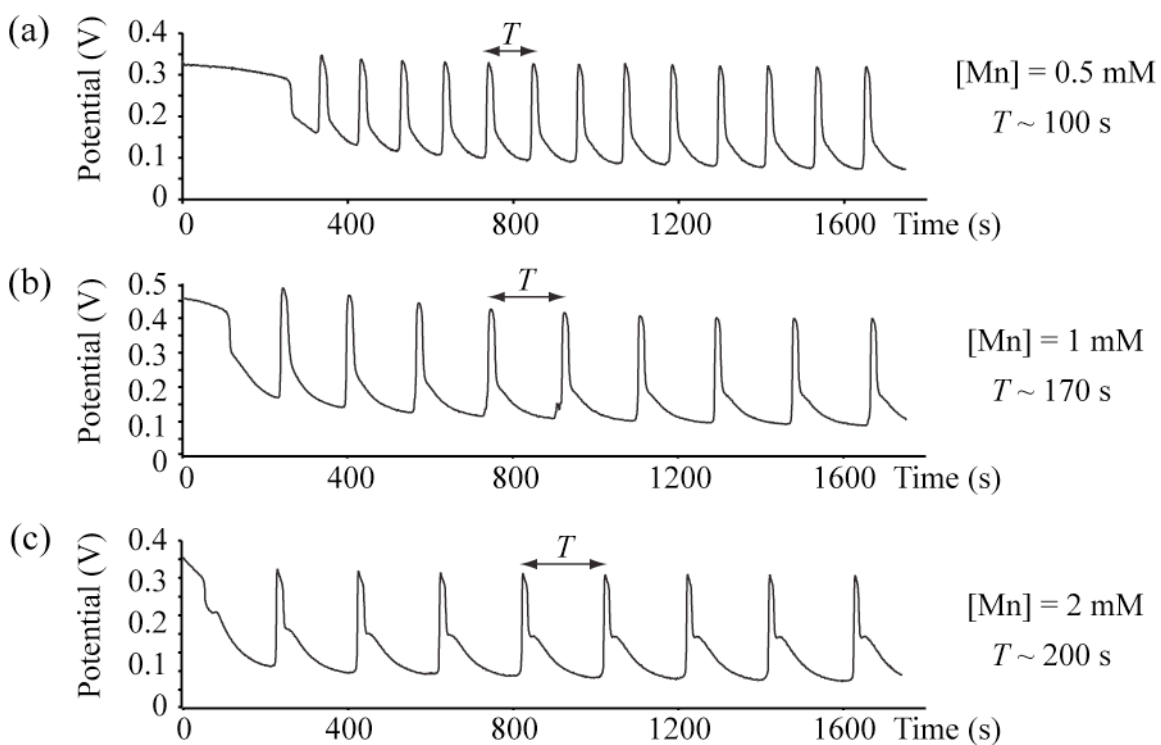
Figure 7.3. (a-c) Pt-electrode measurements of temporal oscillations in the BZ reaction for increasing Mn concentrations. The period T represents the average oscillation period over the observation time.

To investigate FDOs in the manganese-catalysed reaction, BZ systems with different Mn concentrations were pumped into the Couette cell at $Q = 7.2$ cm^3 min^{-1} and $\omega = 1$ Hz (Figure 7.4). The grey-scale allows for a better visualisation of the resulting pattern. Dark bands in the space-time plots correspond high $[Mn^{3+}]$ (pink), while light grey areas correspond to high $[Mn^{2+}]$ (colourless).
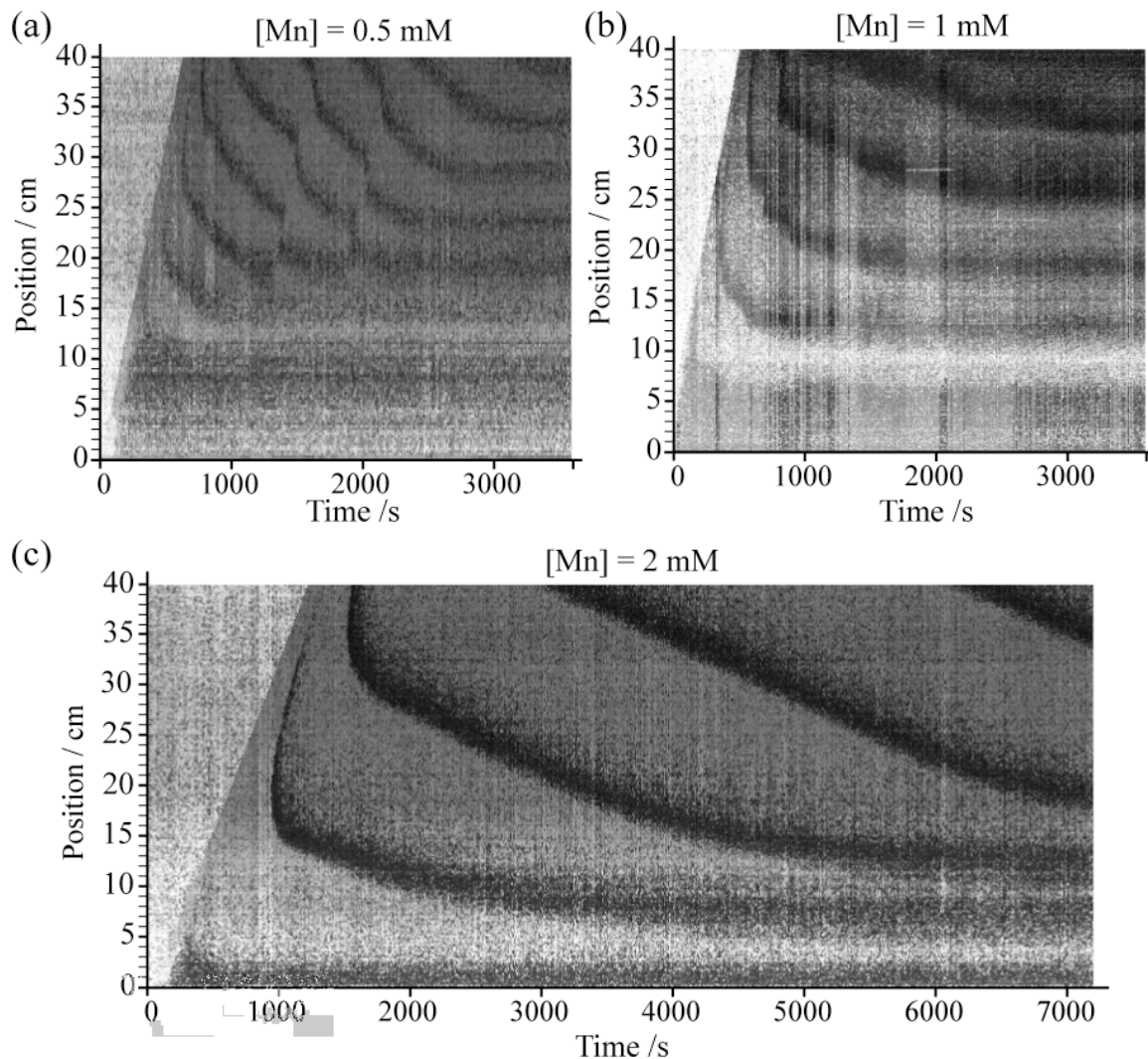
Figure 7.4. Chemical pattern formation of the Mn-catalysed BZ reaction at ω = 1 Hz and Q =

7.2 cm³ min⁻¹ for (a) [Mn] = 0.5 mM, (b) [Mn] = 1 mM and (c) [Mn] = 2 mM.

It was observed that stationary bands formed for all Mn concentrations at this flow regime.

For [Mn] = 0.5 mM (Figure 7.4a), the bands formed via a convective instability (CI-FDO).

This is probably due to the lower oscillation period of the reaction. For [Mn] ≥ 1 mM the

bands form via the FDO mechanism involving a single wave-splitting, where a part of the

wave leaves the reactor while the other settles at stationary position[14].

For [Mn] = 1 mM (Figure 7.4b), where the oscillation period is close to the previously studied ferroin-catalysed BZ system, a similar λ_{FDO} was found ($\lambda_{FDO} \sim 10$ cm). For [Mn] = 2 mM, the speed of the descending waves is found to decrease dramatically and the bands take more time to settle to the stationary position. Almost 1 hour was required for the first band to settle. Hence, 2-hour experiments were required to observe stationary bands at this Mn concentration. During the wave-splitting, the distance between successive bands is greater than for the lower Mn concentration systems. However, the resulting λ_{FDO} is found to be shorter, although the oscillation period is higher than for the [Mn] = 1 mM system. This is not in accordance with the kinematic model for FDO formation ($\lambda_{FDO} = U_{TV} \times T$), as at constant U_{TV} a BZ system with higher T should result in a higher λ_{FDO}. Also, since the flow conditions are the same for all BZ systems, the differences in behaviour should be attributed to the properties of the BZ reaction. These results provide more evidence for the limitations of the kinematic model and suggest an important role of chemistry in defining the resulting patterns.

Due to poor image quality, the acquired pattern formation pictures provide with limited insight into the chemical wave propagation through the vortices. However, an expanded region of the pictures, with enhanced contrast, allows the structure of the bands to be seen. A field of view of 10 cm was selected in the area where the stationary bands were formed. Figure 7.5a shows a close-up picture of the first FDO band for the [Mn] = 1 mM system at $t = 1800$ s.
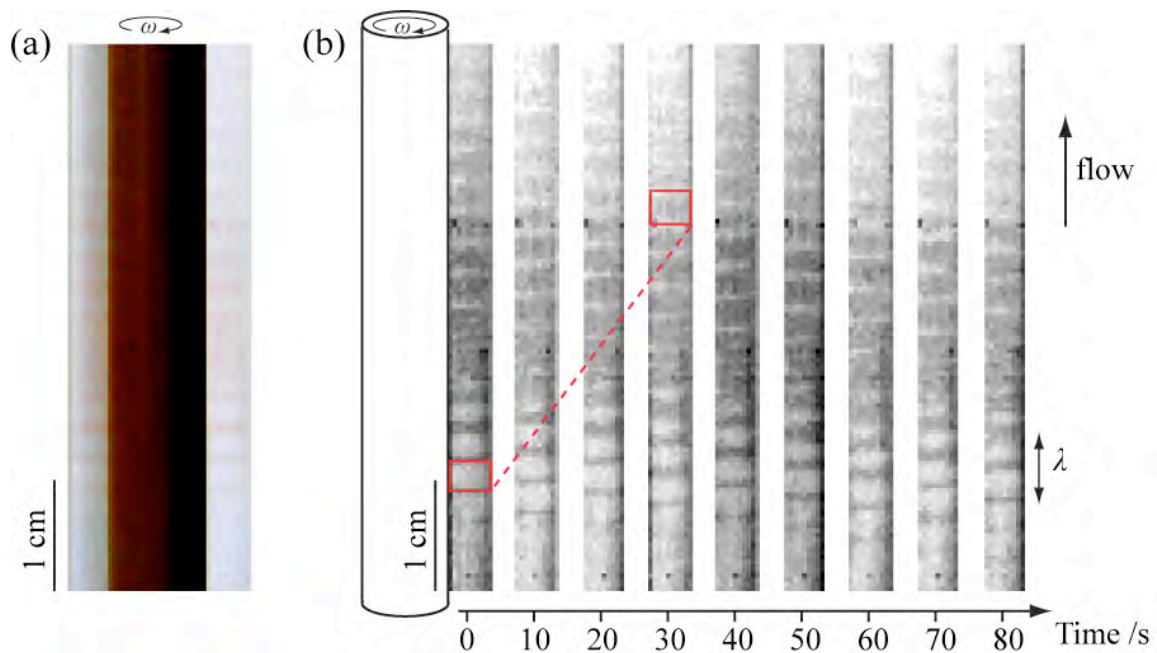
Figure 7.5 (a) Expanded region for the first FDO band of the [Mn] = 1 mM system at t = 1800 s, with enhanced optical contrast (b) Time series of pictures in grey scale of the right-hand side gap of the Couette cell in the same space-time plot. The red boxes indicate the position of a vortex at t = 0 s and t = 30 s and the dotted line its trajectory.

The use of a grey scale provides better optical contrast. Figure 7.5b shows a time series of images of the same band taken at 10 s intervals. Upstream (bottom of the images), the cores are in the reduced state (light grey) but the vortex outer parts start switching to the oxidised state (dark grey). In the middle of the band, the entire vortex is in the oxidised state (Mn^{3+}). Downstream (top of the images), the reversed is observed, with the outer parts switching to the reduced state before the vortex cores. Regardless of the relative position of the travelling vortices, the bands appear stationary over time.

The vortex translation U_{TV} is of about 5 cm min^{-1} in the downstream direction at this regime. During the formation, when the chemical waves travel against the flow, the velocity of the chemical wave has to overcome this value. For the band to settle at a stationary position, the chemical wave has to propagate at the same speed as the vortices. This shows the fine balance that has to be reached between the mixing properties of the flow and the oscillatory behaviour of the BZ reaction for the stationary condition to be reached.

Previous results showed that MR techniques could be used to analyse the mixing properties of vortical flows. Comparison of these results with MR images of the chemical wave propagation is expected to provide with a deeper insight into these coupling properties. To obtain good quality images of the chemical waves one has to identify the MR parameters that produce good MRI contrast between the oxidised and reduced states.

7.3.2 Chemistry-induced MR contrast

To evaluate the MR contrast properties of the BZ reaction, T_1 and T_2 relaxation measurements were performed on the oxidised and reduced state solutions. Figure 7.6a shows plots of the MR relaxation times as a function of Mn concentration. Both T_1 and T_2 follow an inverse decay with increasing [Mn]. Plots of the relaxation rates against Mn concentration give information on the expected MR contrast (Figure 7.6b). The higher relaxation rate differences between the oxidised and reduced species, expected to result in the best contrast mixtures, are found at high [Mn]. In the range considered for the chemical pattern experiments presented previously (0.5 mM $\leq$ [Mn] $\leq$ 2mM), T_1 and T_2 times of the oxidised state solution are found

to be at least 2 times longer than the ones of the reduced state solution. Hence, the resulting

BZ solutions are expected to provide good MR contrast.
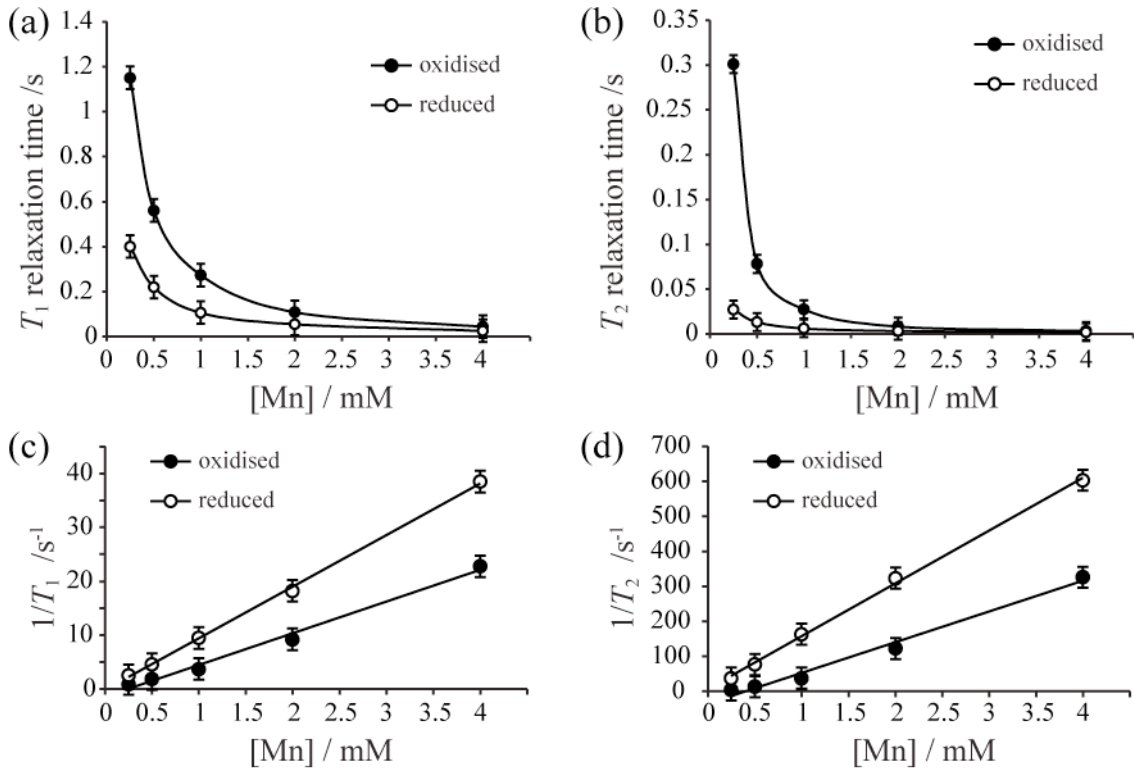
Figure 7.6 Relaxation times, T_1 (a) and T_2 (b), and relaxivities, $1/T_1$ (c) and $1/T_2$ (d), of the oxidised and reduced states of the BZ reaction against Mn concentration. A linear curve was fitted to the relaxivity plots.

Phantom samples containing the oxidised and reduced solutions at a range of Mn concentrations were imaged at different echo times to identify their effect on the resulting contrast. A spin echo imaging pulse sequence was used to acquire horizontal images. Taking into account the transient nature of the chemical waves, a short repetition time, $T_R = 100$ ms, was used to minimise the experiment time. Contrast in the spin echo experiment is obtained through a combination of T_1 and T_2 weighted contrast. Pure T_1 contrast is expected for $T_E = 0$

ms while pure T_2 contrast is expected for $T_R > 5T_1$. However, neither of these can be achieved, hence, a balance must be struck.

Figure 7.7 shows images of the phantom samples at different echo times, T_E.

(a) [Mn] = 0.5 mM

$T_E = 3$ ms $T_E = 5$ ms $T_E = 10$ ms $T_E = 15$ ms $T_E = 20$ ms

(b) [Mn] = 1 mM

$T_E = 3$ ms $T_E = 5$ ms $T_E = 10$ ms $T_E = 15$ ms $T_E = 20$ ms

(c) [Mn] = 2 mM

$T_E = 3$ ms $T_E = 5$ ms $T_E = 10$ ms $T_E = 15$ ms $T_E = 20$ ms
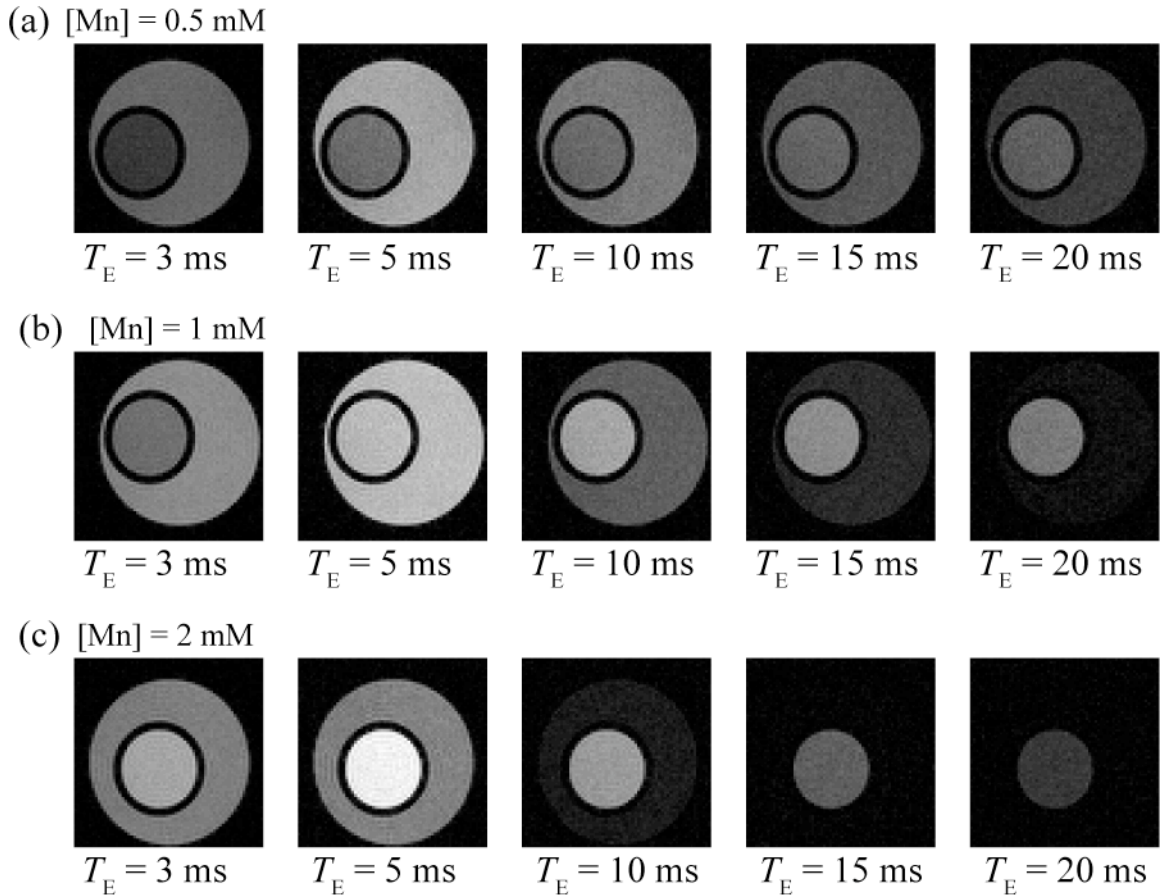
Figure 7.7 Phantom images at increasing T_E for different concentrations of Mn: (a) [Mn]=0.5mM, (b) [Mn]=1 mM and (c) [Mn]=2 mM. The inner tube contains the oxidised solution (Mn^{3+}) and the outer tube contains the reduced solution (Mn^{2+}). A T_R of 100 ms was used for all the experiments.

With T_R set at 100 ms ($<5T_1$), the conditions for pure T_2 are not met for all the studied Mn concentrations, so for the lower T_E values T_1 contrast dominates the signal. Where T_1 contrast is dominant, samples exhibiting longer relaxation times produce less signal intensity and appear darker. The inverse is observed where T_2 contrast is dominant, with samples exhibiting longer relaxation times appearing brighter. For the solutions at [Mn] = 0.5 mM (Figure 7.7a), at low echo times ($T_E \leq 5$ ms) the contrast is primarily due to T_1 relaxation, resulting in a low signal oxidised phase (inner tube) and a high signal reduced phase. For $10 \leq T_E \leq 15$ ms, the effects of T_1 and T_2 relaxation cancel out, resulting in poor contrast. For $T_E \geq 20$ ms, T_2 relaxation produces the contrast. The same trend is observed for solutions at [Mn] = 1 mM (Figure 7.7b), but the echo time where T_1 and T_2 contrast cancel each other out is found for T_E = 5 ms. This is due to the fact that relaxation times for this Mn concentration are closer to the $T_R > 5 \times T_1$ condition. For solutions at [Mn] = 2 mM (Figure 7.7b), $T_R > 5T_1$ and only T_2 contrast is observed. Note that for [Mn] > 1 mM the signal of the reduced state solution is almost fully relaxed for the higher echo times.

To evaluate which set of parameters provide the best contrast, a profile was selected in these images through the diameter of the samples that allowed calculating the average signal intensity for the oxidised and reduced state solutions at each echo time. Figure 7.8 shows plots of the average signal intensity against T_E, for different Mn concentrations. The maximum contrast is expected when the difference in signal of the oxidised and reduced state solutions is at a maximum. These results lead to an optimisation for T_E values at T_R = 100 ms. For the solutions at [Mn] = 0.5 mM, T_E = 10 ms produces the highest T_1 contrast and T_E = 20 ms the highest T_2 contrast in this range. For the solutions at [Mn] $\geq$ 1 mM, poor or no T_1

contrast is obtained. Optimal T_2 contrast is expected for $T_E \geq 10$ ms at [Mn] = 1 mM and for

10 ms $\leq T_E \leq 20$ ms at [Mn] = 2 mM.
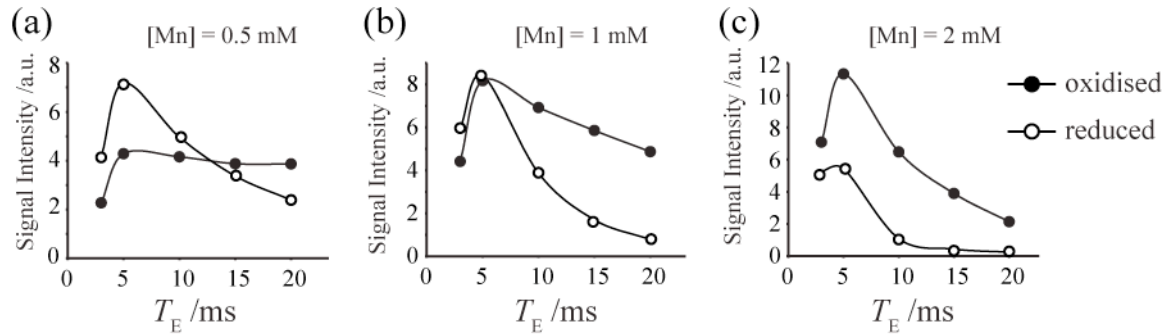
Figure 7.8. Average NMR signal of the oxidised and reduced BZ states in the phantom images

for different concentrations of Mn.

The BZ system at [Mn] = 1 mM, was used to probe chemical wave propagation in systems

without flow. The reactants were pumped into the gap between two NMR tubes and vertical

images were taken at different T_E and T_R times (Figure 7.9). For $T_R \geq 200$ ms, good contrast is

obtained for all T_E values except for $T_E = 5$ ms, where the contrast was poor. As expected

from the results of the phantom solutions at $T_R = 100$ ms (Figure 7.8b), no contrast is obtained

from the BZ waves at $T_E = 5$ ms, while enhanced contrast is obtained for 10 ms $\leq T_E \leq 20$ ms.

Image quality, however, deteriorates at higher values of T_E. This effect is expected to be even

stronger with the addition of flow. Hence, in this study the minimum value of T_E, which gives

good contrast, will be used.
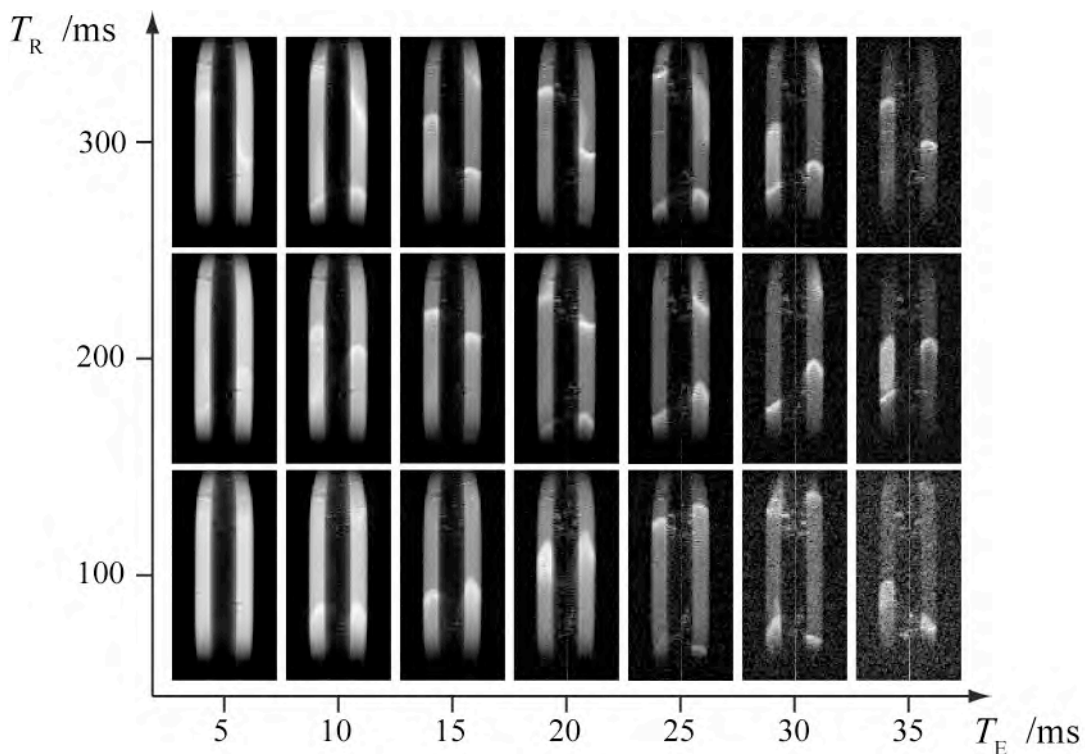
Figure 7.9. T_2 weighed images of chemical wave propagation ([Mn]= 1 mM) in a Couette cell without flow for different Echo and Repetition times.

Chemical wave imaging showed that good T_2 contrast can be obtained for all the Mn concentrations in this range. But both MR relaxation and MR imaging are sensitive to flow artifacts. The flow-induced MR contrast has to be evaluated prior to the chemical wave propagation studies so as to distinguish it from the chemical wave propagation.

7.3.3 Flow-induced MR contrast

Flow is known to produce MR artifacts that depend both on the flow properties (velocity, direction and pulsatility) and on the pulse sequence used. The simplest artifact associated with flow is signal loss due to flowing excited spins, which exit the selected slice or even the rf

coil, being replaced with spins that have a different rf excitation history. This results in a reduction or even total loss of signal in a given voxel. One solution to this is to reduce either the flow rate or the experiment time. But the motion of the spins can also affect the phase of the signal. In a magnetic field gradient, spins accumulate phase depending on their position. If spins move in a region of higher magnetic field, their phase will increase with time; while if they move in a region of lower magnetic field, their phase will decrease. This can induce a loss of phase coherence related to the distribution of velocities in a sample. This loss of phase coherence will depend on both the flow properties and the applied gradients.

In order to investigate the influence of flow on images, a series of imaging experiments were performed using tap water. The imaging sequence used is shown in figure 2.11. The Couette cell was placed into the magnet and the solution was pumped into the gap. The effect of flow and rotation rate on the resulting contrast was investigated. These experiments were performed at the shorter echo and repetition values that gave good contrast during the Mn wave imaging experiments (Figure 7.9), T_E was of 10 ms and T_R of 100 ms. For all the images, the read gradient direction was the same as the axial flow direction (vertical direction in the images) while the phase direction is perpendicular to the axis of the inner cylinder of the Couette cell.

Figure 7.10 shows the effect of pipe flow on imaging with the tap water. When no flow is imposed to the system the signal intensity is constant in the gap region. At a flow rate of $Q = 7.2$ cm min^{-1} ($U_{max} \sim 1$ mm s^{-1}) flow does not seem to affect significantly the signal intensity. At $Q = 13.6$ cm min^{-1} ($U_{max} \sim 2$ mm s^{-1}), flow-induced contrast artifacts are produced in the read gradient direction on both sides of the gap. These artifacts are to be related with the

231

change in position of the excited spins over the course of the acquisition and frequency encoding. A maximum read gradient of 2.9 G cm^{-1} was applied during 2.56 ms. As discussed earlier, spin movements in the read direction during this time cause flow-induced frequency shifts. At Q = 13.6 cm min^{-1}, spin displacements become significant enough so as to produce contrast in the image. Notice that the observed artifacts have a parabolic shape, similar to the distribution of velocities in the sample. These artifacts could be minimised by increasing the pixel size, hence decreasing the gradient strength.
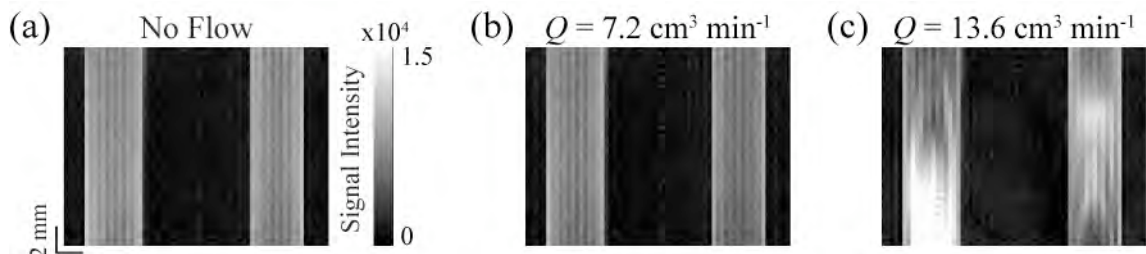
Figure 7.10. T$_1$ weighed images of tap water in a Couette cell with axial flow: (a) no flow, (b) Q = 7.2 cm^3 min^{-1} (U$_{max}$ ~ 1 mm s^{-1}) and Q = 13.6 cm^3 min^{-1} (U$_{max}$ ~ 2 mm s^{-1}).

For the stationary TVF, enhanced flow induced contrast was expected, both from phase coherence loss and spin loss caused by the rotation of the fluid around the inner cylinder. Spin loss is occurring during the time between the first rf pulse exciting the spins and the end of the acquisition, where spins can leave the region corresponding to the selected 2D slice. As MR contrast depends on NMR signal attenuation, spin loss generates contrast by producing signal loss.

This time lapse for which the spins can leave the slice, or spin flowing time, t_f, is given by $2T_E + ACQ/2$, where ACQ is the acquisition time. For the experiments presented here, this

time corresponds to approximately 22 ms. During t_f, the inner cylinder will rotate by an angle $\theta = 2\pi\omega\, t_f$, and the molecules on the surface of the cylinder will travel a distance $d = 2\pi R_i \omega\, t_f$ (Figure 7.11). For a slice of 1 mm and a rotation rate ω of 1 Hz, the molecules on the inner cylinder surface would travel over a distance d of 0.58 mm. A spin loss of about 58 % is expected on the inner cylinder surface. The spin loss would vary across the slice with much lower values expected towards the outer cylinder. Nevertheless, this calculation stresses the need for working at low T_E values so as to reduce t_f and spin loss.
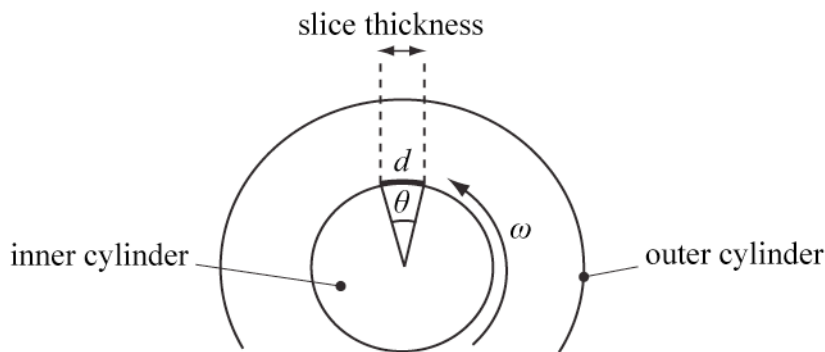
Figure 7.11. View of the Couette cell gap from above. d represents the displacement of a molecule on the inner cylinder surface when the cylinder rotates of θ degrees.

Flow-induced artifacts cannot be avoided in the studied system. However, imaging this contrast could allow it to be recognised and distinguished from chemistry-induced contrast. Figure 7.12 shows MR images of tap water in the Couette cell at increasing rotation rates.
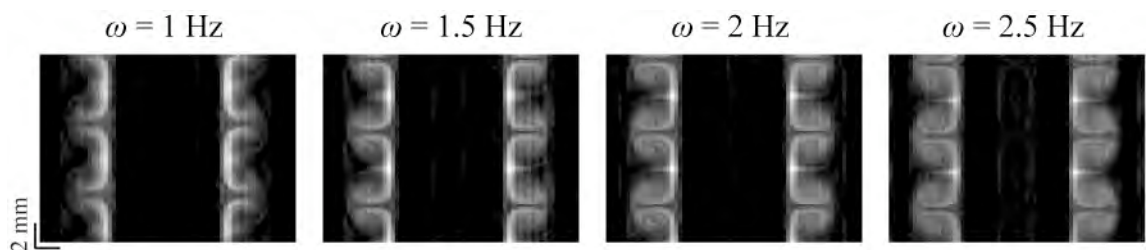
Figure 7.12. MR images of tap water in TVF flow for different rotation rates.

The flow-induced artifacts reflect the vortical structure as vortex pairs can be distinguished. Higher contrast is observed in the regions close to the inner cylinder, where the velocities in the azimuthal direction are stronger. Increasing the rotation rate leads to higher spin loss and more uniformly distributed in the vortex areas. Also, at 2.5 Hz, phase-encoding artifacts caused by the periodic motion of the inner cylinder can bee noticed in the centre of the inner cylinder regions.

Similar results are observed for the translating vortex flow obtained at Q = 7.2 cm min^{-1} and for different rotation rates (Figure 7.13). However, additional flow artifacts are generated by the translation of the vortices, causing a significant image quality decrease (blurring) and phase artifacts appearing as replicates in the phase direction. For $\omega \leq$ 2.5 Hz, measurements of the vortex pair size, λ, are in agreement with the dye experiment results presented previously (cf. 4.3.2). For ω = 2.5 Hz, the λ value measured in the MR images appears significantly larger than the one measured by the dye experiments, indicating the presence of image distortion.
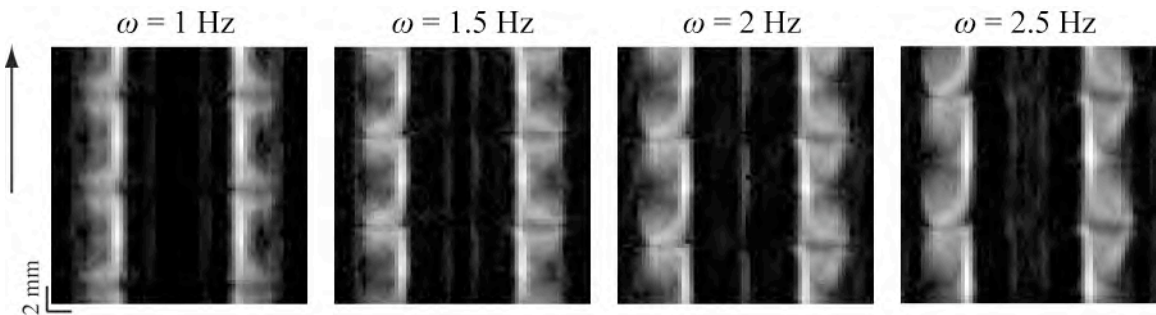
Figure 7.13. MR images of tap water in VFR flow at Q = 7.2 cm^3 min^{-1} and for different rotation rates. The arrow indicates the direction of the flow.

Figure 7.14 shows series of images of translating vortices at $\omega = 1$ Hz and $Q = 7.2$ cm min^{-1}. By following the translation of a vortex pair over time it is possible to measure the translation velocity of the vortices. These results show, that at low flow regimes imaging artifacts can provide with information on flow properties.
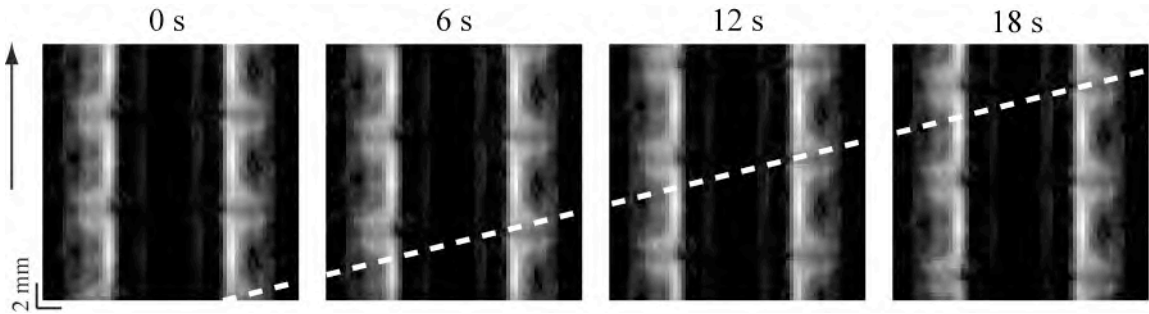
Figure 7.14. Time series of MR images of tap water in VFR flow at $\omega = 1$ Hz and $Q = 7.2$ cm^3 min^{-1}. The black arrow indicates the direction of the flow and the dotted white line the translation velocity of the vortices ($U_{TV} \approx 0.8$ mm s^{-1}).

It is important to understand how this flow-induced contrast will affect the images of BZ chemical waves coupled with these flows. If the flow-induced signal loss is equal or overcomes the signal difference between the reduced and oxidised states of the reaction, then flow-induced contrast might dominate the resulting image contrast. Since the imaging of the BZ chemical waves is going to rely mainly on T_2 contrast, measurements of the overall T_2 evolution at different flow regimes were performed. Figure 7.15 shows plots of tap water T_2 relaxation times against rotation, for stationary and translating vortex flow.
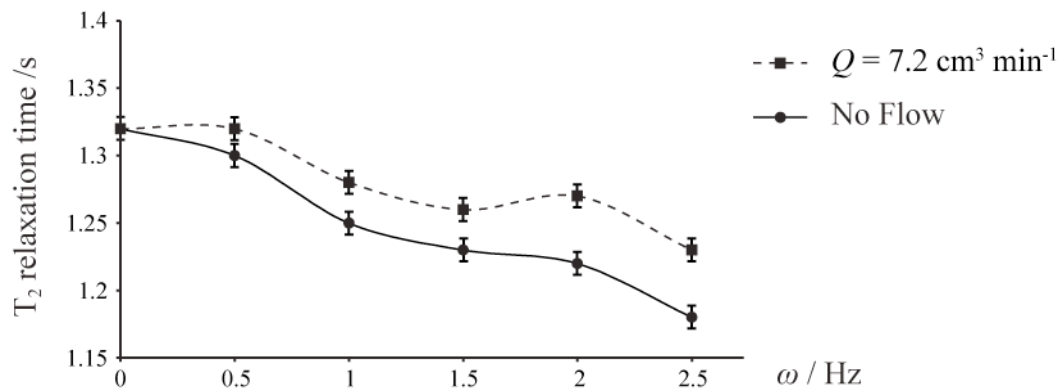
Figure 7.15. T_2 relaxation time against rotation rate for tap water in a Couette cell without flow and at $Q = 7.2$ cm^3 min^{-1}.

The results allow evaluating the relaxation time decrease induced by the flow and compare it to the relaxation time difference between the reduced and oxidised states. At these flow regimes, the reduction in relaxation time caused by flow corresponds to less than 10 % of the relaxation time of tap water. The reduction in relaxation from the oxidised to the reduced states of the BZ reaction was of the order of 100 % (Figure 7.6b). These results suggest that chemistry-induced contrast is going to dominate the MR image contrast. However, in the oscillating BZ system the states are not fully separated and transitions occur where the relaxation time oscillates with the reaction. Flow-induced contrast is expected to have a higher effect on the resulting images close to the regions where the reaction is in intermediate phases or for parameters where the difference in signal between the oxidised and reduced phases is low. The present analysis provides with a tool for distinguishing flow-induced contrast from the contrast generated by the propagation of chemical waves.

7.3.4 MRI of chemical waves in stationary vortices

Figure 7.16 shows MR images of travelling waves through stationary TVF at $\omega = 1$ Hz. The chemical waves (in light grey on the images) are clearly visible at all Mn concentrations. Flow-induced artifacts, can be distinguished at the bottom of Figure 7.16a. As expected, flow-induced contrast is more apparent for the images at Mn = 0.5 mM, where the signal difference between the oxidised and reduced states was found to be lower. These artifacts allow identifying the vortex positions and analysing the wave propagation with respect to the flow.
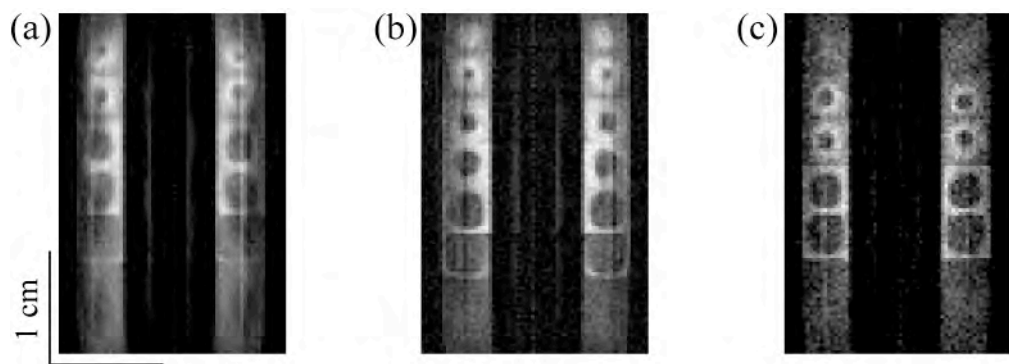
Figure 7.16. MR images of chemical wave propagation in TVF flow at $\omega =1$ Hz for (a) [Mn] = 0.5 mM at $T_E = 20$ ms, (b) [Mn] = 1 mM at $T_E = 15$ms and (c) [Mn] = 2 mM at $T_E =10$ ms.

The waves are first consuming the reactants in the outer vortex regions, appearing to wrap around the vortex cores. The core region of the vortices is longer to consume, probably due to the poor intra-vortex mixing at this regime. Hence, the propagation of the waves on the outer vortex regions has several vortices of advance to the consumption of the vortex cores. A similar behaviour was observed in the propagation of bromate-sulfite fronts at this regime (cf. 5.4.6), but also in the experiments of Thompson *et al.*[8].

7.3.4.1 Wave initiation points

The initiation region of the chemical waves seems to depend on the filling conditions. When the inner cylinder was rotating during the filling of the Couette cell as in Figure 7.16, the waves were initiated from pacemakers located at the top of the reactor. This is probably due to the plug-like properties of the reactor. The first reactants to penetrate the cell, found towards the outlet of the cell, reach the end of the BZ induction period prior to the reactants at the inlet. An oxidative wave is therefore initiated at the top of the reactor and propagates downwards.

If the rotation of the inner cylinder is activated after the filling of the cell, the reactants are not distributed in space according to their entrance time so pacemakers can appear at different positions along the length of the reactor. Figure 7.17 shows the onset of a chemical wave from a pacemaker site.
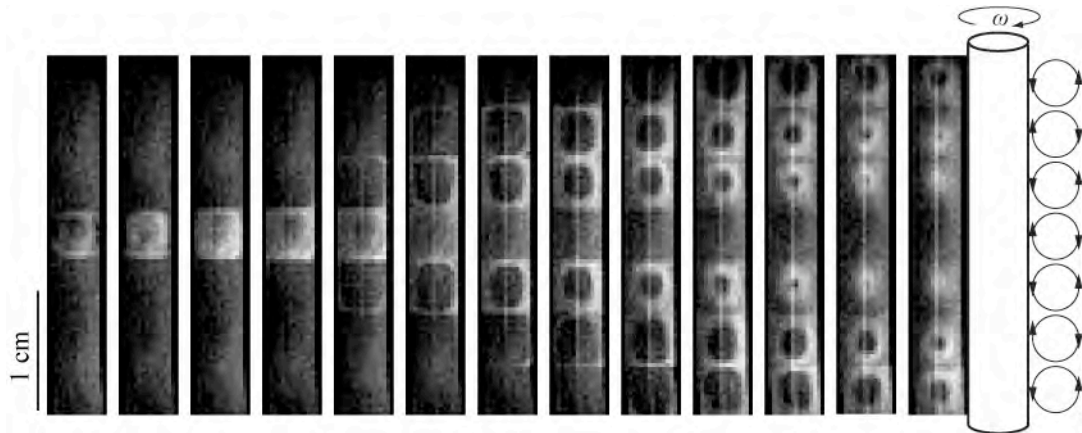
Figure 7.17. Series of MR images of chemical wave pacemaker in TVF flow at ω =1 Hz and for [Mn] = 1 mM. Each image shows the left hand side of the reactor. Time interval between the images is of 6 s.

Here again, flow-induced contrast, appearing along the inner cylinder, allows identifying the vortex positions. Initially, a single vortex switches to the oxidised phase. The reaction seems to first consume the reactants within the initiation vortex, before a wave starts propagating to the neighbouring ones. As for the systems seen previously, the core region of the vortices is longer to consume. Hence, the waves travelling on the outer regions can attain several vortices before the core of the initial one is fully consumed.

Note that the chemical waves are propagating slower close to the pacemaker position. Studying chemical waves generated by random pacemaker positions does not allow comparing chemical wave propagation speed, since the wave velocity is affected close to the pacemakers. Therefore, for all the subsequent experiments, the inner cylinder was rotating during the filling of the reactor so that the pacemakers are located at the outlet, and the system was left to equilibrate for 5 minutes before acquisition.

7.3.4.2   Wave propagation

Figure 7.18 shows series of images of chemical wave propagation. At [Mn] = 0.5 mM and at [Mn] = 1 mM (Figure 7.18a), a similar wave propagation speed was found (about 3 cm min^{-1}) while for the BZ system with [Mn] = 2 mM (Figure 7.18b) the waves travelled much slower (about 1.5 cm min^{-1}). This result seems to be in agreement with the previously presented space-time plots of pattern formation (Figure 7.4), where much longer time for the wave settlement was observed at [Mn] = 2 mM.
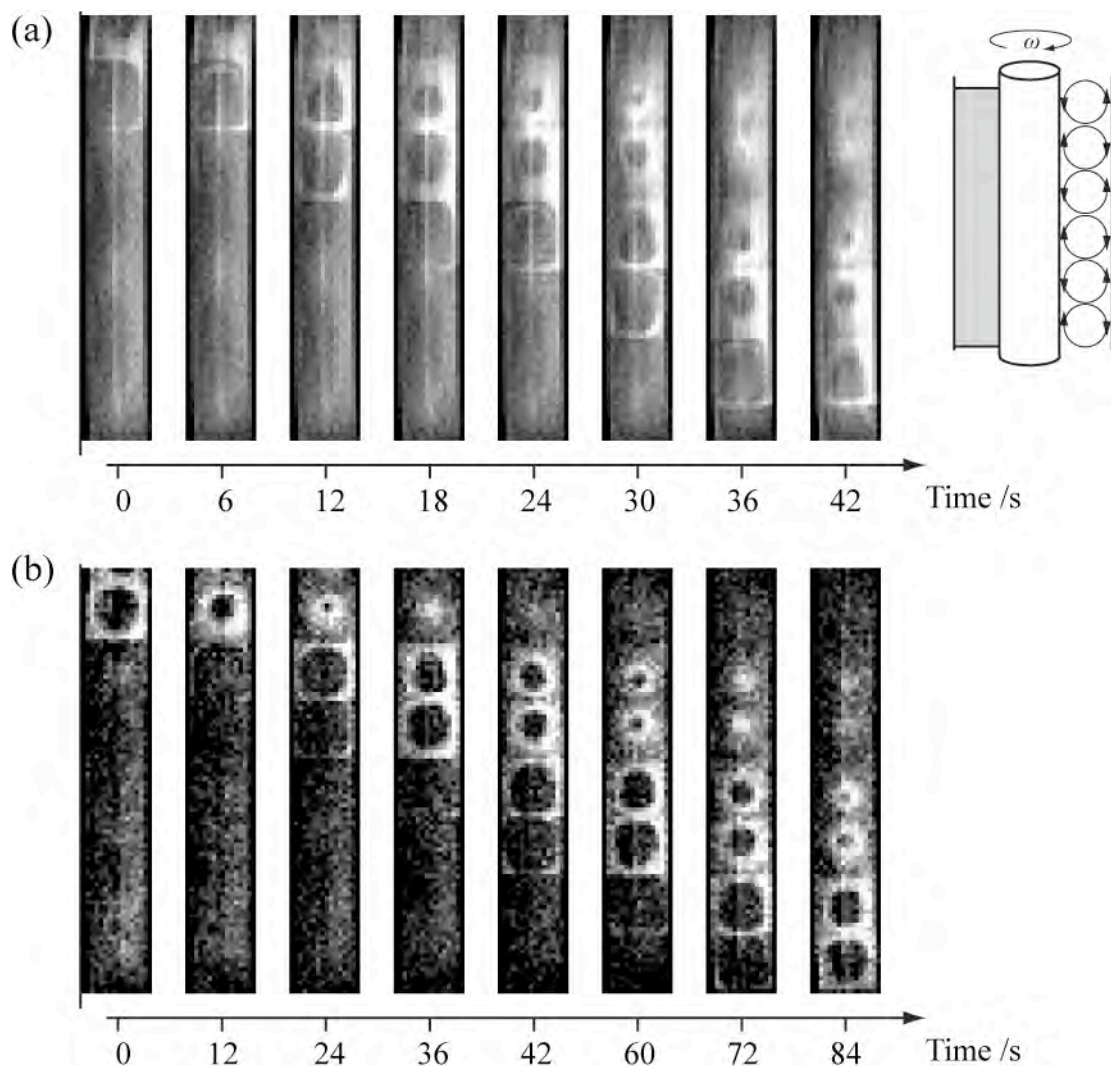
Figure 7.18. Series of MR images of chemical wave propagation in TVF flow at ω =1 Hz for (a) [Mn] = 1 mM and (b) [Mn] = 2 mM. Each image shows the left hand side of the reactor as indicated in the schematic diagram (a). Time interval between the images is of 6 s.

7.3.4.3 The effect of rotation on wave propagation

In order to study the effect of rotation on the propagation of chemical waves, experiments at higher rotation rates were conducted. As enhanced flow artifacts were expected at these

regimes only the systems with [Mn] = 1 mM and [Mn] = 2 mM were considered, where less artifacts were observed at ω = 1 Hz (Figure 7.16).

Figure 7.19 shows series of images of chemical waves for the BZ system at [Mn] = 1 mM. At higher rotation rates, the speed of the wave propagation and the consumption time of the core region are increased. This is probably due to enhanced intra-vortex mixing properties at these regimes.
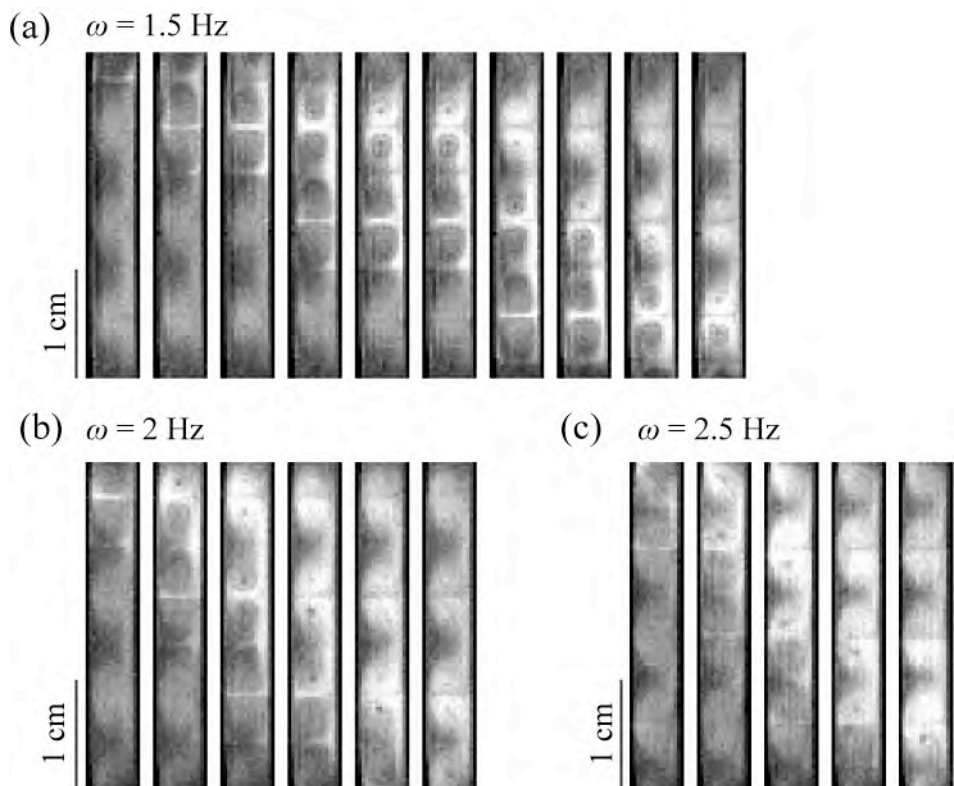
Figure 7.19. Series of MR images of chemical wave propagation ([Mn] = 1 mM) in TVF flow at ω values of (a) 1.5 Hz, (b) 2 Hz and(c) 2.5 Hz. Each image shows the left hand side of the reactor. Time interval between the images is of 6 s.

A similar behaviour is observed for the reaction at [Mn] = 2 mM (Figure 7.20). Note that for $\omega \geq 1.5$ Hz, the speed of the wave propagation is increased and found to be of the same order as for the solutions with lower Mn concentrations.
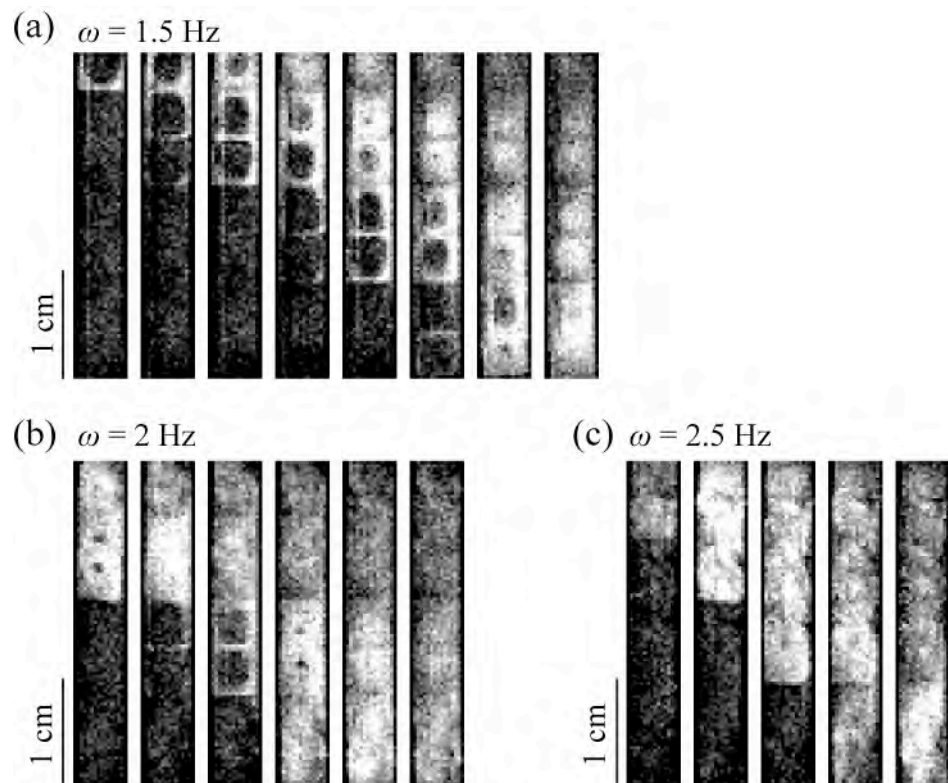
Figure 7.20. Series of T_2 weighed images of chemical wave propagation ([Mn] = 1 mM) in TVF flow at ω values of (a) 1.5 Hz, (b) 2 Hz and(c) 2.5 Hz. Each image shows the left hand side of the reactor. Time interval between the images is of 6 s.

The poor quality of the images at higher rotation rates makes it not easy to define an effective speed for the wave propagation. However it is easier to evaluate the time taken by a wave to consume the core of a vortex. This consumption time corresponds to the time between the moment that the oxidised phase wave wraps around the vortex to the moment it reaches the centre of the vortex. Figure 7.21 shows plots of the consumption time of the vortex core as a

function of the rotation rate. Error bars in these plots correspond to the time between image acquisitions (6 s). Linear decrease is found for the [Mn] = 1 mM system for all rotation rates. For the [Mn] = 2 mM system the decrease is sharp between 1 Hz and 1.5 Hz and follows a linear trend for higher rotation rates.
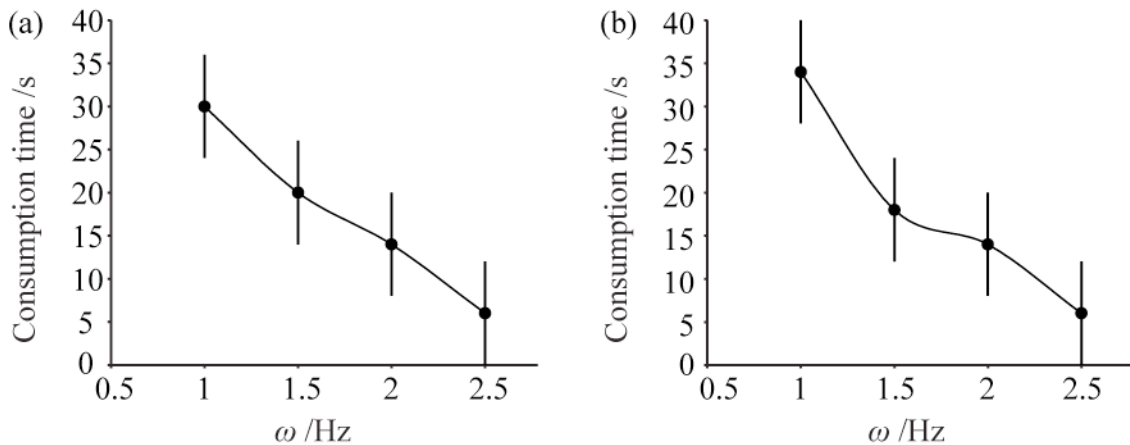
Figure 7.21 Intra-vortex consumption time at different rotation rates for (a) [Mn] = 1 mM and (b) [Mn] = 2 mM.

The decrease in the consumption time can be related to the increase of intra-vortex velocities and dispersion with rotation rate, but the differences in the plots for Mn =1 mM and Mn =2 mM cannot be explained by the flow properties. Substances are distributed in space by the interplay of flow driven molecular paths with local chemical reactions converting substances into each other. Thompson *et al.*[8] showed how the behaviour of propagating waves in such systems depends on the characteristic times of flow and chemistry. Mn concentration can affect both the wave velocity and the BZ reaction oscillation period. In the later case, mode-locking phenomena can occur between flow and chemistry characteristic times[15,16]. To have a better understanding of the role of chemistry on the propagation of the chemical wave,

comparison can be made with the molecular path simulation results obtained in chapter 5 (cf. 5.4.5).

7.3.4.4   Comparison with molecular path simulations

Molecular paths at the same flow regime appear to reproduce the main features of the chemical wave propagation within TVF (Figure 7.22).
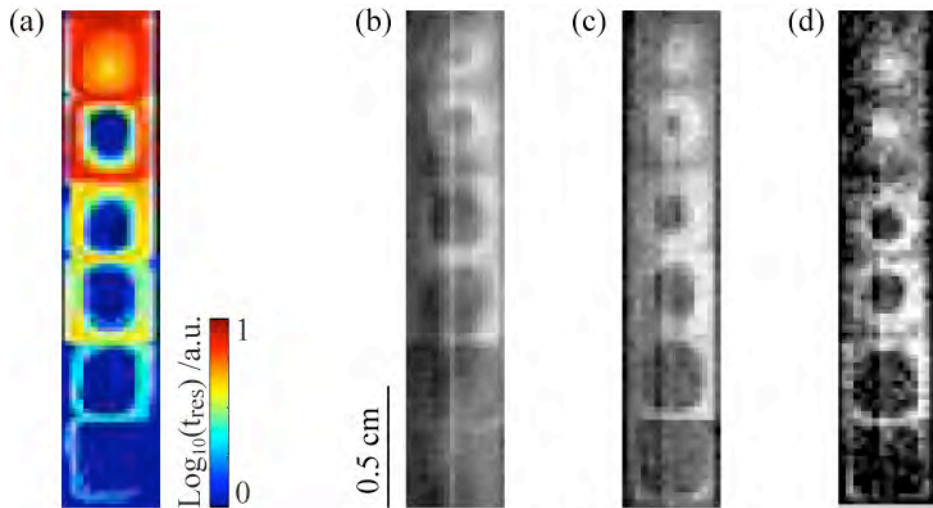
Figure 7.22 (a) Molecular path simulations for TVF flow at ω =1 Hz. (b-d) T_2 weighed images of chemical wave propagation in TVF flow at ω =1 Hz for (a) [Mn] = 0.5 mM, (b) [Mn] = 1 mM and (c) [Mn] = 2 mM at T_E =10 ms. The inner cylinder is situated at the left-hand side of each image.

The chemical wave wraps around the vortex core in a similar way as the molecular paths. Nugent *et al.*[17] have also observed strong correlation between pattern formation of the BZ reaction and passive tracer mixing in vortical flow. This suggests that the chemical wave shape in this system is mainly defined by the flow properties. Note that molecules take more

time to reach the vortex core in the simulation, than the time taken by the chemical wave to consume the vortex core in the experimental results. The difference between these times could provide with information on the relative input of flow and chemistry into the propagation of this front. This analysis is expected to be more complicated in the case of travelling vortex flow as the molecular paths simulations in a stationary reference frame gave very complex outcomes.

7.3.5 MRI of travelling chemical waves in translating vortices

In the previous chapter it was shown that travelling BZ waves could be obtained in a VFR. The waves were observed for unstable boundary conditions, when the CSTR at the inlet of the reactor was oscillating. Similar conditions can be created if an oscillating BZ reaction mixture is pumped in the VFR.

Figure 7.23 shows images of BZ waves (in light grey) in translating vortex flow at $\omega =1$ Hz and $Q = 7.2$ cm3 min^{-1}. The phase oscillations of the mixture at the inlet produced waves that travelled through the translating vortex flow until reaching the outlet of the reactor. At this flow regime the vortices were found to travel at about 0.8 mm s^{-1} (Figure 7.14). Although the wave velocity is difficult to determine with accuracy in this system, the waves appear to travel at a similar velocity to the vortices. Also, in contrast to the results obtained for stationary vortices, the speed of the wave is found to be similar for both Mn concentrations studied (1 mM and 2 mM). This could be due to the dominant role of flow in the wave propagation.
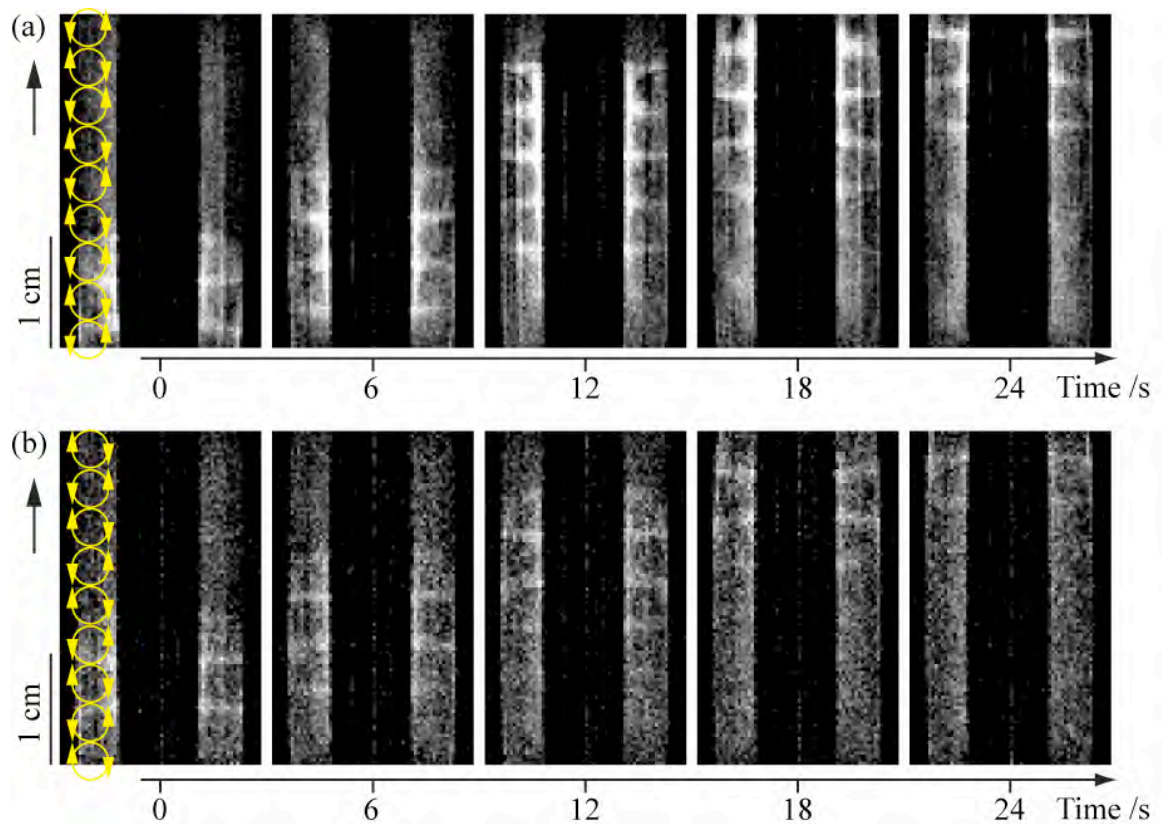
Figure 7.23. Series of MR images of chemical wave propagation in travelling vortex flow at ω =1 Hz and Q = 7.2 cm3 min^{-1}, for (a) [Mn] = 1 mM and (b) [Mn] = 2 mM. Time interval between the images is of 6 s. The black arrow indicates the flow direction and a schematic representation of the vortices is given in yellow.

The analysis of the features of the propagating waves must be done with precaution as these features present similarities with flow artifacts at the same regime (Figure 7.14). For both manganese concentrations studied, the oxidised phase wave is seen mainly in the outer regions of the vortices situated near the inner cylinder and in the inter-vortex areas. Note that one over two inter-vortex areas is bended, with the outer part being lower than the inner one. This has not been noticed in the flow artifact images. But the most surprising feature of these images is that the vortex core and the outer part of the vortices situated near the outer cylinder

are maintained in the reduced phase during the wave propagation. Slight phase changes in these regions seem to affect only one vortex of each pair. This could not be attributed to flow artifacts, as only symmetric structures were observed in flow-induced contrast images. On the other hand, this phenomenon could be explained by the propagators obtained by molecular displacement simulations (cf. 5.4.6) at this regime. The simulations showed both the heterogeneous distribution of molecules into successive vortices and the bending of the inter-vortex areas.

Figure 7.24 shows molecular path simulations in comparison with the propagating wave at the same flow regime. The doted square in Figure 7.24a highlights molecules travelling slower than the vortices (drag flow). Figure 7.24b is obtained by duplicating the highlighted part of the map and changing the contrast so that regions attended by the drag flow appear in black. Similarities can be seen between this image and the MR image of the propagating wave. The constant arrival of molecules in the reduced state from downstream vortices (represented in black in Figure 7.24b) could explain that the regions near the outer wall are not reached by the chemical wave. Moreover, the regions that are not attended by the drag flow in the simulations seem to correspond to the regions in the oxidised state on the MR images. Both light grey regions in Figure 7.24b and the chemical waves in Figure 7.24b travel at a similar speed to the one of the travelling vortices. On the other hand, in the simulations only one over two inter-vortex areas is attended by drag flow molecules while the chemical wave reaches all inter-vortex areas.
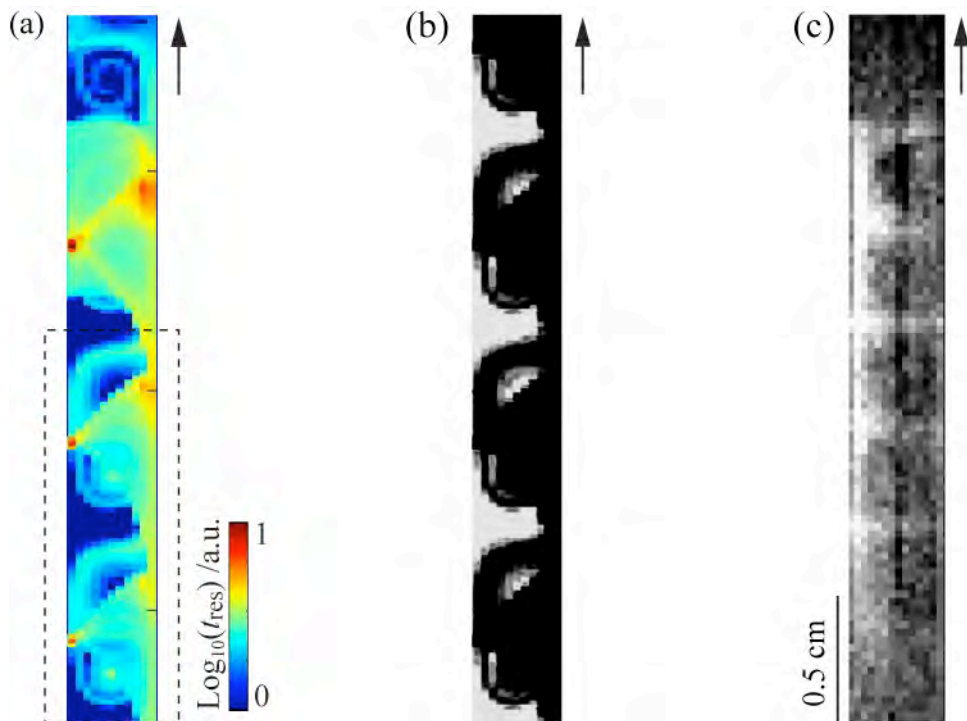
Figure 7.24. (a) Molecular paths in the reference frame of the travelling vortices. (b) Edited version of image (a) where regions attended by the molecules are in black colour and regions not attended are in grey colour. (c) MR images of chemical wave propagation in travelling vortex flow. The inner cylinder is situated at the left-hand side of each image.

As discussed earlier, precaution should be taken in interpreting these results. But even if the simulations do not capture all the features of the propagating waves, they allow identifying regions where the wave propagation is disturbed by the flow. These regions might correspond to "burning invariant manifolds", BIMs. The concept of BIMs was introduced recently by Mahoney *et al.*[18] to describe fixed or space-periodic front propagation barriers. The existence of such barriers, constantly maintained by the inflow of reactants, might explain the observation of vortex areas that are not consumed by the propagating waves.

7.3.6 MR Imaging of Mn-catalysed BZ FDOs

MR imaging was used to investigate stationary waves in translating vortex flow (FDOs). The possibility to obtain FDOs in the VFR using the manganese-catalysed BZ reaction has been demonstrated previously (Figure 7.4). Figure 7.25a shows images of the first stationary band for the [Mn] = 1 mM system.
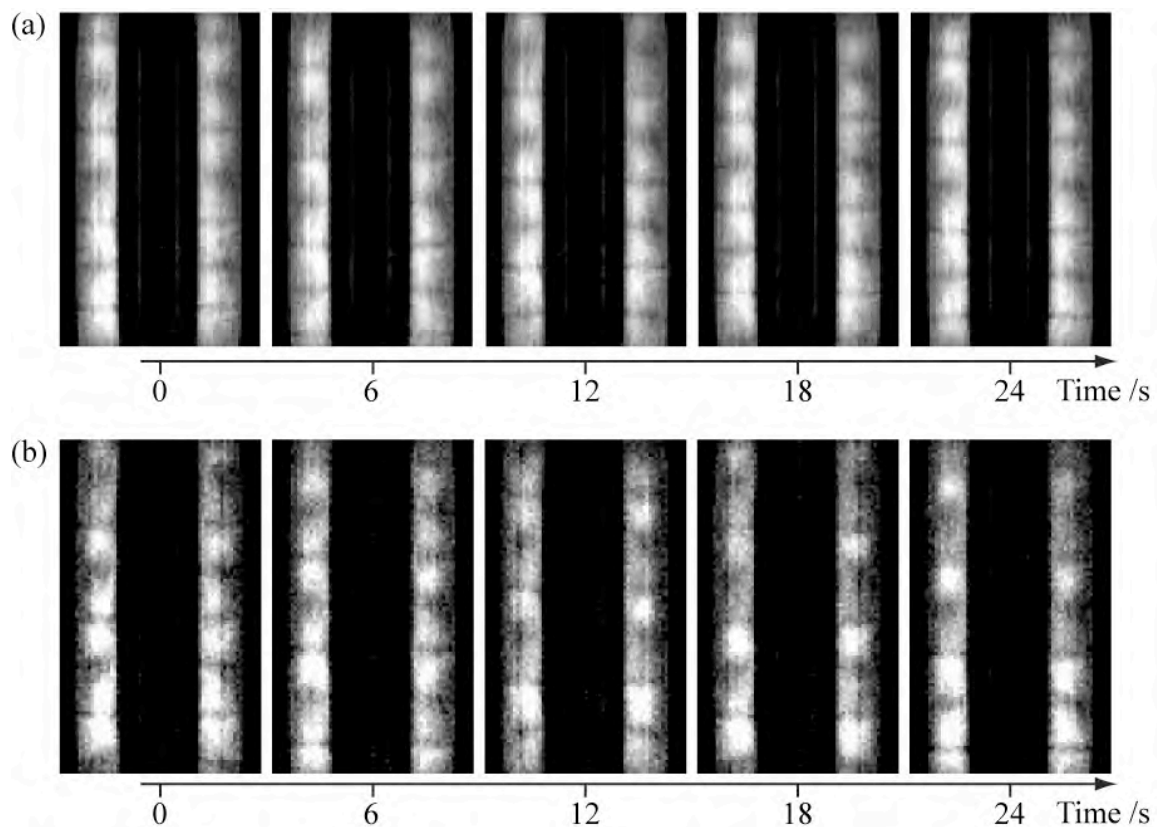
Figure 7.25. Series of MR images of the first FDO band of the [Mn] = 1 mM system at t = 2000 s. Images where taken at the centre (a) and the top (b) of the band.

The band is larger than the field of view, so only the centre of the band is seen. The vortex cores are in the oxidised phase (light grey), while the outer areas appear to be in the reduced phase (dark grey). As differences between phases are expected to be weak in the middle of the

band where phase is more uniform, part of the contrast might be induced by flow. Note that the regions close to the outer cylinder are darker. This could be caused by the molecular drag of molecules in the reduced phase or related to flow induced contrast.

Figure 7.25b shows images of the top part of the same band. At the bottom of the image the waves are similar to the ones in the middle of the band. At the top, vortices in reduced phase can be observed. Similarly to the previously observed behaviour, one over two vortices in this region is in the oxidised phase with the other being in the reduced. This phenomenon, leads to the observation of segmented bands. Similar bands were observed in the ferroin-catalysed BZ system at the same flow parameters (cf. 6.3.2).

While the flow parameters are the same, the heterogeneous phase distribution is less pronounced for the [Mn] = 2 mM system (Figure 7.26). These results stress once more the crucial role of chemistry in defining the resulting pattern formation but also the possible existence of chemistry-flow synchronisation phenomena where the BZ reaction phases in odd and even vortices can synchronise independently[19].
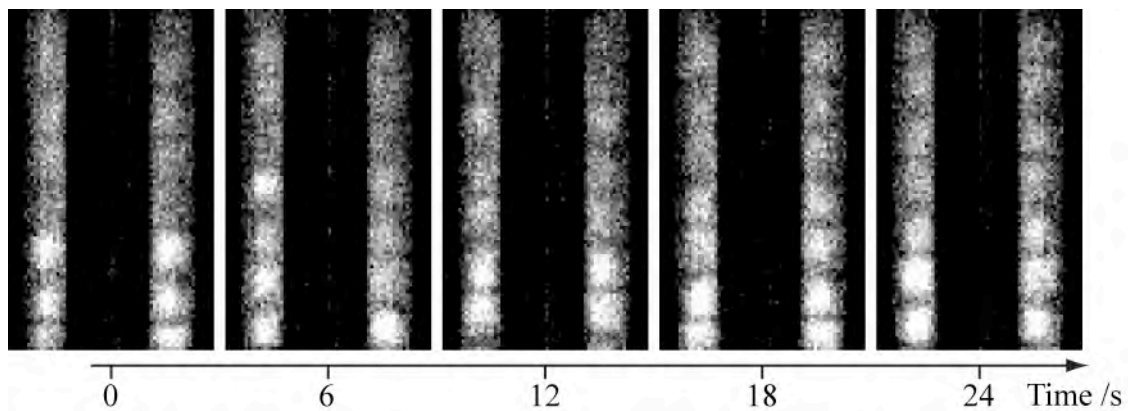
Figure 7.26. Series of MR images of the first FDO band of the [Mn] = 2 mM system at t = 5200 s. Images where taken at the top of the band.

7.4 Conclusions

The methodology and results presented in this section set a framework for more systematic studies that could allow getting a deeper understanding of the flow-chemistry coupling properties of RDA systems involving vortical flow.

This work has shown that stationnary chemical waves (FDOs) can be obtained when the Mn-catalysed BZ reaction is coupled with translating vortex flow. The wavelength of the stationary bands was found to be not linearly dependent on the oscillation period, showing that the chemical oscillations are not simply spatially resolved by plug-flow as suggested by the FDO kinematic model. The catalyst concentration was shown to play an important role, not only in defining the oscillation period of the reaction but also the wave propagation velocity and its shape features.

For travelling waves in stationary vortices (TVF), intra-vortex consumption time was shown to decrease with rotation, stressing the relation between intra-vortex mixing and rotation rate in TVF. The main features of the wave propagation were shown to be similar to those of simulated molecular paths in this flow. The possible use of this comparison in distinguishing flow from chemistry related propagation was discussed.

For travelling chemical waves in translating vortex flow, the vortex core was maintained in the reduced phase during the wave propagation. When stationary chemical waves were obtained the vortex core was constantly in the oxidised phase. These features could be explained by molecular displacements within the system or by the synchronisation between

251

flow and chemistry characteristic times, where inflow and outflow of reactants in a vortex area can maintain the reaction in a stationary state.

(1)   Gao, Y.; Cross, A. R.; Armstrong, R. L. *J. Phys. Chem.* **1996**, *100*, 10159.

(2)   Schlüter, A.; Weiss, A. *Berichte der Bunsengesellschaft für physikalische Chemie* **1981**, *85*, 306

(3)   Binks, D. A. Magnetic resonance studies of chemical reactions in microemulsions, University of Birmingham, 2009.

(4)   Menzinger, M.; Tzalmona, A.; Armstrong, R. L.; Cross, A.; Lemaire, C. *J. Phys. Chem.* **1992**, *96*, 4725.

(5)   Tzalmona, A.; Armstrong, R. L.; Menzinger, M.; Cross, A.; Lemaire, C. *Chem. Phys. Lett.* **1990**, *174*, 199.

(6)   Cross, A. R.; Armstrong, R. L.; Reid, A.; Su, S. Y.; Menzinger, M. *J. Phys. Chem.* **1995**, *99*, 16616.

(7)   Britton, M. M.; Sederman, A. J.; Taylor, A. F.; Scott, S. K.; Gladden, L. F. *J. Phys. Chem. A* **2005**, *109*, 8306.

(8)   Thompson, B. W.; Novak, J.; Wilson, M. C. T.; Britton, M. M.; Taylor, A. F. *Phys. Rev. E* **2010**, *81*.

(9)   Rhodes, F. H.; Barbour, C. B. *Industrial and Engineering Chemistry* **1923**, *15*, 850.

(10)   Cross, A. R. The development of Three dimensional magnetic resonance imaging of the Belousov-Zhabotisky reaction, The University of New Brunswick, 1998.

(11)   Bellon, E. M.; Haacke, E. M.; Coleman, P. E.; Sacco, D. C.; Steiger, D. A.; Gangarosa, R. E. *Am. J. Roentgenol.* **1986**, *147*, 1271.

(12)   Henkelman, R. M.; Bronskill, M. J. *Med. Phys.* **1987**, *14*, 506.

(13)   Bloembergen, N.; Purcell, E. M.; Pound, R. V. *Phys. Rev.* **1948**, *73*, 679.

(14)   Taylor, A. F.; Bamforth, J. R.; Bardsley, P. *Phys. Chem. Chem. Phys.* **2002**, *4*, 5640.

(15)   Paoletti, M. S.; Solomon, T. H. *Phys. Rev. E* **2005**, *72*.

(16)   Paoletti, M. S.; Solomon, T. H. *Europhys. Lett.* **2005**, *69*, 819.

(17)   Nugent, C. R.; Quarles, W. M.; Solomon, T. H. *Phys. Rev. Lett.* **2004**, *93*.

(18)   Mahoney, J.; Bargteil, D.; Kingsbury, M.; Mitchell, K.; Solomon, T. *Europhys. Lett.* **2012**, *98*.

(19)   Paoletti, M. S.; Nugent, C. R.; Solomon, T. H. *Phys. Rev. Lett.* **2006**, *96*.

8 Conclusions and future work

The goal of this thesis was to develop an integrated approach to study transport and reaction in vortical flows. This work has been carried out from two perspectives. The first consisted in combining vortical flow with autocatalytic chemistry studies, in order to understand the properties of the coupling between chemistry and flow within these RDA systems. The second consisted in developing techniques and methodologies allowing systematic studies of such RDA systems to be carried out, from the molecular to the macroscopic level.

The properties of vortical flow in a Couette cell were studied in detail. These studies provided the first MR diffusion/dispersion maps of stationary vortex flow and the first MR velocity maps of translating vortex flow. In the later case, it was shown that adapting the pulse sequence to the flow period could eliminate flow artifacts caused by the periodic translation of the vortices. This work demonstrated that the features of translating vortex flow velocity maps could be reproduced by linear addition of pipe and stationary vortex flow velocity maps. Propagator measurements, traditionally used in porous materials, were extended for the first time to vortical flows. MR propagator experiments were shown to overcome the limitations of velocity and diffusion/dispersion mapping, by addressing the complexity of molecular displacements and micro-mixing properties of vortical flows.

Molecular displacement simulations based on experimental MR velocity and diffusion/dispersion maps were also shown to provide rich information on the micro-mixing properties of the flows. These simulations provided explanations both on experimental propagator results and on molecular transport over longer time-scales, not accessible

experimentally. Molecular dispersion, mixing and residence times were assessed. Also, molecular path maps provided spatial information on molecular displacements and pathways within the flows.

Microscopic information obtained by molecular displacement simulations, was shown to reproduce the main features of chemical wave propagation through vortical flow. Simulated propagators, showing heterogeneous molecular distribution within successive vortices, provided with an explanation to the surprising phenomenon of segmented chemical waves observed in all the autocatalytic systems considered in this thesis (bromate-sulfite clock reaction, ferroin- and manganese-catalysed BZ reaction). These results suggest that precaution should be taken when analysing synchronisation phenomena in systems combining autocatalytic chemistry and vortical flow, since statistically negligible molecular displacements might play an important role on the propagation of autocatalytic fronts. MR imaging studies of the manganese-catalysed BZ reaction waves provided deeper insight into the coupling between autocatalytic chemistry and vortical flow. Several features of the wave propagation were found on the simulated molecular path maps, while their differences could give information on the relative effects of chemistry and flow.

Macroscopic information, obtained by FDO patterns, was shown to provide information on the mixing properties of the flow. This work showed that the combination of the BZ reaction with travelling vortex flow produces stationary flow distributed oscillations (FDOs) for a significant range of chemistry and flow parameters. The catalyst concentration was shown to play an important role, not only in defining the oscillation period of the reaction, but also the wave propagation velocity. These results emphasised the limitation of simple kinematic

models in describing the macroscopic patterns resulting from the coupling of complex plug-like flow with autocatalytic oscillatory reactions.

This thesis explored a series of techniques and methodologies that were found to produce very promising results that would deserve further investigation. One of these techniques is the use of MR propagators for the characterisation of mixing and the quantification of intra-and inter-vortex mixing in vortical flow. The development of this technique could involve systematic studies of various vortical flows at different regimes but also different PGSE gradient axes. Another technique that deserves attention is the use of triggered pulse sequences for the study of periodic flows. Since respiratory-triggered pulse sequences are already commonly used in medical imaging[1], the generalised use of this technique to image periodic flows should only be a matter of time. Recently, a similar technique was used for obtaining velocity maps of pulsatile pipe flow[2]. Finally, molecular displacement simulations based on MR data was shown to provide rich information on molecular displacements within complex systems. This method was shown to introduce quantitative analysis into RDA system studies, which are often limited to qualitative approaches. Further refinements of the simulations could be obtained by comparison with MR propagator data that allow a quantitative evaluation of the simulation quality.

Although these techniques provided deeper insight into the coupling of chemistry and flow within complex RDA systems, the results presented in this work are far from closing the list of open questions regarding these systems. On the contrary, this work has hopefully demonstrated the strong potential of MR techniques not only in addressing open questions, but also in opening new questions, at levels of description that are not accessible with

standard visualisation techniques. The MR techniques used in this thesis are far from exhausting the diverse arsenal of magnetic resonance, and other MR techniques could allow assessing complex features identified in this work. Chemical shift imaging[3] could provide with a functional imaging approach, allowing tracking the evolution of different reactants in space. MR relaxation-resolved propagators[4] could provide with insight into synchronisation phenomena, by probing correlations between reactants and the molecular displacements. Such propagators could be used to evaluate the quality of molecular displacement simulations including chemical information. Ultimately, simulations of molecular displacements, taking into account collisions that convert chemical species into each other, might quantitatively reproduce the molecular processes that lead to the surprising macroscopic features of pattern forming RDA systems.

(1)   Kandpal, H.; Sharma, R.; Madhusudhan, K. S.; Kapoor, K. S. *Am. J. Roentgenol.* **2009**, *192*, 915.

(2)   Shiro, G.; Gladden, L. F.; Sederman, A. J.; Connolly, P. C.; Butler, J. M. *J. Pharm. Sci.* **2011**, *100*, 976.

(3)   Brateman, L. *Am. J. Roentgenol.* **1986**, *146*, 971.

(4)   Britton, M. M.; Graham, R. G.; Packer, K. J. *J. Magn. Res.* **2004**, *169*, 203.

Appendix A: Imaging translating vortices in a VFR

The timed pulse sequence technique presented in chapter 4 (cf.4.2.5), successfully produced velocity maps in a second VFR reactor. The Couette cell used in this study was constructed from an outer glass tube of radius R_o = 8.25 mm and an inner PEEK rod of radius R_i = 5 mm, resulting in a gap, d, of 3.25 mm. The rotation rate was of ω = 1 Hz and the flow rate of Q = 5.5 cm^3 min^{-1}. The PGSE loop time varied from T_{TV} – 500ms to T_{TV} + 500ms. Figure 1 shows a series of intensity maps at different loop times and the respective velocity maps.
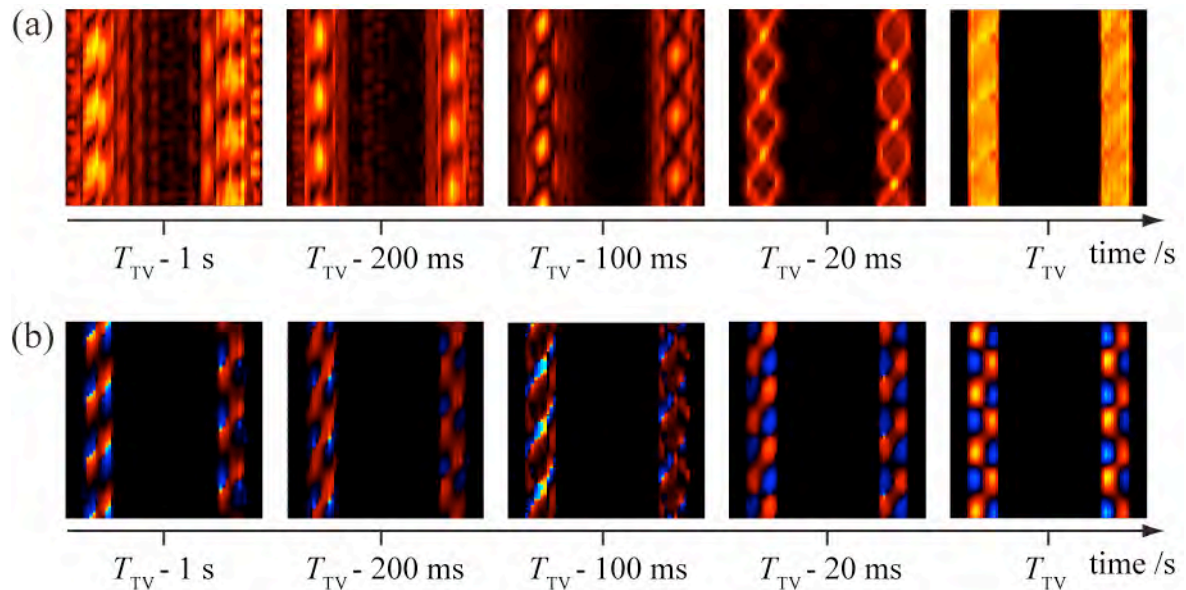
Figure.1. (a) Intensity maps and (b) respective velocity maps of VFR flow (ω = 1 Hz and Q = 5.5 cm^3 min^{-1}), at different PGSE sequence loop timings. The loop that eliminated the artifacts had a period of 3.76 s.

For each one of the imaging series with increasing PGSE loop time, one single measurement produced an intensity map with no appearing artifacts (no signal outside the gap region and no signal loss inside the gap region). The loop time producing this intensity map corresponds

to T_{TV}. The data acquired during this measurement was post-treated to produce a velocity map

of the measured flow. The resulting velocity map is shown in Figure 2.
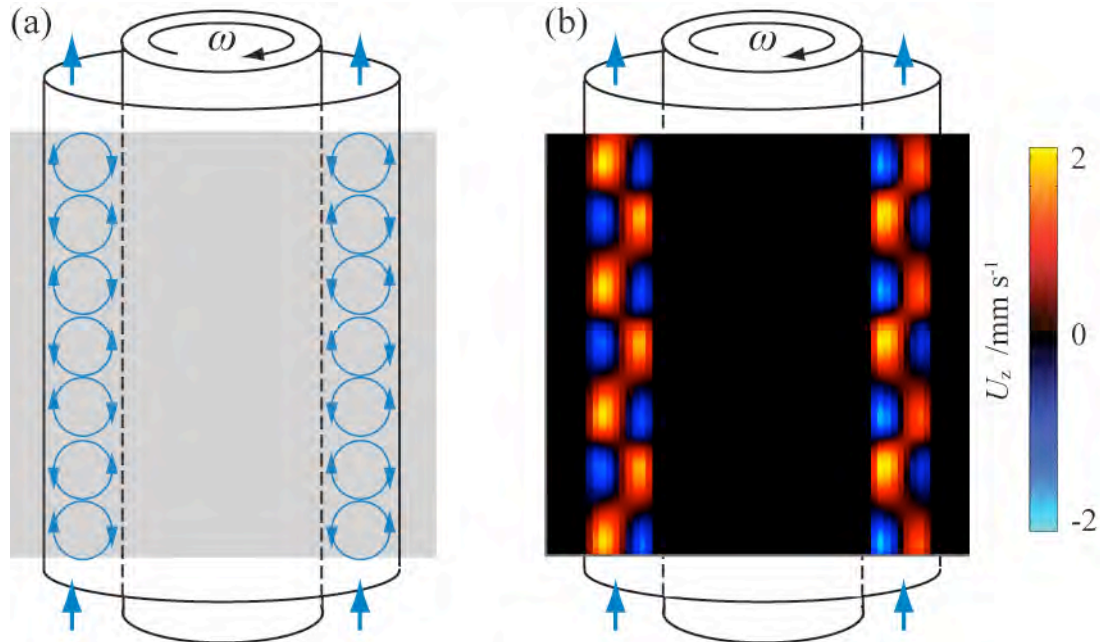
Figure 2. (a) Schematic diagram of translating vortices in a VFR and (b) MR velocity map in

the z direction of VFR flow at ω = 1 Hz and Q = 5.5 cm³ min⁻¹.

Appendix B: MATLAB code for molecular displacement simulations

```
clc % clear command board
```

% I GENERAL PARAMETERS

% Ia Flow parameters

```
lamda=0.0067 % wavelength

gap=0.00475;  % define the y direction distance (in m)

ttv=8.2; %(in s)

vtv=lamda/ttv;  % lamda/Ttv (in m)
```

% Ib Calculation parameters

```
pclm=100 %columns of particles

prow=200 %rows of particles

vpairs=10;

realz=lamda*vpairs; %define the z direction distance as a multiple of one vortex pair wavelength (in m)

init=lamda*3;  % initial position (start third pair of vortices)

fin=lamda*7;  % final position (start fourth pair of vortices)

bins=100;

dt=0.001;  %time step (s)

delta=1;   %mixing time (s)
```

% Ic Velocity/diffusion/dispersion maps parameters

```
yvp=13; %velocity map pixels in the y direction
```

y=yvp+2; %boundary zero velocity condition by adding 2 pixels atvel=0 on each side of the gap

zvprep=45; %pixels repeated in the z direction

zvi=131;

yvi=111;

gapi=44;

gapf=58;

ypix=gap/yvp; %velocity map y direction pixel dimension

zpix=realz/(vpairs*zvprep);%velocity map z direction pixel dimension

% Id Molecule tracking and analysis parameters

maxthresh=0.95;

minthresh=0.05;

mid1=0.1;

mid2=0.3;

maxorigin=zeros(y,vpairs*zvprep);

minorigin=zeros(y,vpairs*zvprep);

disorigin=zeros(y,vpairs*zvprep);

pathmap=zeros(y,vpairs*zvprep);

pathmaphalf=zeros(y,vpairs*zvprep);

pathmap0=zeros(y,vpairs*zvprep);

% II IMPORT AND ADJUST THE VELOCITY AND DIFFUSION/DISPERSION MAPS

% IIa Velocity maps

yvelmap=zeros(y,vpairs*zvprep); %define y direction experimental velocity map

zvelmap=zeros(y,vpairs*zvprep); %define z direction experimental velocity map

```
for v=0:(vpairs-1)

  for k=1:zvprep

    zvelmap(1:y,k+v*zvprep)=transpose(zdata(gapi:gapf,k+zvi));

    yvelmap(1:y,k+v*zvprep)=transpose(ydata(gapi:gapf,k+yvi));

  end

end
```

% IIb Diffusion/dispersion maps

```
ydiffmap=zeros(y,vpairs*zvprep); %define y direction experimental velocity map

zdiffmap=zeros(y,vpairs*zvprep); %define z direction experimental velocity map


for v=0:(vpairs-1)

for k=1:zvprep

    zdiffmap(1:y,k+v*zvprep)=transpose(zdatad(gapi:gapf,k));

    ydiffmap(1:y,k+v*zvprep)=transpose(ydatad(gapi:gapf,k));

  end

end
```

%%% III GENERATE MOLECULE MATRIX

```
n=prow*pclm;%number of molecules followed

position0=zeros(n,2);

zstep=(fin-init)/(prow+1);

ystep=gap/(pclm+1);

x=1;
```

```
for r=0:prow

   for c=0:pclm

      position0(x,1)=ystep/2 + c*ystep;

      position0(x,2)=init +zstep/2+ r*zstep;

      x=x+1;

   end

end
```

%%% IV MOLECULE DISPLACEMENT SIMULATION

```
positiont=position0;

velt=zeros(n,2);

dift=zeros(n,2);

t=0


while(t <= delta) % dt time step loop


   for m=1:n


      %      %Wall bounceback condition

      if positiont(m,1)<=0

         positiont(m,1)=-positiont(m,1);

      elseif positiont(m,1)>gap

         positiont(m,1)=positiont(m,1)-2*(positiont(m,1)-gap);

      end


      %coordinates
```

```
   ycoord=abs(ceil(positiont(m,1)/ypix))+1;

   zcoord=abs(ceil((positiont(m,2)-vtv*t)/zpix))+1;

   coefy=(positiont(m,1)/ypix)/ycoord;


 %velocity

 velt(m,1)=coefy*yvelmap(ycoord,zcoord)+(1-coefy)*yvelmap(ycoord-1,zcoord);

 velt(m,2)=coefy*zvelmap(ycoord,zcoord)+(1-coefy)*zvelmap(ycoord-1,zcoord);


 %diffusion

 rnd=2*pi*rand(1);

 dift(m,1)=cos(rnd)*sqrt(4*(coefy*ydiffmap(ycoord,zcoord)+(1-coefy)*ydiffmap(ycoord-

1,zcoord))*dt);

   dift(m,2)=sin(rnd)*          sqrt(4*(coefy*zdiffmap(ycoord,zcoord)+(1-coefy)*zdiffmap(ycoord-

1,zcoord))*dt);


   pathmap(ycoord,zcoord)=pathmap(ycoord,zcoord)+1;
 end


 if t==dt
   pathmap0=pathmap;
 end


positiont(1:n,1)=positiont(1:n,1)+ dt*velt(1:n,1) + dift(1:n,1);

positiont(1:n,2)=positiont(1:n,2)+ dt*velt(1:n,2) + dift(1:n,2);


t=t+dt;
```

```
    d=1;


end



%%% V DISPLACEMENTS

% Va Overall displacements

displacement=positiont(1:n,2)-position0(1:n,2);

dmax= max(displacement)

dmin=min(displacement)



% Vb Origin of max and min displacement

for m=1:n

    if displacement(m)>=maxthresh*dmax

        ycoord=ceil(position0(m,1)/ypix)+1;

        zcoord=ceil(position0(m,2)/zpix)+1;

        maxorigin(ycoord,zcoord)=maxorigin(ycoord,zcoord)+1;


    elseif displacement(m)<=minthresh*dmax

        ycoord=ceil(position0(m,1)/ypix)+1;

        zcoord=ceil(position0(m,2)/zpix)+1;

        minorigin(ycoord,zcoord)=minorigin(ycoord,zcoord)+1;

    elseif (displacement(m)<=mid2*dmax)&(displacement(m)>=mid1*dmax)

        ycoord=ceil(position0(m,1)/ypix)+1;

        zcoord=ceil(position0(m,2)/zpix)+1;

        disorigin(ycoord,zcoord)=disorigin(ycoord,zcoord)+1;

end
```

```
end


pathlog=log(pathmap);


% Vc Histogram / propagator
dstep=(dmax-dmin)/bins;

xaxis=dmin:dstep:dmax;

histo=hist(displacement,xaxis);

% for m=1:bins

%     nhisto(m)=histo(m)/n

% end

plot(xaxis,histo)

title('Displacements distribution')

xlabel('displacements (m)')

ylabel('Number of particles')
```

Characterising stationary and translating vortex flow using magnetic resonance

Antoine Vallatos, Mark C. T. Wilson, Annette F. Taylor and Melanie M. Britton

Citation:

View online:

Chemical patterns in translating vortices: Inter- and intra-cellular mixing effects

Antoine Vallatos, Rhys Evans, Barnaby W. Thompson, Annette F. Taylor, and Melanie M. Britton

List of Figures

Abbreviations

AI: absolute instability

BZ: Belousov-Zhabotisky

CI-FDO: flow distributed oscillations formed via convective instability

CSTR: continuous stirring tank reactor

FID: free induction decay

FDO: flow distributed oscillations

FDS: flow distributed structures

FNK: Field-Noyes-Koros mechanism

NMR: nuclear magnetic resonance

NS equation: Navier-Stokes equation

MRI: magnetic resonance imaging

PBR: packed-bed reactor

PGSE: pulsed gradient spin echo

PGSTE: pulsed gradient stimulated echo

PIV: particle imaging velocimetry

RD: reaction-diffusion

RDA: reaction-diffusion-advection

rf: radio frequency

TVF: Taylor vortex flow

TW: travelling waves

VFR: vortex flow reactor